



Universidade Federal do Rio de Janeiro
Centro de Ciências Matemáticas e da Natureza
Observatório do Valongo
Programa de Pós Graduação em Astronomia



Tools to discover planetary and symbiotic nebulae in optical multi-band photometric surveys

Luis Angel Gutiérrez Soto

Rio de Janeiro

Dezembro de 2019

Tools to discover planetary and symbiotic nebulae in optical multi-band photometric surveys

Luis Angel Gutiérrez Soto

Tese de Doutorado submetida ao Programa de Pós Graduação em Astronomia, Observatório do Valongo, da Universidade Federal do Rio de Janeiro, como parte dos requisitos necessários à obtenção do título de Doutor em Ciências (Astronomia).

Orientadora: Dra. Denise Rocha Gonçalves

Co-orientador: Dr. Stavros Akras

Rio de Janeiro
Dezembro de 2019

CIP - Catalogação na Publicação

S718t Soto, Luis Angel Gutiérrez
Tools to discover planetary and symbiotic
nebulae in optical multi-band photometric surveys /
Luis Angel Gutiérrez Soto. -- Rio de Janeiro, 219.
166 f.

Orientadora: Denise Rocha Gonçalves.
Coorientador: Stavros Akras.
Tese (doutorado) - Universidade Federal do Rio
de Janeiro, Observatório do Valongo, Programa de Pós
Graduação em Astronomia, 219.

1. Evolução estelar. 2. Nebulosas planetárias. 3.
Estrelas simbióticas. 4. Fotometria. 5.
Espectroscopia. I. Gonçalves, Denise Rocha, orient.
II. Akras, Stavros, coorient. III. Título.

Tools to discover planetary and symbiotics nebulae in optical multi-band photometric surveys

Luis Angel Gutierrez Soto

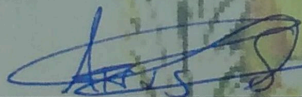
Dr^a. Denise Rocha Gonçalves (Orientadora)
Dr. Stavros Akras (Coorientador)

Tese de doutorado submetida ao Programa de Pós-Graduação em Astronomia, Observatório do Valongo, da Universidade Federal do Rio de Janeiro - UFRJ, como parte dos requisitos necessários à obtenção do título de Doutor em Ciências - Astronomia.

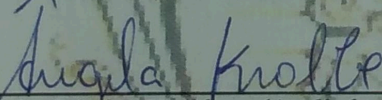
Aprovada por:



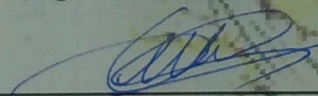
Presidente, Dr^a. Denise Rocha Gonçalves - (Orientadora) - OV/UFRJ



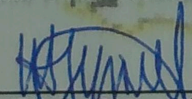
Dr. Stavros Akras - (Coorientador) - FURG



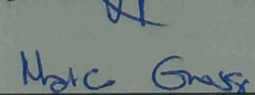
Dr^a. Angela Cristina Krabbe - (Avaliadora Externa) - UNIVAP



Dr^a. Isabel Regina Guerra Aleman - (Avaliadora Externa) - UNIFEI



Dr. Helio Jaques Rocha Pinto - (Avaliador Interno) - OV/UFRJ



Dr. Marco Grossi - (Avaliador Interno) - OV/UFRJ

Rio de Janeiro
Dezembro de 2019

O presente trabalho foi realizado com apoio da Coordenação de
Aperfeiçoamento de Pessoal de Nível Superior – (Brasil)
CAPES – Código de Financiamento 001

Dedicated to my parents: Delvis and Luis José.

Acknowledgements

This thesis was carried out at Observatório do Valongo of the Universidade Federal do Rio de Janeiro, in Rio de Janeiro, Brazil, from 2015 to 2019. It was financed by Coordenação de Aperfeiçoamento de Pessoal de Nível Superior-CAPES a national institution for the scholarships granted to the post-graduate students within the Brazilian government.

I am deeply grateful to my supervisors Prof. Denise R. Gonçalves and Dr. Stavros Akras who provided guidance and direction over the time taken to complete this thesis.

To my nephews Mariangel, Sofia and Mateo for believing that I am the best uncle in the world, even though I have been away for most of their lives.

To Claudia F., my absolute gratitude for being such a warm, intelligent and helpful person.

I would like to thank all my friends in Rio de Janeiro, with whom I have shared moments of big excitement.

This theses is based on observations made with the JAST/T80 telescope at the Observatorio Astrofísico de Javalambre (OAJ), in Teruel, owned, managed and operated by the Centro de Estudios de Física del Cosmos de Aragón. Funding for the J-PLUS Project has been provided by the Governments of Spain and Aragon through the Fondo de Inversiones de Teruel, the Spanish Ministry of Economy and Competitiveness (MINECO: under grants AYA2015-66211-C2-1-P, AYA2015-66211-C2-2, AYA2012-30789 and ICTS-2009-14), and European FEDER funding (FCDD10-4E-867, FCDD13-4E-2685).

The T80-South robotic telescope (Mendes de Oliveira et al., 2019) was founded as a partnership between the São Paulo Research Foundation (FAPESP), the Observatório Nacional (ON), the Federal University of Sergipe (UFS) and the Federal University of Santa Catarina (UFSC), with important financial and practical contributions from other collaborating institutes in Brazil, Chile (Universidad de La Serena) and Spain (CEFCA).

This thesis has made extensive use of Python language libraries from the NUMPY (Oliphant, 2006), ASTROPY (Astropy Collaboration et al., 2013) and SKLEARN (Pedregosa et al., 2011) projects.

La ciencia ha eliminado las
distancias, pregonaba Melquíades.
Dentro de poco, el hombre podrá
ver lo que ocurre en cualquier lugar
de la tierra, sin moverse de su casa.

— Gabriel García Márquez
Cien años de soledad

Resumo

Ferramentas para descobrir nebulosas planetárias e simbióticas em levantamentos fotométricos ópticos multibanda

Luis Angel Gutiérrez Soto

Orientadores: Dra. Denise R. Gonçalves & Dr. Stavros Akras

As nebulosas planetárias (PNe) e estrelas simbióticas (SySt) são objetos com linhas de emissão, bem conhecidos, os quais representam os estágios finais da evolução de estrelas de baixa massa e de massa intermediária. Das aproximadamente 3.500 PNe e 300 SySt descobertas em nossa Galáxia, apenas quatorze PNe e umas poucas simbióticas são membros do halo galáctico. No entanto, nunca foi realizada uma busca sistemática desses objetos no halo da Galáxia. Esta tese apresenta ferramentas fotométricas e os primeiros resultados da busca de PNe compactas e SySt no halo galáctico, os quais advêm da primeira liberação de dados dos levantamentos J-PLUS (Javalambre Photometric Local Universe Survey) e S-PLUS (Southern-Photometric Local Universe Survey). O objetivo desse trabalho é a elaboração, o desenvolvimento e a validação de novas ferramentas de diagnóstico para identificar PNe e SySt utilizando o novo sistema de 12 filtros dos projetos J-PLUS e S-PLUS. Para esse fim utilizou-se a fotometria sintética de um conjunto de modelos que simulam PNe do halo, algumas nebulosas planetárias e simbióticas observadas, bem como vários objetos com linhas de emissão que assemelham-se às PNe e às SySt (galáxias com formação estelar, variáveis cataclísmicas, quasares, regiões H II extragaláticas, estrelas B[e] e estrelas T-Tauri). Também foram criadas ferramentas fotométricas para o levantamento, vindouro, Javalambre-Physics of the Accelerating Universe Astrophysical Survey (J-PAS). Além disso, as técnicas de análise de componentes principais (PCA) e análise discriminante linear (LDA) foram exploradas como ferramentas suplementares para uma melhor discriminação das PNe e das SySt de seus imitadores que possuem linhas de emissão.

Os diagramas cor-cor do J-PLUS e do S-PLUS foram validados usando-se duas PNe do halo, as quais foram observados pelo J-PLUS durante a fase de verificação científica, e também através da aplicação dos novos critérios aos primeiros dados liberados por esses projetos. Uma candidata a nebulosa planetária foi identificada, no catálogo do projeto J-PLUS. Suas características, obtidas via espectroscopia ótica, são aqui discutidas. Nenhuma outra candidata, quer PN ou SySt, foi encontrada, provavelmente devido à limitadíssima área observada até então (~ 1190 graus²). No entanto, nessa mesma área, os novos critérios de seleção recuperaram três objetos conhecidos os quais têm fortes linhas de emissão – uma PN e duas galáxias H II. Esses objetos foram usados para validar o desempenho das técnicas de aprendizado automático. As ferramentas de seleção criadas nesse trabalho para a identificação e discriminação de nebulosas planetárias e estrelas simbióticas de suas imitações são muito eficientes, como consequência dos sistemas dos 12 filtros dos projetos J-PLUS e S-PLUS e da combinação de vários índices de cor no regime óptico.

Palavras-chave: Estágios finais de evolução estelar, objetos com linhas de emissão, levantamentos fotométricos, nebulosas planetárias, estrelas simbióticas, técnica: fotometria, espectroscopia

Abstract

Tools to discover planetary and symbiotic nebulae in optical multi-band photometric surveys

Luis Angel Gutiérrez Soto

Advisors: Dr. Denise R. Gonçalves & Dr. Stavros Akras

Planetary nebulae (PNe) and symbiotic stars (SySt) are well known emission-line objects that represent the final stages in the evolution of low- and intermediate-mass stars. From the approximately 3,500 PNe and 300 SySt discovered in our Galaxy, only fourteen PNe and a handful SySt are known to be members of the Galactic halo. Nevertheless, a systematic search for halo PNe and SySt has never been performed. This thesis presents photometric tools and the very first results of searching for Galactic halo compact PNe and SySt in the J-PLUS (Javalambre Photometric Local Universe Survey) and S-PLUS (Southern-Photometric Local Universe Survey) first data releases (DR1). The objective of this work is the elaboration, development and validation of new photometric diagnostic tools to identify PNe and SySt making use of the novel 12-filter system of the J-PLUS and S-PLUS projects. For that, synthetic photometry for a grid of photo-ionization models of halo PNe, few observed halo PNe and SySt, as well as a number of emission-line objects that resemble PNe and SySt (star-forming galaxies, cataclysmic variables, quasi-stellar objects, extragalactic H II regions, B[e] stars and young stellar objects) were computed. The thesis also devises such tools for the forthcoming Javalambre-Physics of the Accelerating Universe Astrophysical Survey (J-PAS). In addition, principal component analysis (PCA) and linear discriminant analysis (LDA) are explored as supplementary tools to better discriminate PNe and SySt from their emission-line mimics.

The J-PLUS and S-PLUS colour-colour diagnostic diagrams are validated using two known halo PNe observed by J-PLUS during the science verification phase and by applying the new criteria to the DR1s of J-PLUS and S-PLUS. One PN candidate was identified, in the J-PLUS DR1, of which the optical follow-up spectroscopy is discussed. No other candidates, either of PNe or SySt are found, probably due to the short area so far observed ($\sim 1,190 \text{ deg}^2$). Although, the new selection criteria recovered three known strong emission-line objects – one PN and two H II galaxies – in this area. These objects were used to validate the performance of the statistical techniques. The selection of tools devised in this work for the identification and discrimination of PNe and SySt from their emission-line mimics proved to be very efficient due to the 12-filter systems of the surveys and the combination of various optical colour indices.

Key-words: Final stages of stellar evolution, emission-line objects, photometric surveys, planetary nebulae, symbiotic stars, technique: photometry, spectroscopy

List of Figures

| | | |
|------|--|----|
| 1.1 | Herzsprung-Russel diagram of a 2 M _⊙ star | 18 |
| 1.2 | Schematic structure of the planetary nebulae | 21 |
| 1.3 | Flux-calibrated optical spectrum | 23 |
| 1.4 | Aitoff projection taken from Frew (2017) | 24 |
| 1.5 | H α surface brightness versus nebular radius | 26 |
| 1.6 | Blue plus red spectra of two symbiotic | 30 |
| 1.7 | Two objects with very similar morphologies | 31 |
| 1.8 | Diagnostic diagram to discriminate symbiotic | 32 |
| 1.9 | Diagnostic diagram based in IJK two-colour diagram | 33 |
| 1.10 | Diagnostic diagram using He I ratio | 33 |
| 1.11 | H α images of several PN mimics | 35 |
| 1.12 | Spectra of different emission line objects | 36 |
| 1.13 | Diagnostic diagram to separate PNe, H II regions and SNRs | 39 |
| 1.14 | Diagnostic colour-colour diagrams for symbiotic | 40 |
| 1.15 | Diagram showing the location of PNe | 40 |
| 1.16 | The 2MASS/AllWISE (W3–W4) versus (Ks-W3) | 41 |
| 2.1 | The colour-colour diagram ($r' - H\alpha$)vs($r' - i'$) | 46 |
| 2.2 | View of the JAST/T80 telescope | 47 |
| 2.3 | Overall transmission curves measured for the set of 12 J-PLUS filters | 49 |
| 2.4 | Footprint of the J-PLUS DR1 | 50 |
| 2.5 | T80S is located on Cerro Tololo | 51 |
| 2.6 | Overall transmission curves measured for the set of 12 S-PLUS filters | 52 |
| 2.7 | The J-PAS transmission curves. | 54 |
| 3.1 | J-PLUS synthetic photometry | 62 |
| 3.2 | Synthetic magnitudes of a CLOUDY modelled PN | 64 |
| 3.3 | Synthetic photo-spectrum of the SySt LMC1 | 64 |
| 3.4 | <i>First panel</i> : synthetic photo-spectrum in magnitude units | 66 |
| 3.5 | As Figure 3.4 <i>First panel</i> : | 67 |
| 3.6 | J-PLUS and S-PLUS ($r - J0660$) vs ($r - i$) colour-colour diagram . | 69 |
| 3.7 | J-PLUS and S-PLUS colour-colour diagrams | 72 |
| 3.8 | J-PLUS and S-PLUS colour-colour diagrams | 73 |
| 3.9 | J-PAS synthetic photo-spectra of several emission-line objects | 76 |

| | | |
|------|--|-----|
| 3.10 | Six J-PAS colour-colour diagrams to separate PNe and SySt from other emission line sources | 78 |
| 3.11 | Example of an arbitrary data set relative to PC1 and PC2. | 79 |
| 3.12 | (<i>Upper panel</i>) J-PLUS PC2 vs PC1 and (<i>lower panel</i>) PC3 vs PC1 diagrams | 81 |
| 3.13 | J-PAS PC2 vs PC1 (<i>upper panel</i>) and PC3 vs PC1 (<i>lower panel</i>) diagrams | 84 |
| 3.14 | <i>Left column:</i> J/S-PLUS weights associated with PC1 | 85 |
| 3.15 | Example of two class scatter relative to LD1 and LD2 | 86 |
| 3.16 | (<i>Upper panel</i>) J-PLUS LD2 vs LD1 and (<i>lower panel</i>) LD3 vs LD1 diagrams | 87 |
| 3.17 | Weights associated with LD1 | 88 |
| 4.1 | Comparison between J-PLUS synthetic and observed photometry . . | 90 |
| 4.2 | J-PLUS ($r - J0660$) vs ($r - i$) colour-colour diagram with objects from J-PLUS DR1. | 92 |
| 4.3 | J-PLUS and S-PLUS diagnostic diagrams | 93 |
| 4.4 | The photo-spectrum and 3RGB colour (g , r and i) image of the J-PLUS PN candidate. | 94 |
| 4.5 | The INT IDS spectrum of the J-PLUS PN source | 95 |
| 4.6 | J-PLUS photo-spectra and corresponding images | 98 |
| 4.7 | J-PLUS photo-spectra and corresponding composite images of HASH sources | 99 |
| 4.8 | Composite - $J0660$, r , and i - image of Jacoby 1 taken from JAST/T80 | 100 |
| 4.9 | S-PLUS photo-spectrum of Fr 2-21 and its corresponding 3RGB image | 100 |
| 4.10 | Schematic representation of how works the SMOTE algorithm | 102 |
| 5.1 | Recovered number of point like sources as a function of magnitude . | 108 |

List of Tables

| | | |
|-----|---|-----|
| 1.1 | Known hPNe in the Milky Way. | 25 |
| 2.1 | The <i>J-PLUS</i> filter systems | 48 |
| 2.2 | The <i>S-PLUS</i> filter systems | 52 |
| 3.1 | Proposed criteria for PNe and SySt | 74 |
| 4.1 | J-PLUS synthetic and observed magnitudes of H 4-1 and PNG 135.9+55.9 | 90 |
| 4.2 | Emission line fluxes of the J-PLUS PN candidate in UGC 5272. | 96 |
| 4.3 | J-PLUS and S-PLUS, SDSS and Pan-STARRS photometry for the HASH objects | 101 |
| 4.4 | The probability of each object to be classified as PN, SySt | 104 |
| 4.5 | The probability of each object | 105 |
| 5.1 | Fundamental properties of three known hPNe | 109 |
| 5.2 | Expected number of hPNe per survey for two case | 110 |
| 5.3 | Expected number of SySt per model and per survey | 111 |
| B.1 | Abundances used to computed the grid of modelled spectra | 144 |

Contents

| | | |
|----------|---|-----------|
| 1 | Introduction | 17 |
| 1.1 | Planetary nebulae (PNe) | 17 |
| 1.1.1 | Detailing the origin of the planetary nebulae | 18 |
| 1.1.2 | Planetary nebulae spectra | 22 |
| 1.1.3 | Planetary nebulae in the Milky Way | 24 |
| 1.1.4 | Detection techniques of planetary nebulae | 26 |
| 1.2 | Symbiotic stars | 27 |
| 1.2.1 | Symbiotic stars nature | 28 |
| 1.2.2 | Symbiotic stars spectra | 29 |
| 1.3 | Planetary nebulae versus symbiotic stars | 29 |
| 1.4 | PNe, SySt and their mimics | 34 |
| 1.4.1 | Compact H II regions | 34 |
| 1.4.2 | Herbig-Haro objects and young-stellar objects | 37 |
| 1.4.3 | Cataclysmic variable stars | 37 |
| 1.4.4 | Wolf-Rayet stars | 37 |
| 1.4.5 | Be and B[e] stars | 38 |
| 1.4.6 | Galaxies | 38 |
| 1.4.7 | Supernova remnants | 38 |
| 1.4.8 | Diagnostic diagrams: separating PNe and SySt from other emission line sources | 38 |
| 1.5 | Thesis overview | 41 |
| 2 | Description of the surveys | 43 |
| 2.1 | Previous PNe and SySt surveys | 43 |
| 2.1.1 | The AAO/UKST H α Survey | 44 |
| 2.1.2 | SHASSA | 44 |
| 2.1.3 | VTSS | 45 |
| 2.1.4 | IPHAS | 45 |
| 2.2 | Multi-band photometric surveys: a new era for planetary nebula and symbiotic stars | 47 |
| 2.2.1 | J-PLUS | 47 |
| 2.2.2 | S-PLUS | 50 |
| 2.2.3 | J-PAS | 53 |

| | | |
|----------|--|------------|
| 3 | Photometric techniques | 55 |
| 3.1 | Stellar photometry | 55 |
| 3.2 | System of magnitudes | 60 |
| 3.3 | Wavelength characterization of a photometric system | 60 |
| 3.4 | AB magnitude system | 61 |
| 3.5 | J-PLUS and S-PLUS synthetic photometry | 62 |
| 3.5.1 | Halo planetary nebulae and symbiotic stars | 62 |
| 3.5.2 | Other emission line objects | 65 |
| 3.6 | Synthetic colour-colour diagrams: selection criteria | 68 |
| 3.6.1 | IPHAS equivalent colour-colour diagram | 68 |
| 3.6.2 | New colour-colour diagrams | 70 |
| 3.7 | J-PAS synthetic photometry | 75 |
| 3.8 | J-PAS synthetic colour-colour diagrams | 75 |
| 3.9 | Statistical tools | 79 |
| 3.9.1 | Principal component analysis | 79 |
| 3.9.2 | PCA: J/S-PLUS | 80 |
| 3.9.3 | PCA: J-PAS | 82 |
| 3.9.4 | Linear discriminant analysis | 83 |
| 3.9.5 | LDA: J/S-PLUS | 86 |
| 4 | Applying the techniques to the observational data | 89 |
| 4.1 | J-PLUS SVD | 89 |
| 4.2 | Colour criteria versus the DR1s | 91 |
| 4.2.1 | J-PLUS photometry of the PN candidate | 92 |
| 4.2.2 | Spectroscopy of the PN candidate | 94 |
| 4.2.3 | Recovering DR1 known H α emitters | 95 |
| 4.2.4 | DR1s vs. the HASH PN catalog | 96 |
| 4.3 | Machine learning: approach improving the classification | 100 |
| 4.3.1 | Handling imbalanced samples in machine learning techniques | 100 |
| 4.3.2 | Principal component analysis | 103 |
| 4.3.3 | Linear discriminant analysis | 104 |
| 5 | Discussions, conclusions and perspectives | 106 |
| 5.1 | Discussion | 106 |
| 5.1.1 | Selection of halo PNe and SySt | 106 |
| 5.1.2 | Expected number of halo planetary nebulae | 107 |
| 5.1.3 | Expected number of halo symbiotic stars | 110 |
| 5.1.4 | Compact versus extended PNe | 111 |
| 5.2 | Conclusions | 112 |
| 5.3 | Perspectives | 113 |
| | Bibliography | 114 |
| | A Python codes | 125 |
| | A.1 | 125 |

| | |
|---|-----|
| A.2 | 134 |
| B Chemical abundances used to build the PN models | 144 |
| C J-PLUS AstroQueries | 145 |
| D Refereed papers | 148 |
| E Talks and posters in scientific meetings | 111 |

Chapter 1

Introduction

Planetary nebulae and symbiotic stars are some of the most interesting and fascinating objects of the universe. Planetary nebulae are bubbles of ionized gas, produced from low- and intermediate-mass stars towards the end of **their** evolution. They represent evolutionary phase in the lifetimes of a significant fraction of Milky Way (MW) stars. Approximately 3,500 PNe have been identified in the Milky Way, but only 14 are located in the Galactic halo. Halo PNe are interesting objects because they provide important clues about the final evolution of old, low-mass halo stars and they are able to convey fundamental information of the early chemical conditions of the Galaxy including its star formation history. On the other hand, symbiotic stars are binary systems formed by an evolved cool giant star and an evolved hot star (in general a white dwarf). They are important objects in Astrophysics because they allow the study of physical mechanisms such as the powering mechanism of supersoft X-ray sources, the thermonuclear outbursts, the collimation of stellar winds and formation of jets or their relation with the formation of bipolar PNe. Symbiotics are, probably, progenitors of Type Ia supernovae. In this work we have developed diagnostic tools to identify planetary nebulae and symbiotic stars in the Galactic halo by using photometric surveys that contain narrow- and broad-band filters. These topics will be addressed in subsequent chapters in this thesis.

1.1 Planetary nebulae (PNe)

PNe are the result of the evolution of low- and intermediate-mass stars, with masses between 0.8 and 8.0 M_{\odot} . During their evolution, these stars go through many **nu-****cleosynthetical** and mixing processes that change their initial surface composition. The central stars of PNe are evolved stars in the phase of white dwarfs with very high temperatures (typically $\geq 4 \times 10^4$ K), which have expelled in the interstellar medium large amount of their mass. This circumstellar envelope around the remnant stars expand with velocities of the order of ~ 30 km/s. Due to this expansion, the density of PNe decreases with time resulting in weak emission. This process makes PNe to become rapidly very faint and un-detectable. The PN phase is very short ($\sim 20,000 - 30,000$ yr) compared to the entire lifetime of the star.

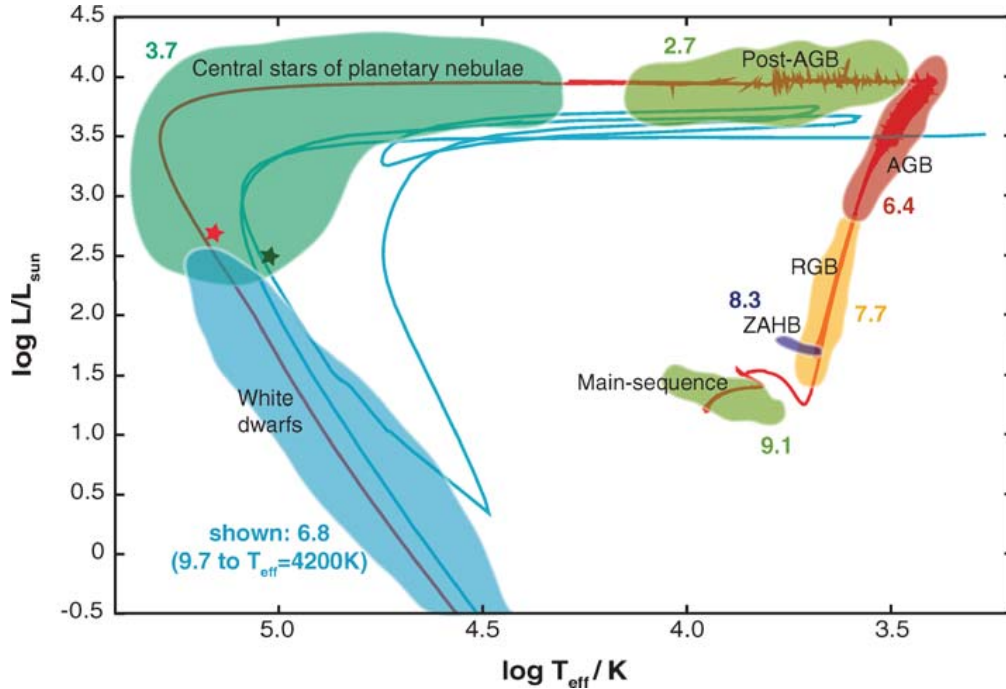


FIGURE 1.1: Hertzsprung-Russell diagram of a $2 M_{\odot}$ **evolutionary track** from the main sequence to the white dwarf phase (red track) for a solar metallicity star. The blue track indicates a born-again evolution (triggered by a very late thermal pulse) for the same mass, but slightly offset in $\log T$ and $\log L$. The red and green stars represent the position of the central star of NGC 6853 (H-rich) and the naked PN nucleus PG 1159-035 (H-deficient), respectively. Shaded areas represent the covered range in $\log T$ and $\log L$ in each evolutionary stage of the star and the numerical labels with refer to the log of the approximate duration of each evolutionary phase. In the cooler section of the post-AGB phase, wiggles in the track are caused by numerical convergence difficulties (Herwig, 2005).

In short, at the end of the evolution of low- and intermediate-mass stars, their outer layers are ejected resulting in an enrichment of the interstellar medium (ISM) with heavy elements (Karakas & Lattanzio, 2014). Note that PN phase is reached when the previously ejected material is eventually ionized by the UV radiation field of the central star before being diluted in the ISM. The ionized gas contains information about the chemical composition at the time and the place the progenitor stars were formed and gives chemical clues of the former stellar nucleosynthesis.

1.1.1 Detailing the origin of the planetary nebulae

In the main-sequence (MS) phase, low- and intermediate-mass stars spend most of the time converting hydrogen into ${}^4\text{He}$ in the their cores, by nuclear fusion. In the end of the MS phase, stars begin to exhaust the hydrogen in the nucleus. Then the radiation pressure is not enough to stop the gravitational collapse. When the nucleus starts to compress, its temperature increase causing that the outer layer of the star expand. The star now moves away from the main sequence and climbs up the first red giant branch (RGB) in the Hertzsprung-Russell (HR) diagram. During this phase the luminosity increases considerably, by a factor of $\sim 10^3$ for a solar-mass MS star, the superficial area of the star also increases distributing the released energy

over a much larger surface area, so the surface cools to an effective temperature around 3,500 K (corresponding to a M spectral type), this is a direct consequence of the Stefan-Boltzmann law. At this point the star is in the phase known as first-ascent red-giant branch (RGB). In Figure 1.1 we show a schematic description of the full evolution of intermediate-mass stars ($2 M_{\odot}$) in the HR diagram.

In the RGB phase the outer layers become less gravitationally bound due to the large increase of the radius. This causes the mass-loss to accelerate (Reimers, 1975). Convection becomes the main mechanism of energy transport in the envelope due to the increased hydrogen opacity at lower temperatures. As the convection extends inwards, it can reach regions where there was early H burning, and hence CNO cycle producing ^{14}N from ^{12}C and ^{16}O . Therefore, the advance of the convective envelope produces an increase of ^{14}N and simultaneous decrease in ^{12}C and ^{16}O in the envelope; this process is called *first dredge up*.

In low-mass stars ($M < 2 M_{\odot}$), after the MS phase, the He core becomes denser, hotter and electron-degenerate. When the temperature in the degenerated core is high enough to trigger the He burning – via the triple α **reaction** – the energy released increases the temperature in the core, as the core can not expand given to degenerate state. Therefore, the burning rate increases rapidly ending up as thermonuclear runaway. This process is known as the *core helium flash* (Iben & Renzini, 1983; Herwig, 2005). The energy released by the flash changes the equation of state in the core. The core leaves the degenerated state and is dominated by the equation of an ideal gas. It takes more than one of these flashes to remove the degeneracy in the nucleus. After the He flash becomes weaker in the core, it eventually reaches a steady He burning. This mean that the star rapidly cools and becomes less luminous, moving left down in the HR diagram, thus arriving on the zero-age horizontal branch (ZAHB, see Figure 1.1).

The more massive stars ($2 M_{\odot} < M < 8 M_{\odot}$) do not form a degenerate nucleus and hence do not have the He flash, but these stars eventually have He ignition¹ in the center getting a central C + O-rich core, an intermediate He-rich region and an outer H-rich zone. There are He-burning and H-burning shell sources at the inner edges, and the star evolves with an increasing luminosity and decreasing temperature along the asymptotic giant branch (AGB) and towards the red giant tip again.

As the He is exhausted in the core the luminosity increases and the star cools down, returning to the second-ascent red giant. Given to the position of the evolutionary track of these stars in the HR diagram, they are called the asymptotic giant branch (AGB) stars. As the outer layers are becoming cold and less dense, the convection again is the dominant heat-transfer mechanism. The convective shell penetrates the H-burning shell, then it brings to the surface the primary resulting nucleosynthesis products of H burning (He plus ^{14}N from the CNO cycle), and this is the *second dredge up*. This process occurs only in stars with mass above $\sim 4 M_{\odot}$ (Herwig, 2005).

¹The stars have two energy sources: a He-burning core and a H-burning shell exterior to it.

The AGB phase is divided into two sub-phases: the early-AGB (E-AGB) and the thermally pulsing AGB (TP-AGB). In the E-AGB the star consists of a degenerated CO core surrounded by a He-burning shell and this is surrounded by a convective hydrogen envelope. When the He-burning stops in the shell, the TP-AGB phase begins, characterized by a double shell of H and He that alternatively switch off and on to provide the energy source of the star. As the He is exhausted, the hydrogen shell is compressed and fire up, exterior to the now dormant helium shell.

Approximately every 10^5 years, the helium shell becomes thick enough to trigger its ignition again by helium flashes or thermal pulses, causing the outer layers of the star to expand. The H burning is now pushed to upper zones where the temperature and density are lower, here the fusion stops. When the He in the inner shell is exhausted, the shell of hydrogen is compressed and its ignition begins again. Hence one dozen of thermal pulses occur during the TP-AGB phase (Herwig, 2005).

TP-AGB stars are generally larger and more luminous than the RGB stars (the luminosity can exceed the $10^4 L_{\odot}$, and the diameters are in the order of 2 AU). The temperature can be as low as $\sim 2,500$ K (spectral type M8). The internal instabilities in these objects make them to exhibit Mira variability (periodicity of ~ 1 yr). The mass-loss is increased with the time, and after each thermal pulse, the processed materials are brought up to the surface via convection mechanism, what is called *third dredge up*. The surface becomes enriched with helium, CNO, and slow neutron capture (s-process) elements (Iben & Renzini, 1983, 1984; Herwig, 2005; Sterling & Dinerstein, 2008).

Eventually, as the star leaves the AGB phase, it ejects almost all its outer layers in a final and powerful mass-loss phase through stellar winds (Wachter et al., 2002). The final stage of a planetary nebula can be recognized as a nebular shell that expands into the ISM, while the central star evolves to be a white dwarf. The expansion velocity of the nebular gas is approximately 33 km s^{-1} (Pereira et al., 2013), which is very low in comparison with the escape velocity from the central stars, about $1,000 \text{ km s}^{-1}$. It is, therefore quite unlikely that any impulsive process that throws off an outer shell from these stars would provide just a little more energy than the necessary escape energy. To explain that, the expansion velocities of the nebular shells are compatible with the escape velocities of the red giants, therefore suggesting that these shells are ejected during the red-giant phase (Osterbrock & Ferland, 2006). In fact, radiation pressure from the stellar continuum (observed in the infrared by the presence of dust) and the presence of the trapped $L\alpha$ photons can accelerate this expansion. Thus, the presence of dust in the PNe also suggests that the material in the shell comes from a cool stellar component, which further supports the evolution of PNe from red giant stars.

There is a strong observational evidence that stars in the AGB phase lose mass by stellar winds. These winds have low velocities ($\sim 10 \text{ km s}^{-1}$) and relatively higher mass-loss rate, $10^{-5} M_{\odot} \text{ yr}^{-1}$. This process produces a large, cool and slowly expanding shell surrounding the central star.

After most of the envelope mass has been expelled into the ISM, the hot core

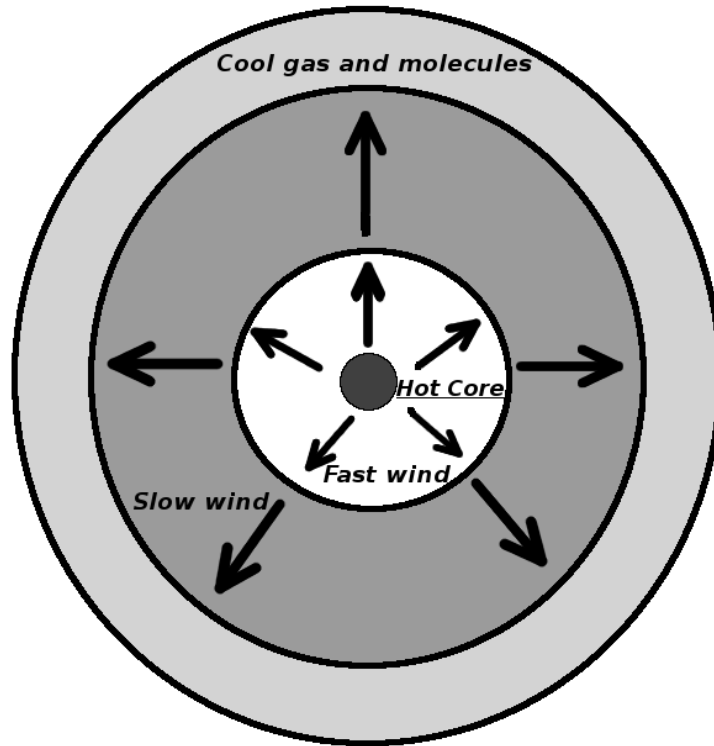


FIGURE 1.2: Schematic structure of a planetary nebula. It consists of three regions: the innermost zone with a fast wind ($\sim 10^3 \text{ km s}^{-1}$) from the hot core, an external shell with a slow wind ($\sim 10 \text{ km s}^{-1}$) and an outermost layer composed by cool gas, molecules and dust.

is exposed and a second and faster wind arises. The velocity of this wind is similar to the escape speed from the central star ($\sim 10^3 \text{ km s}^{-1}$) and it is driven by the radiation pressure, with smaller mass-loss rates, typically $\sim 10^{-8} M_{\odot} \text{ yr}^{-1}$. This new fast wind interacts with the cold and slowly-moving outer shell, producing a central cavity (Osterbrock & Ferland, 2006). Simultaneously the material is ionized by the UV strong radiation field of the central star. At this stage, the system consists of three regions, the innermost wind from the core, an external shell where the fast wind interacts with the material previously ejected from the cool star and an outermost layer of molecular species, as it is shown in Figure 1.2.

Diverse PNe imaging catalogs have showed that they display a variety of morphologies, originated from stars with a range of masses, and the ejected envelopes are characterized by a wide range of abundances. Very few PNe exhibit spherically shape, while the vast majority show ellipsoidal or bipolar morphologies (e.g. Kwok, 2007; Balick & Frank, 2002) suggesting that the mass loss is more efficiently in the poles of the central stars. Various mechanism have been proposed to explain the deviation from the spherical symmetry such as magnetic fields (García-Segura et al., 2005) or binary systems (e.g. Soker, 1998, 2002a). Over the last decades, it has been found that binary systems and the common envelope phase are crucial for the formation of non-spherical nebula (Balick & Frank, 2002). Faint outer shells have

been observed well outside of the bright PNe, indicating the presence of multiple ejection processes (e.g. Iben & Tutukov, 1993).

In order to understand the chemical abundances observed in PNe, we need to consider the processes that bring the processed elements to the stellar surface and then to the ejected PN. Overall, the first dredge up occurs when the H core of the star is exhausted and the star becomes a red giant. In this first dredge up the material enriched in N and diluted in C is brought to the surface layers. The second dredge up, following the exhaustion of central He and creation of a degenerate C + O core, results in a large amount of He and N mixed to the surface layers (this only occurs for stellar masses above $\sim 4 M_{\odot}$). The third dredge up occurs when the He-burning occurs in a convective shell, and higher C abundances and lower N abundances are brought to the stellar surface by the thermal pulses. This is the situation at high metallicities, however, third dredge up contribution is important only for galaxies with the lowest metallicities (Gonçalves, 2019).

1.1.2 Planetary nebulae spectra

The high temperature of the central stars (CS) of PNe implies that most of their UV photons flux is blueward of the Lyman limit. The gas shell previously ejected in the AGB phase is photo-ionized and produces an emission-line spectrum. The principal emission lines in the optical region are the recombination lines of hydrogen and helium plus a few of the strongest lines of oxygen, nitrogen and carbon, and the prominent emission of collisionally-excited forbidden lines of heavy elements such as O, N, S, Ne, and Ar (Kwitter & Henry, 2001). In their spectra, it is also present a nebular continuum produced by recombination, two photon emission and free-free emission. The continuum tend to be more intense in the blue part. Planetary nebulae show a variety of optical spectra and have spectral features also in common with symbiotic stars, H II regions, Wolf-Rayet stars and some supernova remnants (Frew, 2008).

PNe can be very low excitation objects with strong Balmer lines and [O II] emission, like BD +30°3639 and He 2-131, in which the surrounding gas is ionized by a relatively cool star ($T_{\text{eff}} \simeq 30,000$ K). They can also be moderate and high excitation objects in which [O III] $\lambda\lambda 4959, 5007$ lines are the dominant emission lines in the optical spectrum. There are also very high excitation PNe in which the [He II] emission-line is stronger than the $H\beta$ suggesting a very hot central source. These PNe also exhibit [Ne V] lines and generally have little or no trace of low-ionization species such as [O II], [N II], and [S II]. Occasionally, the highest-excitation PNe show in their spectrum fluorescent lines of O III and N III. In general PNe exhibit a wide range of excitation states. Their spectra can show emission lines from [O I] to [Ne V]. These PNe are often optically thick (Jacoby & Kaler, 1989; Kaler & Jacoby, 1989) and frequently have an extended molecular shell (e.g. Zuckerman & Gatley, 1988).

In Figure 4.5 we show the optical spectrum of M 1-57, a typical middle-aged

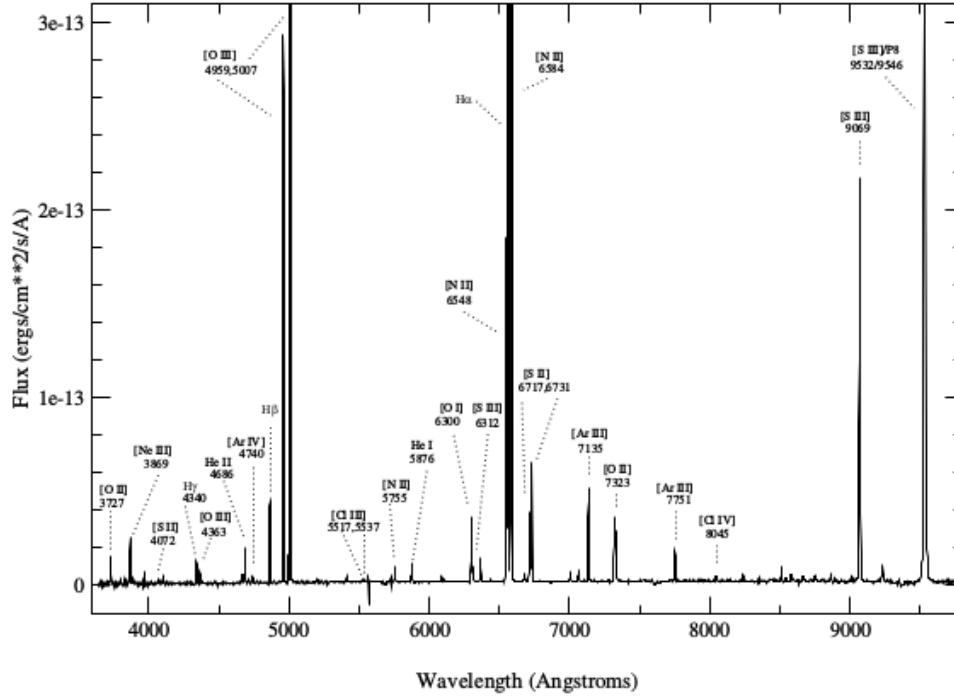


FIGURE 1.3: Flux-calibrated optical spectrum of the medium excitation PN Minkowski 1-57 (Kwitter & Henry, 2001). Important emission lines are indicated.

PN. In this spectrum, it is possible to see a wide variety of low- and high-excitation emission lines. The term “excitation class” was introduced to explain the wide variety of spectral signature of the PNe (Gurzadian & Egikian, 1991). The temperature of the CS is the primary parameter associated with the excitation class, but it can also be affected by other second-order parameters: the abundances of the elements (depending on the line species used in the definition) and the optical depth of the PN, which reflects on the size and density of the PN shell.

Aller (1956) defined a scale of semi-quantitative measure of the excitation of PN, a scale from 1 to 10. Strengths of the [O II] $\lambda 3727$ and [O III] $\lambda 4959$ lines relative to $H\beta$ were used to define low-excitation PNe, whilst the strength of He II $\lambda 4686$ and [Ne V] $\lambda 3426$ were used for high-excitation nebulae. Dopita & Meatheringham (1990) introduced the decimal excitation class and gave two equations depending on whether or not the He II emission is detectable. $(F_{[\text{O III}]5007} + F_{[\text{O III}]4959})/F_{H\beta}$ is also used to measure the excitation class. This method has been adopted by Stanghellini et al. (2002a) where high-excitation He II lines were not available. More recently, Reid & Parker (2010) proposed a new method for estimating excitation classes incorporating both the [O III]/ $H\beta$ and the He II $4686\text{\AA}/H\beta$ ratios. This is the most robust method for estimating excitation class and ultimately central star temperatures.

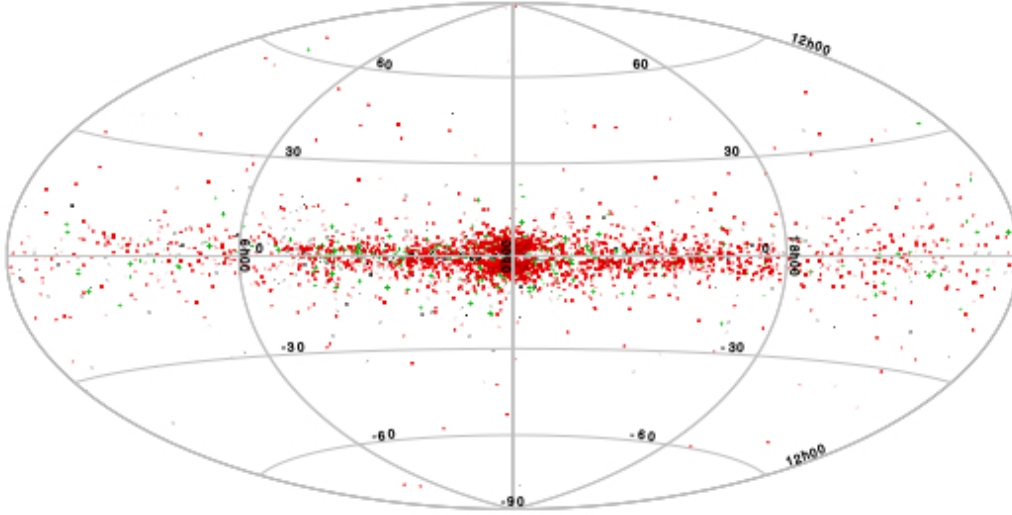


FIGURE 1.4: Aitoff projection taken from Frew (2017), showing the Galactic distribution of all 3,540 PNe current cataloged in HASH. Confirmed, likely and possible PNe are the red, green, and black symbols respectively.

1.1.3 Planetary nebulae in the Milky Way

The most recent compilation of PNe is published in the Hong Kong/AAO/Strasbourg/ $H\alpha$ PN database (HASH; Parker et al., 2016). To date, HASH contains 2401 true, 447 likely, and 692 possible Galactic PNe. And, of course, the number of Galactic PNe continues growing. For instance, 291 PN candidates have been very recently identified by the UKIRT Wide-Field Imaging Survey (UWISH2) of the Northern Galactic Plane (Gledhill et al., 2018) and 152 PNe in the CORNISH catalogue (Irbor et al., 2018; Fragkou et al., 2018). Small, private photometric surveys have also contributed to the discovery of new Galactic PNe (e.g. Boumis et al., 2003, 2006). However, this current number of PNe represents only about 15-30% of the estimated total of Galactic PNe (Frew, 2008; Jacoby et al., 2010) showing that a small fraction of the PNe have been cataloged (Frew, 2017). Fig. 1.4 shows the distribution of the current population of the Galactic PNe.

Planetary nebulae in the Galactic halo

Of these $\sim 3,500$ PNe identified in our Galaxy, only fourteen objects have been confirmed to be members of the Galactic halo, Table 1.1 list these objects. Halo planetary nebulae (hPNe) are objects having low-metallicity and high peculiar velocity. They are of great interest because they provide important clues about the final evolution of old, low-mass halo stars, and they are able to convey fundamental information of the low-mass evolution and the early chemical conditions of the Galaxy (Otsuka et al., 2010).

In general, PNe are divided in five types based on their chemistry, vertical distance from the Galactic plane and their peculiar velocities (Peimbert, 1978). Based on this scheme, PNe can be of Type I, which result from the most massive progenitor

| Object | Other name | RA | Dec | Comments | Ref |
|--------------|------------|-------------|--------------|------------------|-------------------------------|
| K648 | Ps 1 | 21 29 59.38 | +12 10 27.50 | – | Adams et al. (1984) |
| DdDm-1 | – | 16 40 18.15 | +38 42 20.00 | – | Clegg et al. (1987) |
| PN006-41.9 | PRMG-1 | 21 05 53.56 | -37 08 40.26 | – | Pena et al. (1989) |
| NGC 2242 | – | 06 34 07.36 | +44 46 38.09 | – | Shaw & Bidelman (1987) |
| NGC 4361 | – | 12 24 30.76 | -18 47 05.40 | – | Torres-Peimbert et al. (1990) |
| M 2-29 | – | 08 06 40.91 | -26 54 56.38 | – | Pena et al. (1991) |
| BB-1 | BoBn-1 | 00 37 16.03 | -13 42 58.60 | – | Pena et al. (1991) |
| H4-1 | – | 12 59 27.77 | +27 38 10.50 | – | Pena et al. (1990) |
| PN243-37.1 | – | 05 03 01.73 | -39 45 44.50 | – | Pena et al. (1990) |
| GJJC-1 | – | 18 36 22.82 | -23 55 18.26 | – | Howard et al. (1997) |
| PN135.9+55.9 | – | 11 53 24.74 | +59 39 57.10 | Classified as CV | Tovmassian et al. (2001) |
| NGC 2438 | – | 07 41 50.51 | -14 44 07.70 | – | Dalnodar (2012) |
| PN232.0+05.7 | – | 07 48 03.67 | -14 07 40.40 | – | Pereira & Miranda (2007) |
| BD+33 2642 | – | 15 51 59.88 | +32 56 54.30 | Post AGB (P-PN) | Napiwotzki et al. (1994) |

TABLE 1.1: Known hPNe in the Milky Way.

stars in the intermediary mass range, being the youngest of all disk PNe. They are associated with the Galactic thin disk (closer to the Galactic plane). These objects are He and N rich, presenting extremely filamentary structure, with $\text{He}/\text{H} \geq 0.125$ or $\log(\text{N}/\text{O}) \geq -0.30$, are located $\langle z \rangle = 150$ pc from the Galactic plane and have peculiar velocities of $\langle \Delta V \rangle = 20.5 \text{ km s}^{-1}$.

Type II PNe, belong to the intermediate disk population. They are associated with the thin disk and have approximately circular orbits. Members of this group are generally older than Type I PNe, having been formed at a time when the interstellar medium was more metal-poor in heavy elements. Therefore, they may present slight underabundances of elements such as O, S and Ne. Moreover, their low mass prevents strong He or N enrichments (Quireza et al., 2007). They have $\text{He}/\text{H} < 0.125$ and $\log(\text{N}/\text{O}) < -0.3$ (Peimbert, 1978). This group is subdivided in Type IIa with $\langle z \rangle = 280$ pc and $\langle \Delta V \rangle = 21.3 \text{ km s}^{-1}$ and Type IIb with $\langle z \rangle = 420$ pc and $\langle \Delta V \rangle = 22.1 \text{ km s}^{-1}$.

Type III PNe are high velocity objects from the thick disk population with $\langle \Delta V \rangle > 60.0 \text{ km s}^{-1}$. Such PNe were produced from stars generally older than most thin disk stars. As most of the thick disk stars, they are on moderately elliptical orbits that typically reach higher distances from the Galactic plane. The thick disk have a scale height of 1450 pc (Reddy et al., 2006). Type III nebulae should also present lower abundances of heavy elements than the thin disk stars.

Finally, Type IV PNe are low metallicities objects. They exhibit $\langle z \rangle = 7.2$ kpc and $\langle \Delta V \rangle = 173 \text{ km s}^{-1}$ (Peimbert & Serrano, 1980; Peimbert & Torres-Peimbert, 1983). The hPNe are classified as Type IV, due to the high vertical distance from the galactic plane and the large peculiar velocity relative to the rotation of the Galaxy (Costa et al., 1996). It should be noted that all halo PNe are found to be metal poor (Quireza et al., 2007). For instance, the halo PNe BoBn1 (Otsuka et al., 2010), H4-1 (Otsuka & Tajitsu, 2013) and K648 (Kwitter et al., 2003) are extremely low-metallicity sources, showing $[\text{Fe}/\text{H}] \sim -2.45$ (Otsuka et al., 2015).

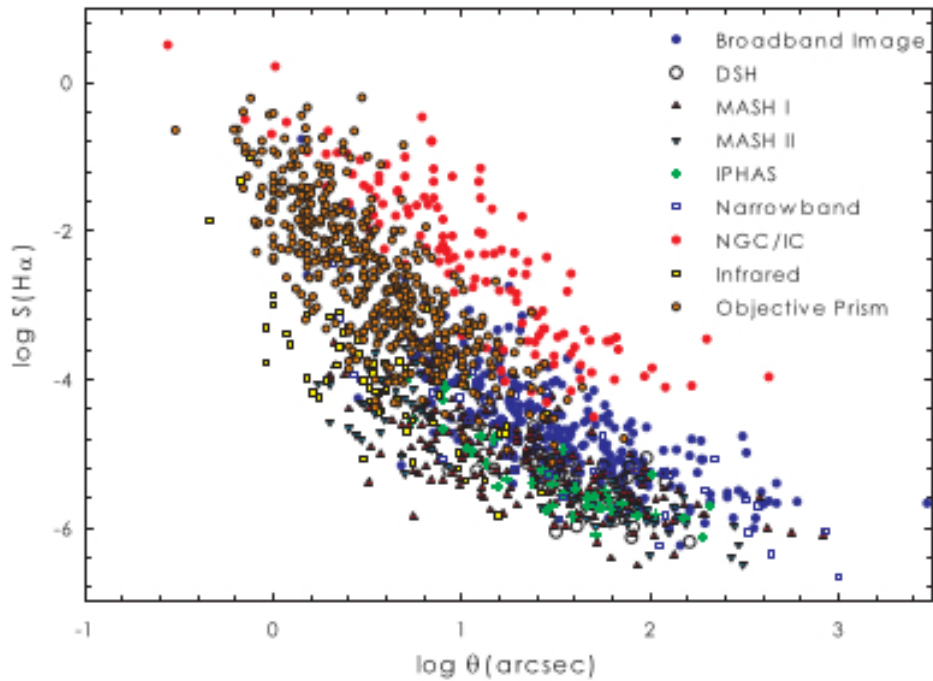


FIGURE 1.5: $H\alpha$ surface brightness versus nebular radius. Different discovery techniques are sensitive to different samples of PNe (Frew, 2017).

1.1.4 Detection techniques of planetary nebulae

Several different techniques have been used to find new Galactic PNe over the last two centuries (see Frew & Parker, 2010). Each technique is sensitive to PNe of differing sizes and surface brightness as illustrated in Fig. 1.5 and summarized as follow:

1. *Visual discoveries.* This technique is typified by the NGC² PNe, many of them are relatively bright and large (see Fig 1.5). Several well-known PNe were found at the eyepiece by W. and J. Herschel between 1780 and 1838.
2. *Broadband photographic imagery.* This technique was used by Abell (1966) and more recently by Deep-Sky Hunters (DSH) team, an amateur-professional consortium (Jacoby et al., 2010; Kronberger et al., 2016). The PN candidates were identified by direct inspection of the images and the online scanned data in the case of DSH discoveries.
3. *Narrowband imagery.* The Macquarie/AAO/Strasbourg $H\alpha$ Planetary Nebula Catalog (MASH catalog, Parker et al., 2006), the Isaac Newton Telescope (INT) Photometric $H\alpha$ Survey of the Northern Galactic Plane (IPHAS; Vironen et al., 2009a,b; Sabin et al., 2010), some new discoveries finds by the DSH team (Kronberger et al., 2014, 2016) and other smaller surveys (Fig.

²New General Catalogue of Nebulae and Clusters of Stars (NGC).

1.5) are representative of this technique. The PNe candidates are identified in colour-colour diagrams, visual inspections and image processing.

4. *Near-infrared (near-IR) imagery.* Narrow-band images are used to find very weak PNe. Near-IR have been used to find optically faint and/or more reddened PNe; e.g Jacoby & Van de Steene (2004) in the light of [S III] λ 9532. Discoveries from the UWISH2 survey in terms of molecular hydrogen (Froebrich et al., 2015) were also performed. Near-IR imaging (2MASS, Spitzer GLIMPSE, MSX and IRAS data) of obscured IRAS post-AGB and PN candidates has been useful to classified new PNe (Ramos-Larios et al., 2009, 2012).
5. *Mid-IR imagery.* WISE mid-IR imagery has also been used to find very faint PNe (Kronberger et al., 2016).
6. *Low-resolution objective-prism spectroscopic surveys.* This technique was initially implemented by E. C. Pickering and W. Fleming resulting in the Henry Draper catalog at Harvard Observatory (see Hearnshaw, 1990). It also have been especially addressed to detect modestly bright and generally compact PNe.
7. *Higher-resolution spectroscopy.* Spectroscopic discoveries using multiplexed fiber spectroscopy (Yuan & Liu, 2013).
8. *Direct discoveries of low-mass central stars.* The method is based on finding isolated white dwarfs that may be surrounded by low-surface brightness and hardly detectable nebulae (Kanarek et al., 2015, 2017).

Probably most of the undiscovered PNe are invisible at optical wavelength, because they are very extended and correspond to very low-surface brightness sources. Therefore, future discoveries confirmations will require the exploration of surveys in the IR and in radio domains in wide areas of the sky with enhanced sensitivity and resolution. In this thesis, we use narrow- and broad-band filter surveys to identify compact PN candidates in the optical regimen. Note that spectroscopy is the only way to confirm the nature of PN candidates identified by most of the above methods.

1.2 Symbiotic stars

Several types of stars characterized by an emission line spectrum have been discovered by the implementation of low angular and spectral resolution objective prism technique (Frew & Parker, 2010). Many of these objects have been misconceived as compact PN in previous catalogs (see Acker et al., 1987). One of the most common PN mimic of stellar appearance are the symbiotic stars (SySt). The traditional definition of SySt cover those interacting systems that exhibit a composite spectrum with emission lines of H I and He I and often [O III] and He II in conjunction with absorption signatures present in evolved giant star (Kenyon, 1986; Belczyński et al., 2000).

1.2.1 Symbiotic stars nature

Symbiotic stars (SySt) are long-period interacting binary systems, in which a late-type giant star transfer mass to a much hotter and compact companion. The typical configuration of a SySt consists of a red giant transferring material to a white dwarf star via stellar wind. Part of the wind of the giant star is ionized by the radiation of the WD, producing a spectrum with two components: one component is described by absorption features from the cool stellar photosphere of the giant and the second component by the emission lines of the excited ions (Corradi et al., 2008; Allen, 1984b). SySt are divided into three categories: (i) The S-type (*stellar*) in which the giant has a M-spectral type and dominates the emission in the near-IR, showing the presence of stellar photospheres at 3,000 – 4,000 K (Belczyński et al., 2000; Akras et al., 2019a). (ii) The D-type systems (*dusty*) in which the cool companion is a Mira variable star. The near-IR emission corresponds to the dusty envelope around the systems. And (iii) D'-type symbiotic stars which are characterized by a F, G or K type cool giant surrounded by a dust shell (Allen, 1984a). An additional type of SySt namely S+IR, an S-type with an infrared excess in the 11.6 and/or 22.1 μm bands, was just proposed by Akras et al. (2019a).

SySt are important objects in Astrophysics because they allow the study of physical mechanisms such as the powering mechanism of supersoft X-ray sources (Jordan et al., 1996), the thermonuclear outbursts (Munari, 1997), the collimation of stellar winds and formation of jets (Tomov, 2003) or their relation with the formation of bipolar PNe (Corradi et al., 2003). Another important aspect is that SySt are, probably, progenitors of Type Ia supernovae (see e.g Whelan & Iben, 1973; Hachisu et al., 1999; Lü et al., 2009; Di Stefano, 2010; Chen et al., 2011).

Various catalogues of SySt have been generated over the last 40 years. Allen (1984a) made the first catalogue of these sources and 15 years later Belczyński et al. (2000) presented a more updated and comprehensive census of SySt. Last year, Akras et al. (2019b) presented the latest catalogue of SySt with all known members until 2018. So far, only 323 SySts are known, from which 257 are Galactic and 66 are extragalactic (Akras et al., 2019b). These numbers are considerably lower than the predicted number of SySt in the Galaxy, from 3,000 (Allen, 1984a) up to 4×10^5 (Magrini et al., 2003). However, a great effort has been made over the years to create and improve tools that allow to distinguish SySt from other $\text{H}\alpha$ emitters including compact PNe. Corradi et al. (2008, 2010); Rodríguez-Flores et al. (2014) identified symbiotic star candidates using colour-colour diagrams built from IPHAS³ and near-IR (2MASS⁴) catalogs. Later, follow-up observations were obtained to reveal the true nature of the sources. More recently, Akras et al. (2019a) presented a new approach for identifying and distinguishing SySt from other sources in photometric surveys using machine learning techniques such as classification tree, linear discriminant analysis and K-nearest neighbor.

³The INT/WFC Photometric $\text{H}\alpha$ Survey of the Northern Galactic Plane (Drew et al., 2005)

⁴Two Micron All-Sky Survey (Skrutskie et al., 1995)

1.2.2 Symbiotic stars spectra

As already mentioned, the spectra of the SySt are composed by emission lines produced in the giant wind and absorption bands from the surface of the giant (Kenyon, 1986). The spectrum of a SySt displays strong recombination lines of H I, He I and He II as well as a number of forbidden high-excitation lines such as [O III] or [Ne V] and include typical forbidden emission lines of [O II], [Ne III] and [Fe VII]. The absorption component from the red giant includes bands such as TiO and VO, H₂O, CO and CN bands, as well as Ca I, Ca II, Fe I and Na I absorption lines (see, for instance, Gonçalves et al., 2015).

SySt were found to exhibit two very broad lines at 6825 Å and 7082 Å. These lines are known as Raman O VI scattered lines. Schmid (1989) identified them as produced by the Raman scattering of the O VI $\lambda\lambda$ 1032, 1038 resonance lines by neutral hydrogen. An incident O VI photon with frequency ν_i excite atomic hydrogen from its ground state $1s^2S$ to an intermediate state from where the Raman photon ν_f is emitted, leaving the hydrogen atom in the state $2s^2S$. The principle of the energy conservation requires that the frequency of the Raman scattered photon will be $\nu_i - \nu_{if}$, where ν_{if} is the energy difference between the initial and final state, $1s^2S$ and $2s^2S$ respectively (Schmid & Schild, 1994). The frequency displacement $\Delta\nu$ of the incoming O VI photons, due to Doppler broadening or any other phenomenon, is conserved. Therefore the relative widths $\Delta\nu/\nu_f$ of the Raman lines are approximately 6.7 times larger than the $\Delta\nu/\nu_i$ of the initial O VI lines, thus causing a large FWHM of ≈ 25 Å for the $\lambda\lambda$ 6825, 7082 emission lines. Allen (1980) showed that these Raman O VI lines are present in 50% of the SySt. Recently, Akras et al. (2019b) calculated this fraction as 55%, by using a large sample with all the known SySt in 2018. Moreover, it was shown that Raman O VI lines are an unique characteristic of the SySt.

Symbiotic stars exhibit a wide variety of spectral features, see Munari & Zwitter (2002) for a comprehensive spectral atlas of symbiotic stars. Figure 1.6 shows the spectrum of two SySt in NGC 205, in which is possible to see some of the most important signatures of the symbiotic systems. The first SySt (top panel) shows the O VI Raman scattered lines at 6830 Å, 7088 Å. In addition, the spectrum exhibits the typical H α and [N II] emission lines. The second SySt (bottom panel) shows the H β emission line and the high ionization lines of He II and Ne VII or N III.

1.3 Planetary nebulae versus symbiotic stars

PNe and SySt are objects that share similar spectroscopic characteristics which make difficult to properly identify them. Even, their morphologies are quite similar. Fig. 1.7 shows a bipolar PNe and a symbiotic system with similar morphologies.

Symbiotic stars can be discriminated from PNe using either near-IR colours or in the optical spectra the presence of the red continuum and strong [O III] λ 4363 relative to λ 5007 in higher-excitation objects. Gutierrez-Moreno (1988) and Gutierrez-Moreno et al. (1995a) used the [O III] λ 4363/ λ 5007 line ratio to separate PNe from

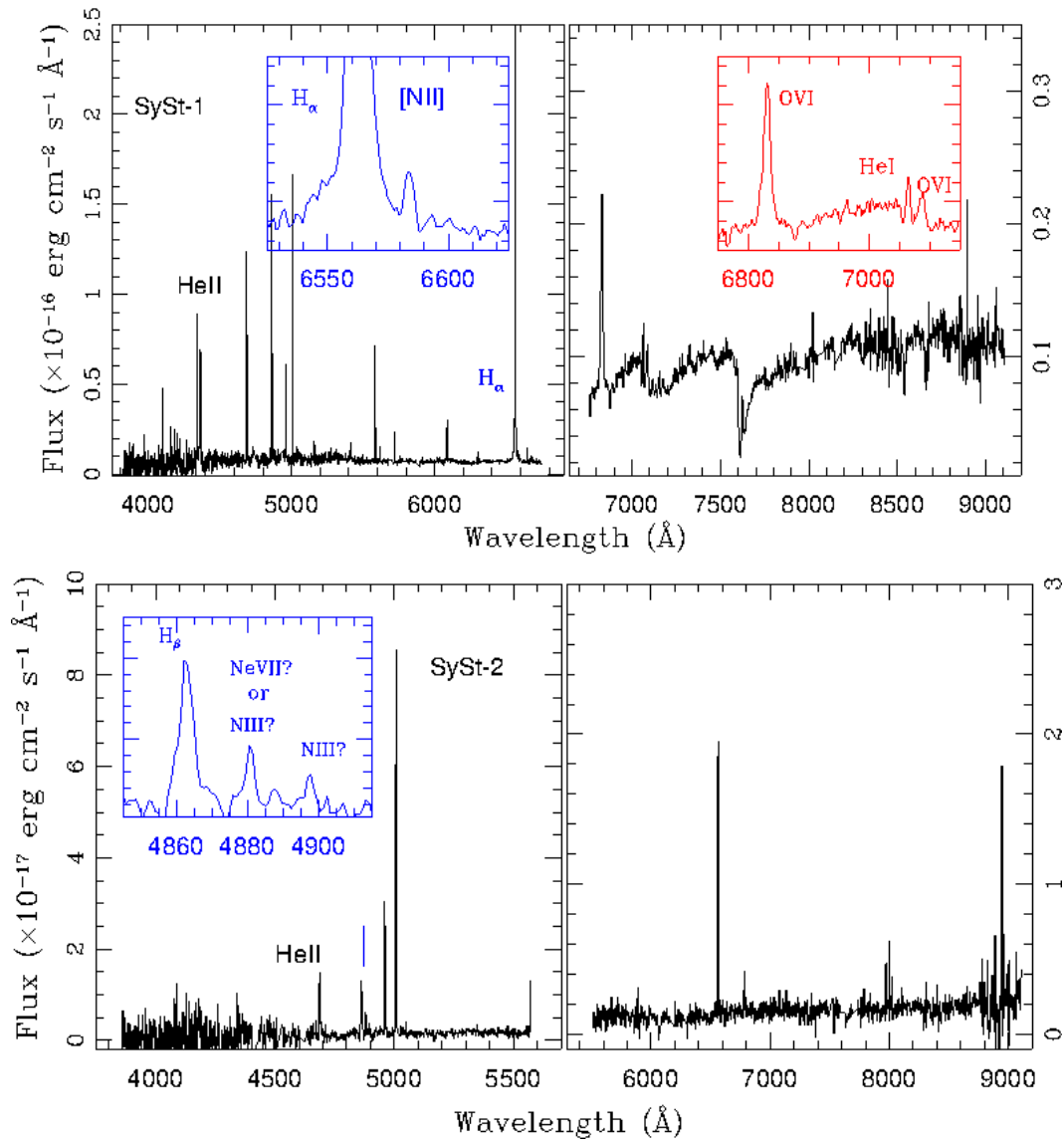


FIGURE 1.6: Blue plus red spectra of two symbiotic systems in NGC 205. The first spectrum (*top panel*, SySt-1) shows the typical single-peaked broad $\text{H}\alpha$ profile, and the Raman O VI scattered lines (at 6830 \AA and 7088 \AA). The second spectrum (*bottom panel*, SySt-2) displays the $\text{H}\beta$ line as well as the Raman-scattered Ne VII λ 973 (see Lee, Heo & Lee 2014) or N III at 4881 \AA line (Gonçalves et al., 2015).



FIGURE 1.7: Two objects with very similar morphologies. *Top panel* shows NGC 6537, a bipolar type I PN with a very hot central star. *Bottom panel* shows the bipolar SySt He 2-104, consisting of a WD and a cool Mira star. NGC 6537 G. Mellema et al., HST, ESA, NASA; He 2-104 R. Corradi et al., IAC, STScI, NASA.

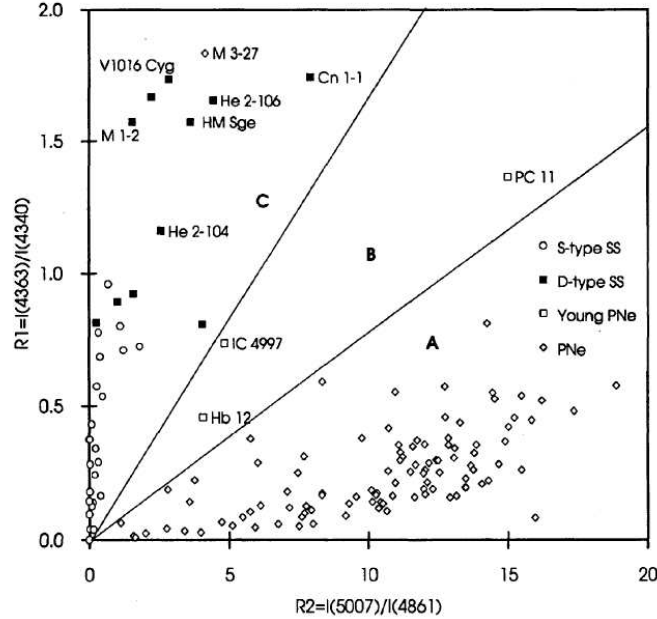


FIGURE 1.8: Diagnostic diagram to discriminate symbiotic stars and PNe from Gutierrez-Moreno et al. (1995b). It is a plot of $R1=[\text{O III}] \lambda 4363/H\gamma$ versus $R2=[\text{O III}] \lambda 5007/H\beta$. The two straight lines correspond to the locus of $R3=(5007)/(4363) = 13.1$ and 27.5 (upper and lower lines, respectively). The different symbols represent D-type, S-type symbiotic stars, young PN and more evolved PNe. The regions A, B, and C define the regimes of PNe, young PNe and symbiotic stars, respectively.

symbiotics. This ratio is a good temperature indicator at densities typical of PNe as well as a density indicator at typical densities of SySt. Symbiotic systems are generally denser than even the youngest PNe. Figure 1.8 displays the diagnostic diagram based on emission lines intensities in the optical regime (Gutierrez-Moreno et al., 1995b) while Figure 1.9 shows the colour-colour diagram using near-IR colours (Schmeja & Kimeswenger, 2001; Ramos-Larios & Phillips, 2005; Corradi et al., 2008). In Figure 1.8 is possible to represent points corresponding to different values of $R3 = (5007)/(4363)$. Gutierrez-Moreno et al. (1995a) found that the locus of $R3$ is a straight line passing through the origin, with the slope $[I(H\beta)/I(H\gamma)] \times (R3)^{-1}$. They used the value $I(H\beta)/I(H\gamma) = 2.132$, corresponding to $T_e = 10,000$ K and $\log N_e = 4$, these values were taken from Brocklehurst (1971). These diagnostic tools are good criteria to differentiate PNe from SySt. Iłkiewicz & Mikołajewska (2017) also proposed a number of new diagnostic diagrams in the optical regime for discriminating SySt from PNe. One of these diagnostic diagrams is based on the He I recombinations as it can be seen in Fig. 1.10. The latter diagram allows to correctly identify SySt that have been misclassified using the standard $[\text{O III}]$ diagnostic diagram (Iłkiewicz & Mikołajewska, 2017).

Corradi et al. (2003) have shown, by purely statistical arguments, that it is highly improbable that a true PN central star would have a binary Mira companion. On the other hand, evolutionary links between PNe and symbiotic systems are likely. Many current symbiotic stars may have gone through the PNe phase, when the

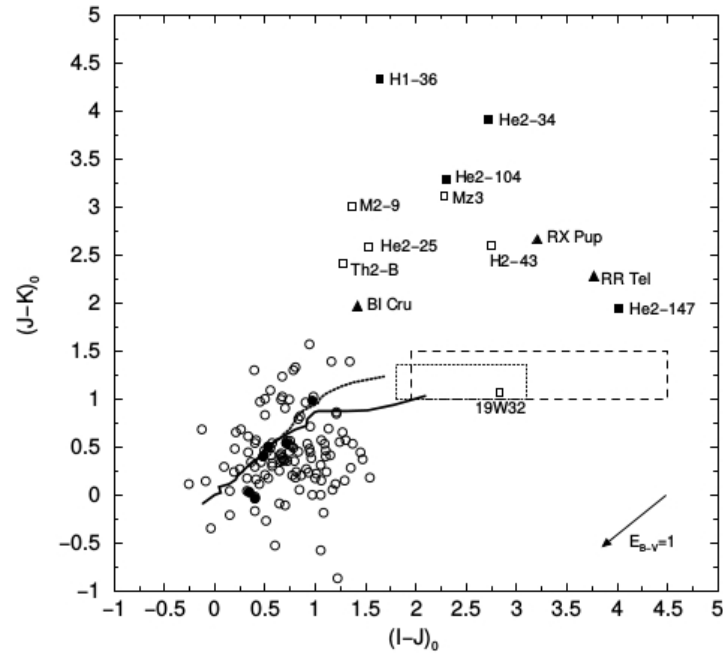


FIGURE 1.9: Diagnostic diagram based in IJK two-colour diagram using DENIS data taken from Schmeja & Kimeswenger (2001). The diagram shows PNe (open circles), bipolar PNe that do not show any symbiotic behaviour are represented by filled circles, symbiotic Mira classified in the literature as PN are filled square, symbiotic Mira not cataloged as PN (filled triangles), and suspected SySt (open squares). It also is showed the stellar main sequence (solid line), the giants (dotted line), and the Miras and semi-regular variables (dashed and dotted box, respectively).

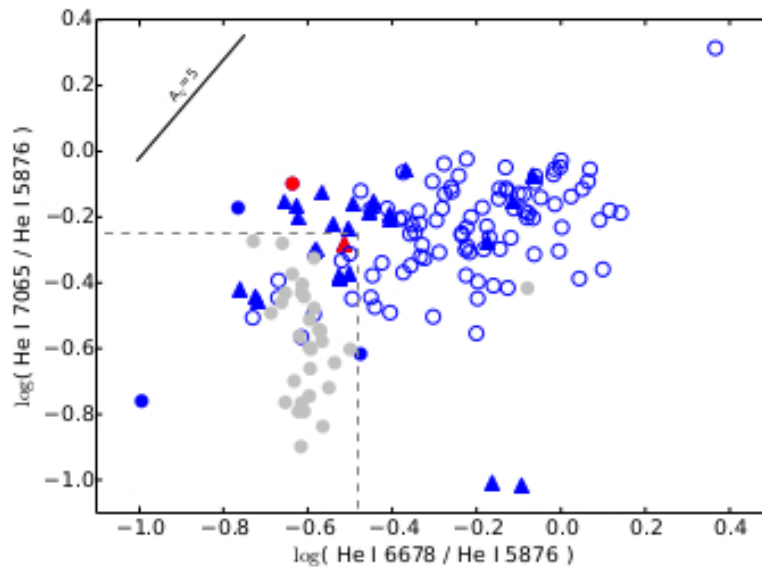


FIGURE 1.10: Diagnostic diagram using He I ratio implemented to distinguish between PNe and SySt. PNe are marked with gray symbols and SySt with blue symbols. The SySt that share the same location with PNe into the [O III] diagnostics diagrams are represented with red symbols. The S-type SySt are marked with open circles, the D'-type with full circles and D-type with triangles. The gray lines represent the criteria of selection for SySt. Figure adapted from Ikiewicz & Mikołajewska (2017).

current WD companion was at an early phase in its evolution. Similarly, many PN with a binary system may go through a symbiotic in the future when the companion stars evolves into AGB phase (Frew & Parker, 2010).

Notice that in the present section we have discussed the different diagnostic diagrams previously used to distinguish PNe from SySt and vice versa. In the following section, we expand the discussion to other emission-line objects that resemble PNe and SySt and the diagnostic tools used to differentiate them from these contaminants.

1.4 PNe, SySt and their mimics

There is a great variety of nebular and stellar objects with many properties in common with PNe and SySt, thus many objects may have been mis-classified as planetary nebulae. Similarly, several PNe have been found in catalogues of H II regions, low-surface brightness galaxies, reflection nebulae or Herbig-Haro objects. The possible confusion is such that even three candidate Galactic globular clusters turned out to be PNe, after spectroscopic analysis (Bica et al., 1995; Parker et al., 2006). Parker et al. (2006); Miszalski et al. (2008) examined in detail more of 1,200 PN candidates, by using a multiwavelength approach to reject non-PNe. Many of the objects previously accepted as PNe have been shown to be H II regions ionized by hot stars (Frew, 2008).

Figure 1.11 and 1.12 show the H α images and the spectra of some of the most common PNe and SySt mimics. All these objects share similar morphological and spectroscopic characteristics. Below, it will discuss these type of mimics in more details.

1.4.1 Compact H II regions

H II regions are emission line nebulae as PNe with O and/or B spectral type stars responsible for their ionization. Generally, the flux of ionizing photon that ionize the neutral gas in H II region comes from one or several OB stars. They are low excitation objects in comparison with the PNe. For this reason, the spectra of the H II regions lack of the He II lines and of other high excitation lines. Some compact H II regions have symmetric form, and they have been confused with PNe. Examples of compact H II regions classified as planetary nebulae are He 2-77 (Caswell & Haynes, 1987), Abell 77 = Sh 2-128 (Mampaso et al., 1984; Bohigas & Tapia, 2003), see Fig. 1.11), We 1-12 (Kimeswenger, 1998), Wray 16-185 (Acker et al., 1987; Ogura & Noumaru, 1994; Gyulbudaghian et al., 2004; Roman-Lopes & Abraham, 2006) and M 2-62 (see Fig. 1.11).

Generally, it is enough to differentiate PNe from compact H II regions taking into consideration the spectral features, environment, radio fluxes and near- and mid-IR characteristics. Usually, compact H II regions in external galaxies can be classified as wrongly PNe. However those objects appear more extended, if they are not too distant (Jacoby, 2006).

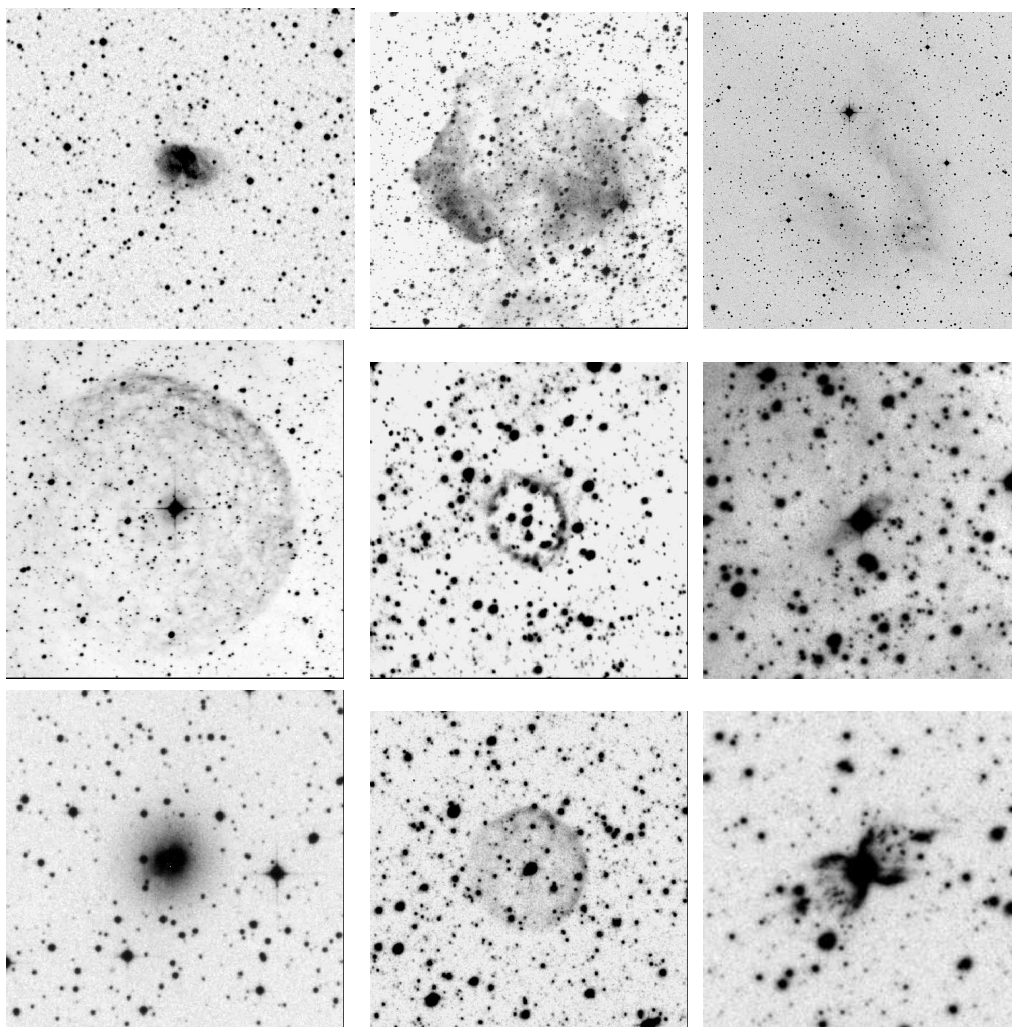


FIGURE 1.11: $H\alpha$ images of several PN mimics, adapted from SHS and DSS images. *Top row*, from left to right: Abell 77 (SH 2-128), a compact H II region; vBe 1, a low-surface brightness and diffuse H II region and Sh 2-174, a H II region ionized by a hot ‘naked’ low-mass stars. *Middle row*, in the same order: The faint shell around the Wolf-Rayet star WR 16; the WR ejecta nebula, PCG 11 and the faint bipolar nebula around the B[e] star, He 3-1191. From left to right, *bottom row*: the blue compact galaxy He 2-10, the true PN PHR J1424-5138 and the bipolar symbiotic outflow, He 2-104.

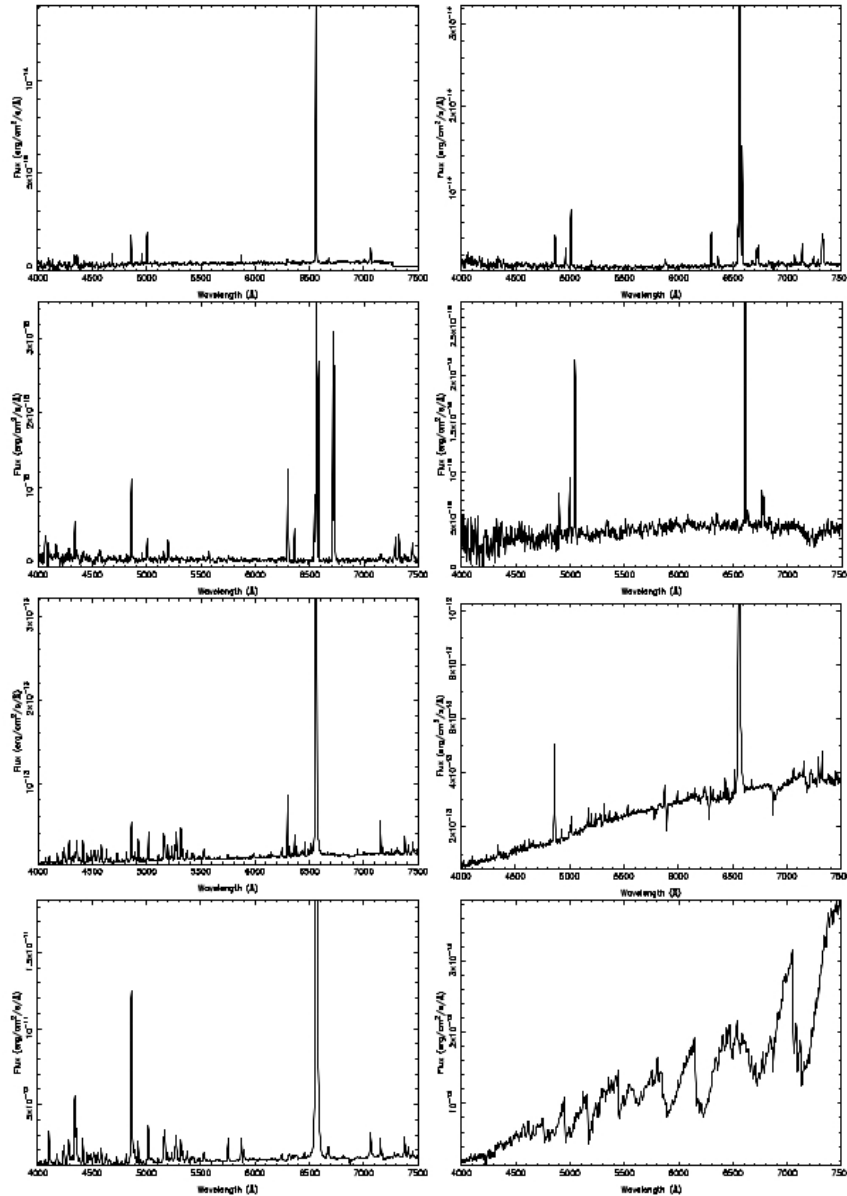


FIGURE 1.12: Spectra of different emission line objects that can be mimics of PN. Top row: (*left*) PTB 15, a ring-shaped nebula with a CS that shows symbiotic characteristics; (*right*) M 2-62, a reddened, compact H II region. Second row: (*left*) PHR J0818-4728, a compact knot in the Vela supernova remnant, which shows strong [S II] and [O I] lines; (*right*) PHR J0950-5223, an emission-line galaxy with a velocity of 2,300 km s⁻¹. Third row: (*left*) He 3-1191, a B[e] star surrounded by a faint bipolar outflow with intense, broad H α line, strong [O I] λ 6300, and the forest of Fe II and [Fe II] lines; (*right*) BI Crucis, a low-excitation symbiotic star with weak B[e] characteristics. Bottom row: (*left*) Eta Carinae, a LBV star with a rich emission-line spectrum which resembles a B[e] star. (*Right*) A M-type giant where the continuum peak near 6550 Å can mimic H α emission in narrowband filters. All spectra cover the same wavelength range (4000-7500 Å) and were taken with the SAO 1.9-m reflector (Frew & Parker, 2010).

1.4.2 Herbig-Haro objects and young-stellar objects

Herbig-Haro (HH) objects are small nebulae with characteristic emission lines in their spectra. They are recognized as manifestations of outflow activities from newborn stars (Reipurth & Bally, 2001). HH objects can usually be differentiated from PN due to their distinctive morphology, the presence of shocked-excited spectral features such as strong [S II], [N I] and [O I] emission lines (Canto, 1981; Cappellaro et al., 1994) and the proximity to star-forming regions and associated molecular clouds with high levels of surrounding extinction. Given the combination of low-excitation and high-density, the blue [S II] $\lambda\lambda 4068, 4076$ lines are frequently strong relative to the $H\beta$ line in HH objects, if the impact of the reddening is not important.

Related with HH objects are the young-stellar objects (YSOs). The spectra of these objects have emission lines such as Balmer lines (Witham et al., 2008), which emerges from the accretion disk. In their spectra it is clearly perceptible their reddened nature like in the SySt spectra. The strong reddening is an indicative of the cool effective temperature of these sources. YSOs are among the most common contaminants of SySt (Corradi et al., 2008).

1.4.3 Cataclysmic variable stars

Cataclysmic variables (CVs) are a large class of variable stars that includes recurrent novae and dwarf novae. They are binary systems of very short orbital period, in which a white dwarf is accreting material from a close, Roche lobe-filling companion, usually a main sequence G-, K- or M-type star (Patterson, 1984).

Novae in the nebular phase show strong Balmer and [O III] emission lines and sometimes confused with PNe on objective prism plates. At later stages in the evolution of classical and recurrent novae, resolved shells become visible, comprised of ejected gaseous produced in the nova eruption. Nova shell shows both spherical and axisymmetric structures (e.g. Downes & Duerbeck, 2000), and they can have spectral signatures reminiscent of PNe.

1.4.4 Wolf-Rayet stars

Wolf-Rayet (WR) stars are evolved, massive and hot stars, with particularly strong winds, which caused the loss of their hydrogen envelopes, leaving their helium cores exposed. In particular, WR stars have wind densities one order of magnitude higher than the massive O stars (Crowther, 2007). The high mass-loss rates arise due to the very broad emission lines of helium, carbon, nitrogen and oxygen. The ejected material and the wind-blown bubbles surrounding Wolf-Rayets have occasionally been cataloged as PNe. This mis-classification is based on their spectral features, but in general the width of the emission-lines is enough to differentiate the WRs from PNe. There are two classes of WR stars: WN stars, which show broad emission lines of nitrogen and helium and WC stars with broad helium, carbon and oxygen lines. Fig. 1.11 shows the $H\alpha$ images of two WR (WR 16 and PCG 11), in which it is possible to see emission shells around these stars.

1.4.5 Be and B[e] stars

Be stars are main-sequence and giant stars with strong Balmer lines. The prominent emission is produced in a circumstellar disk or an envelop, due to the rapid rotation or by the presence of magnetic field. B[e] stars are sub-giant stars which have additional emission lines of species such as Fe II, [Fe II], [O II] and [S II], and occasionally P-Cygni absorption profiles. B[e] stars are not homogeneous structures and many of them appear to have a surrounding nebula, produced by large-scale mass-loss events involving one or more eruptions (Marston & McCollum, 2006). The B[e] star He 2-90 have features very similar to those of PNe, and it is surrounded by a bipolar nebula (see figures 1.11 and 1.12). These objects are also very similar to the symbiotic systems and YSOs. Therefore they can be potential contaminants for SySt. Follow-up spectroscopic surveys of the IPHAS PN and SySt candidates have shown that the majority of their candidates are Be stars (Corradi et al., 2008).

1.4.6 Galaxies

In the past low-surface brightness (LSB) dwarf galaxies have also been mis-classified as evolved PN by using morphological criteria alone. Occasionally, via resolved stellar population (deep imaging e. g. Hoessel et al., 1988) or spectroscopy (redshift) of emission objects the true identity as dwarf galaxy has been revealed. A few emission-line galaxies appeared in the early PN catalogues (e.g. Acker et al., 1991). Several galaxy sub-types have strong Balmer and forbidden emission-lines, and are potentially confused with PN on objective prism plates, where the lack of spectral resolution precluded an extragalactic identification for low redshift examples. He 2-10 (Fig. 1.11) and IC 4662, were classified as possible PN by Henize (1967), are now known to be nearby starburst dwarf galaxies. Additionally, there were at least five emission-line galaxies in the preliminary MASH catalog. They were later spectroscopic confirmation by determining their redshifts, for example, PHR J0950-5223 is one of these galaxies (Fig. 1.12).

1.4.7 Supernova remnants

Supernova remnants (SNR) are nebulae resulting from the explosion of massive stars. The one-sided filamentary PNe, the Medusa nebula (Abell 21) and Sh 2-188 were identified as SNR in the past. Several compact knots of extended SNRs have been classified as PN candidates. For instance, Haro 2-12 which is a bright knot in Kepler's SNR of 1604 (Acker et al., 1987; Riesgo & López, 2005) and PHR 0818-4728 (Parker et al., 2003), which turned out to be a compact knot in the Vela SNR.

1.4.8 Diagnostic diagrams: separating PNe and SySt from other emission line sources

Here we discuss the optical diagnostic diagrams that were used in the past to select planetary nebulae and symbiotic stars. In general, diagnostic diagrams use several

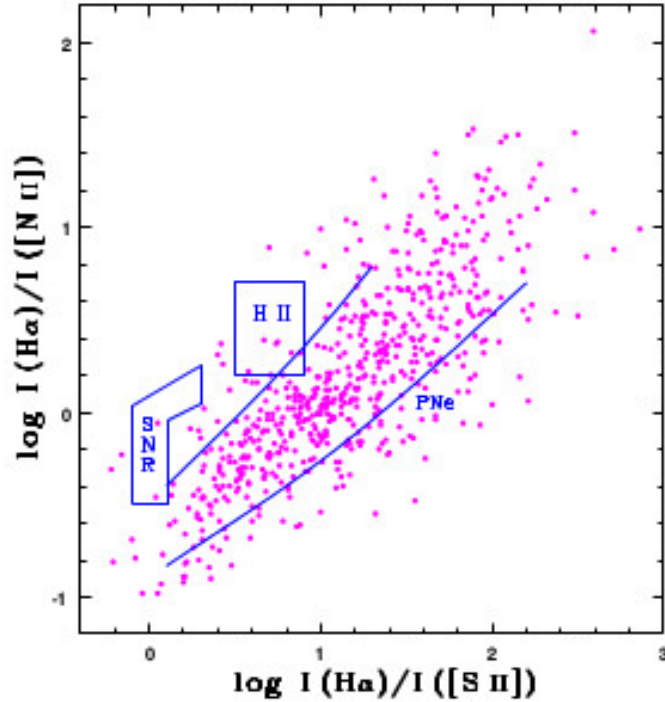


FIGURE 1.13: $\log(I(\text{H}\alpha)/I[\text{N II}])$ versus $\log(I(\text{H}\alpha)/I[\text{S II}])$ diagnostic diagram, which are used to separate PNe, H II regions and SNRs. Plot taken from Riesgo & López (2006).

emission-line intensities and are useful for differentiating resolved emission sources such as PN from H II regions, SNRs and other objects. For example, Figure 1.13 shows a diagnostic diagram based on the $\text{H}\alpha/[\text{N II}]$ and $\text{H}\alpha/[\text{S II}]$ emission-line ratios (Sabbadin et al., 1977; Canto, 1981; Fesen et al., 1985; Riesgo & López, 2006). The selection criteria were empirically derived in these diagrams, by using emission lines ratios observed in supernova remnants, PNe and H II regions.

Corradi et al. (2008) have used a method of selecting SySt candidates by combining IPHAS and IR (2MASS) colours, this methodology allows to differentiate symbiotic systems from both normal stars and $\text{H}\alpha$ point sources emitters, including compact PN. Figure 1.14 displays the two IPHAS and 2MASS colour-colour diagrams used for in Corradi's work. With the combination of these diagnostic diagrams it is possible to discriminate SySt and PNe from cataclysmic variables, B[e] and Mira stars in an effective way. Later, Viironen et al. (2009a,b) also used these two (IPHAS and 2MASS) colour-colour diagrams to discriminate PNe from stellar and other emission lines sources in the Galactic context. Figure 1.15 displays the two colour-colour diagrams, in which the PN locus is emphasized. In the IPHAS diagram, the $(r - \text{H}\alpha)$ axis mainly indicates increasing values of the $\text{H}\alpha$ emission line equivalent width, while the $(r - i)$, for normal stars, represent a sequence of increasing spectral type and reddening. The 2MASS color-color diagram $[(J - H) \text{ vs } (H - K_s)]$ allows to explore the reddened nature of emission line objects.

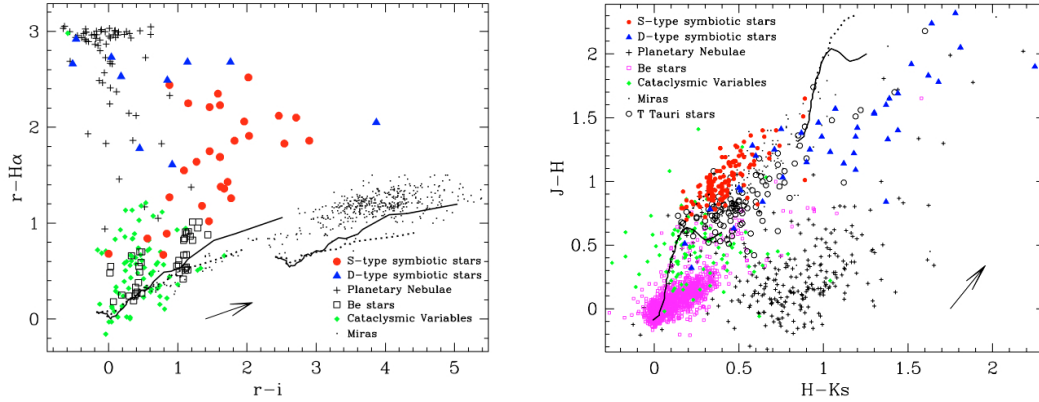


FIGURE 1.14: Diagnostic colour-colour diagrams for symbiotic stars and other objects based in IPHAS (*left plot*) and 2MASS (*right plot*) catalogues. The $H\alpha$ emitters are given in distinct regions of the diagrams. The locus of main-sequence and RGB stars is indicated by the solid and dotted lines, respectively. Two sequences are shown, corresponding to the reddening values $E(B-V)=0$ and $E(B-V)=4$. The arrow indicates the length of the reddening vectors, which corresponds to $A_V = 3$ mag. Figures are taken from Corradi et al. (2008).

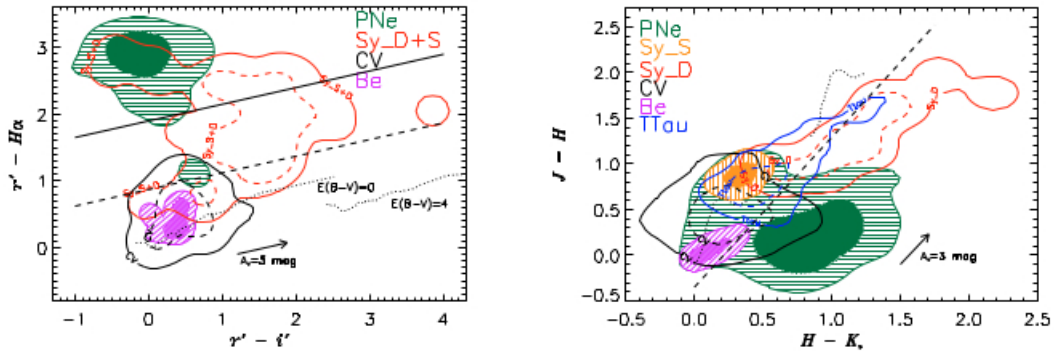


FIGURE 1.15: *Left panel* diagram showing the location of PNe (area filled with green horizontal lines), D- and S-type symbiotic stars (Sy-D+S, red lines), cataclysmic variables (CV, black lines), and Be-stars (area filled with diagonal lines coloured magenta) in the IPHAS (INT photometric $H\alpha$ survey) colour-colour diagram. The location of main-sequence (MS) stars (Drew et al. 2005) with reddenings of $E(B-V)=0$ and $E(B-V)=4$ are shown as dotted lines. *Right panel* 2MASS colour-colour diagram for the same objects and the same MS reddening tracks as in the left. The symbiotic stars are divided into S-type (SySt-S, areas filled with vertical orange lines) and D-type (SySt-D, red lines). The location of T-Tauri stars (TTau, blue lines) is also shown. Figure adapted from Viironen et al. (2009a).

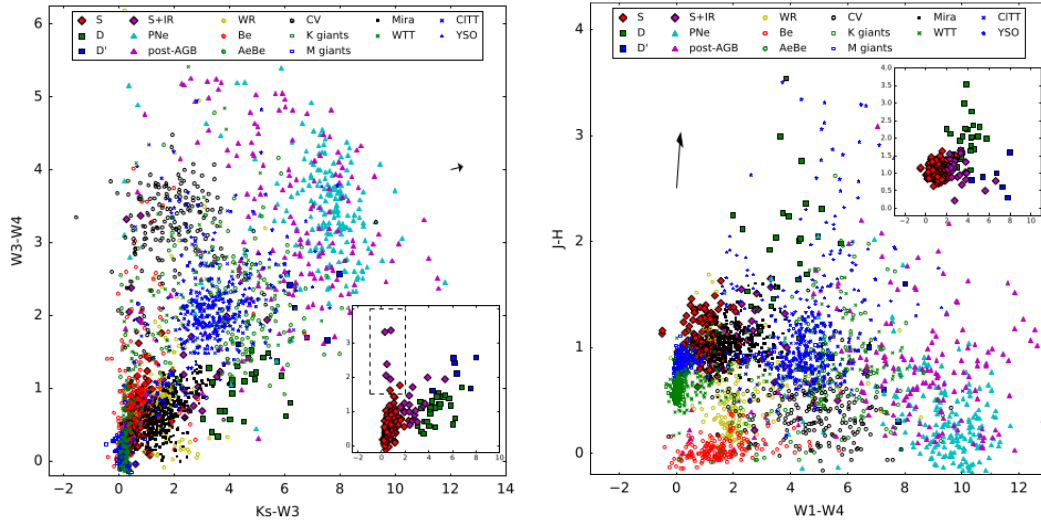


FIGURE 1.16: The 2MASS/AllWISE ($W3-W4$) versus ($Ks-W3$) (*Left panel*) and ($J-H$) versus ($W1-W4$) (*Right panel*) colour-colour diagnostic diagrams for different classes of objects as well as for the four type of SySt presented in the inset plot. The arrow represents the vector extinction at 4 mag in the V-band. The dashed box in the inset plot indicates the vertical branched region of SySt. The $W3$ and $W4$ magnitudes of the majority of CVs correspond to upper limit values. Figures adapted from Akras et al. (2019a)

Recently, Akras et al. (2019a) used the photometric data from the 2MASS and WISE surveys to construct various diagnostic diagrams that show the distribution of SySt and other $H\alpha$ -mimics in the near-mid infrared space. Fig. 1.16 shows the ($W3 - W4$) versus ($Ks - W3$) and ($J - H$) versus ($W1 - W4$) colour-colour diagnostic diagrams. Akras, Guzman-Ramirez, & Gonçalves (2019c) using the classification tree model (Grubinger et al., 2011) found new colour criteria to identify compact PNe of the best possible way by using both 2MASS and AllWISE photometric data. By combining these two catalogues, they found that $W1-W4 \geq 7.87$ and $J-H < 1.10$; $H-W2 \geq 2.24$ and $J-H < 0.50$; and $Ks-W3 \geq 6.42$ and $J-H < 1.31$ are optimal criteria to discover new PNe.

1.5 Thesis overview

The thesis is organized as follows. In Chapter 2, I present a description of the Javalambre Photometric Local Universe Survey (J-PLUS), the Southern-Photometric Local Universe Survey (S-PLUS) and the Javalambre Physics of the Accelerating Universe Astrophysical Survey (J-PAS). These new multi-band surveys, which contain both narrow- and broad-bands filters, provide a unique opportunity to find PNe and SySt in the Galactic halo. In Chapter 3, I discuss the new colour criteria based on these three surveys. I also present the machine learning techniques, more precisely principal component analysis (PCA) and linear discriminant analysis (LDA), which were used to discriminate objects classes. Chapter 4 discusses the validating strategy to the J-PLUS and J-PLUS colour-colour diagnostic diagrams. It also presents the first results on applying the colour criteria to the first J-PLUS

data release (DR1) and S-PLUS DR1. The objects recovered in the DR1s were used to validate the machine learning methodologies. In Chapter 5, I provide a general discussion, the conclusions and perspectives.

Chapter 2

Description of the surveys

The Javalambre Photometric Local Universe Survey (J-PLUS, Cenarro et al., 2019; <https://www.j-plus.es>) and the Southern-Photometric Local Universe Survey (S-PLUS, Mendes de Oliveira et al., 2019; <http://www.splus.iag.usp.br>) are two akin projects that are mapping the Northern and Southern celestial hemispheres, respectively. This thesis makes use of the data from the J-PLUS Science Verification, first J-PLUS Data Release and first S-PLUS Data Release. The Javalambre Physics of the Accelerating Universe Astrophysical Survey (J-PAS, Benítez et al., 2015; <http://www.j-pas.org/>) is a multi-band survey that will also observe high latitudes of the Northern sky. The J-PLUS filter set allows to relieve accurate spectral energy distributions (SEDs) for millions of calibration stars that will be used to transport the photometric calibration from J-PLUS to J-PAS (Gruel et al., 2012). The main purpose of J-PLUS was thus to calibrate the J-PAS project.

Given that these surveys are defined by a set of narrow- and broad-band filters able to cover the whole optical spectra, they provide an unique opportunity to search for PNe and SySt in the Galactic halo. J-PLUS and S-PLUS have a filter designed to detect the H α recombination line. In the case of J-PAS other emission line such as [O III], will be also detected by a specific filter, altogether J-PAS filter system allows much better ways to isolate PNe and SySt.

In the following chapter I discuss some of the previous photometric surveys that resulted in the detection of PNe. Then, I introduce the new J-PLUS, S-PLUS and forthcoming J-PAS surveys.

2.1 Previous PNe and SySt surveys

Several surveys have been used to find new PNe in our Galaxy, since an accurate census of them is needed for a reliable calculation of the numbers, scale height, space density and birth rate of PNe in the Milky Way. Surveys previous than those discussed bellow have resulted in an extensive sample, out to a radius of ~ 2.0 kpc from the Sun (Frew, 2008). However, this sample is much less complete at the faint end of the PN luminosity function.

The following subsection, it presents the AAO/UKST H α survey, SHASSA, VTSS and IPHAS surveys.

2.1.1 The AAO/UKST H α Survey

The Anglo-Australian Observatory/UK Schmidt Telescope (AAO/UKST) is a high resolution, narrow-band H α survey of the Southern Galactic plane and Magellanic Clouds. It covers $\sim 4,000$ deg² of the sky extending to a galactic latitude of $|b| \sim 10 - 13^\circ$. The survey is available online as the scanned SuperCosmos H α Survey (SHS; Parker et al., 2005b).

The survey uses a high-quality optical interference filter (see Parker & Bland-Hawthorn, 1998) of 70 Å width centered close to the H α line. It has a very good sensitivity to faint diffuse H α emission down to a surface brightness of $\sim 1 - 3 \times 10^{-17}$ erg cm⁻² s⁻¹ arcsec⁻¹. The H α photometric images have been scanned and digitized by the high speed SuperCOSMOS plate scanning machine at the Royal Observatory, Edinburgh (Hambly et al., 1998) and they are available in the SHS database <http://www-wfau.roe.ac.uk/sss/halpha/>.

Macquarie/AAO/Strasbourg H α (MASH) Catalogue

The MASH catalogue includes all the PNe found in AAO/UKST H α Survey. A total of $\sim 1,200$ new Galactic PNe were identified in SHS (Parker et al., 2005a, 2006; Miszalski et al., 2008). Most of these PNe are of very low surface brightness and are often highly reddened. The MASH catalog includes several PNe of very large angular diameter. Once the SHS H α data became available it was possible to verify and confirm the previous visual identification of the sources as well as to obtain more accurate estimates about of nebular size, morphology and position. By using the MASH catalog many of the PNe mimics such as H II regions have been removed and during this process a significant number of new PNe were identified. Overall, it contains around 60% more PNe than all the previous catalogs.

2.1.2 SHASSA

Given that the AAO/UKST H α Survey was restricted to an area in the range from 10 to 12° of the Galactic plane, it is obvious that additional searches were necessary. Therefore, the AAO/UKST Survey was performed in the Southern Sky H-Alpha Survey Atlas (SHASSA; Gaustad et al., 2001), up to a Galactic latitude of $|b| = 10^\circ$, with the principal goal of discovering new evolved PNe in the Solar neighborhood. SHASSA is a robotic wide-angle digital imaging survey aimed of detecting H α emission from the warm ionized interstellar medium. It is formed by a narrow-band filter (H α + [N II]) and continuum images of a large proportion of the Southern sky (17,000 deg²). SHASSA consists of 2168 images covering 542 fields south of +16° declination. There are four kind of images available for each field: H α , red continuum, continuum-corrected H α ¹ and a smoothed H α image. Images

¹These are generated by subtracting each continuum image from the corresponding H α image.

of individual fields in the surveys may be accessed on the Web <http://amundsen.swarthmore.edu/SHASSA/> or <http://www.lco.org/SHASSA/>.

A visual inspection of the SHASSA images resulted in a discovery of 17 nebulae (PNe) with a radius larger than 5 arcmin. All previously known PNe larger than this size were recovered in SHASSA's blind search. Good example are Hewett 1 (Hewett et al., 2003), PG 0108 and PG 0109 (Frew et al., 2006).

2.1.3 VTSS

A complementary survey to SHASSA, the Virginia Tech Spectral line Survey (VTSS; Dennison, Simonetti, & Topasna, 1998) covers a wide strip around the Northern Galactic plane, $|b| \leq 30^\circ$. Like SHASSA, the combination of fast optics, narrow-band filters and a CCD detector provides a high sensitivity to diffuse $H\alpha$ emission. VTSS used the Spectral Line Imaging Camera (SLIC) of the Celestron-5 telescope, which obtains circular images with a diameter of 10° , with a resolution of 96 arcsec per pixel. This survey is formed by a narrow-band $H\alpha$ filter with $\text{FWHM}^2 = 17.5 \text{ \AA}$ and continuum filters as well as a [S II] filter centered in 6725 \AA . Each VTSS field was planned to have four images: $H\alpha$, continuum-corrected $H\alpha$, [S II] and continuum-corrected [S II].

Due to the low spatial resolution of the survey, only three nebulae (PNe) were identified (Frew et al., 2006).

2.1.4 IPHAS

The Isaac Newton Telescope (INT) Photometric $H\alpha$ Survey of the Northern Galactic Plane (IPHAS; Drew et al. 2005) is a direct consequence of the success of the SHS. The IPHAS survey was carried out with the 2.5-meter INT equipped with the wide field camera (WFC) and it covers $1,800 \text{ deg}^2$ of the Northern Galactic plane between $-5^\circ < |b| < +5^\circ$. It is formed by a narrow-band filter for the $H\alpha$ emission and two Sloan r' and i' broad-band filters. The $H\alpha$ filter is very similar to the SHS one, with a FWHM of 95 \AA . For point sources, the limit magnitude of the survey was $r' \sim 20$ mag.

Using IPHAS i' and r' broad-band filters it is possible to construct a colour-magnitude diagram that reveals sequences at different reddening. On the other hand, the $(r' - H\alpha)$ vs $(r' - i')$ colour-colour diagram, turned out to be very useful to separate objects with an excess in $H\alpha$ emission, from stellar objects. Thus, in Figure 2.1, sources with an $H\alpha$ excess appear at the top of the diagram, while the most reddened objects are placed to the right (Drew et al. 2005).

González-Solares et al. (2008) presented the IPHAS first data release, which includes a photometric catalog of about 200 million point-source objects. Witham et al. (2008) have presented a catalog of 4,853 $H\alpha$ point-source emitters, based on the IPHAS colour-color diagram, which covers the magnitude range $13.0 < r' < 19.5$. This diagram was derived from $1,500 \text{ deg}^2$ data, which represents 80% of the final

²Full width at half maximum (FWHM).

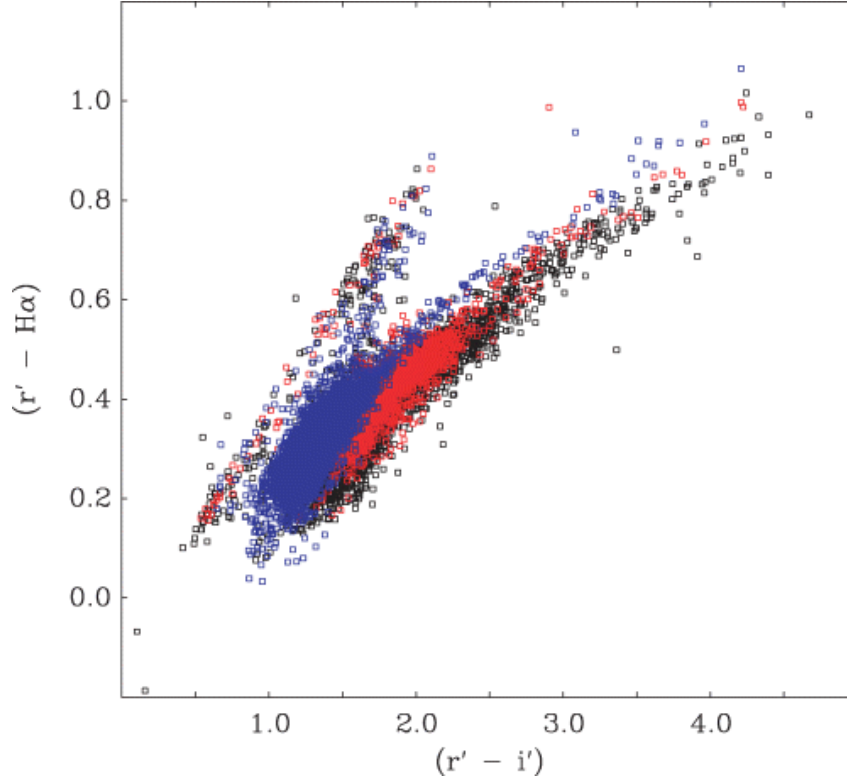


FIGURE 2.1: The colour-colour diagram $(r' - H\alpha)$ vs $(r' - i')$ for 13,818 point sources from the overlap area of the paired exposures for IPHAS fields 4199 (black points), 4090 (red points) and 4095 (blue points), in Aquila constellation. Note the very well defined upper edge to the upper sequence, this is where unreddened main sequence stars are located. The few stars above it are candidate emission line objects. Adapted from Drew et al. (2005)

IPHAS survey area. The spectra (~ 300) of these objects have shown that more than 95% are genuine emission line stars or compact nebulae. Corradi et al. (2008) classified 1,183 of them as possible symbiotic stars, since they also exhibit strong $H\alpha$ emission. A follow-up spectroscopic survey of candidate SySt confirmed the symbiotic nature of eight candidates: 7 S-type and 1 D-type symbiotic systems (Corradi et al., 2010). Recently, Akras et al. (2019a) proposed new IR criteria for SySt and combining them with the photometric data of IPHAS and VPHAS+³ ended up with a new shorter list of candidate SySt.

Viironen et al. (2009b,a) reported on the results of the specific search for compact PN candidates from IPHAS data. These sources were identified using IPHAS $(r' - H\alpha)$ vs $(r' - i')$ and 2MASS $(J - H)$ vs $(H - K_s)$ colour-colour diagrams. Akras et al. (2019c) used photometric data from the 2MASS and WISE surveys in order to get those IR criteria that can better distinguish PNe from other $H\alpha$ sources. By applying these new IR criteria to the IPHAS list of PN candidates and the entire IPHAS and VPHAS+ DR2 catalogues, 39 new likely genuine compact ($< 6''$) PNe were found.

³VPHAS+ is a photometric survey similar to IPHAS for the southern hemisphere (Drew et al., 2014).



FIGURE 2.2: View of the JAST/T80 telescope inside its dome at the Observatorio Astrofísico de Javalambre. Figure is taken from Cenarro et al. (2019).

Sabin et al. (2010) also reported on new PN candidates found in IPHAS data, in this case for extended PNe. With the spectroscopic follow-up, many of the candidates result to be $H\alpha$ emission line stars, most probably YSOs. Extended PNe were also found by visual inspection of the IPHAS continuum-subtracted $H\alpha$ image mosaics. This has led to the discovery of several resolved PN, including a number of highly evolved nebulae (Sabin et al., 2010).

2.2 Multi-band photometric surveys: a new era for planetary nebula and symbiotic stars

2.2.1 J-PLUS

J-PLUS is a multi-filter survey, which is being conducted from the Observatorio Astrofísico de Javalambre (OAJ⁴, Cenarro et al., 2014). This is ongoing for another couple of years, to cover a total area of $\sim 8,500 \text{ deg}^2$ of the Northern sky by using the Javalambre Auxiliary Survey Telescope (JAST/T80). JAST/T80 is a 83 cm telescope mounting T80cam, a panoramic camera that provides a FoV of 2 deg^2 which drives a plate scale at the Cassegrain focal plate of $55.56 \text{ arcsec mm}^{-1}$. Figure 2.2 illustrates the JAST/T80 telescope inside of the 6.2 m dome at the OAJ.

The JAST/T80 is constituted by a set of 12 narrow, medium and broad-band filters. The filter set is defined in such way to be sensitive to key spectral features in the rest frame, thus being optimal to study of Milky Way objects and the stellar population of galaxies in the local universe. In addition, the survey strategy has been well-tuned to optimize the scientific return in a wide range of applications in many other areas of Astrophysics. Therefore, the J-PLUS filters are sensitive both to the continuum and to important spectral features such as the emission

⁴The OAJ is an astronomical facility located at the Pico del Buitre of the Sierra de Javalambre, in Teruel, Spain.

| Filter | λ (Å) | $\Delta\lambda$ (Å) | $m_{\text{lim}}^{\text{J-PLUS}}$ | $m_{\text{lim}}^{\text{DR1}}$ | ZP^{DR1} | σ_{zp}^{DR1} | Comments |
|--------------|---------------|---------------------|----------------------------------|-------------------------------|-------------------|----------------------------|--------------------------------|
| <i>u</i> | 3485 | 508 | 20.5 | 20.8 | 21.13 | 0.025 | Common with J-PAS |
| <i>J0378</i> | 3785 | 168 | 20.5 | 20.7 | 20.54 | 0.026 | [O II]; common with J-PAS |
| <i>J0395</i> | 3950 | 100 | 20.5 | 20.7 | 20.32 | 0.024 | Ca H+K |
| <i>J0410</i> | 4100 | 200 | 20.7 | 20.9 | 21.30 | 0.018 | H δ |
| <i>J0430</i> | 4300 | 200 | 20.7 | 20.9 | 21.37 | 0.018 | G-band |
| <i>g</i> | 4803 | 1409 | 21.5 | 21.7 | 21.7 | 0.013 | SDSS |
| <i>J0515</i> | 5150 | 200 | 20.7 | 20.9 | 21.52 | 0.010 | Mgb Triplet |
| <i>r</i> | 6254 | 1388 | 21.5 | 21.6 | 23.52 | 0.010 | SDSS |
| <i>J0660</i> | 6600 | 138 | 20.7 | 20.9 | 21.04 | 0.014 | H α ; common with J-PAS |
| <i>i</i> | 7668 | 1535 | 21.2 | 21.1 | 23.25 | 0.012 | SDSS |
| <i>J0861</i> | 8610 | 400 | 20.0 | 20.2 | 21.54 | 0.016 | Ca Triplet |
| <i>z</i> | 9110 | 1409 | 20.2 | 20.3 | 22.63 | 0.016 | SDSS |

TABLE 2.1: The *J-PLUS* filter systems. The first column shows the filter names. Columns 2 to 7 present the J-PLUS central wavelengths, FWHM, expected limit magnitude, DR1 limit magnitude, DR1 zero points and DR1 zero point uncertainties. And, finally, column 8 shortly describes the filters.

lines produced in ionized nebulae. In agreement with the J-PLUS strategy, the 12 filters are formed of six intermediate-band filters of 200-400 Å width centered in key absorption features. The *J0378* is designated to detect the Ca H+K, *J0410* for H δ , *J0430* for the G band, *J0515* for the Mg b triplet and *J0861* for the Ca triplet. The J-PLUS intermediate-band filter *u*, in common with J-PAS filter system, is located at the blue part of the Balmer-break region. The J-PLUS filter set is also defined by two narrow-band filters, *J0378* and *J0660*, which are common with two J-PAS filter system. These two filters are designated to isolate the [O II] λ 3727 and H α λ 6563 emission lines, respectively. The *J0660* filter has a particular relevance for this thesis, since H α emission line is a typical spectral feature of PNe and SySt. Finally the J-PLUS is completed by four broad-band SDSS-like filters: *g*, *r*, *i* and *z* (Fukugita et al., 1996). Table 2.1 specifies the characteristics of the filters and the features targeted by the narrow-band ones. The medium zero points (*ZPs*) of the filters are also listed in Table 2.1.

Figure 2.3 shows the efficiency of the transmission curves of the J-PLUS filters. The spectrum of the PN Minkowski 1-57 is overplotted. As it is expected, the H α emission line is detected by one of the narrow-band filter (*J0660*). Another advantage of this project is that the J-PLUS filter set can characterize the whole optical spectrum, unlike a number of previous surveys. This filter set allows to construct accurate spectral energy distributions (SEDs) for millions of calibration stars as well as analyzing the stellar population of nearby galaxies up to limiting redshift of ~ 0.015 (Cenarro et al., 2019). In addition, the two narrow-band filters are perfect to map the star formation rates in galaxies in the redshift range $0 < z < 0.05$ and in conjunction with the others narrow- and broad-band filters, they permit

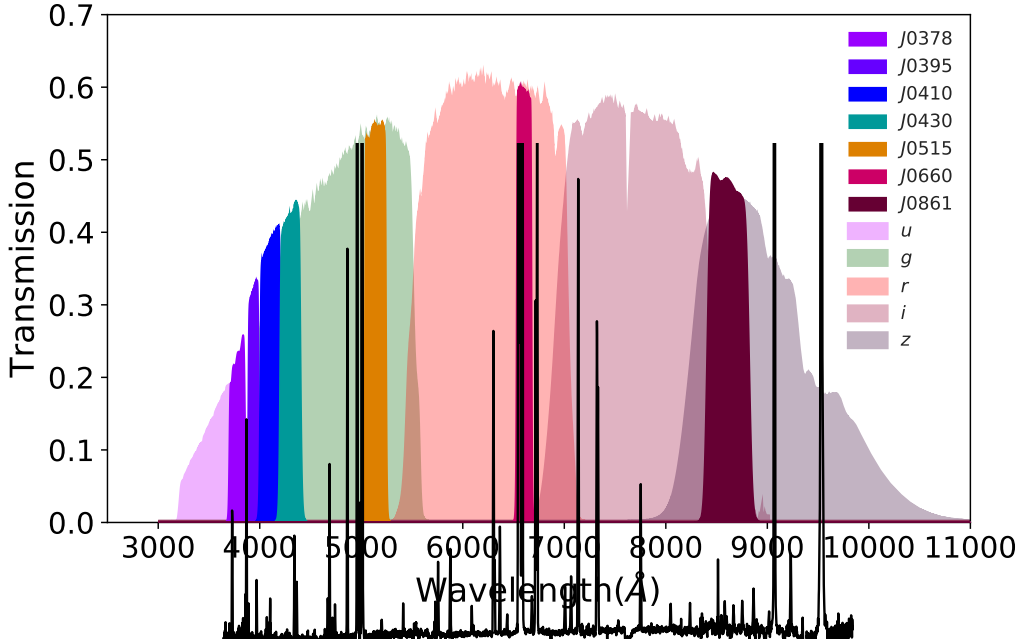


FIGURE 2.3: Overall transmission curves measured for the set of 12 J-PLUS filters, including the effect of the entire system (sky, mirrors, lenses and CCD). Overplotted is the spectrum of Galactic PN Minkowski 1-57.

to search for PNe and SySt.

Science verification data (SVD)

These data comprise a group of well-known objects to test and challenge the science capabilities of J-PLUS (Cenarro et al., 2019). One pointing of J-PLUS during this phase was centered at the MW globular cluster M15 (Bonatto et al., 2019). The J-PLUS SVD made available observations of the galaxy clusters A2589 and A2593, M101, M49, the Arp313 triplet of galaxies and a few nearby galaxies including NGC 4470 and the Coma cluster. The analysis of these data are presented in Molino et al. (2019); Logroño-García et al. (2019); San Roman et al. (2019). The Galactic halo PNe H 4-1 (Pena et al., 1990) and PNG 135.9+55.9 (Tovmassian et al., 2001) were also included in the SVD. The photometric results of these two PNe will be discussed in Section 4.1 of the Chapter 4.

First Data Release (DR1)

The J-PLUS first data release (DR1; https://www.j-plus.es/datareleases/data_release_dr1) is composed by 511 fields observed with the 12 narrow- and broad-band filters and cover 1,022 deg² of the sky ($\sim 900\text{deg}^2$ after masking). Fig 2.4 displays all the tiles of J-PLUS DR1 (red squares). DR1 is based on images collected by the JAST/T80 telescope from November 2015 to January 2018. Around 9 million objects at $r < 21$ were included in this first data release. Limiting magnitude (5σ in 3 arcsec aperture) distributions and typical uncertainties in the calibration of

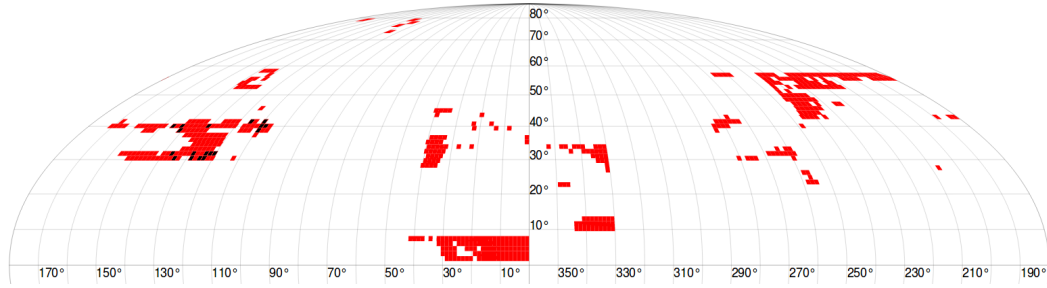


FIGURE 2.4: Footprint of the J-PLUS DR1. Red squares are the 511 pointing of 2 deg^2 each one provide by the T80Cam. Black squares represent the subset of 18 pointing that constitute the EDR. Overall, the DR1 amount effectively to $\sim 900 \text{ deg}^2$ after masking low-exposure regions, the surroundings of brighter stars, observational reflections or artifacts and overlapping areas.

the DR1 in each filter are presented in Table 2.1. The J-PLUS DR1 also comprises a set of valued-added properties: a Bayesian star/galaxy classification with a prior based of Gaia data (López-Sanjuan et al., 2019), effective temperature estimations for MW stars (Whitten et al., 2019) and photometric redshift for galaxies.

The limiting magnitudes (5σ , $3''$ aperture) in each filter is presented in Table 2.1. The median FWHM in the DR1 r -band images is $1.1''$. The detection of sources was made in the r -band using SExtractor (Bertin & Arnouts, 1996). The aperture for the photometry of the 12 J-PLUS bands is defined in the r -band image. Different types of apertures were used to perform the photometry of the 9 million sources in this catalogue. (i) Circular aperture photometry (SEXTRACTOR’s MAG_APER). Photometry in simple circular apertures of different sizes ($3''$ and $6''$). (ii) Isophotal photometry (SEXTRACTOR’s MAG_ISO). (iii) Kron photometry (SEXTRACTOR’s MAG_AUTO). (iv) Petrosian photometry (SEXTRACTOR’s MAG_PETRO). (v) Photometry after degrading the images of all the bands to the worst PSF. (vi) Photometry after convolving all the images with a Gaussian kernel of $\sigma=1.5''$. (vii) And photometry applying a PSF correction as that applied in (Molino et al., 2014). In the present work we use the $6''$ aperture. This choice follows the automatic method used by IPHAS photometry to find compact PNe, with small angular diameter (typically $\leq 5''$, Viironen et al., 2009b). A similar $6''$ -aperture was also considered by Akras, Guzman-Ramirez, & Gonçalves (2019c), who found that PNe with angular sizes larger than $6''$ exhibit very low ($r - H\alpha$) color indexes.

2.2.2 S-PLUS

S-PLUS is the Southern counterpart of the J-PLUS project. Therefore, this survey shares very similar characteristics with J-PLUS. S-PLUS is carried out with the T80-South (T80S). This is a new telescope optimized for robotic operations; it is equipped with a wide FoV camera ($\sim 2 \text{ deg}^2$). This camera is identical to the camera of the T80/JAST installed at the Observatorio Astrofísico de Javalambre. Up to the end of the project, T80S will observe a total area of around $9,000 \text{ deg}^2$ of the southern hemisphere.



FIGURE 2.5: T80S is located on Cerro Tololo besides the PROMPT telescopes. T80S is the largest dome on the left (Mendes de Oliveira et al., 2019).

T80S telescope is located near the summit of Cerro Tololo in Chile. Fig. 2.5 shows a picture of the telescope and its neighborhood. T80S sits at a altitude of 2,178m above sea level, at geodetic position $-30:10:04.31$, $-70:48:20.48$ (Mamajek, 2012). The median total seeing is $0.95''$ (FWHM) and the best 10-percentile is $0.64''$ (Tokovinin et al., 2003).

S-PLUS is formed by 12 narrow-, intermediate- and broad-band filters. This filter set is very similar to the J-PLUS, though with some differences in its configuration. Table 2.2 summarizes the main characteristic of the 12 S-PLUS filters. As in J-PLUS, the u-band is designated to detect the blue emission of the sources, the intermediate-band filters ($J0395$, $J0410$, $J0430$, $J0515$ and $J0861$) are used to detect absorption features, the two broad-band filters ($J0378$ and $J0660$) are designated to isolate two emissions lines ($[O II]$ and $H\alpha$) and finally the broad-band filters are for the continuum. Figure 2.6 displays the S-PLUS transmission curves. They are similar to those from J-PLUS filters (see Figure 2.3), with a slight difference in throughput and the width of the filters. Therefore, both surveys can be used to carry out a systematic search for PNe and SySt, by applying the same methodology.

First Data Release (DR1)

The S-PLUS DR1 includes 80 fields of the Stripe-82 area, a rectangular area with coordinates $4^h < RA < 20^h$ and $-1.26^\circ < Dec < 1.26^\circ$. These fields were observed during the scientific validation process of the survey. DR1 contains about one million sources and the limiting magnitude of each filter is presented in Table 2.2.

Given that S-PLUS DR1 represents the scientific validation of the project, the Stripe-82 data were used to verify the average variation of the FWHM of stellar

| Filter | $\lambda(\text{\AA})$ | $\Delta\lambda(\text{\AA})$ | $m_{\text{lim}}^{\text{DR1}}$ | Comments |
|--------------|-----------------------|-----------------------------|-------------------------------|--------------------------------|
| <i>u</i> | 3480 | 506 | 21.38 | Common with J-PAS |
| <i>J0378</i> | 3768 | 154 | 20.88 | [O II]; common with J-PAS |
| <i>J0395</i> | 3939 | 103 | 20.38 | Ca H+K |
| <i>J0410</i> | 4093 | 201 | 20.62 | H δ |
| <i>J0430</i> | 4291 | 200 | 20.62 | G-band |
| <i>g</i> | 4742 | 1560 | 21.62 | SDSS |
| <i>J0515</i> | 5132 | 206 | 20.62 | Mgb Triplet |
| <i>r</i> | 6251 | 1840 | 21.12 | SDSS |
| <i>J0660</i> | 6613 | 147 | 20.88 | H α ; common with J-PAS |
| <i>i</i> | 7698 | 1525 | 20.88 | SDSS |
| <i>J0861</i> | 8613 | 412 | 19.88 | Ca Triplet |
| <i>z</i> | – | – | 20.12 | SDSS |

TABLE 2.2: The *S-PLUS* filter systems. The first column shows the filter names. The S-PLUS central wavelengths, FWHM and DR1 limit magnitudes are given in columns 2 to 4. And, column 5 shortly describes the filters.

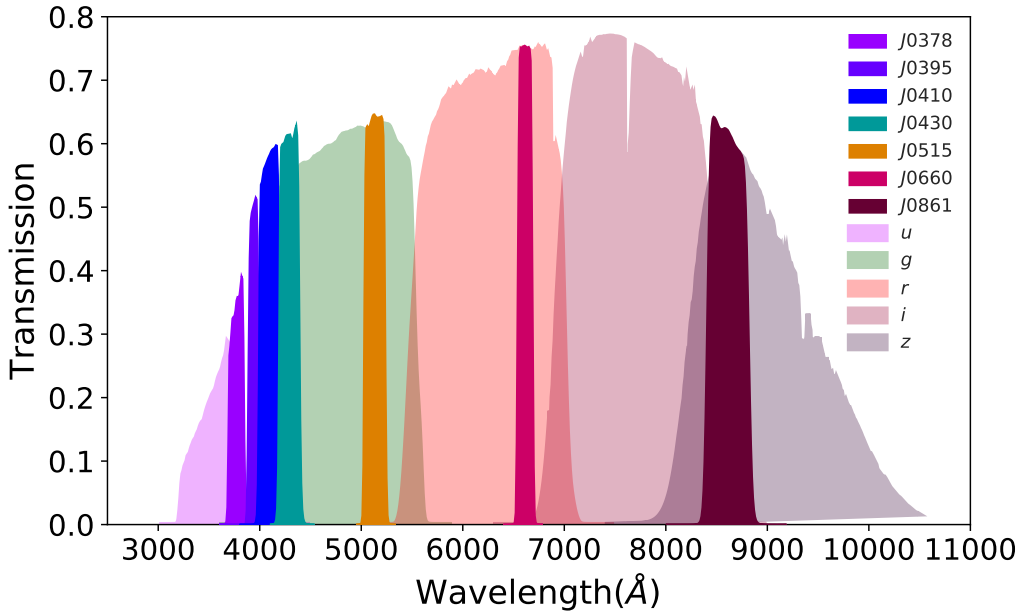


FIGURE 2.6: Overall transmission curves measured for the set of 12 S-PLUS filters.

objects across the fields. For this task it was necessary to do a combination of the g, r, i and z bands. And the difference of the FWHM of the four filters was never more than half a pixel. S-PLUS DR1 was also used to estimate the average photometric depth of the S-PLUS images (Mendes de Oliveira et al., 2019). S-PLUS Stripe-82 data served to characterize the performance of the photo- z estimates for different magnitudes and redshift range. The detection of the sources was made using SExtractor. Photometry was performed within 3 types of apertures. i) Circular apertures of $3''$ of diameter (SETRACTOR's APER). ii) Kron photometry (SETRACTOR's AUTO. iii) And petrosian photometry (SETRACTOR's PETRO). Differently of the case with J-PLUS, here we used the circular aperture of $3''$. This is so because $3''$ is the available aperture in S-PLUS. In addition to the arguments given in Section 2.2.1, this aperture is the best within the three possibilities, since it assures that large objects with high surface brightness like emission line galaxies or H II regions will not be recovered with the automated methods.

2.2.3 J-PAS

The Javalambre-Physics of the Accelerating Universe Astrophysical Survey (J-PAS; <http://www.j-pas.org>) original conception is outlined in Benítez et al. (2015) and Cenarro et al. (2017). J-PAS is a narrow-band imaging, very wide field cosmological survey to be carried out from a dedicated 2.5m telescope and a 4.7 sq. deg. camera with 1.2 Gpix. It will be operational for 5 years and it will observe 8,500 deg² of Northern sky to a 5-Sigma magnitude depth for point sources, equivalent to $i \sim 23.3$ over an aperture of 2 arcsec².

The J-PAS filter systems consists of 54 contiguous narrow-band filters of 145 Å FWHM. The filter set spans the optical range from ~ 3700 to 9200 Å, plus 1 medium-band filter that covers the UV edge and 1 broad-band filter redwards 9100 Å. In addition, the survey also include three regular broad-band filters, u, g and r . The first of these filters has a redder cutoff than SDSS u band. The other two filters are similar to those used in the SDSS. After the end of the J-PAS survey, the redshift and SEDS for ~ 200 million galaxies, with an accuracy of $\Delta z/(1+z) \leq 0.3\%$ will be determined (Cenarro et al., 2017). J-PAS uses 5 deg² low-resolution integral field unit (IFU) which will produce a 3D image of the Galactic halo and the extragalactic Northern sky. J-PAS will provide a low-resolution spectrum for every pixel of the sky and it will allow to carry out science in different fields of the Astrophysics. The galaxy evolution and star forming rate at different redshift can be studied as well as two dimensional star population, SNRs, gamma rays, very low mass objects, etc.

Halo PNe and SySt can be detectable by J-PAS, because of their spectral features with strong emission lines. Figure 2.7 shows the J-PAS transmission curve overlapping a known PN. Important low- and high-ionization emission lines such as H α , H β , [N II] $\lambda 6584$, doublet [O III] $\lambda \lambda 4959, 5007$, He II $\lambda 4686$, pair [S II] $\lambda \lambda 6717, 6731$, [S III] $\lambda 9069$, [O II] $\lambda 3727$, among others fall into the narrow-band filters. At the moment, there are no data published by the survey.

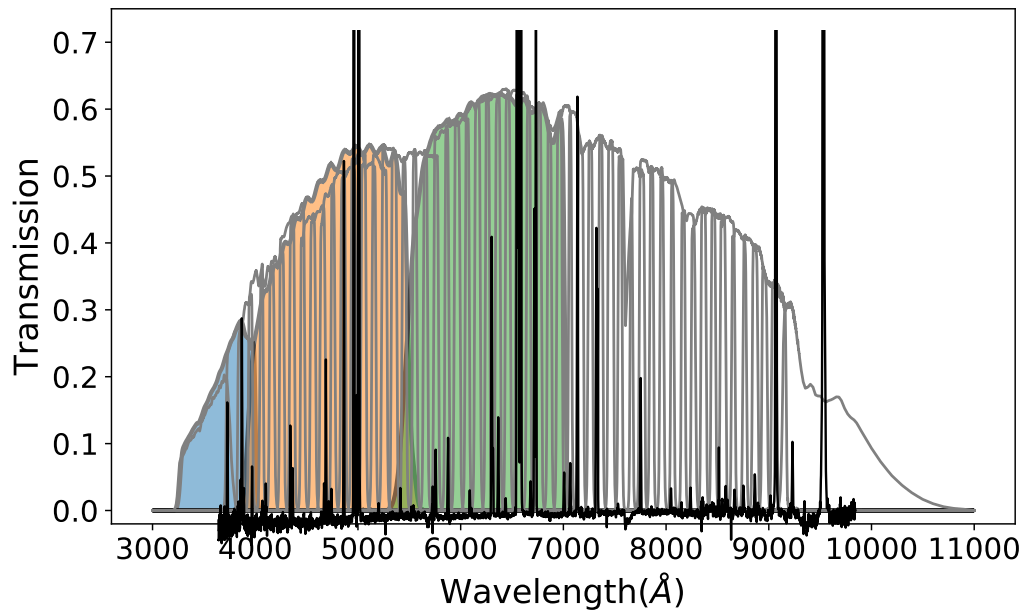


FIGURE 2.7: The J-PAS transmission curves. The filters are spaced around 100\AA but have FWHM of 145\AA , what produces an overlap among them. The *solid lines* represent the narrow-band filters and the *coloured areas* represent the *u*, *g* and *r* SDSS broad-band filters. Overplotted is the same spectrum of the Fig. 2.3.

Chapter 3

Photometric techniques

The radiation emitted by a star can be measured integrating it for all the wavelengths. This total energy emitted by a star is called bolometric brightness or magnitude (Straižys, 1992). It follows from the Stefan-Boltzmann law in which the luminosity, L , of a star, its radius, R , and effective temperature, T_{eff} , in solar units, are related by the equation

$$\log \frac{L}{L_{\odot}} = 2 \log \frac{R}{R_{\odot}} + 4 \log \frac{T_{\text{eff}}}{T_{\text{eff}\odot}}. \quad (3.1)$$

The luminosity of a star, in solar units, can be expressed in absolute bolometric magnitudes

$$M_{\text{bol}} = -2.5 \log \frac{L}{L_{\odot}} + M_{\text{bol}\odot}. \quad (3.2)$$

3.1 Stellar photometry

The following definitions follow Straižys (1992). All stars, except the Sun, are considered as point sources because of their large distance from us. Considering a star at a distance r from the telescope, which has an area ds perpendicular to the line of sight, the total energy received/collected by the telescope, neglecting the losses due to the interstellar medium and the atmosphere, is given by the formula:

$$dE(\lambda) = I(\lambda)d\omega dt d\lambda \quad (3.3)$$

where $I(\lambda)$ is the specific intensity of the radiation that is emitted from the star, $d\omega$ is the solid angle under which the area ds is seen from the star ($d\omega = r^{-2}ds$), dt is the interval of time and λ is the wavelength. Equation 3.3 represents the definition of intensity.

The amount of energy dropping on the area ds per unity interval of time is called the radiation flux

$$dF(\lambda) = \frac{dE(\lambda)}{dt} = I(\lambda)d\omega d\lambda. \quad (3.4)$$

The radiation flux per unit surface and per time is called illuminance,

$$dH(\lambda) = \frac{dF(\lambda)}{ds} = \frac{dE(\lambda)}{dt ds} = \frac{I(\lambda)}{r^2} d\lambda. \quad (3.5)$$

Since r is constant for a given star, the illuminance per unit of interval of wavelength can be considered as a measure of the specific intensity which is called the energy distribution of the spectrum (see Straižys, 1992). Instead of unity wavelength the Eq. 3.5 can also be expressed in unit frequency by considering

$$I(\lambda) = I(\nu) \frac{c}{\lambda^2}. \quad (3.6)$$

In practice, the illuminance is called brightness and is measured in stellar magnitudes. The brightness of a star given in magnitudes m is related with illuminance H as follows

$$m = -2.5 \log H + \text{const} \quad (3.7)$$

where *const* represents the zero point of a magnitude scale. The coefficient -2.5 defines the magnitude scale and is called the Pogson coefficient. The sign “minus” indicates that magnitudes decrease with increasing brightness.

Considering two stars with illuminances H_1 and H_2 , their magnitude are

$$\begin{aligned} m_1 &= -2.5 \log H_1 + \text{const} \\ m_2 &= -2.5 \log H_2 + \text{const}. \end{aligned}$$

and the magnitude difference is defined as

$$m_1 - m_2 = -2.5 \log \frac{H_1}{H_2}. \quad (3.8)$$

It is important to mention that the illuminance of a star, and thus its magnitude depends on the intrinsic luminosity and on the distance of the star. If all stars were at the same distance the ratio of their magnitudes would correspond to the ratio of their intrinsic magnitudes. If considering one of the stars with magnitude m_2 , as the known object, and the other star with magnitude m_1 , as the unknown source, the relation of the magnitudes between the two stars can be obtained from Eq. 3.8 taking $m_1 = m$ and $m_2 = m_0$:

$$m - m_0 = -2.5 \log \frac{H}{H_0} = -2.5 \log H + 2.5 \log H_0 = -2.5 \log H + \text{const} \quad (3.9)$$

where H_0 is a calibration parameter and H is the brightness.

So far, we have worked with the definition of illuminance, brightness and magnitudes without any specific interval of wavelengths. In reality the brightness of a star can be related with the integrated energy radiated in all wavelength range or with a certain interval of wavelength. The first case is the bolometric brightness (see the

bolometric magnitude expressed in Eq. 3.2). The second case is the magnitude of a star in a specific wavelength range.

We now can obtain the monochromatic magnitude from the illuminance, per units of wavelength. This means by using the equations 3.5 and 3.9,

$$m_{\text{mon}} = -2.5 \log \frac{\frac{I(\lambda)}{r^2}}{\frac{I_0(\lambda)}{r^2}} = -2.5 \log \frac{I(\lambda)}{I_0(\lambda)} = -2.5 \log I(\lambda) + \text{const} \quad (3.10)$$

where $I(\lambda)$ is the specific intensity (defined from Equations 3.4 and 3.5) of the star at a wavelength λ and the term “const” denotes the zero point of a magnitude scale.

Several photometric systems have been defined so far. The most widely known, in the optical regime, are (i) the BVRI of Johnson-Morgan systems (Bessell, 2005) and (ii) the uvby or Strömrgren photometric system (Crawford, 1958). Because the observations are obtained from different telescopes and slightly different filters, in order to be consistent they have to be corrected for the differences. The response function S of the filter system, the telescope and the detector do exactly that.

If the response function of the system is $S(\lambda)$, the observed magnitudes are called heterochromatic and they are defined as

$$m_{\text{hetero}} = -2.5 \log \frac{\int I(\lambda)S(\lambda)d\lambda}{\int S(\lambda)d\lambda} + \text{const} \quad (3.11)$$

usually $S(\lambda)$ function is described by

$$S(\lambda) = T_t(\lambda)T_f(\lambda)T_a(\lambda) \quad (3.12)$$

where $T_t(\lambda)$ is the product of the throughput of the telescope, the instrument and the quantum efficiency of the detector, $T_f(\lambda)$ is the filter transmission and $T_a(\lambda)$ is the atmospheric transmission.

Assuming m_1 and m_2 as the monochromatic magnitudes of a star at λ_1 and λ_2 , respectively, Eq. 3.8 gives

$$m_1 - m_2 = -2.5 \log \frac{I(\lambda_1)}{I(\lambda_2)} \quad (3.13)$$

here $m_1 - m_2$ is known as color index. In the case of the heterochromatic magnitudes the color index is defined as:

$$m_1 - m_2 = -2.5 \log \frac{\int I(\lambda)S(\lambda_1)d\lambda}{\int I(\lambda)S(\lambda_2)d\lambda} + \text{const} \quad (3.14)$$

where

$$\text{const} = -2.5 \log \frac{\int S(\lambda_1)d\lambda}{\int S(\lambda_2)d\lambda}. \quad (3.15)$$

Equations 3.13 and 3.14 define the color indices, the value of this index shows at which wavelength the star emit more light or in other words is brighter.

At this point, the term “synthetic photometry” can be added, which is the name given to magnitudes and colors derived by convolving observed spectroscopic data with the response function of a specific filter systems (Bessell, 2005). In the telescope the magnitude measured is the instrumental magnitude that is described according to the number of counts scored by the detector, such as:

$$m_{\text{inst}} = -2.5 \log n_{\lambda} \quad (3.16)$$

where n_{λ} is the rate of detected photons. The synthetic and instrumental magnitude are related by the *instrumental zero point* (zp), in the following way,

$$m_{\text{synt}} = n_{\text{inst}} + zp \quad (3.17)$$

where zp makes possible to obtain the magnitude for any system from the instrumental magnitude measured with the telescope.

Considering now that the radiation ($I_0(\lambda)$) emitted from a star passes through a absorbing medium with optical thickness x , the final intensity of the radiation will be reduced and be given by the following formula

$$I(\lambda) = I_0(\lambda)e^{-\kappa_{\lambda}x} \quad (3.18)$$

where κ_{λ} is the extinction coefficient at the wavelength λ . The absorbed radiation expressed in magnitude, is

$$A(\lambda) = -2.5 \log \frac{I(\lambda)}{I_0(\lambda)} = 2.5\kappa_{\lambda}x \log e = 1.086\kappa_{\lambda}x. \quad (3.19)$$

Given that $\tau(\lambda) = \kappa_{\lambda}x$, Eq. 3.18 becomes

$$I(\lambda) = I_0(\lambda)e^{-\tau(\lambda)} \quad (3.20)$$

$\tau(\lambda)$ is called optical depth and it can take values $\ll 1$ for optically thin regions (transparency) and $\gg 1$ for optically thick regions (opaque).

By measuring the monochromatic brightness of a star in two spectral bands, and considering no interstellar extinction, the intrinsic color index is given by $m_1 - m_2$. If the radiation of a star passes through an interstellar cloud of unit optical thickness ($x = 1$), then, magnitudes m_1 and m_2 convert into $m_1 + e_1$ and $m_2 + e_2$, where e_1 and e_2 are the extinctions when $x = 1$. The color index of the star will then be

$$(m_1 + e_1) - (m_2 + e_2) = m_1 - m_2 + (e_1 - e_2) \quad (3.21)$$

here $(e_1 - e_2)$ is an additional reddening given by the absorbing interstellar cloud and it is called color excess:

$$E_{m_1-m_2}^{(x=1)} = e_1 - e_2. \quad (3.22)$$

The color excess caused by x units of absorbing matter is

$$E_{m_1-m_2} = xe_1 - xe_2 = xE_{m_1-m_2}^{(x=1)}. \quad (3.23)$$

The value xe (extinction) is usually denoted by A . It is produced by scattering and absorption of light by interstellar dust.

If $m_1 - m_2$ is the color index of a star and $E_{m_1-m_2}$ its color excess, then the intrinsic color will be

$$(m_1 - m_2)_0 = m_1 - m_2 - E_{m_1-m_2}. \quad (3.24)$$

Eventually, the extinction in the magnitude m_1 can be written as a function of the magnitude m_2 , $A_1 = kA_2$. In this case Eq. 3.23 turn in

$$E_{m_1-m_2} = kA_2 - A_2 = (k - 1)A_2 \quad (3.25)$$

if we denote $(k - 1)^{-1}$ by R , then

$$A_2 = RE_{m_1-m_2} \quad (3.26)$$

coefficient R is the ratio of extinction to color excess and it is one of the most important parameters of a two colors photometric system. By replacing m_1 and m_2 by B and V bands, we obtain the well known color excess:

$$A_V = RE_{B-V}. \quad (3.27)$$

Photometric systems with more than two colors can generate an important parameter, the color excess ratio. Considering three bands in a photometric system m_1 , m_2 and m_3 which correspond to three wavelengths, a colour-colour diagram can be construct based on these bands, $m_1 - m_2$ versus $m_2 - m_3$. In this diagram the unreddened stars form a definite sequence. When there is interstellar reddening each star in the diagram moves along the reddening line with the slope

$$\chi = \frac{E_{m_1-m_2}}{E_{m_2-m_3}}. \quad (3.28)$$

This ratio depends on the properties of the interstellar medium.

Now, with the χ ratio and the two color indices defined it is also possible to define the Q -parameter as

$$Q_{m_1, m_2, m_3} = (m_1 - m_2) - \frac{E_{m_1-m_2}}{E_{m_2-m_3}}(m_2 - m_3). \quad (3.29)$$

The Q -parameter is independent of the interstellar reddening. In fact, the Q -parameter is the ordinate of the point at which the reddening line of a star intersects the axis $m_1 - m_2 = 0$.

3.2 System of magnitudes

Any photometric system is defined by a set of narrow-, intermediate- or broad-band filters. Three types of photometric systems can be considered according to the definition of the *zero point*:

- *ST system*: H_0 is the flux density of Vega at $\lambda = 5500\text{\AA}$.
- *AB system*: H_0 is the flux density of Vega at $\lambda = 5500\text{\AA}$ in frequency.
- *VEGA system*: H_0 is defined based on the spectral energy distribution of Vega. This implies that the magnitudes of Vega are zero for all filters.

There is a linear relation between AB and Vega magnitudes:

$$\text{mag}_{\text{AB}}(\text{Obj}) = \text{mag}_{\text{VEGA}}(\text{Obj}) + \text{mag}_{\text{AB}}(\text{Vega}) \quad (3.30)$$

that is, the magnitudes of an object in a system is the VEGA magnitude of that object plus the AB magnitude of VEGA in that system (Aparicio Villegas et al., 2010).

3.3 Wavelength characterization of a photometric system

The heterochromatic magnitudes defined by the response function $S(\lambda)$ in some cases can be equal to the monochromatic magnitudes at specific wavelengths. According to definition, the effective intensity of the radiation of a star with the response function is

$$I_e(\lambda) = \frac{\int I(\lambda)S(\lambda)d\lambda}{\int S(\lambda)d\lambda} \quad (3.31)$$

and corresponds to a specific wavelength which is called the isophotal wavelength. At this wavelength the heterochromatic and monochromatic magnitudes coincide. Unfortunately, the isophotal wavelength can only be found from the intensity distribution, but not calculated.

If the second derivative of the intensity distribution $I(\lambda)$ is equal to zero in the wavelength interval covered by the response function $S(\lambda)$, the difference between the heterochromatic magnitudes of two stars is equal to that of their monochromatic magnitudes at the mean wavelength (Stromgren 1937),

$$\lambda_0 = \frac{\int S(\lambda)}{\int S(\lambda)d\lambda}. \quad (3.32)$$

In practice the intensity distribution $I(\lambda)$ always has some discontinuities and bands. Therefore, $I''(\lambda) \neq 0$, which causes a heterochromatic magnitudes to deviate from the monochromatic ones measured at λ_0 .

It is important to know at which wavelength the heterochromatic extinction is equal to the monochromatic one. King (1952) has shown that this condition can be fulfilled by the effective wavelength

$$\lambda_e = \frac{\int I(\lambda)S(\lambda)}{\int I(\lambda)S(\lambda)d\lambda}. \quad (3.33)$$

If the object is an iso-energetic source with $I(\lambda) = \text{const}$, the mean wavelength λ_0 works as the effective wavelength.

For extragalactic studies, where the redshift is important, Schneider et al. (1983) introduced the definition of the effective frequency:

$$\bar{\nu}_e = \exp \left[\frac{\int I(\nu)S(\nu) \ln \nu d\nu}{\int I(\nu)S(\nu)d\nu} \right] \quad (3.34)$$

Notice that this definition is in a sense halfway between an effective frequency and an effective wavelength.

3.4 AB magnitude system

After exploring the basic concepts of photometry, we can relate the magnitudes with the transmission function of any photometric system and the standard star systems to estimate the zero point. So, we can describe the magnitude system that used in this work. Magnitudes of any photometric system are set in the AB magnitude system (Oke & Gunn, 1983). The advantage of the AB magnitude system is that it is directly related with the flux in physical units,

$$\text{AB}_\nu = -2.5 \log f(\nu) + 48.6 \quad (3.35)$$

where $f(\nu)$ is the flux in $\text{ergs cm}^{-2} \text{ s}^{-1} \text{ Hz}^{-1}$ and the constant comes from the expression

$$48.60 = -2.5 \log F_0 \quad (3.36)$$

with $F_0 = 3.63 \times 10^{-20} \text{ erg cm}^{-2} \text{ s}^{-1} \text{ Hz}^{-1}$ is the flux of VEGA at $\lambda = 5500\text{\AA}$.

The synthetic AB magnitudes presented in this work are calculated using the following equation

$$\text{AB}_\nu = -2.5 \log \frac{\int f(\nu)S(\nu)d\nu/\nu}{\int S(\nu)d\nu/\nu} - 48.60 \quad (3.37)$$

where $S(\nu)$ is the response function of the system corresponding to the atmosphere, telescope, filter and detector combinations. If the spectrum is in flux per unit of Angstroms, by using $f(\nu) = (\lambda^2/c)f(\lambda)$ it is possible to go back to the wavelength units. Thus Eq. 3.37 becomes

$$\text{AB}_\lambda = -2.5 \log \frac{1}{c} \frac{\int f(\lambda)S(\lambda)\lambda d\lambda}{\int S(\lambda)d\lambda/\lambda} - 48.60 \quad (3.38)$$

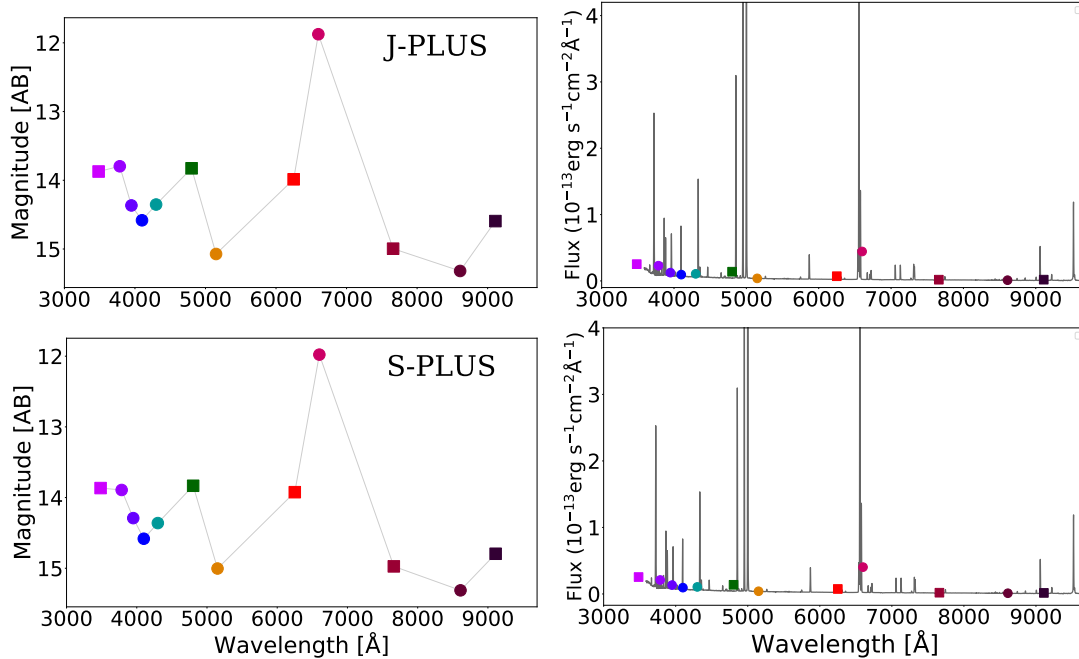


FIGURE 3.1: *Top panel:* J-PLUS synthetic photometry (*left*) and the spectrum in flux units (*right*) of the PN DdDm 1. *Bottom panel:* S-PLUS synthetic magnitudes (*left*) and corresponding spectrum (*right*) of the same PN. The J-PLUS and S-PLUS synthetic photometry in flux units are also shown overlapping the optical spectrum of the PN. The square symbols represent the SDSS-like broad-band filters, from left to right u , g , r , i and z . The circle symbols are the narrow-band filters and from left to right, $J0378$, $J0395$, $J0410$, $J0515$, $J0660$ and $J0861$.

where c is the light speed and the units of $f(\lambda)$ are $[\text{erg s}^{-1} \text{cm}^{-2} \text{\AA}^{-1}]$. Therefore, Eq. 3.38 allows to estimate the synthetic photometry (AB magnitude) in a specific photometric system.

3.5 J-PLUS and S-PLUS synthetic photometry

We are now able to introduce the optical synthetic photometry for the J-PLUS and S-PLUS filter systems using Eq. 3.38. Several emission line sources – PNe, SySt, cataclysmic variables (CV), quasi-stellar objects (QSO), extragalactic H II regions, young stellar objects (YSOs), B[e] stars and star forming galaxies (SFGs) – are described through the convolution of this optical spectra with the theoretical transmission curves (see Chapter 2). For this exercise the Python library NUMPY¹ is used. Appendix A.1 shows the codes developed to perform this task.

3.5.1 Halo planetary nebulae and symbiotic stars

The J-PLUS and S-PLUS synthetic photo-spectra² of six planetary nebulae – PNG 135.9+55.9 (SDSS) and DdDm-1 (Kwitter & Henry, 1998), NGC 2022, BB-1 and H4-

¹<https://pypi.org/project/numpy/>

²Photo-spectra is the name given to indicate the photometry in all bands.

1 (Kwitter et al., 2003) and MWC 574 (Pereira & Miranda, 2007) – were generated using Eq. 3.38, their spectra and the transmission curves. Figure 3.1 displays the J-PLUS (*top left*) and S-PLUS (*bottom left*) photo-spectra, in magnitude units, of the Galactic hPN DdDm 1. Both (J-PLUS and S-PLUS) synthetic photometry of DdDm 1 are shown to illustrate that their filter systems are very similar (also see the transmission curves of S-PLUS and J-PLUS in Chapter 2). For this reason, from now on we refer to the two photometries equivalently. The figure also shows the J-PLUS (*top right*) and S-PLUS (*bottom right*) photometry in flux units superposed to the observed spectrum from which the J- and S-PLUS magnitudes were computed. The object exhibits strong $H\alpha$ emission, with more intense continuum in the blue than in the red part of the spectrum.

A grid of modelled spectra of hPNe was built for this work in order to explore their J-PLUS and S-PLUS photometric features. This grid of models is necessary due to the small number of known PNe located in Galactic halo (14 objects, Howard et al., 1997). The photoionization code CLOUDY (Ferland et al., 2013) was used to build the models. The parameters used to compute the models reflect the typical properties of the PN population in the Galactic halo. They represent different sets of nebular abundances (shown in Appendix B), electron densities ($1,000\text{ cm}^{-3}$, $3,000\text{ cm}^{-3}$ and $6,000\text{ cm}^{-3}$) a spherically symmetric nebula with a radius of $2.7''$, at distance of 10 kpc, black body central star effective temperatures from 50,000 K to 250,000 K, in steps of 10×10^3 K and luminosities of 500, 1,000, 5,000 and 10,000 L_{\odot} . We reddened the modelled spectra by applying the reddening curve by Fitzpatrick (1999) and using three different colour excesses, $E(B - V) = 0.0, 0.1$ and 0.2 , which follow the J-PLUS and S-PLUS average extinction of $E(B - V) = 0.1$ (Cenarro et al., 2019; Mendes de Oliveira et al., 2019).

Figure 3.2 shows the synthetic photo-spectra of two CLOUDY modelled hPNe. Both models have the same chemical abundance (equivalent to that of the hPN DdDm 1) and the same luminosity of $10^4 L_{\odot}$, but different effective temperature and density (*top panel*: 60×10^3 K and $1,000\text{ cm}^{-3}$ and *bottom panel*: 200×10^3 K and $6,000\text{ cm}^{-3}$). The first model (*top panel*) corresponds to a low-excitation PN. The ionizing star is not hot enough to produce such an [O III] or [He II] emission able to stand out significantly in the g broad-band magnitude. The second model (*bottom panel*) represents a high-excitation PN. In this model, the magnitude of the g broad-band filter is dominated by the strong [O III] emission-line. The [He II] line, which is moderately strong in this spectrum, is also affecting the g band. It should be noted that the g -band also includes the $H\beta$ line, and it is not possible to disentangle the $H\beta$, [O III] and [He II] emission-lines, in the J-PLUS and S-PLUS photo-spectra. Therefore it is not possible to robustly quantify the level of excitation.

The spectra of a group of galactic and extragalactic SySt by Munari & Zwitter (2002) were also convolved with the J-PLUS and S-PLUS response function. Symbiotic stars from IPHAS catalog are also included (Corradi et al., 2008, 2010; Rodríguez-Flores et al., 2014). Figure 3.3 presents the synthetic photo-spectrum of the SySt LMC1 (Munari & Zwitter, 2002) in both magnitudes (*left*) and flux units

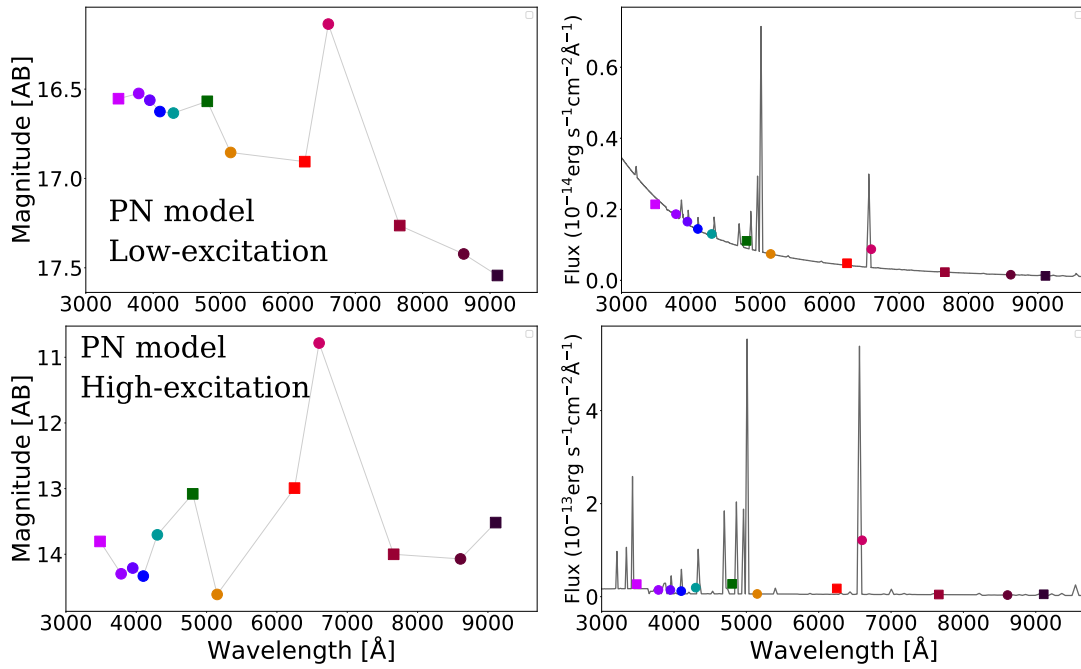


FIGURE 3.2: Synthetic magnitudes of a CLOUDY modelled PN with $T_{\text{eff}} = 60 \times 10^3 \text{ K}$ and electronic density of $1,000 \text{ cm}^{-3}$ (*top left*) and its corresponding spectrum (*top right*) from which the photometry were simulated. Another modelled PN with $T_{\text{eff}} = 200 \times 10^3 \text{ K}$ and electronic density of $6,000 \text{ cm}^{-3}$, in term of the synthetic magnitudes (*bottom left*) and its corresponding spectrum (*bottom right*). The abundance considered in both models are that of the hPNe DdDm 1, with $L = 10,000 L_{\odot}$.

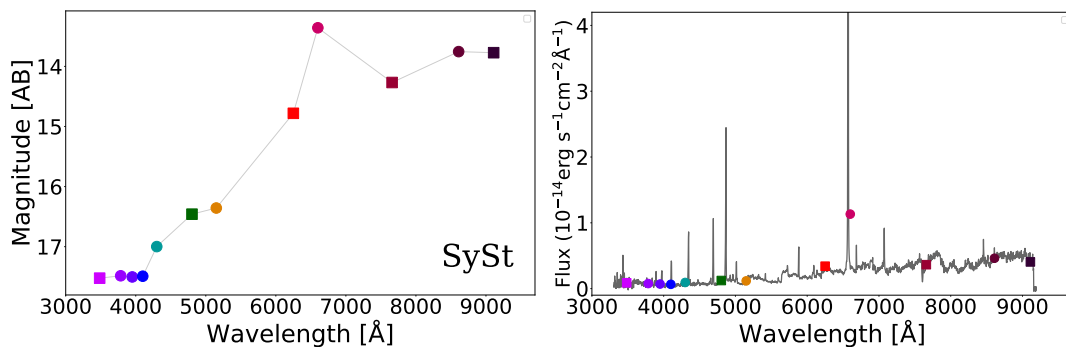


FIGURE 3.3: Synthetic photo-spectrum of the SySt LMC1. *Left panel* shows the photo-spectrum in magnitudes units. The *left panel* displays the real spectrum of the object. Overplotted are the J-PLUS points in flux units.

(*right*). J/S-PLUS points are again superposed on the observed spectrum of the object. It displays a clear $H\alpha$ emission with a continuum increasing to longer wavelengths. The resolution of the J-PLUS and S-PLUS photometry allows to perceive undoubtedly the reddened nature of the SySt, as well as a number of extragalactic SySt: NGC 205 (Gonçalves et al., 2015), IC 10 (Gonçalves et al., 2008) and NGC 185 (Gonçalves et al., 2012)

3.5.2 Other emission line objects

The synthetic photometry for a number of emission lines sources that could be mistaken by PNe or SySt in the J-PLUS and S-PLUS surveys are now concerned. For instance, extragalactic H II regions located in the dwarf galaxy NGC 55 (Magrini et al., 2017). The *first panels* of Figure 3.4 shows the photo-spectrum (*left*) and observed spectrum (*right*) of one of these extragalactic H II regions, in which the $H\alpha$ emission is also perceptible. Note that the [O III] and $H\beta$ have a small impact on the g -band. A comparison between the synthetic and observed spectra of PNe and H II regions shows that these two types of sources display very similar spectral features with emission lines such as $H\alpha$ and [O III] lines, which will make hard to distinguish them within the J-PLUS and S-PLUS catalogues.

The spectra of a group of young stellar objects from Lupus and Sigma Orionis (Rigliaco et al., 2012; Alcalá et al., 2014) are also considered. The *second panels* of Figure 3.4 presents the results for a YSO (RU Lup from Lupus, Alcalá et al., 2014). An accretion disk, from where the $H\alpha$ emission emerges, is also present in this type of (pre-main-sequence) stars. YSO's photometry shows a continuum stronger in the red part of the spectrum, which closely resembles that of the SySt (see Figure 3.3). A CV from the SDSS catalogue is shown in the *third panels*. CVs are interacting binary systems, in which a white dwarf accretes gas from a main-sequence star, via Roche lobe outflow and an accretion disk is formed during this process. The emission-lines are produced in the accretion disk of the binary system (Williams, 1980). Therefore, the presence of the $H\alpha$ emission in their photo-spectrum is indicating the nebular nature of the CVs. It is straightforward to notice that based on their photo-spectra, PNe of high- and low-excitation could be wrongly classified as CVs. The *forth panels* display a B[e] star (Lamers et al., 1998). B[e] stars have a surrounding nebula produced by large-scale mass-loss involving one or more eruptions (Marston & McCollum, 2006). Its photo-spectrum resembles that of both SySt and YSOs.

Figure 3.5 shows a set of J/S-PLUS synthetic spectra of extragalactic objects with emission lines. Several SDSS QSOs, at specific redshift (z) ranges, were also included in our selection of emission-line objects. QSOs at the redshift ranges $1.3 < z < 1.4$, $2.4 < z < 2.6$ and $3.2 < z < 3.4$ have spectroscopic features that resemble those of PNe, in other words, they could be misclassified as $H\alpha$ line-emission at $z = 0$. At these specific redshift ranges, the C IV 1550 Å, C III] 1909 Å and Mg II 2798 Å emission-lines of QSOs fall into the J0660 ($H\alpha$) filter. In the *first panels* we have a QSO at $z = 1.4$, in which the excess of emission in the J0660

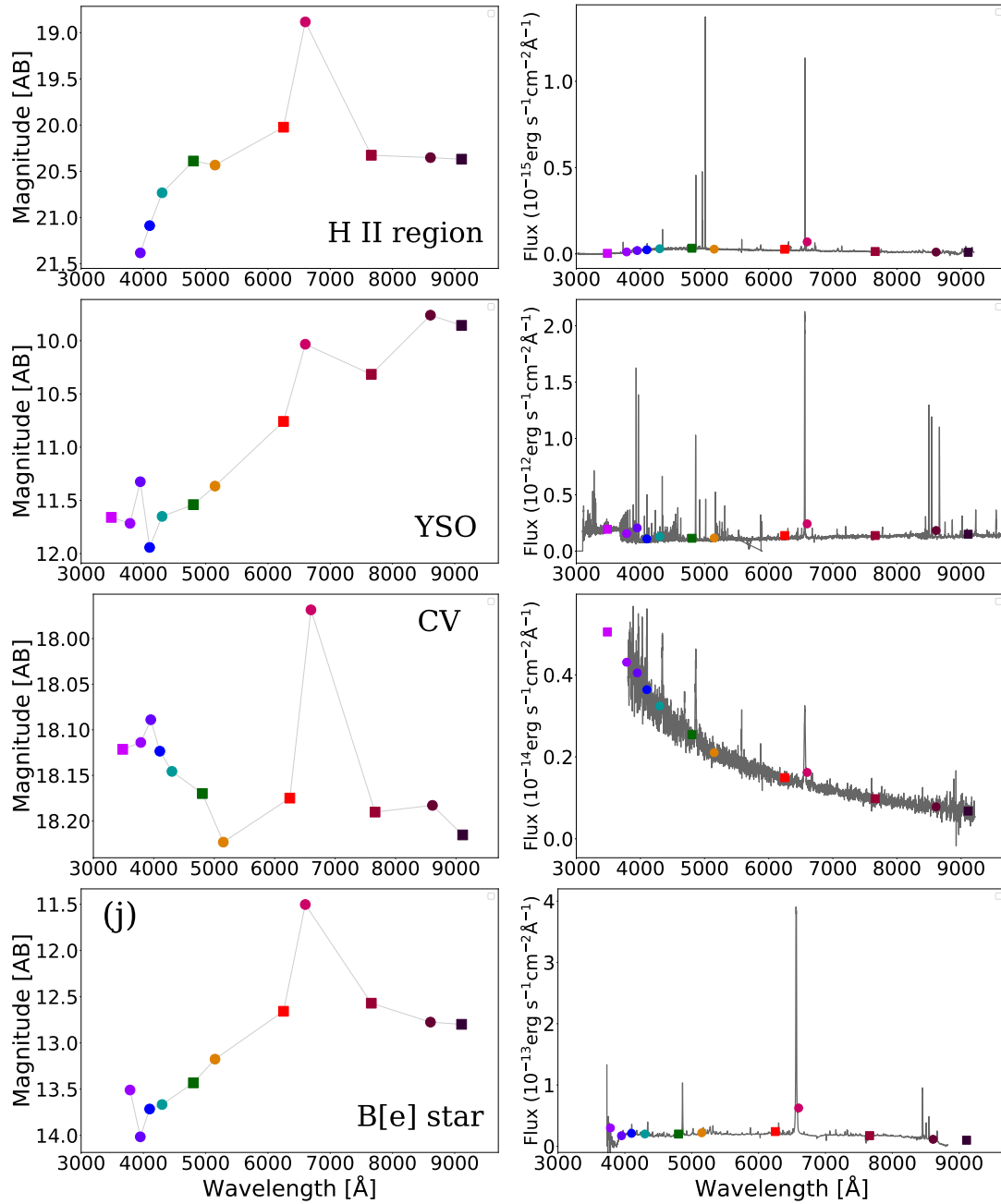


FIGURE 3.4: *First panel:* synthetic photo-spectrum in magnitude units (*left*) of an H II region in the nearby galaxy NGC 55 and its observed spectrum and the synthetic photometry in flux units superposed (*right*). *Second panel:* the photo-spectrum of YSO RU Lup in magnitudes (*left*) and its corresponding spectrum (*right*). *Third panel:* the optical magnitudes of a cataclysm variable from SDSS (*left*) and its corresponding spectrum (*right*). *Fourth panel:* the optical magnitudes of a B[e] star (*left*) and its corresponding spectrum (*right*). All these objects exhibit H α emission.

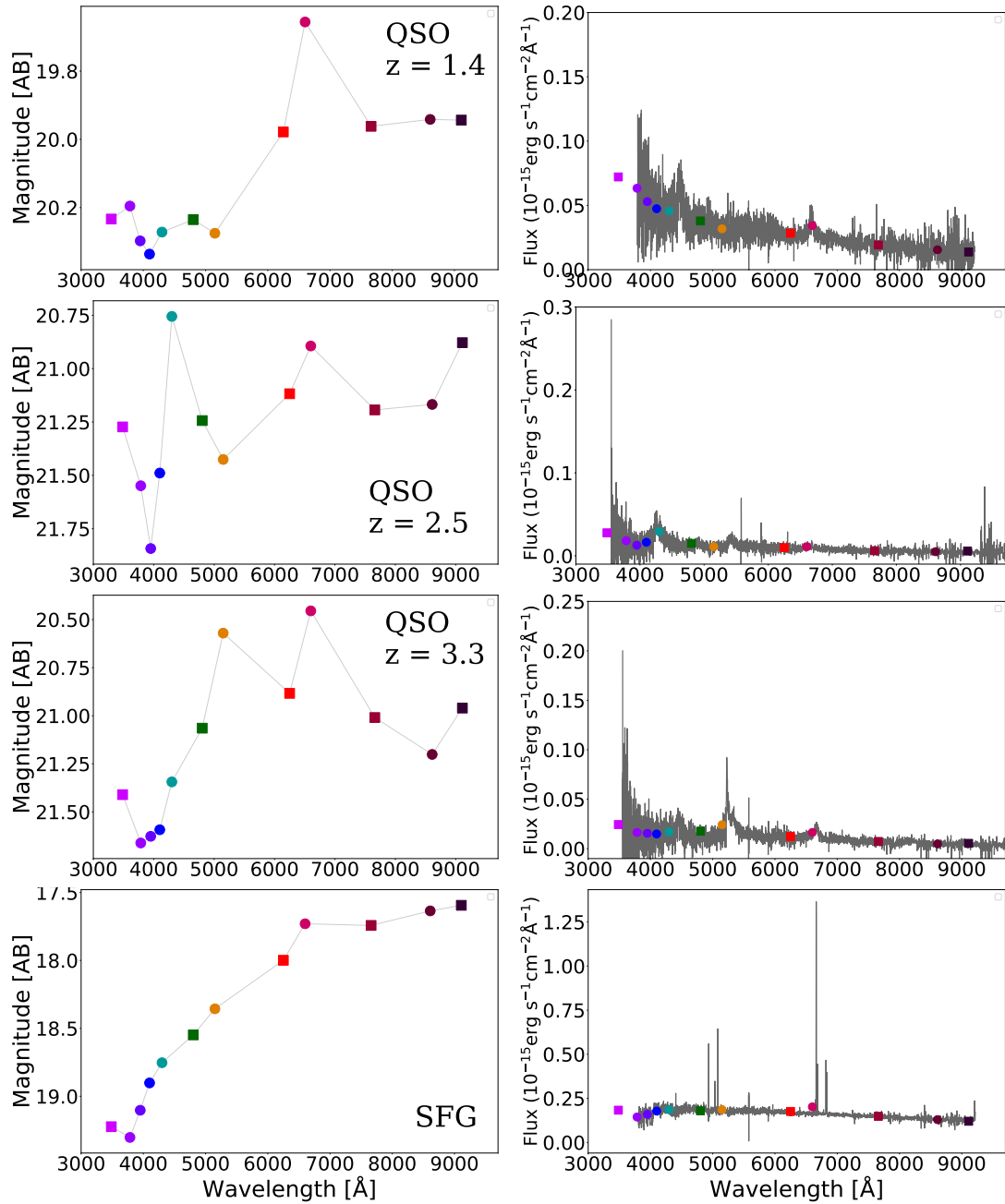


FIGURE 3.5: As Figure 3.4 *First panel*: synthetic photo-spectrum in magnitude units (*left*) of an QSOs at $z = 1.4$ and its observed spectrum with the synthetic photometry in flux units superposed (*right*). *Second panel*: the photo-spectrum of a QSO at $z = 2.5$ in magnitudes (*left*) and its corresponding spectrum (*right*). *Third panel*: the optical magnitudes of a QSO at $z = 3.3$ (*left*) and its corresponding spectrum (*right*). *Fourth panel*: the optical magnitudes of a star forming galaxy from SDSS (*left*) and its corresponding spectrum (*right*).

filter comes from the contribution of the Mg II emission line. Two more QSOs are presented: at $z = 2.5$ (*second panels*) and $z = 3.3$ (*third panels*). At these redshifts, the C III] and C IV emission lines are also detected in the $J0660$ band. Note that the magnitudes of the $J0430$ band for the QSO at $z = 2.5$ and of the $J0515$ band for the QSOs at $z = 3.3$ indicate strong emission provided by the $L\alpha$ emission in both cases. The *fourth panels* of Figure 3.5 show a SDSS star forming galaxy. Its photo-spectrum exhibits a moderate $H\alpha$ emission and a continuum increasing towards longer wavelengths.

Despite the fact that QSOs have strong emission lines that can be mis-identified as $H\alpha$, their photo-spectra are only moderately similar to those of PNe or SySt. It is worth mentioning that J-PLUS and S-PLUS can characterize not only the strong emission lines, but also the continua of these objects, allowing us to correctly differentiate QSO from PNe, which was a problematic task in projects dedicated to the search of PNe using a fewer number of filters (Kniazev et al., 2014). Finally, note that star-forming galaxies have photo-spectra very different from those presented in Figures 3.1 and 3.3 and then they will be easily distinguished from PNe and SySt.

3.6 Synthetic colour-colour diagrams: selection criteria

The photo-spectra of the emission-line sources discussed in Section 3.5 were used to build diagnostic colour-colour diagrams. Our goal is to pinpoint the most relevant ones to discriminate PNe and SySt from all the aforementioned mimics.

3.6.1 IPHAS equivalent colour-colour diagram

Drew et al. (2005) designed the IPHAS survey (see Chapter 1) showing that the $(r' - H\alpha)$ vs $(r' - i)$ diagram, where $H\alpha$ is the name of the narrow-band filter designated to detect the $H\alpha$ emission line, is an optimal tool to select strong $H\alpha$ emission-line sources (Witham et al., 2008). IPHAS PNe and SySt candidates were selected by using the IPHAS colour-colour diagram as well as the common $(J - H)$ vs $(H - K_s)$ 2MASS diagram. Their true nature was confirmed later on, spectroscopically (Corradi et al., 2008; Viironen et al., 2009a; Rodríguez-Flores et al., 2014; Sabin et al., 2014).

Given that the J-PLUS and S-PLUS filter systems include the three IPHAS filters, we reconstructed the IPHAS equivalent diagram (Figure 3.6). The colour $(r - J0660)$ clearly indicates an increasing excess of the $H\alpha$ emission-line, while the $(r - i)$ increases with the reddening, as previously stated by Corradi et al. (2008). Both modelled PNe and observed SySt are found to display $(r - J0660) > 0.6$ due to their strong $H\alpha$ emission lines, with the former occupying the left part $(r - i) < 0$ and the latter the right $(r - i) > 0$ part of the diagnostic diagram. However, note that some SySt (three) have values of $(r - J0660) < 0.6$. The solid (black) and the dashed (red) lines in Figure 3.6 represent the selection criteria for PNe (PNe zone) and SySt (SySt zone), respectively. These lines are meant to include most of the modelled hPNe and the observed SySt while at the same time the majority of the

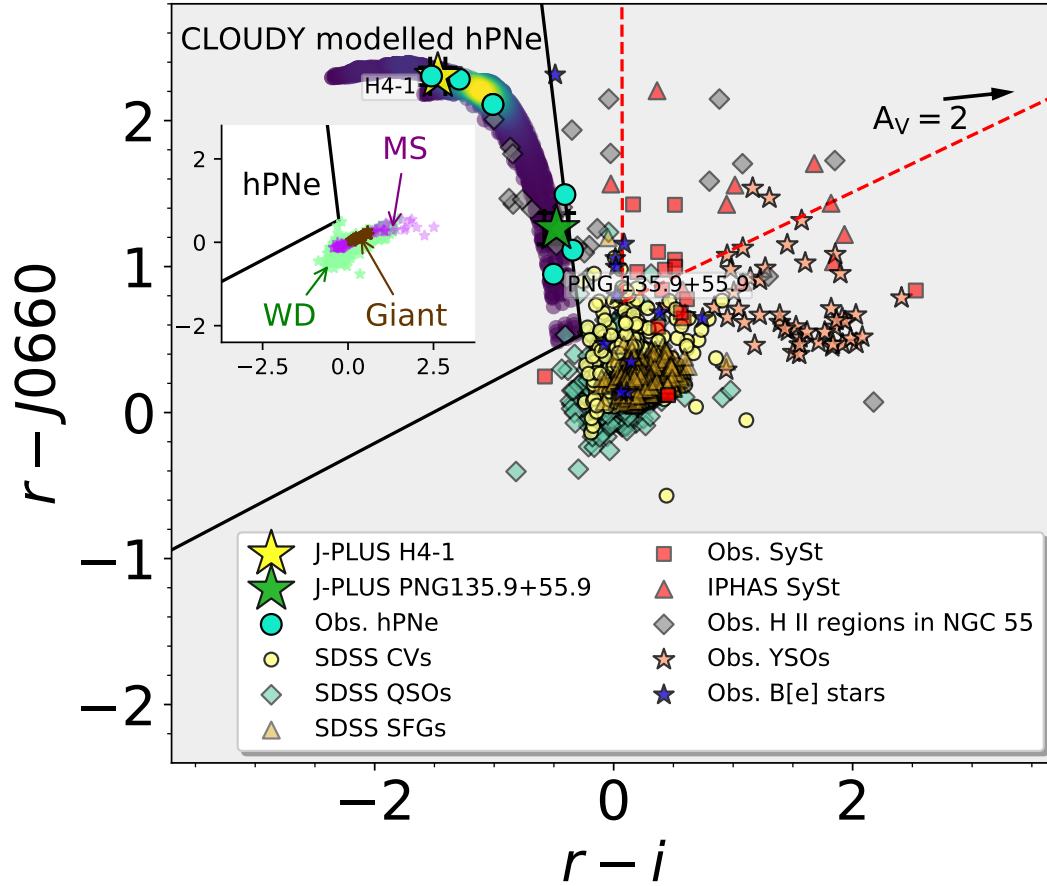


FIGURE 3.6: J-PLUS and S-PLUS ($r - J0660$) vs ($r - i$) colour-colour diagram, equivalent to IPHAS ($r' - H\alpha$) vs. ($r' - i'$). The large yellow and green stars with error-bars are the J-PLUS observations for two hPNe: H 4-1 and PNG 135.9+55.9, respectively. The grid of CLOUDY models for hPNe is shown with the density map region. Cyan circles represent the synthetic colour indices for a number of hPNe: PNG 135.9+55.9 (SDSS), DdDM-1 (Kwitter & Henry, 1998), NGC 2022, BB-1, H4-1 (Kwitter et al., 2003) and MWC 574 (Pereira & Miranda, 2007). Gray diamonds represent H II regions in NGC 55 (Magrini, Gonçalves, & Vajgel, 2017). Red boxes display either galactic or extragalactic SySt from Munari & Zwitter (2002); Munari & Jurdana-Šepić (2002). This group also includes external SySt from NGC 205 (Gonçalves et al., 2015), IC 10 (Gonçalves et al., 2008) and NGC 185 (Gonçalves et al., 2012) and red triangles correspond to IPHAS symbiotics (Rodríguez-Flores et al., 2014). Yellow circles correspond to cataclysmic variables (CVs) from SDSS. Orange triangles refer to SDSS star-forming galaxies (SDSS SFGs). SDSS QSOs at different redshift ranges are shown as light blue diamonds and YSOs from Lupus and Sigma Orionis (Rigliaco et al., 2012; Alcalá et al., 2014) are represented by salmon stars. Blue stars refer to B[e] stars from Lamers et al. (1998). In the insert plot, the synthetic main sequence and giant stars locus from the library of stellar spectral energy distributions (SEDs, Pickles, 1998) are represented by the purple and brown symbols and the loci of white dwarf stars observed by S-PLUS (DR1, Mendes de Oliveira et al., 2019) are the light green symbols. The limiting region applied in the candidate selection are shown as black lines for hPNe. The arrow indicates the reddening vector with $A_V \simeq 2$ mag.

mimics, like H II regions for the case of PNe and H II regions/YSOs for the case of SySt are excluded. The definition of the selection criteria or zones has been made by visual inspection of each diagnostic diagram separately. This may indicate that our list of PNe and SySt candidates will end up not characterized by high purity. The PNe zone is contaminated by extragalactic H II regions, especially for moderately low ($r - J0660$) colour index or, equivalently, low-excitation nebulae. Nevertheless, the observed PNe are well located in the PNe zone with high $(r - J0660) > 1$. On the other hand, the SySt zone is also contaminated by extragalactic H II regions, in addition of YSOs. Recall that SySt and YSOs have very similar photo-spectra, both being brighter in the red part of the optical spectrum. IPHAS also faced the same kind of problem being highly contaminated from other types of H α emitter, as it was demonstrated from the results of spectroscopic follow-up (e.g. SySt: Rodríguez-Flores et al., 2014, PNe: Viironen et al., 2009a,b). The distribution of main sequence (MS) and giant stars (purple and brown symbols in the inset figures) in the ($r - J0660$) vs ($r - i$) diagnostic diagram is such that both groups of stars occupy regions with lower ($r - J0660$) index (< 1.2) and higher ($r - i$) index (> 0) than the PNe zone (Drew et al., 2005; Corradi et al., 2008). White dwarf (WD) stars (light green symbols in insert figures) also present low ($r - J0660$) index (> 0), however they exhibit ($r - i$) colour > -1 . Hence, there is no mixture between PNe and the bulk of MS, giant and WD stars. The arrow indicates the reddening vector with $A_V \simeq 2$ mag. It was estimated by comparing the locus of unreddened models of PNe with the reddened ones.

3.6.2 New colour-colour diagrams

The multi-band filter systems of J-PLUS and S-PLUS (12 narrow- and broad-band filters) allow us to compute several different colour indices for each source and thus construct new colour-colour diagnostic diagrams. In order to search for PN and SySt candidates in the J-PLUS and S-PLUS catalogues, in the most effective way, four new colour-colour diagrams are defined in Figures 3.7 and 3.8 ($J0515 - J0660$) vs ($J0515 - J0861$), ($g - J0515$) vs ($J0660 - r$), ($z - J0660$) vs ($z - g$), and ($J0410 - J0660$) vs. ($g - i$). The PNe and SySt zones are also defined in these new diagnostic diagrams.

Generally, PNe are well separated from all the other H α sources used in this work, except extragalactic H II regions, as it is well known (Parker et al., 2006). High- and low-excitation PNe occupy distinct regions within the PNe zone. For instance H 4-1, a moderate high-ionization PN exhibits $(g - J0515) \approx -2$ (lower panel of Figure 3.7), with T_{eff} around 132×10^3 K ((Henry et al., 1996)), while MWC 574, a very low-excitation PN with $(g - J0515) \approx 0.0$, exhibits an [O III] even weaker than H β emission (Sanduleak & Stephenson, 1972; Pereira & Miranda, 2007). In the case of the SySt zone in the two plots of Figure 3.7 is contaminated by H II regions and YSOs, but not in the two diagrams of Figure 3.8. Apparently, the detection of SySt candidates in all the four diagnostic diagrams is an indispensable condition which increases the possibility of finding genuine SySt. The ($J0515 - J0861$) colour index

is associated with the continuum of the sources. Neither of these two filters contains any strong emission line. The $(J0515 - J0660)$ colour provides an estimation of the $H\alpha$ excess.

Regarding the second diagnostic diagram of Figure 3.7 (lower panel), the $(g - J0515)$ colour index yields the excess of the [O III] lines. Therefore, the higher the $(g - J0515)$ colour is, the higher the excitation of the nebula. This can be seen from the photo-spectra of two CLOUDY models with different stellar temperatures (see Figure 3.2). Recall, however, that the g broad-band filter is also affected by the $H\beta$ and other emission-lines down to about 4,000 Å.

The $(z - J0660)$ colour (upper panel of Figure 3.8) index also gives us an estimation of the $H\alpha$ excess, by taking into account the continuum at the very red part of the spectrum, while the $(z - g)$ colour is directly related to the shape of the continuum from the blue to the red part of the spectrum. QSOs and SFGs are concentrated in a very small area [$-2 < (z - J0660) < 1$ and $-2 < (z - g) < 1$] well separated from PNe. The SySt, on the other hand, have a small overlap with QSOs and SFGs but they are found to be bluer in the $(z - g)$ colour index as well as the dusty YSOs.

Finally, $(g - i)$ is another colour index associated with the shape of the continuum and the $(J0410 - J0660)$ colour with the $H\alpha$ excess, by using different parts of the spectrum in contrast with the previous diagrams. From lower panel in Figure 3.8, we find that QSOs and SFGs show an increase in the $(J0410 - J0660)$ colour as a function of the $(g - i)$ colour, while PNe appear to have a more restricted range of $(g - i)$ values between -2 and 0, and $(J0410 - J0660)$ values from 0 to 4. Hence, the $(J0410 - J0660)$ vs $(g - i)$ colour-colour diagram can distinguish PNe from galaxies. Regarding SySt, most of them have $(J0410 - J0660) > 2$ occupying a distinct region in this colour-colour diagram. Both SySt and YSO are found to lie in the right part of the plot [$(g - i) > 2$], which is indicative of the presence of a cool companion or a dusty envelope. This last diagnostic diagram turns out to be very useful to assure a low contamination by B[e] stars, differently from the first three diagrams.

Figures 3.7 and 3.8 (inset diagrams) also illustrate the loci of main sequence, giant and white dwarf stars in the colour-colour diagrams, which clearly are not mixed with PNe. According to this analysis, we conclude that it is very hard to separate PNe from H II regions in both J-PLUS and S-PLUS projects. However, all the colour-colour diagrams turned out to be very useful to identify good PN and SySt candidates. The combination of several narrow- and broad-band filters to construct colour-colour diagrams allows to characterize the whole optical spectrum of each source. Therefore, if a source satisfies simultaneously all the criteria of either being a PN or SySt, the possibility of a false positive identification, though not negligible, is small making this candidate a good target for spectroscopic follow-up. All of the proposed criteria (equations that represent the lines in the colour-colour diagrams) for PNe and SySt are presented in Table 3.1.

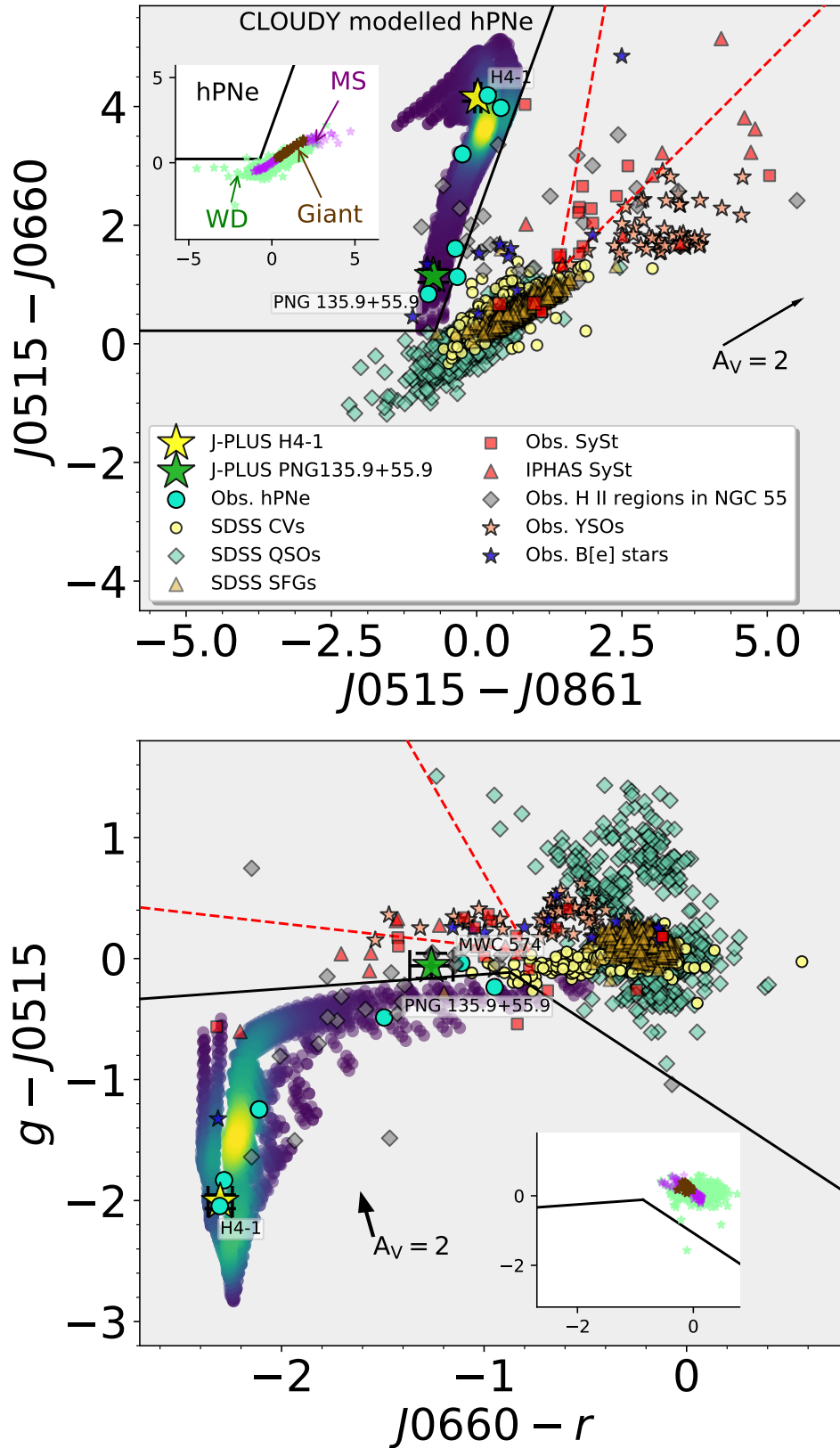


FIGURE 3.7: J-PLUS and S-PLUS (*upper*) ($J0515 - J0660$) vs ($J0515 - J0861$), (*lower*) ($g - J0515$) vs ($J0660 - r$) colour-colour diagrams. The symbols are as in Figure 3.6.

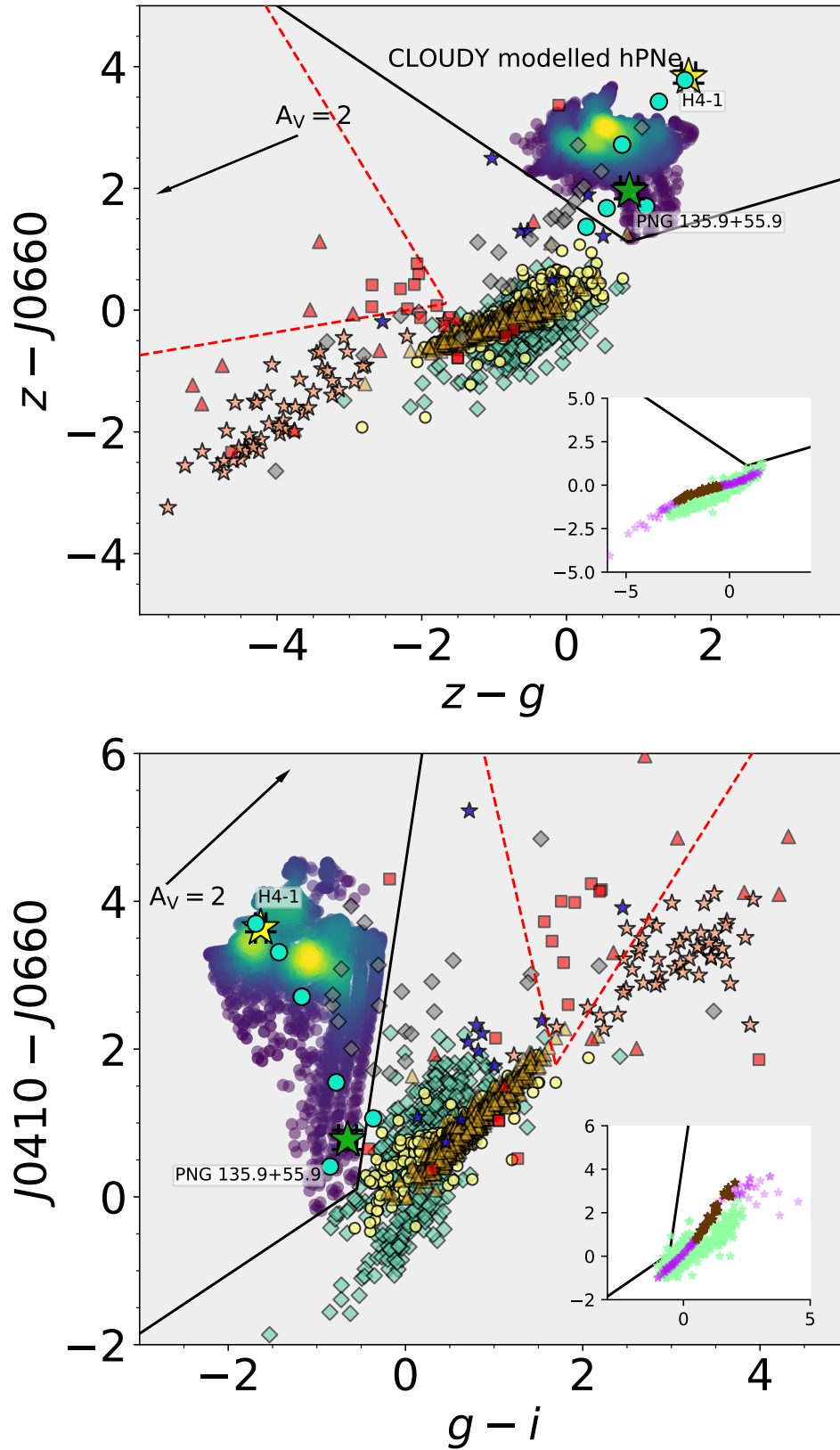


FIGURE 3.8: J-PLUS and S-PLUS (*upper*) ($z - J0660$) vs ($z - g$) and (*textitlower*) ($J0410 - J0660$) vs ($g - i$) colour-colour diagrams. The symbols are as in Figure 3.6.

| <i>Planetary nebulae</i> | |
|---|--|
| $(r - J0660) \geq 0.43 \times (r - i) + 0.65$ | |
| $(r - J0660) \leq -6.80 \times (r - i) - 1.30$ | |
| $(J0515 - J0660) \geq 2.7 \times (J0515 - J0861) + 2.15$ | |
| $(J0515 - J0660) \geq 0.3$ | |
| $(g - J0515) \leq 0.12 \times (J0660 - r) - 0.01$ | |
| $(g - J0515) \leq -1.10 \times (J0660 - r) - 1.07$ | |
| $(z - J0660) \geq 0.35 \times (z - g) + 0.82$ | |
| $(z - J0660) \geq -0.80 \times (z - g) + 1.80$ | |
| $(J0410 - J0660) \geq 8.0 \times (g - i) + 4.50$ | |
| $(J0410 - J0660) \geq 0.8 \times (g - i) + 0.55$ | |
| <i>Symbiotic stars</i> | |
| $(r - J0660) \geq -400 \times (r - i) + 30.4$ | |
| $(r - J0660) \geq 0.39 \times (r - i) + 0.73$ | |
| $(J0515 - J0660) \leq 5.5 \times (J0515 - J0861) - 6.45$ | |
| $(J0515 - J0660) \geq 0.98 \times (J0515 - J0861) - 0.16$ | |
| $(g - J0515) \geq -0.19 \times (J0660 - r) - 0.09$ | |
| $(g - J0515) \leq -2.90 \times (J0660 - r) - 2.20$ | |
| $(z - J0660) \leq -1.96 \times (z - g) - 3.15$ | |
| $(z - J0660) \geq 0.20 \times (z - g) + 0.44$ | |
| $(J0410 - J0660) \geq -5.20 \times (g - i) + 10.60$ | |
| $(J0410 - J0660) \geq 1.90 \times (g - i) - 1.43$ | |

TABLE 3.1: Proposed criteria for PNe and SySt based on J-PLUS colours.

3.7 J-PAS synthetic photometry

Besides the ongoing J-PLUS and S-PLUS surveys, the J-PAS survey with its 59 filters will also cover $\sim 8,000 \text{ deg}^2$ of the Northern hemisphere (see Section 2). The photo-spectra for J-PAS, as well as the colour-color diagnostic diagrams, have also been explored. J-PAS synthetic photometry has been computed for all sources mentioned above using the theoretical transmission curves of the filters and Eq. 3.38.

J-PAS photo-spectra are shown in Figure 3.9. Given that J-PAS has better spectral resolution compared to J-PLUS and S-PLUS, it is possible to obtain additional spectral information of the sources. It is clearly perceptible that emission lines like [O III] and [He II] can be detected in one of the narrow-band filters of J-PAS (see also transmission curve of J-PAS Figure 2.7 of chapter 2), typical emission lines of PNe and SySt. For the case of QSOs, J-PAS photometry has been also calculated for those with redshifts in the range from $3.03 < z < 3.20$. The reason is that the Ly α line at 1216 \AA falls in the $J5001$ band, thus resembling the detection of the [O III] 5007\AA emission line.

3.8 J-PAS synthetic colour-colour diagrams

Based in our knowledge about the spectral emission lines of PNe and SySt (by means of Figure 3.9), we have selected the J-PAS narrow-band filters that include important emission lines of our sources (H α , [O III], [He II], [O II] and [S III]) and, in some cases, the respective adjacent filters for the continua. Using these bands, we have performed the best combinations of colours to produce the best possible colour-colour diagrams to isolate PNe and SySt.

Figure 3.10 presents six colour-colour diagnostic diagrams that discriminate very well PNe from other emission objects. Panel (a) shows the $(J6900 - J6600)$ vs $(J4701 - J6900)$ colour-colour diagram. The $J6600$ and $J4701$ filters detect the H α and [He II] emission lines respectively, while the other two filters do not detect any emission lines of the nebulae (continuum). PNe are placed in the upper zone of the diagram with $(J6900 - J6600) > 0.9$. Given that observed and modelled PNe spanned a wide range of degree of ionization, they exhibit $-2.0 < (J4701 - J6900) < 0.4$. Thus, they occupy a region well separated from other sources even from H II regions. However a small number of H II regions (six) are located in the PNe zone. SySt are also located in the top side of diagram but cover a wide interval of the $(J4701 - J6900)$ color. They are mixed with YSOs and B[e] stars. QSOs, SFGs and CVs share the same area ($0.0 < (J6900 - J6600) < 1.0$ and $-1.0 < (J4701 - J6900) < 1.5$). Panel (b) presents the $(J7300 - J7500)$ vs $(J4701 - J4600)$ colour-colour diagram. The $J7300$ filter detects the [O II] emission line. Note that this diagram also include the [He II] filter. The $J7500$ and $J4600$ bands detect the continuum adjacent to the emission lines ([O II] and [He II]). In this diagnostic diagram PNe occupy a region with colour indices; $-1.5 < (J7300 - J7500) < 0.0$ and $-2.0 < (J4701 - J4600) < 0.0$. This diagram also provides a good separation of

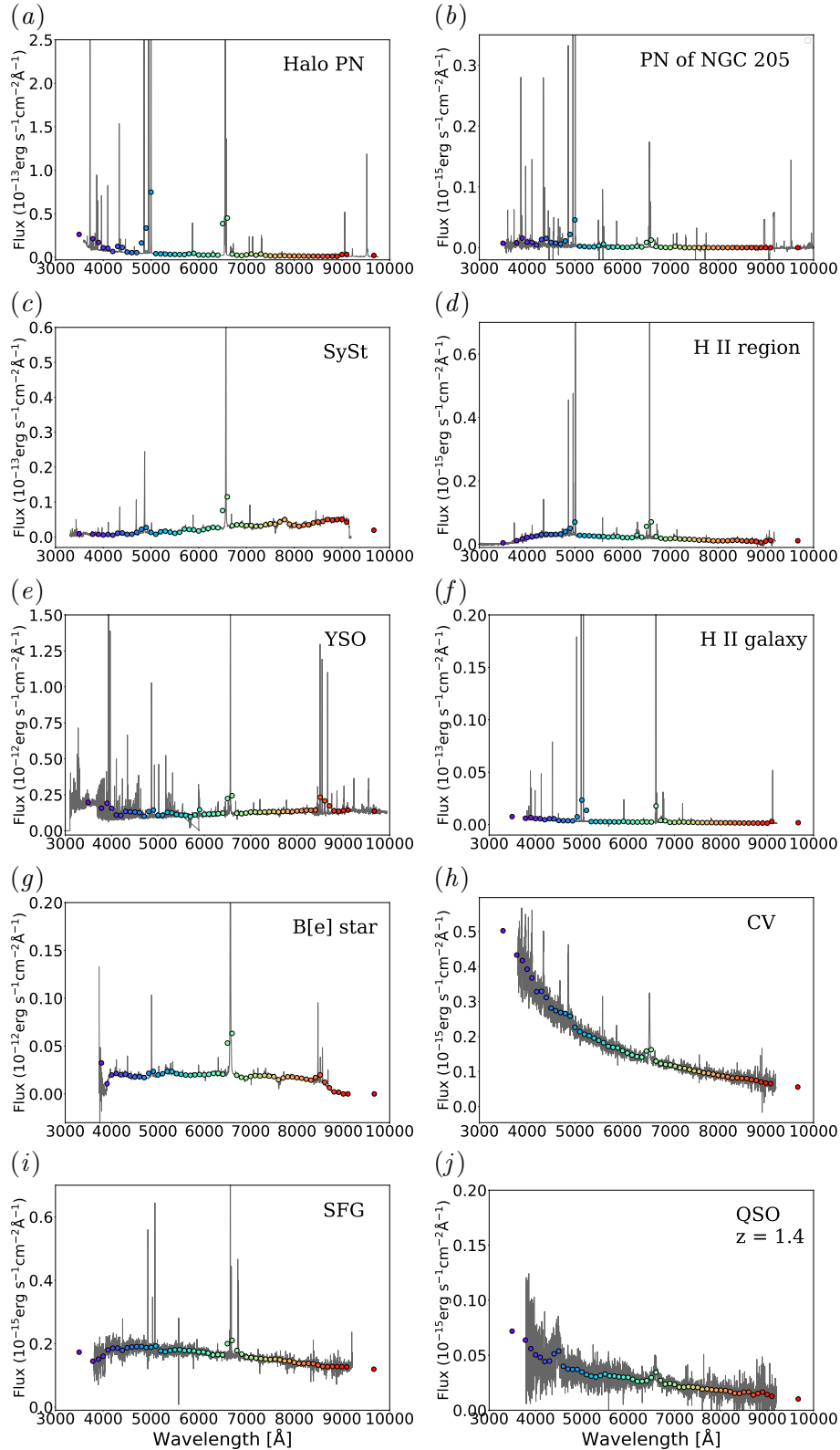


FIGURE 3.9: J-PAS synthetic photo-spectra of several emission-line objects, in flux units (colored points) overlapping the observed spectra (gray lines). The DdDm 1 PN (a). A PN in the dwarf galaxy NGC 205 (b). The SySt LMC 1 (c). A H II region in the nearby galaxy NGC 55 (d). The SySt LMC 1 (f). The YSO RU Lup (e). The H II galaxy Mrk 1318 (f) from SDSS. A B[e] star (g). A CV (h) from SDSS, a star forming galaxy (i) and QSOs with redshift of 1.4 (j), on which the strong emission in the $J6600$ filter, is because of the Mg II $\lambda 2798$.

PNe from H II regions ($(J4701 - J4600) \sim 0.0$). However the PNe G 135.9+55.9 and MWC 574 are mixed with H II regions. On other hand, SySt are well separated. The contamination by YSOs is almost negligible. The bulk of YSOs defines a separated loci in this diagnostic diagram.

Panel (c) of Figure 3.10 displays the $(J9100 - J8600)$ vs $(J4701 - J4600)$ plot. Here the $J8600$ band detects the [S III] line, while the $J8900$ emission corresponds to the continuum. The $(J4701 - J4600)$ colour index is the same as in panel (b). The majority of the PNe occupy a specific region in this diagram with $-3.0 < (J4701 - J4600) < 0.0$. However, low-ionization PNe are found to be mixed with other emission line sources. YSOs share the same region with QSOs, CVs, SFGs. SySt have $(J4701 - J4600)$ colour lower than high-ionization PNe, but they are mixed with low-ionization PNe. Note that the PN BB1 lies outside the PNe locus with $(J9100 - J8600) > 0.0$. Panel (d) presents the $(J6600 - J6800)$ vs $(J5001 - J5010)$ colour-colour diagram. The $J5001$ filter detects the [O III] emission line and the $J5101$ filter the adjacent continuum. PNe lie in a specific region in the lower-left on the diagram due to the presence of the [O III] emission. On the other hand CVs, SFGs, YSOs and some SySt occupy a small region with $(J5001 - J5010) \sim 0.0$ and $-1.5 \leq (J6600 - J6800) \leq 0.0$. QSOs cover a large area in the diagram ($-1.2 \leq (J6600 - J6800) \leq 0.1$ and $(-2.0 \leq J5001 - J5010) \leq 2.0$). The $(J5001 - J5010)$ colour excess is the result of the Ly α line in the $J5001$ band for, QSOs with $3.03 \leq z \leq 3.20$.

Panel (e) presents the $J5001 - J4701$ vs $J5101 - J5001$ colour-colour diagram. PNe define a locus well separated from their contaminants. They exhibit $-5.0 \leq (J5001 - J4701) \leq 1.5$ and $0.0 \leq (J5101 - J5001) \leq 4.8$ colour indices. The PNe MWC 574 and G135.9+55.9 lie in the same region with QSOs, CVs, SFGs, YSOs, SySt and Be stars. This happens because MWC 574 is a very low-excitation PN (Sanduleak & Stephenson, 1972) and PNG 135.9+55.9 is a very oxygen-poor PN (Tovmassian et al., 2001) and therefore they are characterized by a weak [O III] emission line. Note that CVs, SFGs, YSOs, SySt and Be stars are concentrated in a particular region around (0.0, 0.0) coordinate, while the QSOs are located in a wider area ($-2.0 \leq (J5001 - J4701) \leq 1.0$ and $0.0 \leq (J5101 - J5001) \leq 4.8$). Although the H II regions have [O III] emission, they are generally located on the border of the PNe zone. On the other hand, some SySt are located together with PNe.

Finally panel (f) shows the $(J6600 - J4701)$ vs $(J6900 - J6600)$ diagram. This is a combination of the H α and [He II] filters and it uses the $J5101$ band for the continuum. PNe are located in the lower-right of the diagram, as it is expected for objects with intense H α emission. QSOs, SFGs and CVs occupy the same locus [$-2.0 \leq (J5001 - J4701) \leq 1.0$ and $(0.0 \leq J5101 - J5001) \leq 1.8$]. SySt are isolated in the diagram but present contamination by YSOs. The contamination by H II regions is not significant. However, some of the SySt share the same position with PNe in the colour-colour diagram. H II regions lie in a region between SySt and PNe.

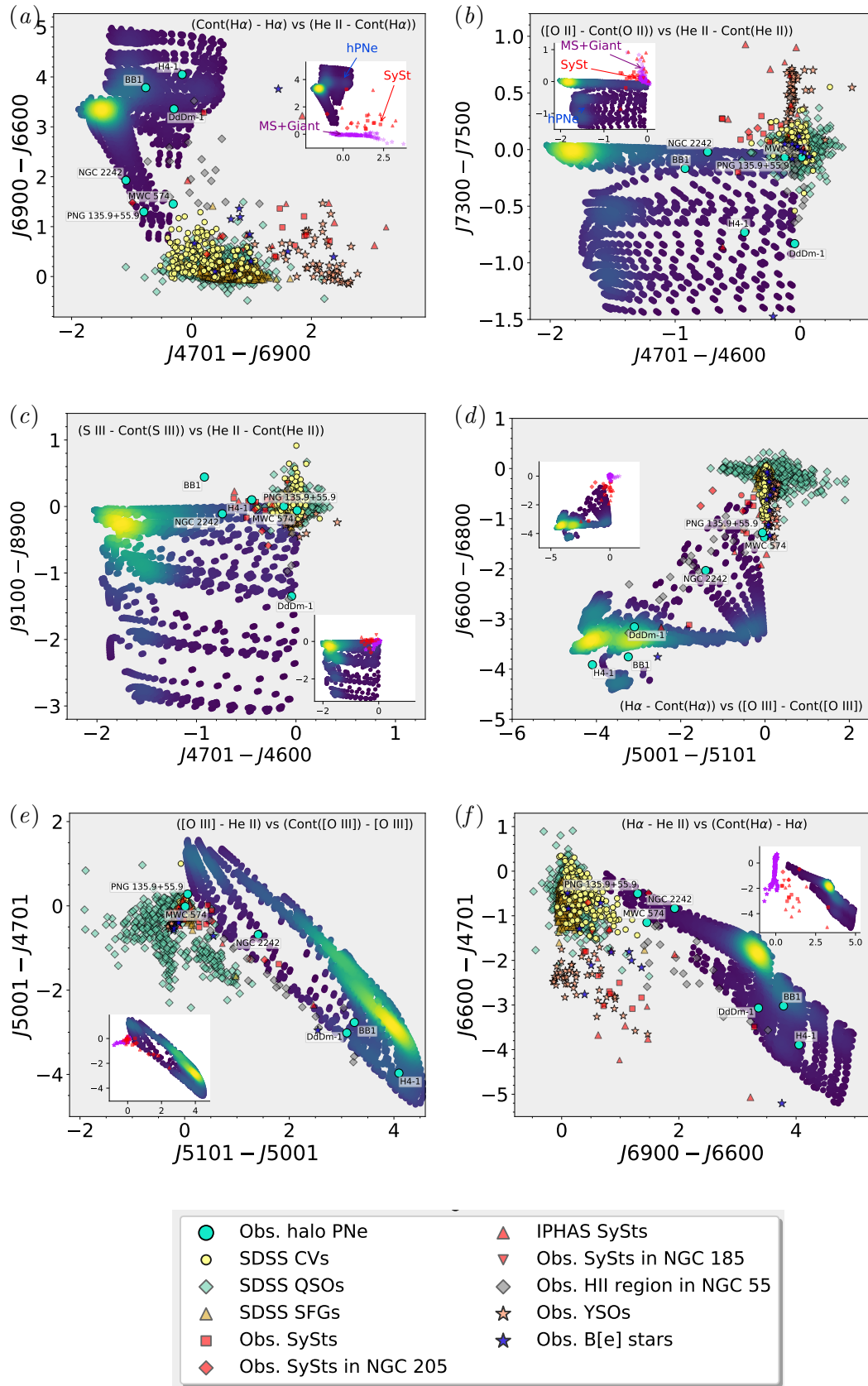


FIGURE 3.10: Six J-PAS colour-colour diagrams to separate PNe and SySt from other emission line sources. The symbols are as in Figure 3.6.

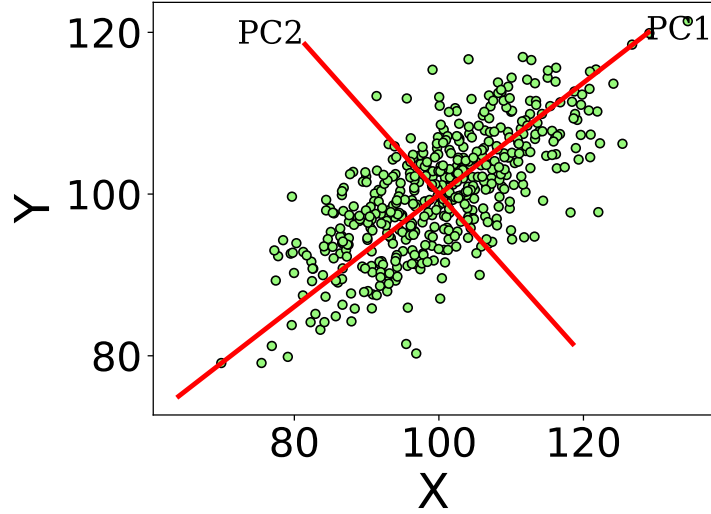


FIGURE 3.11: Example of an arbitrary data set relative to PC1 and PC2.

3.9 Statistical tools

In order to explore other methodologies to identify PNe and SySt we have considered principal component (PCA) and linear discriminant analysis algorithms as alternative tools to the colour-colour diagrams.

3.9.1 Principal component analysis

The principal component analysis (PCA, Pearson, 1901) has been extensively used in Astronomy, for instance, to detect variable stars in multi-band light curves (Süveges et al., 2012; Sokolovsky et al., 2017). It also was used to find the scaling relations of metallicity, stellar mass and star formation rate in metal-poor starbursts (Hunt et al., 2012). The PCA methodology is applied here to the separation of the different emission line sources.

PCA is primordially a linear and orthogonal transformation of a data set of m quantities. Each data point is represented by a vector, \mathbf{x}_J , in the m -dimensional space. The data set is transformed onto a new data set of m uncorrelated axes. These new m -axes are the eigenvectors (principal components, PCs) of the variance-covariance matrix of the data, where the variance of the data is emphasized (Moretti et al., 2018). The PCs are expressed as linear combination of the \mathbf{x}_J

$$\mathbf{PC}_i = w_{i,1}x_1 + w_{i,2}x_2 + \dots + w_{i,j}x_j \quad (3.39)$$

where $w_{i,j}$ are the weights – the elements of the eigenvector – and are also known as loading. The elements in the diagonal of the variance-covariance matrix are commonly called eigenvalues. Eigenvalues are the variance explained by each PC and they are constrained to decrease monotonically from the first principal component to the last.

By applying the PCA method to the variables \mathbf{x}_J , we get a linear combination of \mathbf{x}_J that gives us a rotated coordinate system, for which the first component (PC1) is defined along the direction of the largest variation of the data. The second PC (PC2) is defined to be orthogonal to the PC1 and along the direction of the second largest variation of the data. Figure 3.11 is an example of how the two first PCs explain the direction of the two largest variances of a data set. The space dimension of the rotated system is equal to that of the original system, however the first three PCs are usually enough to describe the new system. In short, PCA is a fundamental tool for data dimensionality reduction.

3.9.2 PCA: J/S-PLUS

PCA³ was applied to the J/S-PLUS synthetic photometry, with the aim to reduce their dimensionality by determining which of these variables (12 filters) contribute significantly to the variance of our sample. The input parameters are the synthetic magnitudes computed for all sources treated in this work.

Given that variance-enhancing PCA is data dependent, it is thus necessary to make a standardization of the data to zero mean and unit variance as the first step of the analysis. High values of a variable may result in numerically high variance, because PCA maximizes the variance impacting directly in PC1. PCA gives more emphasis to the variables with higher variances than to those with very low variances. Thus high values of a variable may result in numerically large variance, although a variable may not contain useful information. The variables were standardized as follows:

$$x_{std} = \frac{x - \langle x \rangle}{\sigma(x)} \quad (3.40)$$

where $\langle x \rangle$ and $\sigma(x)$ are the average and standard deviation of the data points. After applying PCA to the J- and/or S-PLUS data we found that the variance of the first 6 components, PC1-to-PC6, are: 97.02; 1.71; 0.79; 0.18; 0.11 and 0.08. Note that the most important are the first 3 components, which can explain 99.5% of the total variance of our sample.

The upper panel of Figure 3.12 shows the distribution of all emission objects on the PC2 vs PC1 diagram. QSOs, CVs and SFGs occupy the same area in this diagram which makes very hard to distinguish one another. This means that they share similar photo-spectra characteristics. hPNe are found to occupy a different region with $-3.0 < PC1 < 4.9$ and $-0.4 < PC2 < 0.5$ values and their overlap with other H α emitters is almost negligible. For modelled hPNe, three different groups are identified: $-3.5 < PC1 < 0$, $0 < PC1 < 3.5$ and $3.5 < PC1 < 4.9$. The first group (those with negative values on PC1) are mixed with WDs, CVs, SFGs and QSOs, while the other two ones are isolated and well separated from PN mimics. H II regions are concentrated in the left part of the diagram (with negative values of PC1) but well

³PCA is carried out here with the aid of the python library SKLEARN (Pedregosa et al., 2011); <http://scikit-learn.org/stable/> (see Appendix A.2).

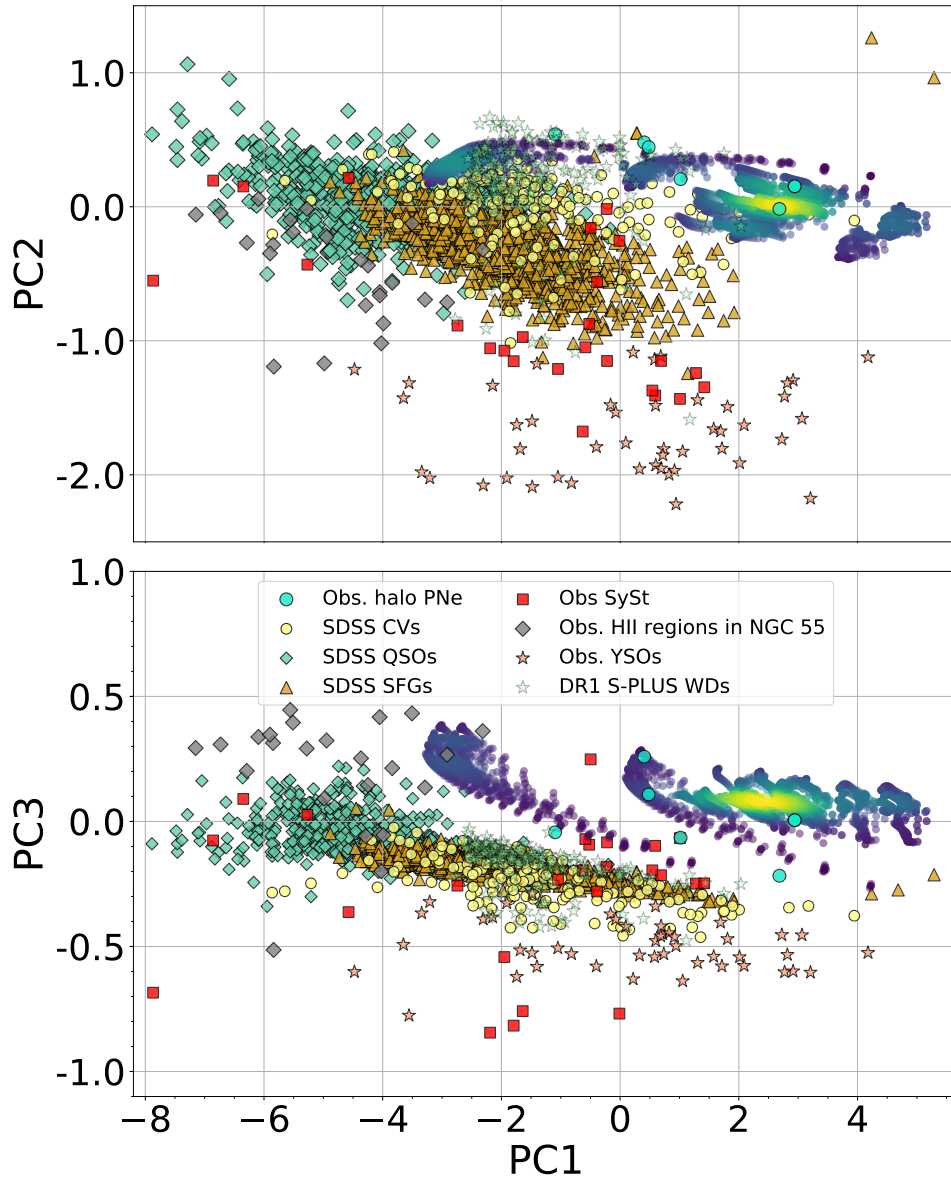


FIGURE 3.12: (*Upper panel*) J-PLUS PC2 vs PC1 and (*lower panel*) PC3 vs PC1 diagrams. The symbols are as in Figure 3.6. The very light green stars correspond to WDs from S-PLUS DR1.

mixed with QSOs and SFGs. SySt and YSOs are found to exhibit very negative PC2 values. SySt are not easily identified in this diagram, whereas YSOs show a minimal overlap with SySt and SFGs. Note that YSOs have the lowest values of PC2.

In the PC3 vs PC1 plane (lower panel of Figure 3.12), QSOs, CVs, SFGs and WDs occupy again the same region and almost all of them are described by negative PC1 and PC3 values. hPNe are isolated and well separated from PN mimics. Note that many hPNe have high values on PC3. SySt cover a wide range of PC1 and PC3 values without occupying a specific regime in the PC1 vs PC3 plane. This makes their identification very difficult. H II regions, on the other hand, exhibit higher PC3 values being separated from the rest of the objects. These diagrams do not include the B[e] stars because this spectra are shorter in the blue (u and $J0378$), and thus we can not modelled the synthetic photometry in all the filters.

Since each PC is a linear combination of all the input variables, in J/S-PLUS photometric systems the input variables are the twelve filters. Therefore eq. 3.39 in this context is,

$$\mathbf{PC}_i = w_{i,1}u + w_{i,2}J0378 + w_{i,3}J0395 + w_{i,4}J0410 + \dots \quad (3.41)$$

considering the eq. 3.40, this last equation is become

$$\begin{aligned} \mathbf{PC}_i = & w_{i,1} \frac{(u - \langle u \rangle)}{\sigma(u)} + w_{i,2} \frac{(J0378 - \langle J0378 \rangle)}{\sigma(J0378)} \\ & + w_{i,3} \frac{(J0395 - \langle J0395 \rangle)}{\sigma(J0395)} \\ & + w_{i,4} \frac{(J0410 - \langle J0410 \rangle)}{\sigma(J0410)} + \dots \end{aligned}$$

on which the coefficients, $w_{i,j}$, are the weights that determine the contribution of each filter (or the emission in each specific band) to the i th principal component. Left column of Figure 3.14 presents the weights ($w_{i,j}$) of each variable i.e. J/S-PLUS magnitudes for the first three principal components.

3.9.3 PCA: J-PAS

We also applied the PCA algorithm to the J-PAS synthetic photometry. We found that the percentage of total variance of first 6 PCs are: 96.94, 1.77, 0.64, 0.25, 0.12 and 0.07. The three first components are the most significant PCs. Here as well about 99.35% of the data variance is captured for the first three PCs.

Figure 3.13 shows two diagrams based on the first three PCs. PNe, SySts and YSOs are separated from the other emission-lines sources. There is a remarkable difference in the distribution of the objects between the J-PAS diagrams (PC2 vs PC1 and PC3 vs PC1) and J/S-PLUS ones. This is because PCA is data-depending – in this J-PAS dataset, WDs are not included –. PNe, SySt and YSOs have PC1 values between -9 and 15. QSOs, CVs, SFGs and H II regions exhibit PC1 values

from -20 to 5. Note that a QSO group contains the most negative values of PC1. On the other hand, SySt and YSOs have the highest PC2 values (from 2 to 6). PNe have both positive and negative PC2 values ($-2.0 \leq \text{PC2} \leq 0.5$). The lower panel shows the PC3 vs PC1 diagrams. Again much unsimilar to the other two surveys. SySt and YSOs have high and positive PC3 values ($0.5 \leq \text{PC3} \leq 3$). Moreover, PNe are found to lie in a locus from -17 to 0.6. This diagram is good for separating SySt from their contaminants, with the exception of YSOs.

Right column of Figure 3.14 presents the weights associated with the first three PCs, which are the coefficients of the linear combinations that define these PCs.

3.9.4 Linear discriminant analysis

Linear discriminant analysis (LDA; Fisher, 1936) is commonly used as a dimensionality reduction technique in the pre-processing step for recognition patterns and machine learning. For instance, LDA has been recently used to identify PNe and SySt from a list of H α emission lines sources using 2MASS and WISE photometric data (Akras et al., 2019b; Akras et al., 2019c). This method projects a data set into a lower-variable space which maximize the separation between classes of data. LDA traces a linear combination of the variables such that the separation between classes of variance is maximized (Hastie et al., 2009). Therefore, LDA is a classification method in statistical and probabilistic learning (Ghojogh & Crowley, 2019). LDA is similar to PCA, since both perform linear combinations to transform a data set in a new one, where the latter is a projection of the old data set. The difference between the two statistical techniques is that LDA aims to find the projection of maximum separability, while PCA finds the projection that maximizes the variance of the data. Figure 3.15 is an illustration of how the new dimension is constructed favoring the separation between the class of dispersion.

To achieve the final goal of LDA, it is necessary to perform three steps. The first step consists of determining the distance between the means of different classes, i. e. the separability between different classes of variance. This is called between-class variance or between-class matrix. The second step is to calculate the distance between the mean and the sample of each class, which is called within-class variance or within-class matrix. The third step includes the construction of a lower-dimensional space that maximize the between class-variance and minimizes the within class-variance (Tharwat et al., 2017).

In the last step, the dimensions of the original data, for example, X , is reduced by projecting it onto the lower-dimensional space of LDA, V_k . Here the number the dimensions of new lower-dimensions is k . Therefore, each sample of X is represented in the k -dimensional space by projecting it onto the lower-dimensional space (V_k) as follows,

$$Y = XV_k$$

where Y represent the projected sample in the new dimensions. It is important to mention that the distance of separation between the different classes is greater when

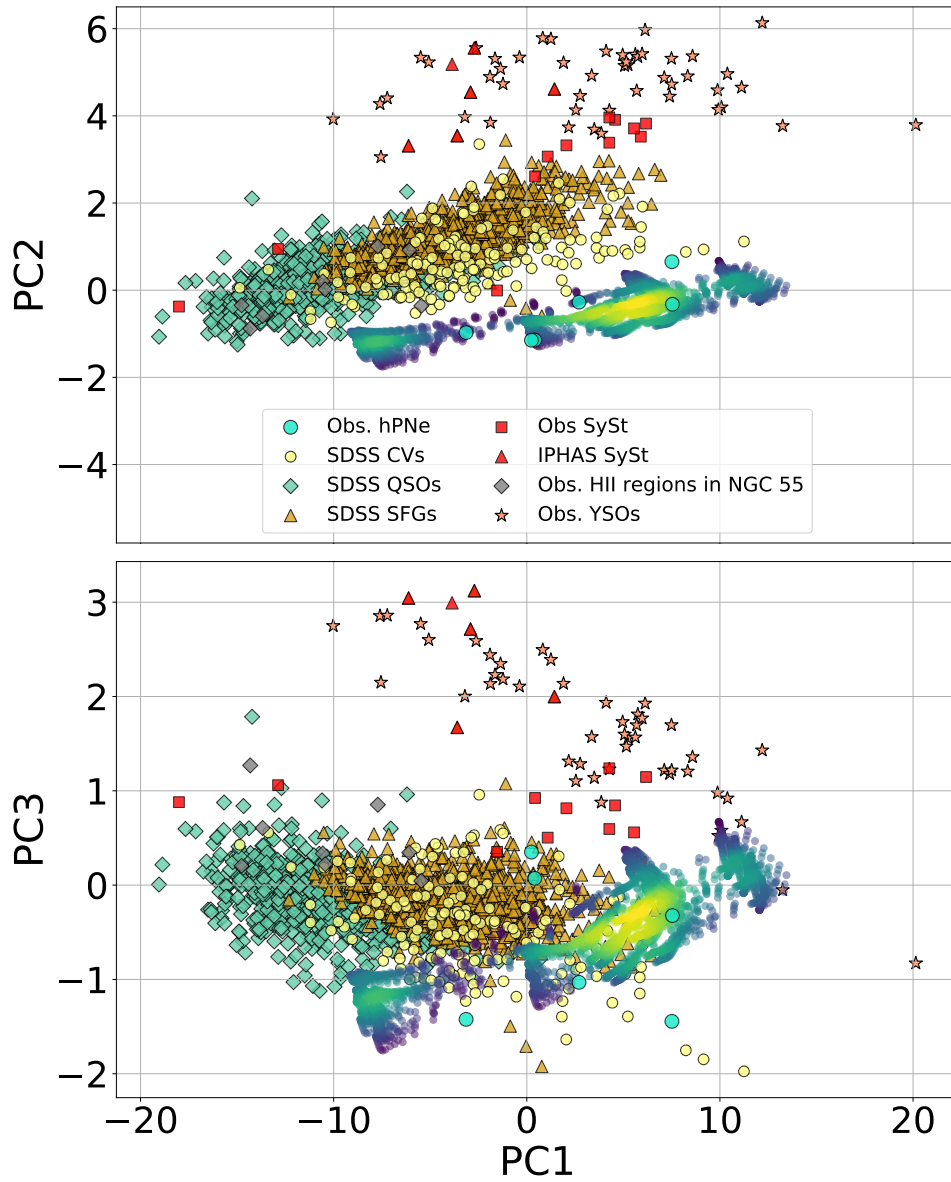


FIGURE 3.13: J-PAS PC2 vs PC1 (*upper panel*) and PC3 vs PC1 (*lower panel*) diagrams. The symbols are as in Figure 3.6.

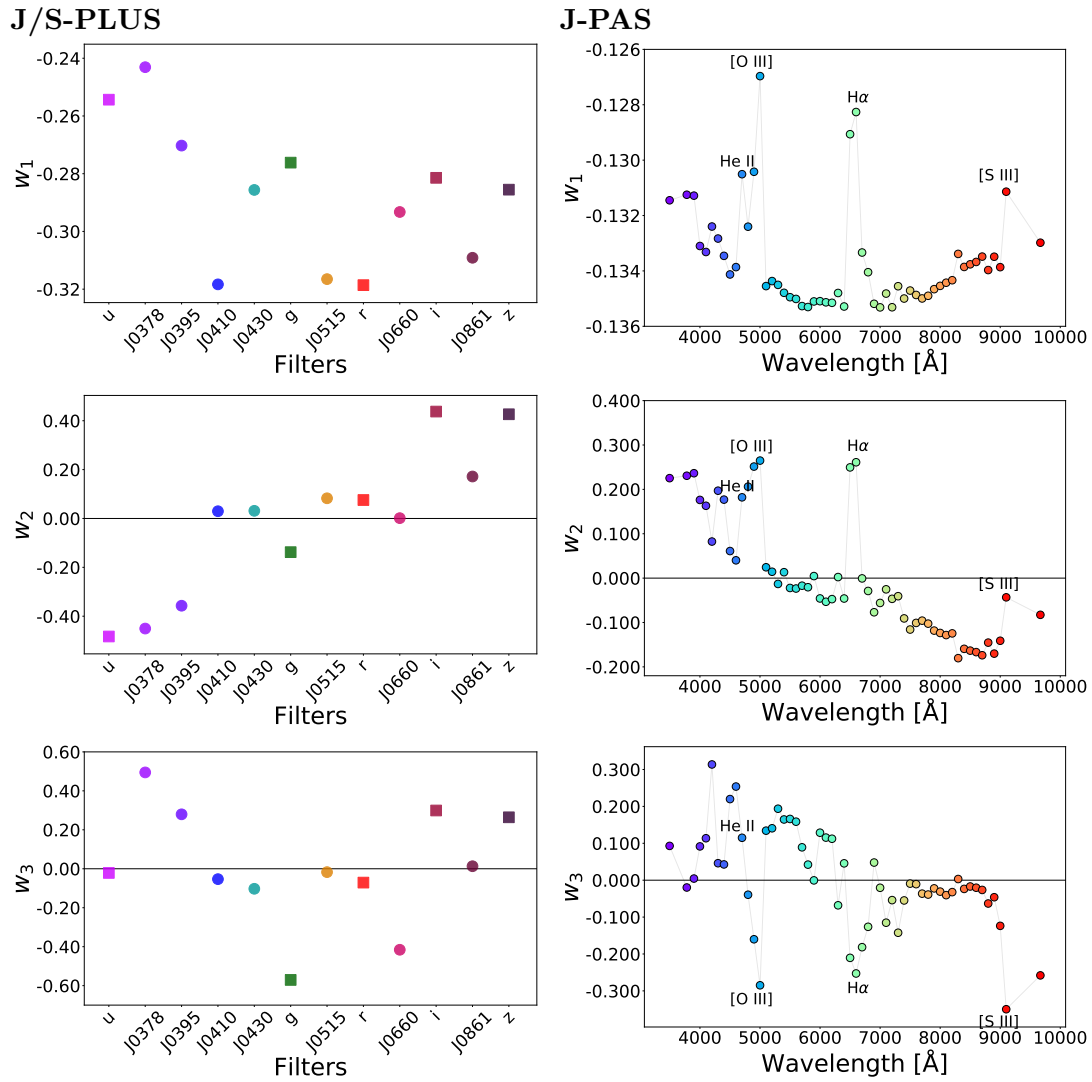


FIGURE 3.14: *Left column:* J/S-PLUS weights associated with PC1 (*upper*), PC2 (*middle*) and PC3 (*lower*) for the sources of the Figure 3.12. *Right column:* J-PAS weights of the J-PAS bands associated with PC1 (*upper*), PC2 (*middle*) and PC3 (*lower*) dimensions. The weights of the J-PAS filters that detect He II, [O III], H α and [S III] lines are indicated. In the plots, the abscissas are the weights (w_i) and the ordinates are the filters.

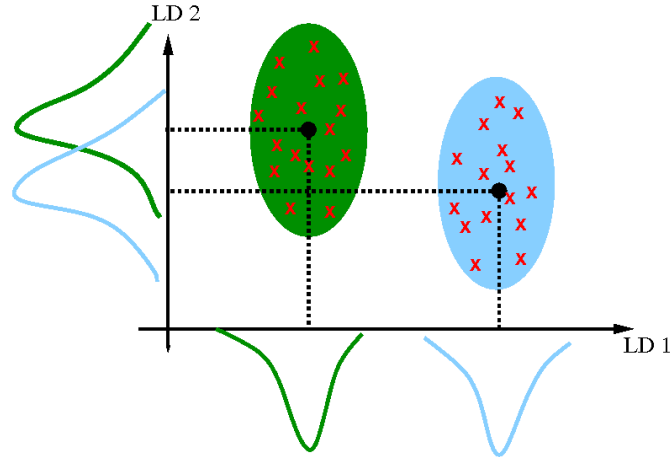


FIGURE 3.15: Example of two class scatter relative to LD1 and LD2. Maximizing the axes for class separation (Gonzalez, 2017).

the data are projected on the first eigenvector (v_1), or first dimension, than when the data are projected on the second eigenvector (v_2).

3.9.5 LDA: J/S-PLUS

At the moment we have implemented LDA to the J/S-PLUS synthetic photometry to explore the possibility to use them to identify PNe or SySt in these surveys. We have reduced the 12 J/S-PLUS bands to the first three dimensions, which are characterized by maximum separation of the class-variance. In this context each kind of object (hPNe, SySt, H II regions, QSOs, SFGs, YSOs and WDs) represent this class-variance.

Figure 3.16 displays the first three LDs. The upper panel presents the LD2 vs LD1 diagram. PNe and SySt are well separated from the other classes of objects (SySt zone are contaminated by YSOs), showing that the strong emission lines and the shape of the continuum (blue continuum for PNe and red continuum for SySt) are the features that most contribute in the maximization of the distance between the objects. PNe are found to occupy a region at the left part of the LD2 vs LD1 diagram with $LD1 < 0$. Only a small number of modelled PNe are found to have $LD1 > 0$. The observed data of hPNe is consistent with this analysis. H II regions, the most common mimic of PNe, are also found in the right part of the diagram with $LD1$ between 0 and 8. Despite PNe and H II regions show different LD1 values, they have similar LD2 (*upper panel*) and LD3 values (*lower panel*). PNe exhibit a very narrow range of LD2 and LD3 values compared to H II regions, which will allow us to discard several H II regions from our final list of PNe candidates. It should also be noted that PNe are very well separated from CVs, SFGs, QSOs, YSOs and SySt. The WDs occupy a region between the hPNe locus and all other sources.

Regarding SySt, even with LDA, their identification is more difficult than that of PNe, since they occupy the same loci as YSOs and H II regions with $LD2 < -2$. However, contamination can be diminished if the LD1 values are used. SySt have

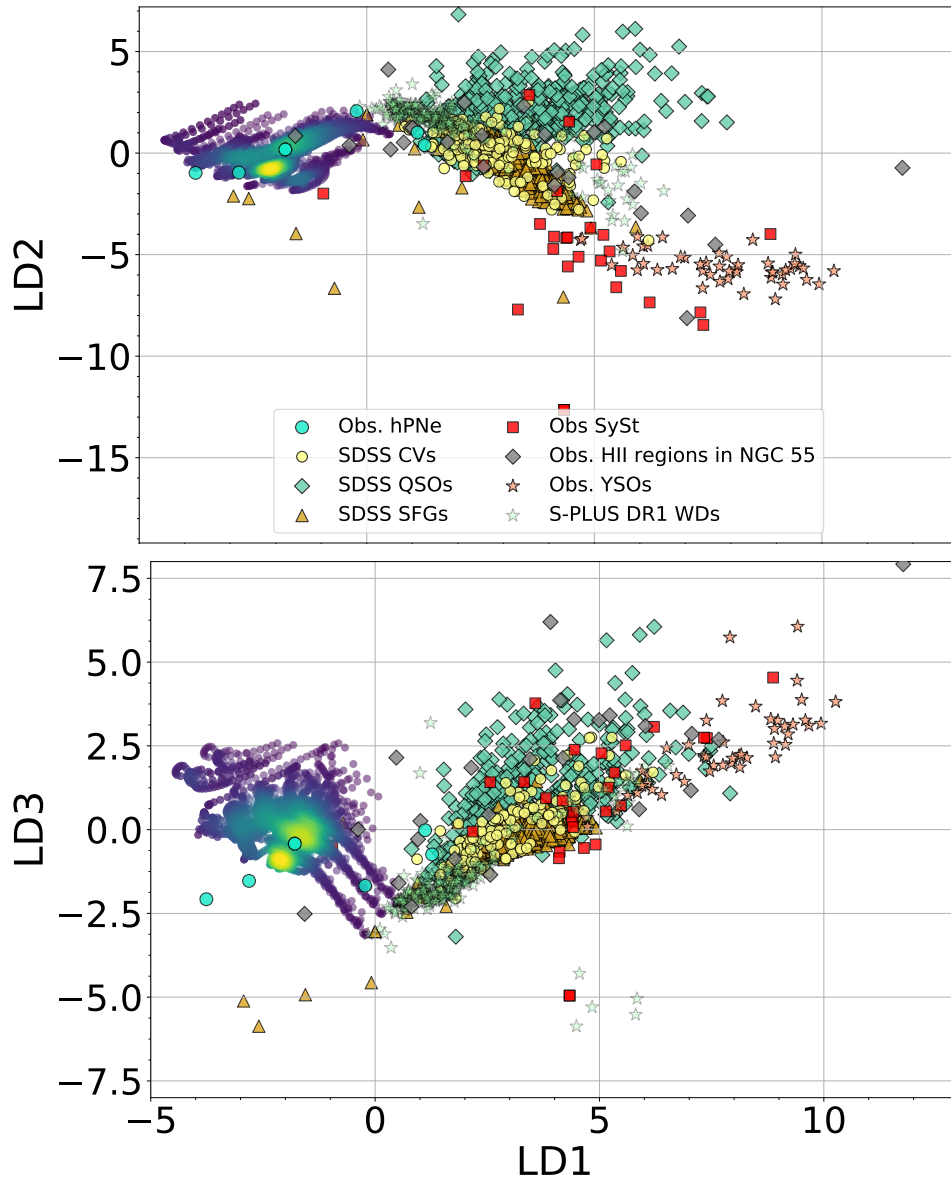


FIGURE 3.16: (*Upper panel*) J-PLUS LD2 vs LD1 and (*lower panel*) LD3 vs LD1 diagrams. The symbols are as in Figure 3.6.

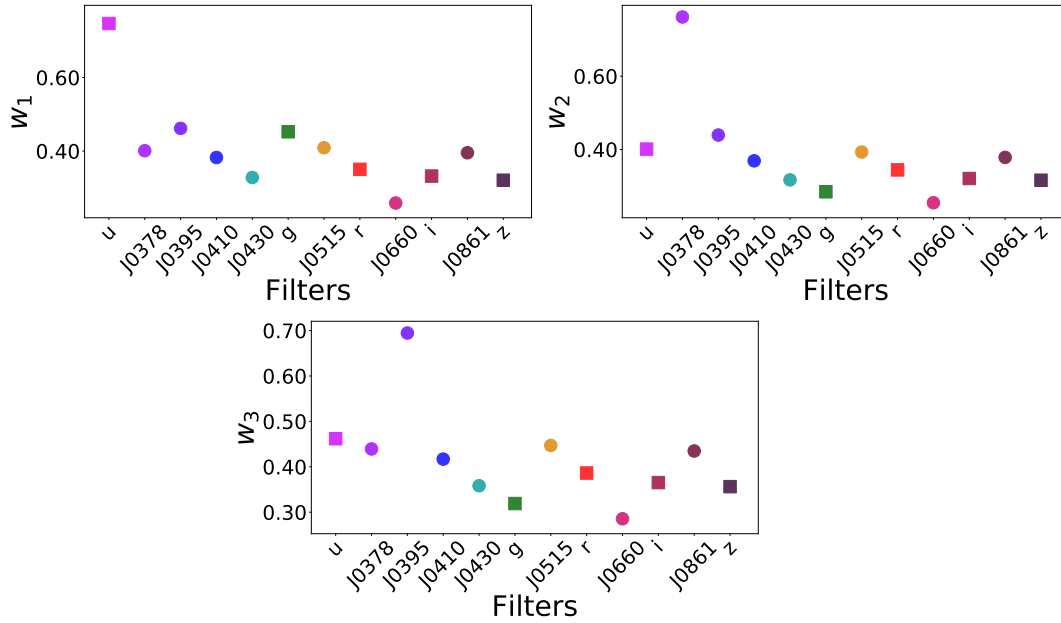


FIGURE 3.17: Weights associated with LD1 (*upper panel*), LD2 (*middle panel*) and LD3 (*lower panel*). In the plots, the abscissas are the weights (w_i) and the ordinates are the filters.

LD1 between 3 and 8, YSOs between 4.7 and 10 and H II regions higher than zero. Unfortunately, the LD3 vs LD1 diagrams do not provide any useful information to further separate SySt from YSOs or H II regions since all these types have LD3 between -2.5 and 7.5.

As in PCA, each LD is expressed as a linear combination of all J/S-PLUS bands, where the coefficients of the correlation are the relevance-weights between classes. Thus, in Figure 3.17, it is presented the weights associated with the first three LDs.

Chapter 4

Applying the techniques to the observational data

This chapter presents the results from the validation of the J- and S-PLUS colour-colour criteria for the identification of PNe in these two surveys. It is also discussed the results of implementing the colour-colour diagrams to the J-PLUS and S-PLUS DR1, from which we selected, within the PN zone, four objects: one PN candidate, one known PN and two H II galaxies. None object was identified in the correspondent area S-PLUS catalog. SySt were not found in these first data releases. The cross-matching of the J- and S-PLUS with the most updated PNe catalog (HASH) is also analyzed. Principal component analysis and linear discriminant analysis were tested and validated by using the recovered objects in J-PLUS and S-PLUS data.

4.1 J-PLUS SVD

Two hPNe, H 4-1 and PNG 135.9+55.9, were observed during the science verification phase of the J-PLUS, as described in Section 4.1. The instrumental magnitudes were calculated for each object using IRAF¹. In order to find the calibrated magnitudes we used the *zero point* provided by the Unit of Processing and Data Analysis (UPAD) inside the J-PLUS collaboration. The photometric results of these two PNe are presented in Figure 4.1 and Table 4.1. The synthetic magnitudes are also presented for a direct comparison with the observations. For H 4-1 the two sets of magnitudes are found to be compatible, with a difference smaller than 0.07, except for the *u* and *J0378* filters, for which a difference of 0.4 and 0.23 mag, respectively, is found. As for PNG 135.9+55.9, the synthetic and observed magnitudes are also in good agreement, with, on average, a difference smaller than 0.1 mag. Only the observed H α magnitude shows a significantly higher difference from the synthetic one. The reason for this discrepancy is probably, the size of the aperture used for the J-PLUS photometry (6'') and the slit width (3'') used for the spectroscopic data, on which synthetic magnitudes are based.

¹Image Reduction and Analysis Facility; <http://iraf.noao.edu/>

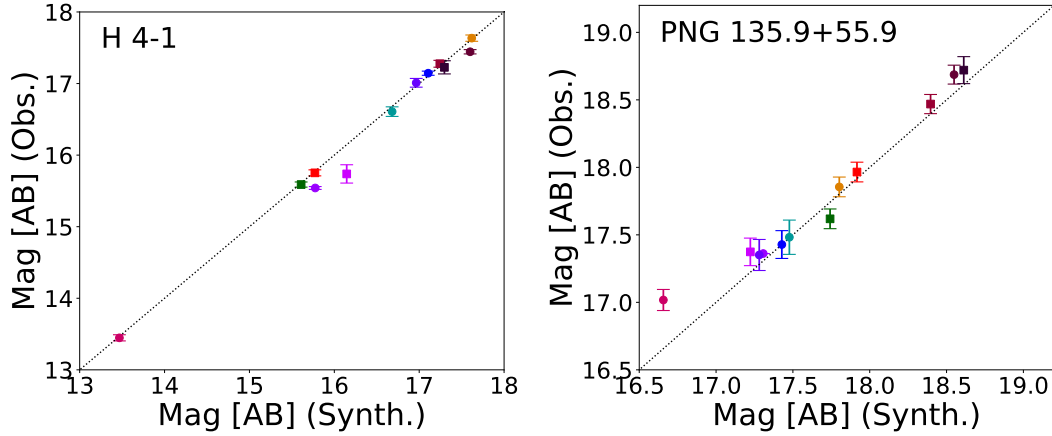


FIGURE 4.1: Comparison between J-PLUS synthetic and observed photometry of the PNe H 4-1 (*left*) and G 135.9+55.9 (*right*). The blue dashed line signifies equality.

| | H 4-1 | | PNG 135.9+55.9 | |
|--------------|-------|--------------|----------------|--------------|
| Filter | Synt. | Obs. | Synt. | Obs. |
| <i>u</i> | 15.74 | 16.14 ± 0.13 | 17.37 | 17.22 ± 0.10 |
| <i>J0378</i> | 15.54 | 15.77 ± 0.02 | 17.36 | 17.31 |
| <i>J0395</i> | 17.01 | 16.97 ± 0.06 | 17.35 | 17.28 ± 0.12 |
| <i>J0410</i> | 17.14 | 17.11 ± 0.03 | 17.43 | 17.43 ± 0.10 |
| <i>J0430</i> | 16.61 | 16.68 ± 0.07 | 17.48 | 17.48 ± 0.13 |
| <i>g</i> | 15.59 | 15.61 ± 0.04 | 17.62 | 17.74 ± 0.07 |
| <i>J0515</i> | 17.63 | 17.62 ± 0.04 | 17.86 | 17.80 ± 0.07 |
| <i>r</i> | 15.75 | 15.77 ± 0.04 | 17.97 | 17.92 ± 0.07 |
| <i>J0660</i> | 13.45 | 13.47 ± 0.04 | 17.02 | 16.66 ± 0.08 |
| <i>i</i> | 17.28 | 17.24 ± 0.05 | 18.47 | 18.40 ± 0.07 |
| <i>J0861</i> | 17.44 | 17.60 ± 0.03 | 18.69 | 18.55 ± 0.07 |
| <i>z</i> | 17.23 | 17.30 ± 0.09 | 18.72 | 18.61 ± 0.10 |

TABLE 4.1: J-PLUS synthetic and observed magnitudes of H 4-1 and PNG 135.9+55.9. The observed magnitudes were derived with a 6'' circular aperture.

The position of H 4-1 and PNG 135.9+55.9 in the colour-colour diagrams –based on their J-PLUS observations– are shown in Figures 3.6 and 3.7 as yellow and green stars, respectively. H 4-1 satisfies all the five criteria of being a PN (see Figures 3.6 and 3.7), while PNG 135.9+55.9 passes four of them, by violating the (g - $J0515$) colour criterion given in panel (b) of Figure 3.7). Note, however, that this PN is located close to the border of the PN zone. This border was defined in a conservative way, to exclude the vast majority of the contaminants such as H II regions given that the former exhibit similar spectroscopic characteristics with PNe, making their separation very difficult.

4.2 Colour criteria versus the DR1s

The color-color criteria for PNe were applied to the J-PLUS and S-PLUS data releases. A number of cleaning instructions (FLAGS) were also considered, in order to avoid artifacts and problematic objects. Two FLAGS were applied to the J-PLUS DR1 catalogue. The first one allows us to exclude bright and nearby objects which can significantly bias the photometry. The second FLAG avoids objects originally blended with another one. For the S-PLUS catalogue, we used only one FLAG, which eliminates sources for which the aperture photometry is likely biased by neighbor sources or by more than 10% of bad pixels. Note that without these FLAGS many sources with problematic photometric measurements would pass our criteria of being PNe.

We also restrict our query to objects with J-PLUS photometry errors lower than 0.2. However, in order to assure that we do not lose sources due to implementation of the error criteria, we follow the steps below. (*i*) By limiting the error associated to the magnitudes corresponding to IPHAS-like magnitudes (i , r and $J0660$) and assuming any error for the remaining 9 bands. (*ii*) By limiting the magnitude errors of the $J0660$ and broad-band filters. And finally, (*iii*) by limiting the magnitude errors of all narrow- and broad-band filters. All the observed magnitudes are measured using a circular aperture of $6''$. The queries are shown in Appendix C.

From step (*i*), which is the less restrictive one, we get the higher number of sources (9) that satisfy our PNe criteria. These sources can be very faint or even not detected at all in the bands except i , r and $J0660$. These 9 sources are classified as 4 H II regions, 2 H II galaxies, 1 WR star and 1 PN, while one is unclassified.

In order to verify how the error criteria in different bands affect the resulting number of PN candidates, we move to step (*ii*). This criterion provides us with sources of weak continuum emission and uncertain narrow-bands photometry (errors larger than 0.2 mag). Only four sources are returned in this case, 2 known H II galaxies, the known PN and the PN candidate from step (*i*). Note that this time we did not recover any H II region.

Finally, we tried the most restrictive selection criteria, step (*iii*), in which all the 12 magnitudes have errors smaller than 0.2 mag. The result is shown in Figures 4.2 and 4.3. By applying the selection criteria (step *iii*), we identify the same 4 sources

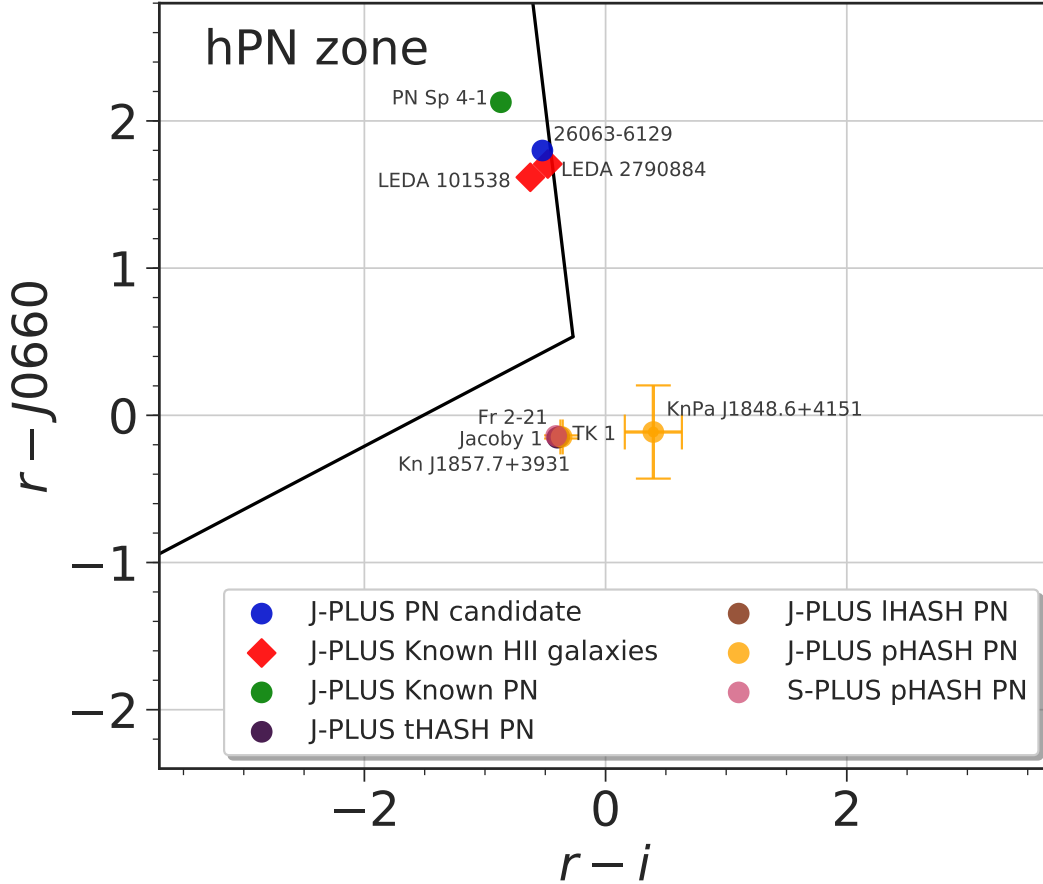


FIGURE 4.2: J-PLUS ($r - J0660$) vs ($r - i$) colour-colour diagram with the objects recovered from the J-PLUS DR1. The blue circle represents the PN candidate, the green circle is the known PN Sp 4-1, the red diamonds are the H II galaxies LEDA 2790884 and LEDA 101538. The matches of the J-PLUS and S-PLUS data with HASH catalog are also presented in the diagrams. The purple circle is the true PN (tHASH PN) Jacoby 1, the brown circle is the likely PN (IHASH PN) TK 1 and the orange circles represent the possible PNe (pHASH PN) Kn J1857.7+3931 and KnPa J1848.6+4151. The position of these four last objects correspond to the J-PLUS photometry. The pHASH PN Fr 2-21 is indicated by the magenta circle. This source was found in S-PLUS DR1. The errorbars are smaller than the symbols.

from step (ii). According to this analysis, we verify that the magnitude errors do not affect the selection of PN candidates.

None PN candidate show up from the S-PLUS DR1. The cross-matching between the J/S-PLUS catalogs and the HASH catalog of PNe resulted in three J-PLUS matches (one true, one likely and two possible PNe) and one S-PLUS match (one possible PNe). All these objects are presented in the selection diagrams below, in Figures 4.2 and 4.3, and discussed in the rest of the present section as well as in Section 4.2.4.

4.2.1 J-PLUS photometry of the PN candidate

The location of the PN candidate (J2000 RA: J09 50 20.92, DEC: 31 29 11.02) in Figures 4.2 and 4.3 is shown by a blue circle. The source displays a clear H α

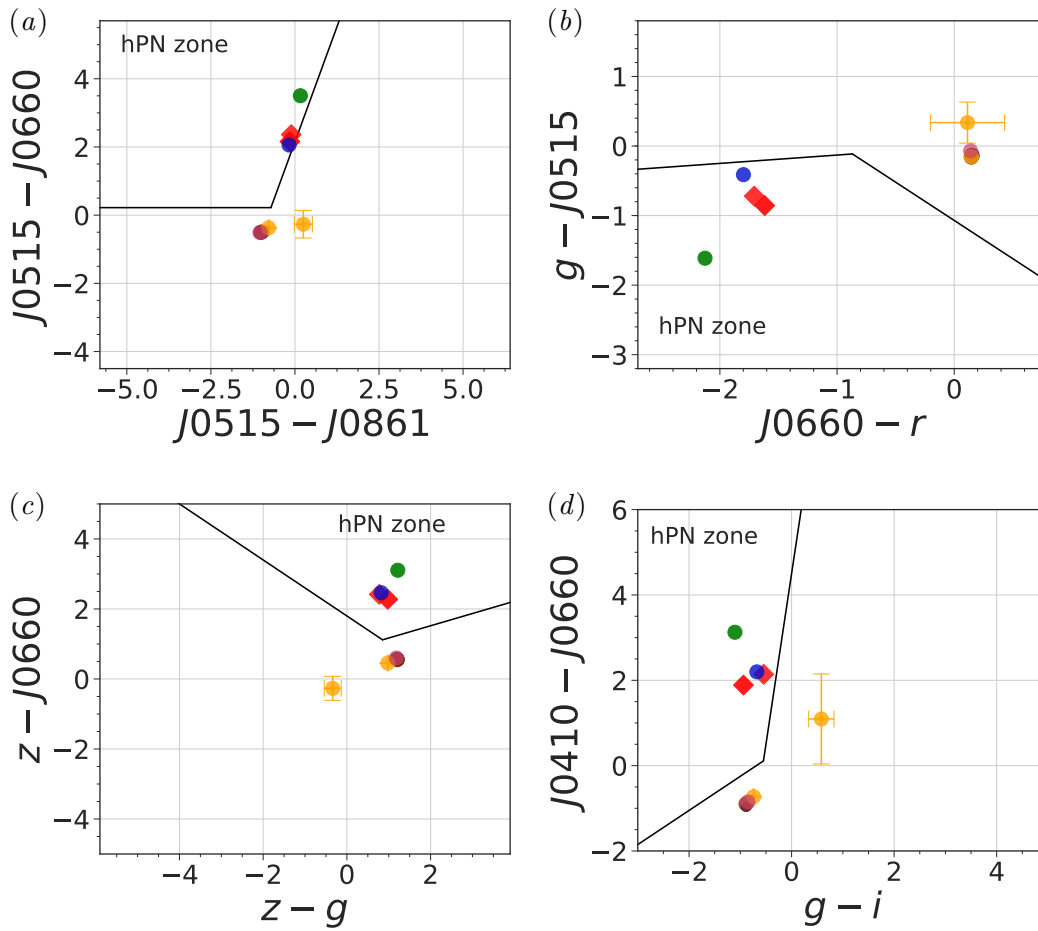


FIGURE 4.3: J-PLUS and S-PLUS diagnostic diagrams: (a) $(J0515 - J0660)$ vs $(J0515 - J0861)$, (b) $(g - J0515)$ vs $(J0660 - r)$, (c) $(z - J0660)$ vs $(z - g)$ and (d) $(J0410 - J0660)$ vs $(g - i)$. The symbols are the same as in Figure 4.2.

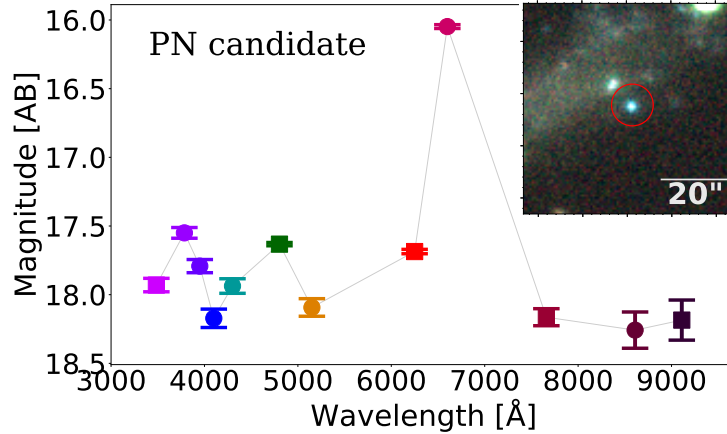


FIGURE 4.4: The photo-spectrum and 3RGB colour (g , r and i) image of the J-PLUS PN candidate.

excess (see Figure 4.4). Based on the (b) , (c) and (d) diagrams of Figure 4.3, it is possible to argue that this candidate has moderate [O III] emission. The candidate has $(g - J0515) = -0.5$, indicating low to moderate contribution of the [O III] and/or $H\beta$ or even [He II] lines to the g -band magnitude. Comparison between the J-PLUS colour of this PN and the grid of photo-ionization hPN models indicate an effective temperature for the central star $\sim 60\text{-}90^3$ K.

Figure 4.4 displays the PN candidate photo-spectrum, whose shape is very similar to that of typical PNe in the J-PLUS and S-PLUS configurations (see, for instance, Figure 3.1), with strong emission-lines and relatively flat continuum. From its J-PLUS $H\alpha$ image, we derived an angular radius of ~ 1.5 arcsec. This figure also presents a composite g , r and i image centred on the candidate. The UGC 5272 galaxy at 7 Mpc (Garrido et al., 2004; Karachentsev et al., 2014), is also presented in Figure 4.4. If the PNe candidate is a member of UGC 5272 galaxy, it should have a linear size of 40-50 pc indicative of an H II region. If we assume that the candidate is a Galactic halo source at a distance of 30-40 kpc, its size should be of 0.2-0.3 pc. In order to verify the nature of the candidate, we proceeded to the optical spectroscopic follow-up.

4.2.2 Spectroscopy of the PN candidate

Low-resolution, long-slit spectroscopic data of our J-PLUS PN candidate was obtained –by Martin Guerrero; a member of the J-PLUS collaboration– with the 2.54-m INT at Roque de los Muchachos observatory in La Palma, Spain. The Intermediate Dispersion Spectrograph (IDS) was used, with the 4096×2048 pixels RED+2 CCD detector. The size of each pixel is $13.5 \mu\text{m}$ or $0.44 \text{ arcsec pixel}^{-1}$. The R400V grating was selected in order to cover the spectral range from 3,600 to 7,000 Å, with a spectral reciprocal dispersion of $1.553 \text{ Å pixel}^{-1}$. The $30 \mu\text{m}$ (equivalently 1.08 arcsec) slit width was used for these observations and it was located through the center of the nebula at $\text{PA} = 300$ degrees. Three exposures of 1,200 sec each were

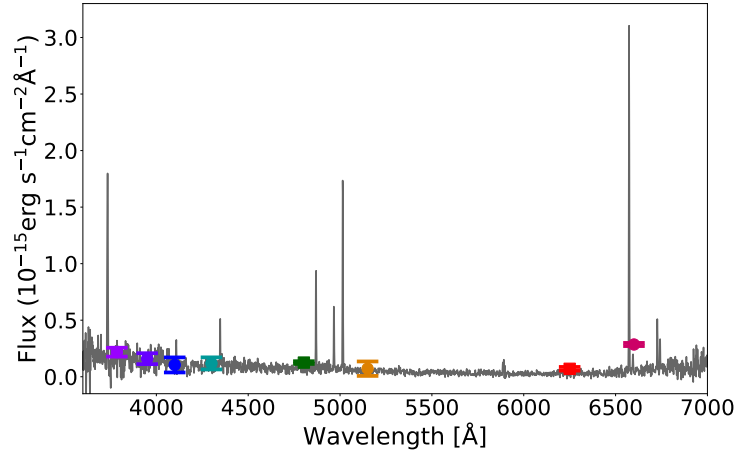


FIGURE 4.5: The INT IDS spectrum (not corrected for extinction) of the J-PLUS PN source. The colored points represent the J-PLUS photometry in flux units.

taken. The CuNe+CuAr lamps were adopted for the wavelength calibration. The standard star G191B2B was also observed for the flux calibration of the data.

The spectrum was bias subtracted, flat fielded, wavelength calibrated and flux calibrated by Martín Guerrero. Standard IRAF routines were used to reduce the long-slit spectrum. The extraction of the spectrum was made using the APALL routine, the spatial aperture used to extract the spectrum was 13 pixel (± 6.5) at 302 center, and all line fluxes were measured from the 1-D flux-calibrated spectra using the SPLOT function in IRAF.

The spectrum of the candidate is shown in Figure 4.5, with the J-PLUS photometric magnitudes overlaid for a direct comparison. The fluxes of the emission lines detected in our spectrum are presented in Table 4.2. Based on the $H\alpha$, $H\beta$, and $H\gamma$ lines, its extinction is 0.35. The $H\delta$ line was not used for these estimation due to its low S/N ratio. From the observed central wavelength of the detected lines, we also derived the heliocentric velocity of the source, 515 km s^{-1} . This value agrees with the heliocentric velocity of the galaxy itself ($513 \pm 2 \text{ km s}^{-1}$ Garrido et al., 2004), and it confirms that our J-PLUS PN candidate belongs to UGC 5272 (at 7 Mpc in distance). The [S II] $\lambda\lambda 6716/6731$ diagnostic ratio of 1.75 that suggests a very tenuous H II region. The oxygen abundance of the H II region, given in units of $12 + \log(\text{O}/\text{H})$, is estimated to lie between 8.39 and 8.93, by using the empirical strong-line methods N2 and O3N2, respectively.

4.2.3 Recovering DR1 known $H\alpha$ emitters

One PN and two H II galaxies were recovered by applying our selection methodology to the J-PLUS catalog.

- *PN Sp 4-1* (J2000 RA: 19 00 26.5, DEC: 38 21 07.99), also called PN G068.7+14.8, is a previously confirmed compact Galactic PN (Acker et al., 1992; Moreno-Ibáñez et al., 2016). In the diagrams of Figures 4.2 and 4.3, Sp 4-1 is repre-

| Line | $\lambda_{\text{rest}}(\text{\AA})$ | $\lambda_{\text{Obs}}(\text{\AA})$ | Flux ^a | Intensity ^a |
|----------------------------|-------------------------------------|------------------------------------|-------------------|------------------------|
| [O II] ^b | 3727.0 | 3734.3 | 290.6 | 357.8 |
| H δ | 4101.7 | 4108.4 | 24.8 | 28.7 |
| H γ | 4340.5 | 4347.3 | 41.7 | 46.2 |
| H β | 4861.4 | 4869.1 | 100.0 | 100.0 |
| [O III] | 4958.9 | 4966.8 | 67.9 | 66.6 |
| [O III] | 5006.8 | 5014.8 | 199.4 | 193.7 |
| [He I] | 5875.6 | 5888.9 | 29.6 | 24.9 |
| H α | 6562.8 | 6573.5 | 373.7 | 288.5 |
| [N II] | 6583.4 | 6594.4 | 22.3 | 17.2 |
| [S II] | 6716.4 | 6727.3 | 53.2 | 40.3 |
| [S II] | 6730.8 | 6742.0 | 30.4 | 23.1 |
| F(H β) ^c | — | — | 3.246 | — |

^aIn units of $H\beta = 100$. ^bBlended line. ^cIn units of $10^{-15} \text{ erg cm}^{-2} \text{ s}^{-1}$.

TABLE 4.2: Emission line fluxes of the J-PLUS PN candidate in UGC 5272.

sented by the green circle. The colours ($J0515 - J0660$) and ($g - J0515$) are estimated equal to 3.4 and -1.6, respectively. The former colour clearly indicates a strong H α emitter, while the latter implies a significant contribution from the [O III] and H β lines to the g-band. The upper-left panel of Figure 4.6 displays its photo-spectrum and corresponding image. There is no doubt that these data correspond to those of a typical PN photo-spectrum, of a roundish and compact object with FWHM \sim 1.3 arcsec.

- *LEDA 2790884* (J2000 RA: 8 25 55.50, DEC: 35 32 32.01) is a H II galaxy (blue compact galaxy) at $z \sim 0.0024$ (Moiseev et al., 2010). The loci where the system is represented in the diagrams of Figures 4.2 and 4.3 (one of the red diamonds) correspond to that of low-excitation PN. The photo-spectrum and image of this source are shown in the upper-right panel of Figure 4.6.
- *LEDA 101538* (J2000 RA: 16 16 23.51, DEC: 47 02 02.64), the red diamond in Figure 4.3, is a H II galaxy (dwarf blue compact) at $z \sim 0.002$, with a very blue colour. It is classified as starburst galaxy (Ann et al., 2015). The photo-spectrum of this galaxy is presented in the lower panel of Figure 4.6. The spectra of the H II galaxies are very similar to those of giant extragalactic H II regions (Sargent & Searle, 1970). For this reason, LEDA 101538 lies in the PN zone, even though it is not a PN.

4.2.4 DR1s vs. the HASH PN catalog

The Hong Kong/AAO/Strasbourg H α (HASH) planetary nebula database (Parker et al., 2016) is the most recent compilation of PNe (see also Section 1.4). This catalogue contains \sim 3,500, on which they are designated as true, likely and possible PNe. We found 4 matches with J-PLUS and one with S-PLUS. The J-PLUS ones

appear in the colour-colour diagrams as purple (1 true PN), brown (1 likely PN) and orange (2 possible PNe) circles, while the S-PLUS match is the dark magenta (1 possible PN) circle in Figures 4.2 and 4.3. It is straightforward noticing from these diagnostic diagrams that none of these sources were classified as PNe by our criteria, being all located outside the PN zone. Below we describe each source individually.

J-PLUS

- *Jacoby 1* (J2000 RA: 15 21 46.56, DEC: 52 22 04.05) also called PG 1520+525 is classified as a true PN in the HASH catalog (tHASH PN). This object was previously reported as a PN by Jacoby & van de Steene (1995). The low ($r - J0660$) and ($J0515 - J0660$) colour indices are indicative of very weak, or totally absent, $H\alpha$ line-emission. For this reason, Jacoby 1 was not recovered from our criteria. Figures 4.2 and 4.3 display the position of this PN in our diagnostic diagrams (purple circle) and it can easily be seen that it lies in an area below the PNe zone. The top-left panel of Figure 4.7 displays the photo-spectrum and corresponding image of Jacoby 1. This photo-spectrum is typical for white dwarfs (e.g. Figure 14 of Cenarro et al., 2019). From its image, we get a very compact source with $\text{FWHM} \sim 1.0''$. These characteristics suggest a WD.

Jacoby 1 is a highly-evolved PN with an angular size around 11 arcmin (Tweedy & Kwitter, 1996). PNe with such large sizes cannot be recovered by automatic photometric criteria, this is only possible by visual inspection of the fields (e.g. Sabin et al., 2014). It is clear that our J-PLUS photometry does not correspond to the PN itself, but to its WD (Werner et al., 2016) central star, which explains why we do not obtain any $H\alpha$ excess. By applying a Gaussian smoothing filter of 10 pixels to the combined RGB – $J0660$, r , and i – image of Jacoby 1, we managed to detect the $H\alpha$ emission from the PN (see Figure 4.8).

- *TK 1* (J2000 RA: 08 27 05.52, DEC: 31 30 08.10) is catalogued as a likely PN in HASH catalogue (lHASH PN). Its position in our colour-colour diagrams (brown circle) is very close to Jacoby 1 suggesting similar spectral characteristics. The size of the nebula of TK 1 is also very large, up to 15 arcmin (Tweedy & Kwitter, 1996), thus no $H\alpha$ emission is expected. Its photo-spectrum is identical to that of Jacoby 1 (top-right panel of Figure 4.7), with a blue continuum stronger than the red one and no $H\alpha$ excess. All these –including the fact that we did not find its corresponding extended nebula– suggest that the recovered source is a WD star, in agreement with Rebassa-Mansergas et al. (2015).
- *Kn J1857.7+3931* (J2000 RA: 18 57 42.24, 39 31 00.13) is classified as a possible PN (pHASH PN). It shares the same position in the diagnostic diagrams (orange circle with a small errorbar) as well as the akin photo-spectra of Jacoby 1 and TK 1 (see Figure 4.7). Though we looked for any extended nebula it was not detected. We argue that *Kn J1857.7+3931* is also a WD star.

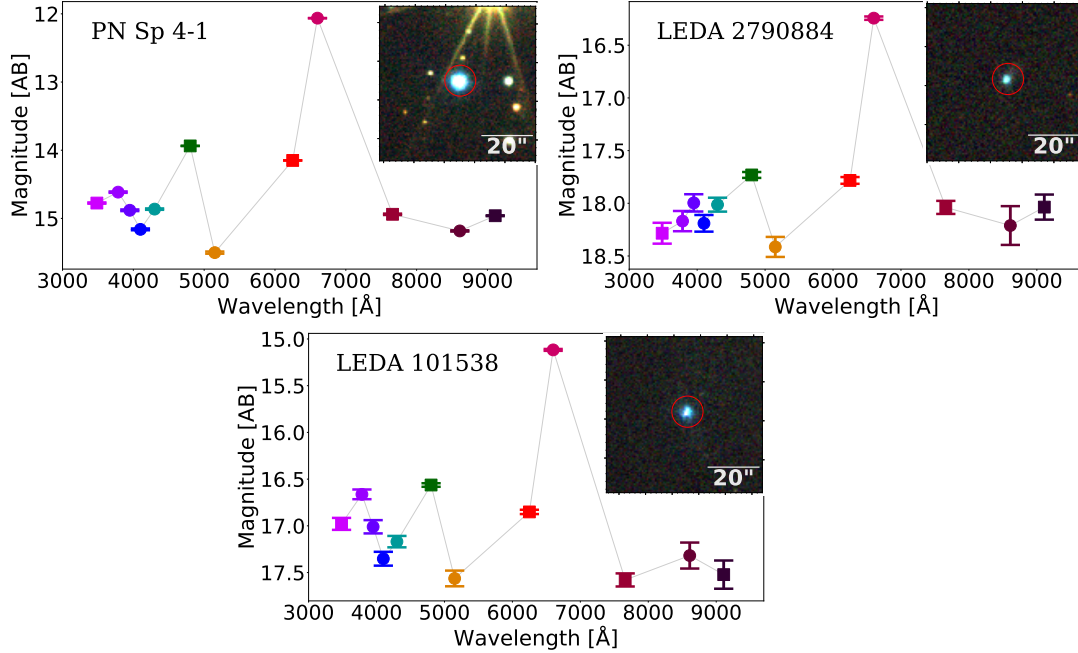


FIGURE 4.6: J-PLUS photo-spectra and corresponding images of the (*upper left*) disk Galactic PN Sp 4-1, (*upper right*) H II galaxy LEDA 2790884 and (*lower center*) H II galaxy LEDA 101538. These objects were recovered by applying the colour-colour diagrams. The inner panels show the 3RGB colour (*g*, *r* and *i*) J-PLUS images for each source.

- *KnPa J1848.6+4151* (J2000 RA: 18 48 38.36, DEC: 41 51 02.52) is also catalogued as a pHASH PN. This object is located a little far from the other HASH objects in our colour-colour diagrams (orange circle with large error bar), and again there is no indication of any H α excess. *KnPa J1848.6+4151* lies in the regime of SDSS SFG and QSOs. The photo-spectrum and image of this source are displayed in the bottom-right panel of Figure 4.7. It is a very faint object with $r \sim 19.5$. Its estimated angular size is of $\sim 10.3''$ indicating an extended source. *KnPa J1848.6+4151* is very likely a galaxy (e.g. Figure 16 of Cenarro et al., 2019) and less probably a genuine PN. In the SDSS DR12 (Alam et al., 2015) and the Kepler-INT DR1 catalogues (Greiss et al., 2012), it is classified as a non-stellar source, probably a galaxy.

S-PLUS

- *Fr 2-21* (J2000 RA: 21 26 21.17, DEC: 00 58 34.22), also called PHL 4 and previously identified as a hot subdwarf (Kilkenny, 1984), in addition of being a pHASH PN. It is located very close to the other HASH objects in the diagnostic diagrams, suggesting a WD nature for this source (Figure 4.9). By combining J0660, *r* and *i* images no extended nebula was found.

Table 4.3 lists the J-PLUS and S-PLUS magnitudes of these five sources as well as their SDSS DR12 (Alam et al., 2015) and Pan-STARRS DR1 (Chambers & Pan-STARRS Team, 2016) magnitudes, for a direct comparison. The average difference

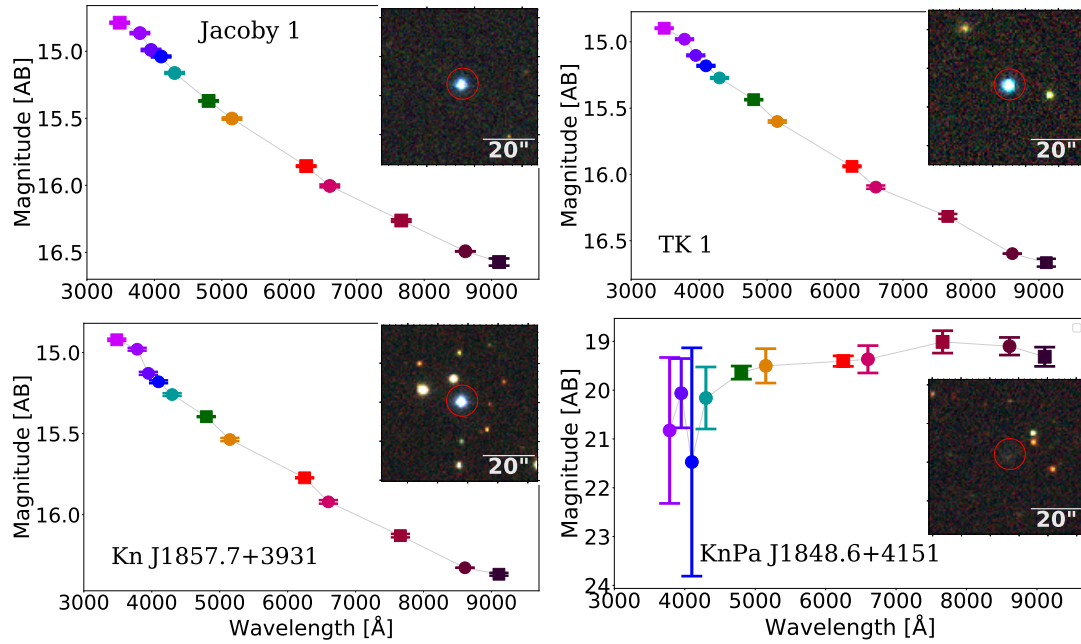


FIGURE 4.7: J-PLUS photo-spectra and corresponding composite images of the HASH PNe, as in Figure 4.6: (*upper left*) tHASH PN Jacoby 1; (*upper right*) lHASH PN TK 1; (*lower left*) pHASH PNe Kn J1857.7+3931; (*lower right*) KnPa J1848.6+4151 of the HASH PN catalog.

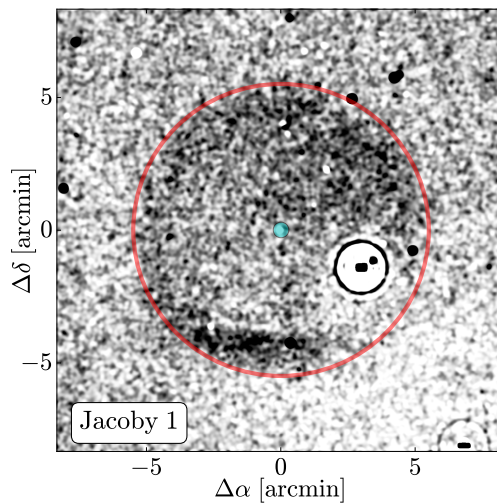


FIGURE 4.8: Composite $-J0660, r,$ and $i-$ image of Jacoby 1 taken from JAST/T80. Extended PN is clearly visible, as indicated by the red circle. The $H\alpha$ emission is detected by applying a Gaussian smoothing filter of 10 pixels. Credits to Rafael Logroño and Carlos López Sanjuan, members of the J-PLUS collaboration.

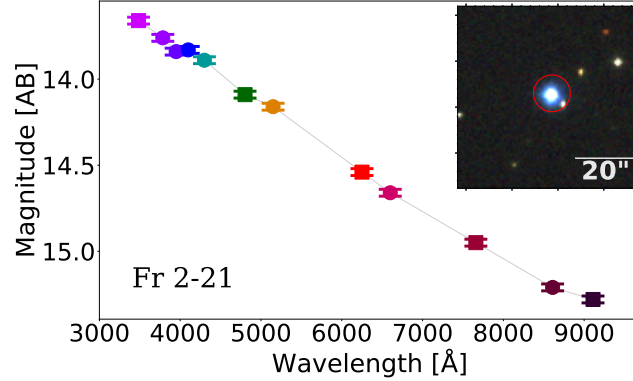


FIGURE 4.9: S-PLUS photo-spectrum of Fr 2-21 and its corresponding 3RGB image. This object is classified as possible PN in HASH catalog.

between the J-PLUS and SDSS photometry is smaller than 0.07 mag. The S-PLUS-SDSS difference of Fr 2-21 is found to be slightly higher, about 0.116 mag. Only the very faint KnPa J1848.6+4151 shows significant difference between the two surveys, up to 0.375 mag. As for the difference between the J-PLUS and Pan-STARRS photometry, two of the objects have very low difference of 0.02 mag and 0.12 mag, while one shows a difference up to 2 mag. The S-PLUS source also shows a small average difference with the Pan-STARRS photometry of 0.06 mag, almost twice smaller than the difference with SDSS photometry. Finally, it is worth noticing that the difference between the SDSS and Pan-STARRS photometry is between 0.0525 and 0.07, while KnPa J1848.6+4151 is again the most discrepant among the sources (1.97). Overall, we find a reasonable match of the J-PLUS and S-PLUS either with the SDSS or the Pan-STARRS photometry. This assures that the no recovery of these possible PNe by our colour-colour criteria is not associated with the (bad) photometry of the sources in our surveys.

4.3 Machine learning: approach improving the classification

This section describes the validation procedures of machine learning techniques (PCA and LDA). The objects identified with our colour criteria and the HASH sources in the J- and S-PLUS catalogs were used for that. After training the algorithms, the class those sources belong to was predicted.

4.3.1 Handling imbalanced samples in machine learning techniques

PCA and LDA are data-dependent algorithms. In the case of imbalance training samples (significant different population of classes of objects; see Akras et al., 2019b), the final classification of source may be biased in favor of the more populated classes. Naseriparsa & Mansour Riahi Kashani (2013) have shown that balancing the data, for instance on lung-cancer dataset, after to reduce the dimensions using

| Object | Jacoby 1 ^a | TK 1 ^a | Kn J1857.7+3931 ^a | KnPa J1848.6+4151 ^a | Fr 2-21 ^b |
|---|-----------------------|-------------------|---------------------------------|-----------------------------------|----------------------|
| <i>J-PLUS DR1 and S-PLUS DR1 photometry</i> | | | | | |
| Kron radius (") | 3.5 | 3.5 | 3.5 | 3.8 | — |
| <i>u</i> | 14.79 ± 0.007 | 14.90 ± 0.006 | 14.92 ± 0.007 | — | 13.66 ± 0.02 |
| <i>J0378</i> | 14.86 ± 0.007 | 14.98 ± 0.006 | 14.98 ± 0.009 | 20.83 ± 1.495 | 13.76 ± 0.02 |
| <i>J0395</i> | 14.99 ± 0.008 | 15.10 ± 0.007 | 15.13 ± 0.009 | 20.06 ± 0.710 | 13.84 ± 0.02 |
| <i>J0410</i> | 15.04 ± 0.006 | 15.18 ± 0.007 | 15.18 ± 0.009 | 21.47 ± 2.339 | 13.83 ± 0.02 |
| <i>J0430</i> | 15.16 ± 0.007 | 15.27 ± 0.007 | 15.26 ± 0.009 | 20.16 ± 0.635 | 13.89 ± 0.02 |
| <i>g</i> | 15.37 ± 0.005 | 15.44 ± 0.005 | 15.40 ± 0.003 | 19.64 ± 0.134 | 14.09 ± 0.02 |
| <i>J0515</i> | 15.50 ± 0.008 | 15.60 ± 0.009 | 15.54 ± 0.010 | 19.50 ± 0.352 | 14.16 ± 0.02 |
| <i>r</i> | 15.86 ± 0.005 | 15.94 ± 0.007 | 15.77 ± 0.003 | 19.40 ± 0.108 | 14.54 ± 0.02 |
| <i>J0660</i> | 16.00 ± 0.010 | 16.10 ± 0.013 | 15.92 ± 0.011 | 19.37 ± 0.280 | 14.66 ± 0.02 |
| <i>i</i> | 16.26 ± 0.009 | 16.32 ± 0.018 | 16.13 ± 0.011 | 19.01 ± 0.229 | 14.95 ± 0.02 |
| <i>J0861</i> | 16.49 ± 0.020 | 16.60 ± 0.020 | 16.33 ± 0.009 | 19.10 ± 0.181 | 15.21 ± 0.02 |
| <i>z</i> | 16.57 ± 0.027 | 16.67 ± 0.029 | 16.37 ± 0.009 | 19.32 ± 0.197 | 15.28 ± 0.02 |
| <i>SDSS DR12 photometry</i> | | | | | |
| <i>u</i> | 14.73 ± 0.003 | 14.91 ± 0.004 | 15.16 ± 0.004 | 21.08 ± 0.307 | 13.54 ± 0.003 |
| <i>g</i> | 15.22 ± 0.003 | 15.35 ± 0.004 | 15.43 ± 0.004 | 19.91 ± 0.038 | 13.95 ± 0.003 |
| <i>r</i> | 15.84 ± 0.003 | 15.94 ± 0.004 | 15.80 ± 0.004 | 19.57 ± 0.042 | 14.47 ± 0.003 |
| <i>i</i> | 16.26 ± 0.004 | 16.30 ± 0.005 | 16.13 ± 0.004 | 19.42 ± 0.061 | 14.84 ± 0.003 |
| <i>z</i> | 16.65 ± 0.009 | 16.69 ± 0.009 | 16.41 ± 0.009 | 19.93 ± 0.382 | 15.14 ± 0.005 |
| <i>Pan-STARRS DR1 photometry</i> | | | | | |
| <i>g</i> | 15.35 ± 0.003 | 15.46 ± 0.005 | 15.57 ± 0.008 | 21.74 ± 0.086 | 14.06 ± 0.005 |
| <i>r</i> | 15.85 ± 0.007 | 15.95 ± 0.002 | 15.90 ± 0.007 | 21.53 ± 0.088 | 14.52 ± 0.004 |
| <i>i</i> | 16.29 ± 0.003 | 16.35 ± 0.002 | 16.19 ± 0.004 | 21.54 ± 0.076 | 14.88 ± 0.002 |
| <i>z</i> | 16.60 ± 0.003 | 16.65 ± 0.003 | 16.49 ± 0.008 | 21.04 ± 0.158 | 15.16 ± 0.002 |
| <i>y</i> | 16.81 ± 0.011 | 16.83 ± 0.005 | 16.63 ± 0.011 | — | 15.36 ± 0.003 |

Kron radius is elliptical Kron apertures used to compute the auto magnitudes.

^aObjects observed by J-PLUS.

^bObject observed by S-PLUS.

TABLE 4.3: J-PLUS and S-PLUS, SDSS and Pan-STARRS photometry for the true, likely and possible PNe from HASH catalog.

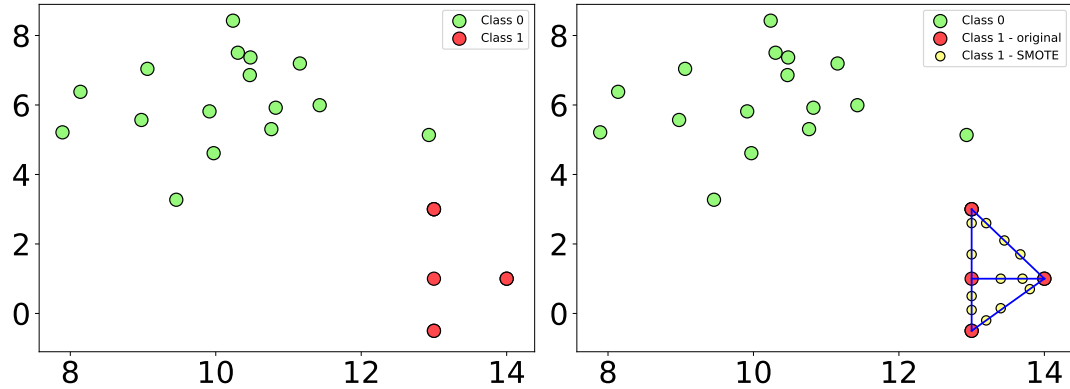


FIGURE 4.10: Schematic representation of how the SMOTE algorithm works. The minority classes are re-sampled creating artificial data from the original data by connecting each point of the minority samples.

PCA, improve the effectiveness of the method used to classify, across four evaluation metrics: overall accuracy, false positive rate, precision and recall. On the other hand, Xie & Qiu (2007) demonstrated that theoretically the imbalanced data sets have a negative effect on the performance of LDA. This theoretical analysis is confirmed by the experimental results. Several sampling methods were applied to imbalanced data sets and it was found that the performance of LDA on the new balanced data sets was improved.

The training data sets used in this thesis are highly imbalanced, 3,700 PNe (including modeled and observed), 25 SySt, 25 H II regions, 48 YSOs, 159 CV, 270 WDs, 1,283 SFGs and 600 QSOs.

There are several sampling methods to deal with this problem: oversampling, synthetic minority oversampling technique (SMOTE), cost sensitive learning (CSL) and others. In this thesis, the SMOTE method, was selected (see, Naseriparsa & Mansour Riahi Kashani, 2013; Ke et al., 2019; Pura Hartati et al., 2018).

SMOTE

SMOTE algorithm (Chawla et al., 2002) creates synthetic data based on the similarities of the minority samples (left panel of Figure 4.10) and proceeds by connecting the points of the minority class with line segment and then places artificial data points on these lines (right panel of Figure 4.10). It generates a random set of minority class observations to shift the classifier learning bias towards minority class. SMOTE algorithm follows the next steps:

- Choose a minority class input vector.
- Find its k nearest neighbors.
- Choose one of these neighbors and place a synthetic point anywhere on the line joining the point under consideration and its chosen neighbor.
- Repeat the steps until the dataset is balanced.

4.3.2 Principal component analysis

PCA is an algorithm to reduce the dimensionality of a sample and highlight the similarities and differences among the different class.

For the first step, PCA is applied on J-PLUS or S-PLUS synthetic photometry (this was described in the previous chapter), then reducing the dimensionality from 12 to 3 for J/S-PLUS. Thus, on the second step, SMOTE resampling method is carried out on the PC dataset. SMOTE was implemented in Python using the IMBLEARN library. To quantify the classification of each source, its probability to belong to each class was derived using the logistic regression model.

Logistic regression (Pregibon, 1982) is a kind of regression analysis or statistical method used for predicting binary classes. It is an extension of the linear regression model for classification problems. It uses a *logistic function* to model a binary dependent variable, although many more complex extensions exist. Mathematically, a binary logistic model has a dependent variable with two possible values, pass/fail, which is represented by an indicator variable, with values “0” and “1” (Cramer, 2004).

Let us, assume that “x” is the input feature and “y” the output, which can be either “0” or “1”. The probability that the output is “1” given the input feature “x” can be represented as: $P(y = 1|x)$. In case of linear regression, the probability $p(X)$ is defined as $\beta_0 + \beta_1 X$ and the probability can take either positive or negative values. On the other hand, in the case of logistic regression we have:

$$\log\left(\frac{p(X)}{1-p(X)}\right) = \beta_0 + \beta_1 X \quad (4.1)$$

where, the left side is called the logit or log-odds function, and $p(x)/(1-p(x))$ is called odds.

If we take the inverse of the above function, we get:

$$p(X) = \frac{e^{\beta_0 + \beta_1 X}}{1 + e^{\beta_0 + \beta_1 X}} \quad (4.2)$$

this is known as the Sigmoid function (Mitchell, 1997) and it gives probabilities from 0 to 1.

For datasets that involve more than two classes problem, multinomial logistic regression is used. As in PCA and LDA algorithm, multinomial logistic regression was carried out by implementing the Python SKLEARN library.

Table 4.4 shows the results after applying the PCA and logistic regression algorithms to our dataset. It has the probability of each object to be classified as PN, SySt, CV, H II region, QSO, YSO, WD and SFG. The objects 26063-6129 (PN candidate), PN Sp 4-1, LEDA 2790884 and LEDA 101538 have probabilities 36%, 82%, 39% and 44% of being PNe. All the HASH sources have $\sim 50 - 62\%$ probabilities to be WDs. Remember that J- and S-PLUS only detect the central WDs of the HASH objects. These results show that PCA makes a good job discriminating

| <i>PCA predicting class</i> | | | | | | | | | |
|-----------------------------|-------------|------|------|------|-------|------|------|------|------|
| Object | Real class | PN | SySt | CV | H IIr | QSO | YSO | WD | SFG |
| 26063-6129 ^a | H II region | 0.36 | 0.00 | 0.10 | 0.00 | 0.04 | 0.00 | 0.47 | 0.03 |
| PN Sp 4-1 | PN | 0.82 | 0.00 | 0.03 | 0.00 | 0.00 | 0.00 | 0.14 | 0.01 |
| LEDA 2790884 | H II galaxy | 0.39 | 0.01 | 0.09 | 0.00 | 0.07 | 0.00 | 0.38 | 0.06 |
| LEDA 101538 | H II galaxy | 0.44 | 0.00 | 0.08 | 0.00 | 0.02 | 0.00 | 0.44 | 0.02 |
| Jacoby 1 | tHASH PN | 0.23 | 0.00 | 0.15 | 0.00 | 0.00 | 0.00 | 0.62 | 0.01 |
| TK 1 | lHASH PN | 0.22 | 0.00 | 0.15 | 0.00 | 0.00 | 0.00 | 0.61 | 0.01 |
| Kn J1857.7+3931 | pHASH PN | 0.23 | 0.00 | 0.20 | 0.00 | 0.00 | 0.00 | 0.55 | 0.01 |
| Fr 2-21 | pHASH PN | 0.35 | 0.00 | 0.17 | 0.00 | 0.00 | 0.00 | 0.48 | 0.01 |

^aID in J-PLUS DR1.

TABLE 4.4: The probability of each object to be classified as PN, SySt, CV, H II region (H IIr), QSO, YSO, WD and SFG.

different classes of objects. The proper classification of PNe and H II regions/galaxies is better using this method than the colour criteria, but, it still provides poor classification.

4.3.3 Linear discriminant analysis

LDA is a supervised algorithm and provides the class to which an observation belongs, based on the classes of objects used to train the model. For this, previously labeled classes of known objects have settled down (see above chapter). These predictions are made by estimating the probability that objects belong to a certain class. The class with the highest probability is the resultant class of each candidate.

In LDA, the estimation of the probabilities is made using the Bayes Theorem (Bayes, 1763). In probability theory, the Bayes' rule describes the probability of an event, based on prior knowledge of conditions that might be related to the event. This theorem can be used to estimate the probability of the output class (k) given the input (x) using the probability of each class and the probability of presence of point x in class k :

$$P(Y = k|X = x) = \frac{P(X = x|Y = k)P(Y = k)}{P(X = x)} \quad (4.3)$$

rewriting this equation:

$$P(Y = k|X = x) = \frac{\pi_k f_k(x)}{P(X = x)} \quad (4.4)$$

where π_k is the overall probability that an observation is associated with the k th class, it is estimated by the fraction of training samples of class k , and $f_k(x)$ denotes the density function (multivariate normal distribution) of X for an observation that comes from the k th class. This means that $f_k(x)$ is large if the probability that an observation of the k th class has $X = x$.

By running SMOTE² and LDA to the synthetic photometry of the different

²SMOTE was applied before to run LDA. Unlike PCA, it is a classifier algorithm.

| <i>LDA predicting class</i> | | | | | | | | | |
|-----------------------------|-------------|------|------|------|-------|------|------|------|------|
| Object | Real class | PN | SySt | CV | H IIr | QSO | YSO | WD | SFG |
| 26063-6129 ^a | H II region | 0.00 | 0.00 | 0.32 | 0.03 | 0.08 | 0.00 | 0.29 | 0.27 |
| PN Sp 4-1 | PN | 1.00 | 0.00 | 0.00 | 0.00 | 0.00 | 0.00 | 0.00 | 0.00 |
| LEDA 2790884 | H II galaxy | 0.01 | 0.00 | 0.31 | 0.04 | 0.03 | 0.00 | 0.30 | 0.30 |
| LEDA 101538 | H II galaxy | 0.01 | 0.00 | 0.41 | 0.05 | 0.05 | 0.00 | 0.27 | 0.22 |
| Jacoby 1 | tHASH PN | 0.00 | 0.00 | 0.14 | 0.00 | 0.02 | 0.00 | 0.82 | 0.02 |
| TK 1 | lHASH PN | 0.00 | 0.00 | 0.14 | 0.00 | 0.02 | 0.00 | 0.82 | 0.02 |
| Kn J1857.7+3931 | pHASH PN | 0.00 | 0.00 | 0.20 | 0.00 | 0.02 | 0.00 | 0.74 | 0.04 |
| Fr 2-21 | pHASH PN | 0.00 | 0.00 | 0.15 | 0.00 | 0.01 | 0.00 | 0.82 | 0.02 |

^aID in J-PLUS DR1.

TABLE 4.5: The probability of each object be classified as PN, SySt, CV, H II region (H IIr), QSO, YSO, WD and SFG.

classes of objects (namely, PNe, SySt, H II regions, QSOs, SFGs, YSOs and WDs) as the input classes that train the algorithm, it is predicted the class of each object. Table 4.5 shows the results (probabilities) for the same objects of Table 4.4. The object 26063-6129 has a probability of 32% to be a CV. It also has 29% and 27% probabilities to be WDs and SFGs, respectively. PN Sp 4-1 has 100% probability to be PN. LEDA 2790884 has 31%, 30% and 30% probabilities to be classified as CV, WD and SFG, respectively. LEDA 101538 has 41%, 27% and 22% probability to be a CV, WD and SFG, respectively. All the HASH sources exhibit an 82% probability being a WD, except Kn J1857.7+3931 whose value is 74%. Therefore, even not classifying all objects in their true classes, LDA clearly allows differentiating PNe from H II galaxies. If instead of the colour criteria this method had been used in advance, the spectroscopic follow-up of the PN candidate had been avoided.

Chapter 5

Discussions, conclusions and perspectives

This dissertation has explored photometric techniques to identify PNe and SySt in the Galactic halo, by using the new surveys: J-PLUS, S-PLUS and J-PAS. The results obtained by applying these techniques to the J-PLUS and S-PLUS first data releases were also presented. We discuss and summarize the main conclusions and perspectives of this work in the following sections.

5.1 Discussion

5.1.1 Selection of halo PNe and SySt

The results described in previous chapter made clear the potential of the data provided by J-PLUS and S-PLUS to explore the population of planetary nebulae, and hopefully of symbiotic stars, in the Galactic halo. The developed photometric tools to identify strong emission-line sources, as it is the case for PNe and SySt, were applied to the very limited area ($\sim 1,190 \text{ deg}^2$) surveyed up to now –in both projects J-PLUS and S-PLUS– with very promising results.

The ability of photometrically distinguish PNe and H II regions is strongly hampered by the similarities between the low-excitation PNe and H II regions. The optical spectroscopic follow-up of the first PN candidate identified in these surveys revealed it to be an H II region located in the UGC 5271 galaxy, and confirms the difficulty to disentangle PNe and H II regions especially compact extragalactic H II regions. This is because none of the five colour-colour diagrams that comprise our selection criteria actually completely isolates these two types of sources. Moreover, our selection criteria were, on the one hand, very successful by avoiding all the other strong emission-line emitters present in the fields, which means that J-PLUS and S-PLUS can really do a good job in terms of searching for PNe and at the same time minimizing the list of spectroscopic follow-up candidates.

5.1.2 Expected number of halo planetary nebulae

PNe comprise an old stellar populations of galaxies, since the majority of them have progenitors between 1.5 and 2.0 M_{\odot} , which correspond to a mean age of $\simeq 1.5$ Gyr (Douglas et al., 2002), assuming an initial mass function (IMF) that produces more low-mass stars than high-mass ones. Their total number depends, therefore, on the stellar population of the galaxy itself. For example, Buzzoni et al. (2006) showed that the reddest elliptical galaxies are poorer in PNe (per unit galaxy luminosity) than spiral galaxies. The PNe luminosity function (PNLF) is universal (Ciardullo et al., 2002) and well described by a double exponential, with an absolute magnitude cut-off $M^*=-4.47$ (Ciardullo et al., 1989)¹. This translates to an apparent magnitude of $m_{5007} = 10.55$ at the distance of 10 kpc, which we use as reference radius to integrate the PNLF as well as to an apparent magnitude of $m_{5007} = 13.5$ at the distance of 40 kpc, which is the radius of the inner halo of the Milky Way (MW; Bland-Hawthorn & Gerhard, 2016).

In order to estimate the number of PNe that we expect to find in the MW halo using the J-PLUS and S-PLUS projects we need to calculate: (i) the number of PNe we expect to find given the survey magnitude limit; (ii) the number of PNe that might get lost due to the contamination/crowding from other objects; and, finally, (iii) the number of PNe that we expect to find given the underlying stellar population of the MW halo.

We thus run a set of simulations, by populating images with the typical J-PLUS and S-PLUS image noise with simulated PNe that mimic the properties of 3 known hPNe (H 4-1, PNG135.9+55.9 and DdDm 1). In order to investigate the completeness limit, we vary the brightness of the simulated PNe from their real brightness to 5 magnitudes fainter, keeping their radii fixed. The known hPNe, for which spectra (Howard et al., 1997; Kwitter & Henry, 1998) are available for us are listed in Table 5.1, together with their fundamental properties. H 4-1 and PNG135.9+55.9 were observed with JAST/T80 (Cenarro et al., 2014) and their radii were obtained by fitting a MOFFAT gaussian function in the g -band images. The radius of DdDm 1 comes from the literature (Howard et al., 1997). We transformed the MOFFAT radius from arcsecs into pixels, by adopting the standard J-PLUS pixel scale (nearly $0.5''/\text{pix}$). We reach 99% completeness till $m_{5007} = 21.8$ for DdDm 1 and PNG 135.9+55.9; see Figure 5.1 for examples of the variation of the recovered number of PNe with magnitude (see also Cortesi et al., 2013). For H 4-1, the limiting magnitude to recover 99% of the objects is $m_{5007} = 21.2$.

We also performed the same test on real J-PLUS images, in order to check how many objects we might loose due to crowding, for instance. We found that we can detect 98% of the objects down to a magnitude of $m_{g,\text{lim}} = 21.2$, which translates into $m_{5007,\text{lim}} = m_{g,\text{lim}} - 0.75 = 20.45$ (Arnaboldi et al., 2002). This estimation

¹In Ciardullo et al. (2002) it is estimated $M^*=-4.51$. In here we use $M^*=-4.47$, by following Buzzoni et al. (2006). Also note that Ciardullo et al. (2002) show that the absolute magnitude of the PNLF cutoff is fainter in small and low-metallicity systems, but the trend is well modelled by the theoretical relation of Dopita, Jacoby, & Vassiliadis (1992)

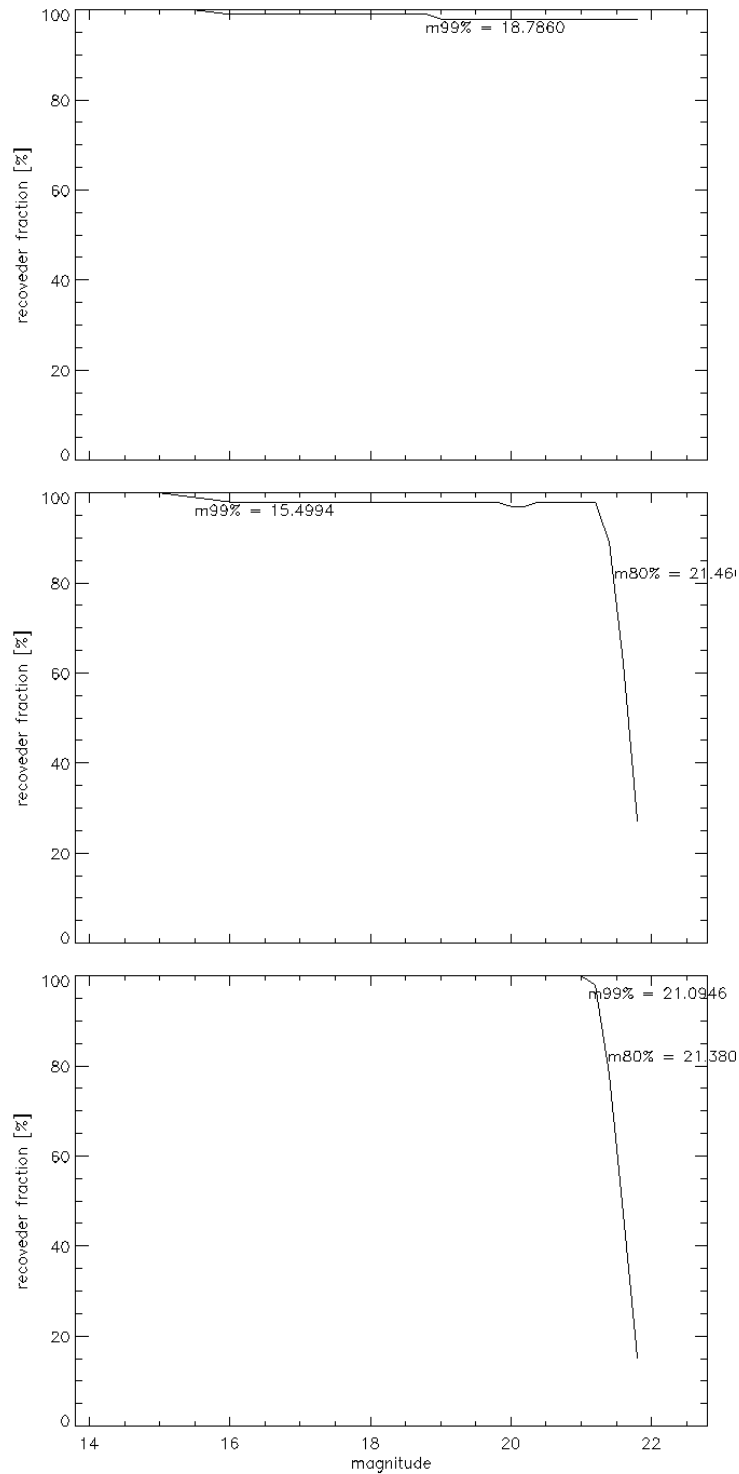


FIGURE 5.1: Recovered number of point like sources as a function of magnitude for (*top*) DdDm 1, (*medium*) H 4-1 and PNG 135.9+55.9 (*bottom*). The simulated PNe are added on an artificial image that mimic the sky and CCD noise, the recovered number decreases for fainter objects, see text for further details. Credits Arianna Cortesi, a member of the J- and S-PLUS collaborations and close collaborator in this project.

| PN | $m_{AB}(g)$ | $m(5007)$ | radius ($''$) |
|---------------|-------------|-----------|-----------------|
| H 4-1 | 15.61 | 14.86 | 4.6 |
| PNG135.9+55.9 | 17.74 | 16.99 | 2.6 |
| DdDm 1 | 13.85 | 13.10 | 1.0 |

TABLE 5.1: Fundamental properties of three known hPNe, on which PN names, g and [O III] magnitudes and PN radii are shown.

suggests that within these surveys we will be able to recover 98% the PNe in the first 6.95 mag interval of the PNLF at 40 kpc. This effect might vary depending on the galactic coordinates, since the number of expected hPNe, as much as of halo stars, depends on the Galactic coordinates (l, b) . In fact, López-Sanjuan et al. (2019) performed a morphological star/galaxy classification of the J-PLUS data and found that the number counts decreases with galactic latitude (b) as we move away from the Galactic plane. Moreover, higher latitude tiles seem to present a double power-law shape. This can be interpreted as the dominance of halo stars in these fields. Therefore, far away from the Galactic plane, where we expect to find more hPNe, our quest would be made easier by the lower number of disk/bulge stars.

We are now left with the not trivial question: how many PNe we expect to find in the MW halo, or in general in the halo of a spiral galaxy? In fact, to calculate exactly the number of PNe in the MW halo we should know its composition and shape. Such a quest eludes from the scope of this thesis, and, on the contrary, the recovered catalog of MW-halo-PNe, resulting from this work, could be used at the purpose of defining the shape and properties of the MW halo. We performed a simple calculation, by integrating the PNLF from the value of M_* at 10 kpc, till the estimated completeness limit $m_{5007,lim}$.

$$N(m) = \int_{m_*}^{m_{lim}} a(0)e^{0.307m}(1 - e^{3(m_*-m)})dm, \quad (5.1)$$

where the parameter $a(0)$ determines the number of PNe we expect to find and varies according to the stellar population of the galaxy. In order to derive the number of PNe in a galaxy we introduced the α parameter (Jacoby, 1980) that indicates the specific frequency of PNe, i.e. the constant of proportionality between the PNe number and the stellar luminosity. The value of $\log \alpha$ varies from $\log \alpha = -5.99$ for Leo A to $\log \alpha = -7.13$ for M33 (Buzzoni et al., 2006). Assuming that the halo of a galaxy is an extension of its bulge, and therefore that their stellar populations are similar, we could use the value for the bulge of M31, $\log \alpha = -6.94$ as a proxy for the MW halo. Alternatively we could assume that the halo of the MW is formed by a metal poor population such as in the SMC, where $\log \alpha = -6.67$. We recover the value of $a(0)$ for the SMC and M31 bulge by integrating Eq. 5.1 within 8mag from the PNLF bright-end tail at 10 kpc, in order to achieve the PN population size inferred according to two different extrapolation methods: 1) standard empirical PNLF from Jacoby (1989), corrected for metallicity (Dopita et al., 1992), for the

| α origin | $\log \alpha$ | # Total | # J-PLUS | # S-PLUS | #(J-PLUS DR1) |
|-----------------|---------------|-----------------------|-------------------|-------------------|----------------|
| Case 1 | -6.94 | $1,766^{+181}_{-189}$ | 353^{+37}_{-39} | 385^{+35}_{-37} | 42^{+4}_{-5} |
| Case 2 | -6.67 | 312^{+41}_{-39} | 62 ± 8 | 68 ± 8 | 7 ± 1 |

TABLE 5.2: Expected number of hPNe per survey for two case. Case 1 and Case 2, equivalent to the M31_{bulge} and SMC metallicities, respectively.

M31 bulge and 2) using the Jacoby (2006) observed SMC PNLF and correcting for metallicity as for the standard case, for the SMC (see Table 4 in Buzzoni et al. (2006)).

Table 5.2 summarizes the expected (total) number of PNe in the MW and the expected numbers to be detected by J-PLUS and S-PLUS at the completion of the surveys (8,500 deg² and 9,000 deg²) out of the 41,253 deg² of the celestial sphere, respectively, for different α values. We, therefore, estimate we shall observe between 7 ± 1 to 42^{+4}_{-5} PNe in the halo of the MW in the J-PLUS DR1.

Finally, the numbers provided in Table 5.2 are purely indicative: in fact, we are here assuming that the PNe are homogeneously distributed on the sky while they might be concentrated in regions that trace the accretion of dwarf satellites. It is in any case interesting seeing how, just by determining the number of PNe we will recover with J-PLUS and S-PLUS, we will be able to distinguish between possible formation scenarios of the MW halo.

5.1.3 Expected number of halo symbiotic stars

Given that there is not a luminosity function for SySt, we can not use the same methodology used for PNe to estimate the expected number of SySt in the halo of the Milky Way. Instead, in this section we present the previously estimated number of SySt, thus roughly indicating their expected number in the S- and J-PLUS areas. We perform this task in four different ways.

- By considering the 40 S-type SySt within 1.0 kpc, data from Freeman (1987) and Gilmore et al. (1989), for the density gradient and the dimension of the thick disk and bulge (Munari & Renzini, 1992).
- By estimating the formation rate of RG + WD symbiotic system:

$$r_{ss} = r_{\text{bin}} * f_1 * f_2 * f_3$$

where r_{bin} is the binary formation rate, f_1 is the fraction of binaries with orbital period, $P_{\text{orb}} = 1 - 10$ yr, f_2 is the fraction of binary that survive to the first tidal mass-loss phase and f_3 is the fraction of binaries with the secondaries massive enough to evolve to red giant dimensions in the age of the Galaxy. The total number of symbiotic stars follows the relation, $N_{ss} = r_{ss} t_{ss}$, where t_{ss} is the lifetime of the SySt phase (Kenyon et al., 1993).

- By obtaining a rough estimate of the red giant population in each galaxy can be computed from the K and B magnitudes from LEDA Lyon-Meudon Extra-

| Reference | # SySt (all galaxy) | # Total (Halo) | # J-PLUS | # S-PLUS |
|-------------------------|---------------------|----------------|----------|----------|
| Munari & Renzini (1992) | 3×10^5 | 27,273 | 5,619 | 5,950 |
| Kenyon et al. (1993) | 3×10^4 | 2,727 | 562 | 595 |
| Magrini et al. (2003) | 4×10^5 | 36,364 | 7,493 | 7,933 |
| Lü et al. (2006) | 1,200 - 15,000 | 109 - 1,363 | 22 - 281 | 24 - 297 |

TABLE 5.3: Expected number of SySt per model and per survey.

galactic Database², the distances (Van den Bergh, 2000) and the contribution in near infrared light of young stars (Chiosi & Vallenari, 1996). A typical luminosity of $100 L_{\odot}$ for a cool giant is taken in computing the number of red giants per galaxy. The number of symbiotic stars can be taken to be 0.5% of the total number of red giants plus AGB stars (Magrini et al., 2003).

- By considering the galactic birth rate of SySt from the WD accretors in the Galaxy, by means of a population synthesis code (Lü et al., 2006).

Table 5.3 summarizes these expected numbers of SySt from the four methods. In the Galactic plane the thick disk outnumber the halo by a factor of 10 to 20 (Freeman, 1987). If we suppose that the population of symbiotic meets this same relation, from which it is consider that the population of SySt of the disk is 10 times that of the halo, we can obtain the number of SySt in the Galactic halo and in the total areas covered for J-PLUS and S-PLUS, $\sim 8,500 \text{ deg}^2$ and $\sim 9,000 \text{ deg}^2$, respectively (see Table 5.3). For instance, from the Lü et al. (2006) results, it is expected between 22 - 281 SySt in J-PLUS and 24 - 297 in S-PLUS. Even though these estimations are not all robust ones, they give us an idea about the population of SySt in the Galactic halo.

5.1.4 Compact versus extended PNe

The sizes of the 14 PNe in the Galactic halo go from 1.0 to more than 50 arcsec (Howard et al., 1997). Even though, our tools were developed to search for compact PNe within the photometric catalogs of J-PLUS and S-PLUS using apertures of 6 and 3 arcsec, respectively. In fact, any search for PNe in photometric surveys seems to be complete for those with angular sizes smaller than 6 arcsec (Viironen et al., 2009b; Akras et al., 2019c).

The larger planetary nebulae with lower density and corresponding lower surface brightness are more difficult to discover. These objects are essentially undetectable by the survey methods. The cross-matching between the HASH and J-PLUS/S-PLUS catalogs made this point very clear. The magnitudes of the resultant PNe matches correspond only to the photometry of the central WDs, as it can be seen from their photo-spectra, which return no nebular $H\alpha$ emission.

²<http://leda.univ-lyon1.fr/> and Fioc & Rocca-Volmerange (1999).

As in the case of the IPHAS, with the present surveys a parallel work needs to be done in order to find extended PNe (Sabin et al., 2014). It is necessary to bin the images in order to increase the surface brightness of extended nebula and make their recovery feasible by visually inspecting one by one of the surveys' fields. It will only be worth to persecute such an exercise at a later stage of the surveys' development.

An additional important issue is the limit magnitude of the surveys, which hampers the detection of very extended sources. The J-PAS survey (which will cover the same sky-area as the J-PLUS survey) will be more efficient for the discovery of extended PNe due to the larger collective area of the telescope (2.5-m instead of the 0.80-m of those here discussed) as well as deeper images.

With the method developed in this work we recovered one PN. Four objects (identified as true, likely or probable) PNe in the HASH catalogue are also present in the J-PLUS and S-PLUS catalogues, but they were not recovered due to their faint and diffuse H α emission. So, in total we have 5 potential PNe in the combined area of the J-PLUS DR1 + S-PLUS DR1 data releases. Is this number reasonable?

If we assume that the MW halo has a metallicity typical of dwarf galaxies, in the J-PLUS DR1 + S-PLUS DR1, we have estimated that we shall find 7 ± 1 PNe. This estimation, which in itself is purely indicative, is more or less in agreement with the number of PNe recovered in the DR1 of these surveys.

5.2 Conclusions

Considering the photometric systems of two twin imaging surveys, and the convolution of the spectra of different types of strong emission-lines sources, we used the synthetic photometry to select the best combination of filters to construct colour-colour diagrams from the multi-band filter systems of J-PLUS and S-PLUS. We reproduced the IPHAS equivalent and constructed four new diagnostic colour-colour diagrams to separate hPNe and SySt from cataclysmic variables, QSOs, extragalactic H II regions, star forming galaxies and young stellar objects, by using the J-PLUS and S-PLUS synthetic photometry. We have found that the two surveys (J-PLUS and S-PLUS) are not completely successful at discriminating low-excitation PNe from H II regions and SySt from H II and YSOs.

There is a high probability that a potential candidate found by our criteria will end up being a genuine PN or SySt, if it is located well within the PN/SySt zones, simultaneously, in the IPHAS equivalent and the other four colour-colour diagrams we proposed. We have validated our colour-colour diagrams through the photometry of the known hPNe H 4-1 and PNG135.9+55.9 observed by J-PLUS during the SVD phase.

By applying these new colour criteria to the J-PLUS DR1 and S-PLUS DR1, which add up an observed area of the sky of $\sim 1,190$ deg², we identified one PN and none SySt candidates. The optical spectroscopic follow-up of the candidate unveiled a giant H II in the UGC 5272 galaxy.

After cross-matching the J-PLUS DR1 and S-PLUS DR1 with the HASH PN

catalog, five common sources were found. None of these sources is a strong $H\alpha$ emitter. Four of them have photo-spectra with a stronger blue continuum compared to the red one, similar to WDs. In the colour-colour diagrams, these WDs are found to lie in an area below the PNe zone. These HASH sources are located in the zone of very blue WDs. The fifth source has a photo-spectrum that resembles those of galaxies, not PNe.

Merrett et al. (2006) have shown that for low luminosities objects it is hard to distinguish between PNe and H II regions, using the ratio between [O III] and $H\alpha + [N II]$ emission lines. We will further investigate this issue, including morphological criteria in the analysis. We have proved that our selection criteria are very effective to select PN candidates, even considering the contamination by H II regions/galaxies. However, the machine learning techniques allow a better classification of classes the objects. Moreover, with these techniques we have achieved to discriminate PNe from H II regions/galaxies. We compared two methods based, respectively, on classical colour-colour criteria and PCA and LDA algorithms to classify PNe. And we finally conclude that the combination of the J/S-PLUS filter system with machine learning methods have a better performance than the colour criteria.

5.3 Perspectives

This thesis opens a number of opportunities to future works on the subject of discovering evolved star's nebulisities in the three multi-band surveys here described. The most relevant of these thesis's developments are as follows.

- Applying the color criteria to the forthcoming J-PLUS and S-PLUS data releases. In this way in hope to provide a more complete list of hPN and SySt candidates for spectroscopic follow-up.
- Applying the J-PAS colour criteria proposed in this thesis to the forthcoming J-PAS data releases.
- Adding blue compact galaxies or H II galaxies to our list of objects to better training the machine learning techniques (PCA and LDA) and use them with the next data releases.
- In the new S- and J-PLUS colour-colour diagnostic diagrams to define a zone that only includes the WDs with a very strong blue continuum. The additional colour criteria should then be applied to the data with the aim to find WDs. Then we will also try to recover the $H\alpha$ emission of extended and low surface brightness PNe through of the combination of the r , $H\alpha$ and i images as we did with the HASH sources (see chapter 4).
- Combining J-PLUS/S-PLUS and J-PAS photometry with photometric data from from other surveys like GALEX, 2MASS, WISE with the aim to improve the rate of true PNe and SySt detection.

Bibliography

- Abell, G. O. 1966, *ApJ*, 144, 259
- Acker, A., Chopinet, M., Pottasch, S. R., & Stenholm, B. 1987, *A&AS*, 71, 163
- Acker, A., Marcout, J., Ochsenbein, F., Stenholm, B., Tylenda, R., & Schohn, C. 1992, *The Strasbourg-ESO Catalogue of Galactic Planetary Nebulae. Parts I, II.*
- Acker, A., Stenholm, B., & Veron, P. 1991, *A&AS*, 87, 499
- Adams, S., Seaton, M. J., Howarth, I. D., Auriere, M., & Walsh, J. R. 1984, *MNRAS*, 207, 471
- Akras, S., Guzman-Ramirez, L., & Gonçalves, D. R. 2019c, *MNRAS*, 488, 3238
- Akras, S., Guzman-Ramirez, L., Leal-Ferreira, M., & Ramos-Larios, G. 2019a, *ApJS*, 240, 21
- Akras, S., Leal-Ferreira, M., Guzman-Ramirez, L., & Ramos-Larios, G. 2019b, *MNRAS*, 483, 5077
- Alam, S., et al. 2015, *ApJS*, 219, 12
- Alcalá, J. M., et al. 2014, *VizieR Online Data Catalog*, 356
- Allen, D. A. 1984a, *Proceedings of the Astronomical Society of Australia*, 5, 369
- . 1984b, *Ap&SS*, 99, 101
- Aller, L. 1956, *Gaseous Nebulae, The International astrophysics series* (Wiley)
- Ann, H. B., Seo, M., & Ha, D. K. 2015, *ApJS*, 217, 27
- Aparicio Villegas, T., et al. 2010, *AJ*, 139, 1242
- Arnaboldi, M., et al. 2002, *AJ*, 123, 760
- Astropy Collaboration et al. 2013, *A&A*, 558, A33
- Balick, B., & Frank, A. 2002, *ARA&A*, 40, 439
- Bayes, T. 1763, *Phil. Trans. of the Royal Soc. of London*, 53, 370

- Belczyński, K., Mikołajewska, J., Munari, U., Ivison, R. J., & Friedjung, M. 2000, *A&AS*, 146, 407
- Benítez, N., et al. 2015, in *Highlights of Spanish Astrophysics VIII*, ed. A. J. Cenarro, F. Figueras, C. Hernández-Monteagudo, J. Trujillo Bueno, & L. Valdivielso, 148–153
- Bertin, E., & Arnouts, S. 1996, *A&AS*, 117, 393
- Bessell, M. S. 2005, *ARA&A*, 43, 293
- Bica, E., Claria, J. J., Bonatto, C., Piatti, A. E., Ortolani, S., & Barbuy, B. 1995, *A&A*, 303, 747
- Bland-Hawthorn, J., & Gerhard, O. 2016, *ARA&A*, 54, 529
- Bohigas, J., & Tapia, M. 2003, *AJ*, 126, 1861
- Bonatto, C., et al. 2019, *A&A*, 622, A179
- Boumis, P., Akras, S., Xilouris, E. M., Mavromataki, F., Kapakos, E., Papamastorakis, J., & Goudis, C. D. 2006, *MNRAS*, 367, 1551
- Boumis, P., Paleologou, E. V., Mavromataki, F., & Papamastorakis, J. 2003, *MNRAS*, 339, 735
- Brocklehurst, M. 1971, *MNRAS*, 153, 471
- Buzzoni, A., Arnaboldi, M., & Corradi, R. L. M. 2006, *MNRAS*, 368, 877
- Canto, J. 1981, in *Astrophysics and Space Science Library*, Vol. 91, *Investigating the Universe*, ed. F. D. Kahn, 95–124
- Cappellaro, E., Benetti, S., Sabbadin, F., Salvadodori, L., Turatto, M., & Zanin, C. 1994, *MNRAS*, 267, 871
- Caswell, J. L., & Haynes, R. F. 1987, *A&A*, 171, 261
- Cenarro, A. J., J-PAS Collaboration, & J-PLUS Collaboration. 2017, in *Highlights on Spanish Astrophysics IX*, 11–19
- Cenarro, A. J., et al. 2014, in *Proc. SPIE*, Vol. 9149, *Observatory Operations: Strategies, Processes, and Systems V*, 91491I
- Cenarro, A. J., et al. 2019, *A&A*, 622, A176
- Chambers, K. C., & Pan-STARRS Team. 2016, in *American Astronomical Society Meeting Abstracts*, Vol. 227, *American Astronomical Society Meeting Abstracts #227*, 324.07
- Chawla, N. V., Bowyer, K. W., Hall, L. O., & Kegelmeyer, W. P. 2002, *J. Artif. Int. Res.*, 16, 321

- Chen, X., Han, Z., & Tout, C. A. 2011, *ApJ*, 735, L31
- Chiosi, C., & Vallenari, A. 1996, in *Spiral Galaxies in the Near-IR*, ed. D. Minniti & H.-W. Rix, 63
- Ciardullo, R., Feldmeier, J. J., Jacoby, G. H., Kuzio de Naray, R., Laychak, M. B., & Durrell, P. R. 2002, *ApJ*, 577, 31
- Ciardullo, R., Jacoby, G. H., Ford, H. C., & Neill, J. D. 1989, *ApJ*, 339, 53
- Clegg, R. E. S., Peimbert, M., & Torres-Peimbert, S. 1987, *MNRAS*, 224, 761
- Corradi, R. L. M., Mikolajewska, J., & Mahoney, T. J., eds. 2003, *Astronomical Society of the Pacific Conference Series*, Vol. 303, *Symbiotic Stars Probing Stellar Evolution*
- Corradi, R. L. M., et al. 2008, *A&A*, 480, 409
- . 2010, *A&A*, 509, A41
- Cortesi, A., et al. 2013, *A&A*, 549, A115
- Costa, R. D. D., Chiappini, C., Maciel, W. J., & de Freitas Pacheco, J. A. 1996, *A&AS*, 116, 249
- Cramer, J. 2004, *Studies in History and Philosophy of Science Part C: Studies in History and Philosophy of Biological and Biomedical Sciences*, 35, 613
- Crawford, D. L. 1958, *ApJ*, 128, 185
- Crowther, P. A. 2007, *ARA&A*, 45, 177
- Dalnodar, S. 2012, in *IAU Symposium*, Vol. 283, *IAU Symposium*, 338–339
- Dennison, B., Simonetti, J. H., & Topasna, G. A. 1998, *PASA*, 15, 147
- Di Stefano, R. 2010, *ApJ*, 719, 474
- Dopita, M. A., Jacoby, G. H., & Vassiliadis, E. 1992, *ApJ*, 389, 27
- Dopita, M. A., & Meatheringham, S. J. 1990, *ApJ*, 357, 140
- Douglas, N. G., et al. 2002, *PASP*, 114, 1234
- Downes, R. A., & Duerbeck, H. W. 2000, *AJ*, 120, 2007
- Drew, J. E., et al. 2005, *MNRAS*, 362, 753
- . 2014, *MNRAS*, 440, 2036
- Ferland, G. J., et al. 2013, *Rev. Mexicana Astron. Astrofis.*, 49, 137
- Fesen, R. A., Blair, W. P., & Kirshner, R. P. 1985, *ApJ*, 292, 29

- Fisher, R. A. 1936, *Annals of Eugenics*, 7, 179
- Fitzpatrick, E. L. 1999, *PASP*, 111, 63
- Fragkou, V., Parker, Q. A., Bojičić, I. S., & Aksaker, N. 2018, *MNRAS*, 480, 2916
- Freeman, K. C. 1987, *ARA&A*, 25, 603
- Frew, D. J. 2008, PhD thesis, Department of Physics, Macquarie University, NSW 2109, Australia
- Frew, D. J. 2017, in *IAU Symposium*, Vol. 323, *Planetary Nebulae: Multi-Wavelength Probes of Stellar and Galactic Evolution*, ed. X. Liu, L. Stanghellini, & A. Karakas, 11–19
- Frew, D. J., Madsen, G. J., & Parker, Q. A. 2006, in *IAU Symposium*, Vol. 234, *Planetary Nebulae in our Galaxy and Beyond*, ed. M. J. Barlow & R. H. Méndez, 395–396
- Frew, D. J., & Parker, Q. A. 2010, *PASA*, 27, 129
- Froebrich, D., et al. 2015, *MNRAS*, 454, 2586
- Fukugita, M., Ichikawa, T., Gunn, J. E., Doi, M., Shimasaku, K., & Schneider, D. P. 1996, *AJ*, 111, 1748
- García-Segura, G., López, J. A., & Franco, J. 2005, *ApJ*, 618, 919
- Garrido, O., Marcelin, M., & Amram, P. 2004, *MNRAS*, 349, 225
- Gaustad, J. E., McCullough, P. R., Rosing, W., & Van Buren, D. 2001, *PASP*, 113, 1326
- Ghojogh, B., & Crowley, M. 2019, arXiv e-prints, arXiv:1906.02590
- Gilmore, G., Wyse, R. F. G., & Kuijken, K. 1989, *ARA&A*, 27, 555
- Gledhill, T. M., Froebrich, D., Campbell-White, J., & Jones, A. M. 2018, *MNRAS*, 479, 3759
- Gonçalves, D. R., Magrini, L., de la Rosa, I. G., & Akras, S. 2015, *MNRAS*, 447, 993
- Gonçalves, D. R., Magrini, L., Munari, U., Corradi, R. L. M., & Costa, R. D. D. 2008, *MNRAS*, 391, L84
- Gonçalves, D. R., Teodorescu, A. M., Alves-Brito, A., Méndez, R. H., & Magrini, L. 2012, *MNRAS*, 425, 2557
- Gonçalves, D. R. 2019, in *IAU Symposium*, Vol. 344, *Dwarf Galaxies: From the Deep Universe to the Present*, ed. K. B. W. McQuinn & S. Stierwalt, 161–177

- Gonzalez, J. C. 2017, Using Linear Discriminant Analysis (LDA) for data Explore: Step by Step, available at <https://www.apsl.net/blog/2017/07/18/using-linear-discriminant-analysis-lda-data-explore-step-step/>
- González-Solares, E. A., et al. 2008, MNRAS, 388, 89
- Greiss, S., et al. 2012, AJ, 144, 24
- Grubinger, T., Zeileis, A., & Pfeiffer, K.-P. 2011, Journal of statistical software, 61
- Gruel, N., et al. 2012, in Proc. SPIE, Vol. 8448, Observatory Operations: Strategies, Processes, and Systems IV, 84481V
- Gurzadian, G. A., & Egikian, A. G. 1991, Ap&SS, 181, 73
- Gutierrez-Moreno, A. 1988, in Astronomical Society of the Pacific Conference Series, Vol. 1, Progress and Opportunities in Southern Hemisphere Optical Astronomy. The CTIO 25th Anniversary Symposium, ed. V. M. Blanco & M. M. Phillips, 12
- Gutierrez-Moreno, A., Moreno, H., & Cortes, G. 1995a, PASP, 107, 462
- . 1995b, PASP, 107, 462
- Gyulbudaghian, A. L., May, J., González, L., & Méndez, R. A. 2004, Rev. Mexicana Astron. Astrofis., 40, 137
- Hachisu, I., Kato, M., & Nomoto, K. 1999, ApJ, 522, 487
- Hambly, N. C., Miller, L., MacGillivray, H. T., Herd, J. T., & Cormack, W. A. 1998, MNRAS, 298, 897
- Hastie, T., Tibshirani, R., & Friedman, J. 2009, The elements of statistical learning: data mining, inference and prediction, 2nd edn. (Springer)
- Hearnshaw, J. B. 1990, The analysis of starlight: one hundred and fifty years of astronomical spectroscopy/J.B. Hearnshaw, 1st edn. (Cambridge University Press Cambridge; New York), xv, 531 p.
- Henize, K. G. 1967, ApJS, 14, 125
- Henry, R. B. C., Kwitter, K. B., & Howard, J. W. 1996, ApJ, 458, 215
- Herwig, F. 2005, ARA&A, 43, 435
- Hewett, P. C., Irwin, M. J., Skillman, E. D., Foltz, C. B., Willis, J. P., Warren, S. J., & Walton, N. A. 2003, ApJ, 599, L37
- Hoessel, J. G., Saha, A., & Danielson, G. E. 1988, PASP, 100, 680
- Howard, J. W., Henry, R. B. C., & McCartney, S. 1997, MNRAS, 284, 465
- Hunt, L., et al. 2012, MNRAS, 427, 906

- Iben, I., & Renzini, A. 1984, *Phys. Rep.*, 105, 329
- Iben, Jr., I., & Renzini, A. 1983, *ARA&A*, 21, 271
- Iben, Icko, J., & Tutukov, A. V. 1993, *ApJ*, 418, 343
- Ikiewicz, K., & Mikołajewska, J. 2017, *A&A*, 606, A110
- Irabor, T., et al. 2018, *VizieR Online Data Catalog*, 748
- Jacoby, G. H. 1980, *ApJS*, 42, 1
- . 1989, *ApJ*, 339, 39
- Jacoby, G. H. 2006, in *Planetary Nebulae Beyond the Milky Way*, ed. L. Stanghellini, J. R. Walsh, & N. G. Douglas, 17
- Jacoby, G. H., & Kaler, J. B. 1989, *AJ*, 98, 1662
- Jacoby, G. H., & van de Steene, G. 1995, *AJ*, 110, 1285
- Jacoby, G. H., & Van de Steene, G. 2004, *A&A*, 419, 563
- Jacoby, G. H., et al. 2010, *PASA*, 27, 156
- Jordan, S., Schmutz, W., Wolff, B., Werner, K., & Muerset, U. 1996, *A&A*, 312, 897
- Kaler, J. B., & Jacoby, G. H. 1989, *ApJ*, 345, 871
- Kanarek, G., Shara, M., Faherty, J., Zurek, D., & Moffat, A. 2015, *MNRAS*, 452, 2858
- Kanarek, G. C., Shara, M. M., Faherty, J. K., Zurek, D., & Moffat, A. F. J. 2017, *MNRAS*, 465, 293
- Karachentsev, I. D., Kaisina, E. I., & Makarov, D. I. 2014, *AJ*, 147, 13
- Karakas, A. I., & Lattanzio, J. C. 2014, *PASA*, 31, e030
- Ke, J., Zhang, S., Yang, H., & Chen, X. M. 2019, *Transportmetrica A: Transport Science*, 15, 872
- Kenyon, S. J. 1986, *The Symbiotic Stars*, Cambridge Astrophysics (Cambridge University Press)
- Kenyon, S. J., Livio, M., Mikołajewska, J., & Tout, C. A. 1993, *ApJ*, 407, L81
- Kilkenny, D. 1984, *MNRAS*, 211, 969
- Kimeswenger, S. 1998, *MNRAS*, 294, 312
- King, I. 1952, *AJ*, 57, 253

- Kniazev, A. Y., Grebel, E. K., Zucker, D. B., Rix, H.-W., Martínez-Delgado, D., & Snedden, S. A. 2014, *AJ*, 147, 16
- Kronberger, M., et al. 2014, in *Asymmetrical Planetary Nebulae VI Conference*, 48
- Kronberger, M., et al. 2016, in *Journal of Physics Conference Series*, Vol. 728, 072012
- Kwitter, K. B., & Henry, R. B. C. 1998, *ApJ*, 493, 247
- . 2001, *ApJ*, 562, 804
- Kwitter, K. B., Henry, R. B. C., & Milingo, J. B. 2003, *PASP*, 115, 80
- Kwok, S. 2007, *The Origin and Evolution of Planetary Nebulae*, Cambridge Astrophysics (Cambridge University Press)
- Lamers, H. J. G. L. M., Zickgraf, F.-J., de Winter, D., Houziaux, L., & Zorec, J. 1998, *A&A*, 340, 117
- Logroño-García, R., et al. 2019, *A&A*, 622, A180
- López-Sanjuan, C., et al. 2019, *A&A*, 622, A177
- Lü, G., Yungelson, L., & Han, Z. 2006, *MNRAS*, 372, 1389
- Lü, G., Zhu, C., Wang, Z., & Wang, N. 2009, *MNRAS*, 396, 1086
- Magrini, L., Corradi, R. L. M., & Munari, U. 2003, in *Astronomical Society of the Pacific Conference Series*, Vol. 303, *Symbiotic Stars Probing Stellar Evolution*, ed. R. L. M. Corradi, J. Mikolajewska, & T. J. Mahoney, 539
- Magrini, L., Gonçalves, D. R., & Vajgel, B. 2017, *MNRAS*, 464, 739
- Mamajek, E. E. 2012, arXiv e-prints, arXiv:1210.1616
- Mampaso, A., Gomez, P., Sanchez-Magro, C., & Selby, M. J. 1984, *MNRAS*, 207, 465
- Marston, A. P., & McCollum, B. 2006, in *Astronomical Society of the Pacific Conference Series*, Vol. 355, *Stars with the B[e] Phenomenon*, ed. M. Kraus & A. S. Miroshnichenko, 189
- Mendes de Oliveira, C., et al. 2019, *MNRAS*, 489, 241
- Merrett, H. R., et al. 2006, *MNRAS*, 369, 120
- Miszalski, B., Parker, Q. A., Acker, A., Birkby, J. L., Frew, D. J., & Kovacevic, A. 2008, *MNRAS*, 384, 525
- Mitchell, T. M. 1997, *Machine Learning*, 1st edn. (New York, NY, USA: McGraw-Hill, Inc.)

- Moiseev, A. V., Pustilnik, S. A., & Kniazev, A. Y. 2010, *MNRAS*, 405, 2453
- Molino, A., et al. 2014, *MNRAS*, 441, 2891
- . 2019, *A&A*, 622, A178
- Moreno-Ibáñez, M., Villaver, E., Shaw, R. A., & Stanghellini, L. 2016, *A&A*, 593, A29
- Moretti, M. I., Hatzidimitriou, D., Karamelas, A., Sokolovsky, K. V., Bonanos, A. Z., Gavras, P., & Yang, M. 2018, *MNRAS*, 477, 2664
- Munari, U. 1997, in *Physical Processes in Symbiotic Binaries and Related Systems*, ed. J. Mikołajewska, 37
- Munari, U., & Jurdana-Šepić, R. 2002, *A&A*, 386, 237
- Munari, U., & Renzini, A. 1992, *ApJ*, 397, L87
- Munari, U., & Zwitter, T. 2002, *A&A*, 383, 188
- Napiwotzki, R., Heber, U., & Koeppe, J. 1994, *A&A*, 292, 239
- Naseriparsa, M., & Mansour Riahi Kashani, M. 2013, *International Journal of Computer Applications*, 77, 33
- Ogura, K., & Noumaru, J. 1994, *AJ*, 108, 1427
- Oke, J. B., & Gunn, J. E. 1983, *ApJ*, 266, 713
- Oliphant, T. 2006, *Guide to NumPy*
- Osterbrock, D. E., & Ferland, G. J. 2006, *Astrophysics Of Gas Nebulae and Active Galactic Nuclei* (Sausalito: University Science Books)
- Otsuka, M., Hyung, S., & Tajitsu, A. 2015, *ApJS*, 217, 22
- Otsuka, M., & Tajitsu, A. 2013, *ApJ*, 778, 146
- Otsuka, M., Tajitsu, A., Hyung, S., & Izumiura, H. 2010, *ApJ*, 723, 658
- Parker, Q. A., Acker, A., Peyaud, A., Frew, D. J., & MASH Consortium. 2005a, in *Planetary Nebulae as Astronomical Tools*
- Parker, Q. A., & Bland-Hawthorn, J. 1998, *PASA*, 15, 33
- Parker, Q. A., Bojčić, I. S., & Frew, D. J. 2016, in *Journal of Physics Conference Series*, Vol. 728, *Journal of Physics Conference Series*, 032008
- Parker, Q. A., et al. 2003, in *IAU Symposium*, Vol. 209, *Planetary Nebulae: Their Evolution and Role in the Universe*, ed. S. Kwok, M. Dopita, & R. Sutherland, 41

- Parker, Q. A., et al. 2005b, MNRAS, 362, 689
- . 2006, MNRAS, 373, 79
- Patterson, J. 1984, ApJS, 54, 443
- Pearson, K. 1901, Philosophical Magazine, 2, 559
- Pedregosa, F., et al. 2011, Journal of Machine Learning Research, 12, 2825
- Peimbert, M. 1978, in IAU Symposium, Vol. 76, Planetary Nebulae, ed. Y. Terzian, 215–223
- Peimbert, M., & Serrano, A. 1980, Rev. Mexicana Astron. Astrofis., 5, 9
- Peimbert, M., & Torres-Peimbert, S. 1983, in IAU Symposium, Vol. 103, Planetary Nebulae, ed. L. H. Aller, 233–242
- Pena, M., Ruiz, M. T., Maza, J., & Gonzalez, L. E. 1989, Rev. Mexicana Astron. Astrofis., 18
- Pena, M., Torres-Peimbert, S., & Ruiz, M. T. 1991, PASP, 103, 865
- Pena, M., Torres-Peimbert, S., Ruiz, M. T., & Maza, J. 1990, A&A, 237, 454
- Pereira, C. B., Jilinski, E. G., Drake, N. A., Ortega, V. G., & Roig, F. 2013, A&A, 559, A12
- Pereira, C.-B., & Miranda, L.-F. 2007, A&A, 467, 1249
- Pickles, A. J. 1998, PASP, 110, 863
- Pregibon, D. 1982, Biometrics, 38, 485
- Pura Hartati, E., Adiwijaya, & Arif Bijaksana, M. 2018, in Journal of Physics Conference Series, Vol. 971, 012007
- Quireza, C., Rocha-Pinto, H. J., & Maciel, W. J. 2007, VizieR Online Data Catalog, J/A+A/475/217
- Ramos-Larios, G., Guerrero, M. A., Suárez, O., Miranda, L. F., & Gómez, J. F. 2009, A&A, 501, 1207
- . 2012, A&A, 545, A20
- Ramos-Larios, G., & Phillips, J. P. 2005, MNRAS, 357, 732
- Rebassa-Mansergas, A., et al. 2015, MNRAS, 450, 743
- Reddy, B. E., Lambert, D. L., & Allende Prieto, C. 2006, MNRAS, 367, 1329
- Reid, W. A., & Parker, Q. A. 2010, PASA, 27, 187

- Reimers, D. 1975, *Circumstellar envelopes and mass loss of red giant stars.*, 229–256
- Reipurth, B., & Bally, J. 2001, *ARA&A*, 39, 403
- Riesgo, H., & López, J. A. 2005, *Rev. Mexicana Astron. Astrofis.*, 41, 57
- . 2006, *Rev. Mexicana Astron. Astrofis.*, 42, 47
- Rigliaco, E., Natta, A., Testi, L., Randich, S., Alcalà, J. M., Covino, E., & Stelzer, B. 2012, *A&A*, 548, A56
- Rodríguez-Flores, E. R., Corradi, R. L. M., Mampaso, A., García-Alvarez, D., Munari, U., Greimel, R., Rubio-Díez, M. M., & Santander-García, M. 2014, *A&A*, 567, A49
- Roman-Lopes, A., & Abraham, Z. 2006, *AJ*, 131, 2223
- Sabbadin, F., Minello, S., & Bianchini, A. 1977, *A&A*, 60, 147
- Sabin, L., Zijlstra, A. A., Wareing, C., Corradi, R. L. M., Mampaso, A., Viironen, K., Wright, N. J., & Parker, Q. A. 2010, *pasa*, 27, 166
- Sabin, L., et al. 2014, *MNRAS*, 443, 3388
- San Roman, I., et al. 2019, *A&A*, 622, A181
- Sanduleak, N., & Stephenson, C. B. 1972, *ApJ*, 178, 183
- Sargent, W. L. W., & Searle, L. 1970, *ApJ*, 162, L155
- Schmeja, S., & Kimeswenger, S. 2001, *A&A*, 377, L18
- Schmid, H. M. 1989, *A&A*, 211, L31
- Schmid, H. M., & Schild, H. 1994, *A&A*, 281, 145
- Schneider, D. P., Gunn, J. E., & Hoessel, J. G. 1983, *ApJ*, 264, 337
- Shaw, R. A., & Bidelman, W. P. 1987, *PASP*, 99, 27
- Skrutskie, M. F., et al. 1995, in *American Astronomical Society Meeting Abstracts*, Vol. 187, 75.07
- Soker, N. 1998, *ApJ*, 496, 833
- . 2002a, *MNRAS*, 330, 481
- Sokolovsky, K. V., et al. 2017, *MNRAS*, 464, 274
- Stanghellini, L., Shaw, R. A., Mutchler, M., Palen, S., Balick, B., & Blades, J. C. 2002a, *ApJ*, 575, 178
- Sterling, N. C., & Dinerstein, H. L. 2008, *ApJS*, 174, 158

- Straižys, V. 1992, Multicolor stellar photometry, Astronomy and Astrophysics Series (Pachart Publishing House)
- Süveges, M., et al. 2012, MNRAS, 424, 2528
- Tharwat, A., Gaber, T., Ibrahim, A., & Hassanien, A. E. 2017, Ai Communications, 30, 169
- Tokovinin, A., Baumont, S., & Vasquez, J. 2003, MNRAS, 340, 52
- Tomov, T. 2003, in Astronomical Society of the Pacific Conference Series, Vol. 303, Symbiotic Stars Probing Stellar Evolution, ed. R. L. M. Corradi, J. Mikolajewska, & T. J. Mahoney, 376
- Torres-Peimbert, S., Peimbert, M., & Pena, M. 1990, A&A, 233, 540
- Tovmassian, G. H., Stasińska, G., Chavushyan, V. H., Zharikov, S. V., Gutierrez, C., & Prada, F. 2001, A&A, 370, 456
- Tweedy, R. W., & Kwitter, K. B. 1996, ApJS, 107, 255
- Van den Bergh, S. 2000, The Galaxies of the Local Group, Cambridge astrophysics series (Cambridge University Press)
- Viironen, K., et al. 2009a, A&A, 502, 13
- . 2009b, A&A, 504, 291
- Wachter, A., Schröder, K. P., Winters, J. M., Arndt, T. U., & Sedlmayr, E. 2002, A&A, 384, 452
- Werner, K., Rauch, T., & Kruk, J. W. 2016, A&A, 593, A104
- Whelan, J., & Iben, Jr., I. 1973, ApJ, 186, 1007
- Whitten, D. D., et al. 2019, A&A, 622, A182
- Williams, R. E. 1980, ApJ, 235, 939
- Witham, A. R., Knigge, C., Drew, J. E., Greimel, R., Steeghs, D., Gänsicke, B. T., Groot, P. J., & Mampaso, A. 2008, MNRAS, 384, 1277
- Xie, J., & Qiu, Z. 2007, Pattern Recogn., 40, 557
- Yuan, H. B., & Liu, X. W. 2013, MNRAS, 436, 718
- Zuckerman, B., & Gatley, I. 1988, ApJ, 324, 501

Appendix A

Python codes

A.1

Python program used to simulate the S-PLUS, J-PLUS and J-PAS photometry. Note that this code can be used to perform synthetic photometry of any photometric system.

```
"""
Find the values in the spectrums (ASCII file)

Estimate the magnitudes for any photometryc system
"""
from __future__ import print_function
import glob
from syntphot import spec2filterset
from readfilterset import readfilterset
from syntphot import photoconv

from astropy.io import fits
import os
import json
import numpy as np
import argparse
#import matplotlib
#matplotlib.use("Agg")
import matplotlib.pyplot as plt
import sys, getopt
from collections import OrderedDict
from urllib.parse import parse_qs

parser = argparse.ArgumentParser(
    description="""Estimate magnitudes of a
                    spectrum for any photometryc system""")

parser.add_argument("source", type=str,
                    default="DdDm-1",
                    help="Name of source, taken the prefix ")
```

```

parser.add_argument("--filters", type=str,
                    default="Alhambra3",
                    help="Filter of the photometryc system")

parser.add_argument("--name", type=str,
                    default="HPNe",
                    help="Name to clasify the source in the JSON file
                    ")

parser.add_argument("--savefig", action="store_true",
                    help="Save a figure showing the magnitude")

parser.add_argument("--debug", action="store_true",
                    help="Print out verbose debugging info
                    about each line in region file")

cmd_args = parser.parse_args()
regionfile = cmd_args.source + ".dat"

# Get any filters that you need
datadir = "../filters/"
filterfile = cmd_args.filters + ".filter"

f = readfilterset()
f.read(os.path.join(datadir, filterfile))
f.uniform()
f.calc_filteravgwls()

# Dictionary
magn = OrderedDict({"id": regionfile.replace(".dat",
                    "-{}".format(cmd_args.name)) })
#magn = {"id": regionfile }

dt = np.dtype([('wl', 'f4'), ('flux', 'f4')])
obs_spec = np.loadtxt(regionfile, delimiter = None,
                    converters = None, skiprows = 0,
                    usecols = None, unpack = False,
                    ndmin = 0, dtype = dt)

# Estimate of magnitude of the photometric system
x = spec2filterset(f.filterset, obs_spec,
                    model_spec = None, badpxl_tolerance = 0.5)
for xx, yy in zip(np.unique(f.filterset['ID_filter']), x['m_ab']):
    xx=str(xx).split("b'")[-1].split("'")[0]
    magn[xx] = float(yy)
if cmd_args.debug:
    print("Calculating the magnitude of:", magn["id"])

# Plot magnitude vs filter or wavelenght
if cmd_args.savefig:
    plotfile = regionfile.replace(".dat",
                    "-{}-{}-magnitude.pdf".format(cmd_args.name,
                    cmd_args.filters.split('am')[0]))

```

```
fig = plt.figure()
ax1 = fig.add_subplot(1,1,1)
#ax1.set_xlim(xmin=-0.5,xmax=2)
#ax1.set_ylim(ymin=15,ymax=-5)
#ax1.set_xlabel(r'$\lambda$')
plt.tick_params(axis='x', labelsz=19)
plt.tick_params(axis='y', labelsz=19)
ax1.set_xlabel(r'Wavelength($\AA$)', size = 19)
ax1.set_ylabel(r'Magnitude', size = 19)
ax1.plot(f.filteravgwls, x['m_ab'], 'ko-')
ax1.set_title(" ".join([cmd_args.source]))
#ax1.plot(Wavelengthh, Fluxx, 'k-')
#ax1.grid(True)
#plt.xticks(f.filteravgwls, np.unique(f.filterset['ID_filter']),
            #rotation='vertical', size = 'small')

plt.margins(0.06)
plt.subplots_adjust(bottom=0.17)
plt.savefig(plotfile)

# Creates the JSON files with the magnitudes
jsonfile = regionfile.replace(".dat",
                              "--{}-{}-magnitude.json".format(cmd_args.name,
                                                                cmd_args.filters.split('am')[0]))
with open(jsonfile, "w") as f:
    json.dump(magn, f, indent=4)
```

The SYNTPHOT code (created by William Schoenell):

```

'''
Created on Jul 17, 2012
@author: william
'''

import numpy as np

from log import logger
import exceptions #import MAGALException

def spec2filter(filter, obs_spec, model_spec=None, badpxl_tolerance =
0.5):
'''
Converts a spectrum on AB magnitude given a filter bandpass.
If there are bad pixels on filter interval on a fraction inferior
to the badpxl_tolerance, it will
interpolate the missing values or, in case of a model_spec is not
None, it will use the values from model_spec.
Parameters
-----
filter : dict
    Filter transmission curve. Dictionary containing the
    following entries:
    {'wl': array_like
        Wavelength (in Angstroms!).
    'transm': array_like
        Filter transmission response.
    }
obs_spec : dict
    Observed Spectra. Dictionary containing the following
    entries:
    {'wl': array_like,
    'flux': array_like,
    'error': array_like, optional,
    'flag': array_like, optional,
    'model_spec': array_like, optional
    }
model_spec : dict, optional
    Model Spectra which could be used when there are
    missing (due to err or flagged). Dictionary
    containing the following entries:
    {    'wl': array_like
        Wavelength (in the same units as filter
        response curve)
        'flux': array_like
        Flux on a given wl
    }
badpxl_tolerance : float, default: 0.5
    Bad pixel fraction tolerance on the spectral
    interval of the filter.

Returns

```

```

-----
m_ab : float
        AB magnitude on given filter
e_ab : float
        AB magnitude error on given filter

See Also
-----

Notes
-----
'''
log = logger(__name__)
#Cut the spectrum on the filterset range. This improves the
    velocity of the rest of the accounts.
obs_cut = obs_spec[np.bitwise_and(obs_spec['wl'] >= np.min(filter
    ['wl']), obs_spec['wl'] <= np.max(filter['wl']))]

if model_spec is not None:
    model_cut = model_spec[np.bitwise_and(model_spec['wl'] >= np.
        min(filter['wl']), model_spec['wl'] <= np.max(filter['wl']
        '))]
    if len(model_cut) == 0:
        #log.warning('No enough MODEL datapoints eval synthetic
            photometry on this filter. Model will NOT be
            considered.')
        model_spec = None
    elif np.any(model_cut['wl'] != obs_cut['wl']):
        #log.warning('Model is not sampled the same way as the
            observed spectrum. Interpolating...')
        aux = np.copy(model_cut)
        # model_cut = obs_cut[:len(model_spec)].copy()
        model_cut = np.zeros(len(obs_cut), dtype=model_cut.dtype)
        model_cut['wl'] = obs_cut['wl']
        model_cut['flux'] = np.interp(obs_cut['wl'], aux['wl'], aux
            ['flux'], left=0.0, right=0.0)
#Check if the filterset is sampled correctly
# - Tip: Resample the filter to your data when reading the filter
    to avoid unnecessary interpolations.
if np.any(obs_cut['wl'] != filter['wl']):
    # log.warning('Filter is not sampled the same way as the
        observed spectrum. Interpolating...')
    wl_ = obs_cut['wl']
    transm_ = np.interp(wl_, filter['wl'], filter['transm'])
else:
    wl_ = filter['wl']
    transm_ = filter['transm']

#Check for bad pixels. Good pixels should be signaled with flag(
    lambda) = 0 or 1.
# The recipe is:
# - If there is LESS bad_pixels than badpxl_tolerance:

```

```

#         And there is a model_spec: use model_spec
#         And there is NOT a model_spec: interpolate values
#         - If there is MORE bad_pixels than badpxl_tolerance:
#         Return a magnitude np.inf and an error of np.inf.
n = len(obs_cut)
not_neg_pix = (obs_cut['flux'] >= 0) #Fluxes CAN NOT be negative!
NEVER!!!!
if('flag' in obs_cut.dtype.names and 'error' in obs_cut.dtype.
names): # First check if there is error AND flag.
    good    = np.bitwise_and(np.bitwise_and(obs_cut['flag'] <= 1,
        obs_cut['error'] > 0), not_neg_pix)
    bad     = np.invert(good)
    n_bad   = np.sum(bad)
elif('error' in obs_cut.dtype.names): # Check if there is ONLY
error.
    good    = np.bitwise_and(obs_cut['error'] > 0, not_neg_pix)
    bad     = np.invert(good)
    n_bad   = np.sum(bad)
elif('flag' in obs_cut.dtype.names): # Check if there is ONLY flag
.
    good    = np.bitwise_and(obs_cut['flag'] <= 1, not_neg_pix)
    bad     = np.invert(good)
    n_bad   = np.sum(bad)
else: # If there is only spectra, all the pixels are good! =)
    good    = np.bitwise_and(obs_cut['wl'] > 0, not_neg_pix)
    bad     = np.invert(good)
    n_bad   = np.sum(bad)
log.debug( 'N_points: %d, N_bad: %d' % (n, n_bad) )

if(n_bad > 0 or n == 0): #If we have problems we have to deal with
them... ;)
    if (n == 0):
        log.debug('# of pixels = 0. m = inf and m_err = inf')
        m_ab = np.inf
        e_ab = np.inf
        return m_ab, e_ab
    p_bad = np.float(n_bad)/np.float(len(obs_cut))
    if(p_bad > badpxl_tolerance): #If we have # of bad pixels
greater than 50%, then make filter flux and error equal
to inf.
        log.debug('# of bad pixels > badpxl_tolerance. m = inf and
m_err = inf')
        m_ab = np.inf
        e_ab = np.inf
        return m_ab, e_ab
    else:
        #If we have # of bad pixels less than 50%, we simply
neglect this point on the error accounts,
        #and make flux = synthetic flux, if available, if not,
interpolate values.
        if model_spec is not None:
            obs_cut['flux'][bad] = model_cut['flux'][bad]

```

```

        else:
            obs_cut['flux'][bad] = np.interp(obs_cut['wl'][bad],
                                             obs_cut['wl'][good], obs_cut['flux'][good])

    else: # If our observed obs_spec is ALL ok. =)
        log.debug('No bad pixel! =)')
    m_ab = -2.5 * np.log10( np.trapz(obs_cut['flux'] * transm_ * wl_,
                                   wl_) / np.trapz(transm_ / wl_, wl_) ) - 2.41

    if('error' in obs_cut.dtype.names):
        e_ab = 1.0857362047581294 * np.sqrt( np.sum(transm_[good]**2 *
                                                    obs_cut['error'][good]**2 * wl_[good] ** 2 )) / np.sum(
                                                    obs_cut['flux'][good] * transm_[good] * wl_[good])
    else:
        e_ab = 0.0

    return m_ab, e_ab

def spec2filterset(filterset, obs_spec, model_spec = None,
                  badpxl_tolerance = 0.5):
    '''
    Run spec2filter over a filterset
    Parameters
    -----
    filterset : object
        Filter transmission curves (see: magal.io.
        readfilterset).
    obs_spec : dict
        Observed Spectra. Dictionary containing the following
        entries:
        {
            'wl': array_like
                Wavelength (in Angstroms!)
            'flux': array_like
                Flux on a given wl.
            'error': array_like, optional
                Flux error. If err < 0, the point will
                be considered as a problem.
            'flag': array_like, optional
                Bad pixel flag. Pixels are considered
                bad if flag > 1.
            'model_spec': array_like, optional
                Model Spectra which could be used
                when there are missing (due to
                err or flagged).
        }

    model_spec : dict, optional
        Model Spectra which could be used when there are
        missing (due to err or flagged). Dictionary
        containing the following entries:
        {
            'wl': array_like
                Wavelength (in the same units as filter
                response curve)
    '''

```

```

        'flux': array_like
                Flux on a given wl
    }
    badpxl_tolerance : float, default: 0.5
                    Bad pixel fraction tolerance on the spectral
                    interval of the filter.

Returns
-----
mags : array_like
      Filterset magnitudes
      Dictionary containing the following entries:
      {
        'm_ab': array_like
                AB magnitude on given filter.
        'e_ab' : array_like
                AB magnitude error on given filter.
      }

See Also
-----
spec2filter, magal.io.readfilterset.FilterSet

Notes
-----
'''
log = logger(__name__)
filter_ids = np.unique(filterset['ID_filter'])
mags = np.zeros(len(filter_ids), dtype = np.dtype([('m_ab', '<f4')
, ('e_ab', '<f4')]))
for i_filter in range(len(filter_ids)):
    filter = filterset[filterset['ID_filter'] == filter_ids[
        i_filter]]
    mags[i_filter]['m_ab'], mags[i_filter]['e_ab'] = spec2filter(
        filter, obs_spec, model_spec, badpxl_tolerance =
        badpxl_tolerance)
    log.debug('Magnitude to filter %s: %3.2f, error: %3.2f' %
        (filter_ids[i_filter], mags[i_filter]['m_ab'], mags[
            i_filter]['e_ab']))
return mags

class photoconv(object):
    """
    Spectrum to Photometry conversion class.
    """

    def __init__(self):
        self.log = logger(__name__)

    def fromStarlight(self, filterset, arq_in, arq_syn,
        starlight_version='starlightv4', badpxl_tolerance=0.5):
        """
        Converts automagically STARLIGHT input and output files into

```

```

    photometric magnitudes

Parameters
-----
filterset : object
    Filter transmission curves (see: magal.io.readfilterset).
arq_in : string
    Starlight input filename (or atpy.TableSet(type='
        starlight_input') object)
arq_syn : string
    Starlight synthesis filename (or atpy.TableSet(type=
        starlight_version) object)
starlight_version : string, default = 'starlightv4'
    Starlight synthesis file version (Default: starlightv4)
badpxl_tolerance : float, default: 0.5
    Bad pixel fraction tolerance on the spectral interval of
    each filter. (Default: 0.5)

Returns
-----
m_ab : numpy.ndarray dtype = [('m_ab', '<f4'), ('e_ab', '<f4')
    ]

See Also
-----
fromSDSSfits, magal.io.readfilterset

"""

try: # Try to import pystarlight...
    import pystarlight.io
    import atpy
except ImportError:
    MAGALException('Could not load pystarlight. Needed to
        convert from STARLIGHT')

try: # Check if it is an atpy or a filename
    obs_spec = arq_in.starlight_input.data.view(
        dtype=np.dtype([('wl', '<f8'), ('flux', '<f8'), ('
            error', '<f8'), ('flag', '<i8')]))
except AttributeError:
    arq_in = atpy.Table(arq_in, type='starlight_input')
    obs_spec = arq_in.data.view(
        dtype=np.dtype([('wl', '<f8'), ('flux', '<f8'), ('
            error', '<f8'), ('flag', '<i8')]))

try: # Check if it is an atpy or a filename
    model_spec = arq_syn.spectra.data.view(dtype=np.dtype(
        [('wl', '<f8'), ('f_obs', '<f8'), ('flux', '<f8'), ('
            f_wei', '<f8'), ('Best_f_SSP', '<f8')]))
except AttributeError:
    arq_syn = atpy.TableSet(arq_syn, type=starlight_version)
    model_spec = arq_syn.spectra.data.view(dtype=np.dtype(

```

```

        [('wl', '<f8'), ('f_obs', '<f8'), ('flux', '<f8'), ('
          f_wei', '<f8'), ('Best_f_SSP', '<f8')]))

    obs_spec['flux'] *= 1e-17
    obs_spec['error'] *= 1e-17
    model_spec['flux'] *= arq_syn.keywords['fobs_norm'] * 1e-17

    return spec2filterset(filterset, obs_spec, model_spec,
        badpxl_tolerance = badpxl_tolerance)

```

These codes are based on version of the SYNTPHOT code of William Schoenell. Detailed information of the code can be found in <https://github.com/wschoenell/magal/blob/master/src/magal/photometry/syntphot.py>.

The output files are JSON files contain dictionaries with the photometry of all bands. Below, it is show an example of these JSON files.

```

{ "id": "DdDm-1-HPNe",
  "F348": 13.872536659240723,
  "F378": 13.796369552612305,
  "F395": 14.366382598876953,
  "F410": 14.582297325134277,
  "F430": 14.353007316589355,
  "g_sdss": 13.825705528259277,
  "F515": 15.072735786437988,
  "r_sdss": 13.98564338684082,
  "F660": 11.874861717224121,
  "i_sdss": 14.99560260772705,
  "F861": 15.319754600524902,
  "z_sdss": 14.59402084350586
}

```

A.2

The code used to apply the PCA algorithm to the J-PLUS or S-PLUS photometry by using SKLEARN library is shown below. The input files are the JSON files like the one shown above.

```

'''
Principal component analysis applied to J-PLUS or S-PLUS photometry
'''
#from __future__ import print_function
import numpy as np
from sklearn.preprocessing import StandardScaler
from sklearn.decomposition import PCA
from mpl_toolkits.mplot3d import Axes3D
import matplotlib.pyplot as plt
from scipy import stats
import sys
import glob

```

```

import json
import seaborn as sns
import os.path
from collections import OrderedDict
from scipy.stats import gaussian_kde
import pandas as pd
from matplotlib.ticker import FormatStrFormatter

X = []
target = []

pattern = "*-spectros/*-JPLUS17-magnitude.json"

def clean_nan_inf(M):
    mask_nan = np.sum(np.isnan(M), 1) > 0
    mask_inf = np.sum(np.isinf(M), 1) > 0
    lines_to_discard = np.logical_xor(mask_nan, mask_inf)
    print("Number of lines to discard:", sum(lines_to_discard))
    M = M[np.logical_not(lines_to_discard), :]
    return M

file_list = glob.glob(pattern)

shape = (len(file_list), 12)
shape1 = (len(file_list), 13)
print(len(file_list))

for file_name in file_list:
    with open(file_name) as f:
        data = json.load(f)
        data = OrderedDict((k, v) for k, v in sorted(data.items(), key
            =lambda x: x[0]))
        X.append(data["F348"])
        X.append(data["F378"])
        X.append(data["F395"])
        X.append(data["F410"])
        X.append(data["F430"])
        X.append(data["F480_g_sdss"])
        X.append(data["F515"])
        X.append(data["F625_r_sdss"])
        X.append(data["F660"])
        X.append(data["F766_i_sdss"])
        X.append(data["F861"])
        X.append(data["F911_z_sdss"])
        target.append(data["F348"])
        target.append(data["F378"])
        target.append(data["F395"])
        target.append(data["F410"])
        target.append(data["F430"])
        target.append(data["F480_g_sdss"])
        target.append(data["F515"])
        target.append(data["F625_r_sdss"])
        target.append(data["F660"])

```



```

target.append(data["F766_i_sdss"])
target.append(data["F861"])
target.append(data["F911_z_sdss"])
if data["id"].endswith("PN Models"):
    target.append(0)
elif data["id"].endswith("HPNe"):
    target.append(1)
elif data["id"].endswith("sys"):
    target.append(2)
elif data["id"].endswith("CV"):
    target.append(3)
elif data["id"].endswith("ExtHII"):
    target.append(4)
elif data["id"].endswith("QSOs"):
    target.append(5)
elif data["id"].endswith("YSOs"):
    target.append(6)
elif data["id"].endswith("DR1SplusWDs"):
    target.append(7)
else:
    target.append(8)

print(label)
XX = np.array(X).reshape(shape)
target_ = np.array(target).reshape(shape1)
print("Data shape:", XX.shape)

m = []

XX = clean_nan_inf(XX)

#Create target to classify the kind of object
target_ = clean_nan_inf(target_)

#XX = np.array(XX[np.logical_not(np.isnan(XX), np.isinf(XX))])
#target_ = np.array(target_[np.logical_not(np.isnan(target_), np.isinf
    (target_))])

for i in target_:
    m.append(i[12])

m = np.array(m)
print(m.shape)
print(XX.shape)

if np.any(np.isnan(XX)):
    print("NaNNNNNNNNNNNNNNNNNNNNNNNNN")
if np.any(np.isinf(XX)):
    print("INNNNNNNNNNNNNNNNNNNNNNNNN")

#create the PCA for S-PLUS photometry
XX1 = StandardScaler().fit_transform(XX.data)

```

```

pca = PCA(n_components=6)
pca.fit(XX1)

XX_pca = pca.transform(XX1)

#Percentage
print("Percentage:", pca.explained_variance_ratio_)
print("Singular Value:", pca.singular_values_)
print("Component:", pca.components_[0]) # eigenvectors
print("Sorted components:", pca.explained_variance_) # eigenvalues

#Lista with the objects
n=11
pc1, pc2, pc3 = [[] for _ in range(n)], [[] for _ in range(n)], [[]
    for _ in range(n)]

#[0,1, 3, 4, 7, 10, 11, 12, 13, 8]

pc1[0].append(XX_pca[m == 0, 0])
pc2[0].append(XX_pca[m == 0, 1])
pc3[0].append(XX_pca[m == 0, 2])
pc1[1].append(XX_pca[m == 1, 0])
pc2[1].append(XX_pca[m == 1, 1])
pc3[1].append(XX_pca[m == 1, 2])
pc1[2].append(XX_pca[m == 2, 0])
pc2[2].append(XX_pca[m == 2, 1])
pc3[2].append(XX_pca[m == 2, 2])
pc1[3].append(XX_pca[m == 3, 0])
pc2[3].append(XX_pca[m == 3, 1])
pc3[3].append(XX_pca[m == 3, 2])
pc1[4].append(XX_pca[m == 4, 0])
pc2[4].append(XX_pca[m == 4, 1])
pc3[4].append(XX_pca[m == 4, 2])
pc1[5].append(XX_pca[m == 5, 0])
pc2[5].append(XX_pca[m == 5, 1])
pc3[5].append(XX_pca[m == 5, 2])
pc1[6].append(XX_pca[m == 6, 0])
pc2[6].append(XX_pca[m == 6, 1])
pc3[6].append(XX_pca[m == 6, 2])
pc1[7].append(XX_pca[m == 7, 0])
pc2[7].append(XX_pca[m == 7, 1])
pc3[7].append(XX_pca[m == 7, 2])
pc1[8].append(XX_pca[m == 8, 0])
pc2[8].append(XX_pca[m == 8, 1])
pc3[8].append(XX_pca[m == 8, 2])

#Weight

w1 = pca.components_[0]
w2 = pca.components_[1]
w3 = pca.components_[2]

print('W:', pca.components_)

```

```

print('Ein:',  pca.explained_variance_)

#####
#PC1 vs PC2 #####
#####

lgd_kws = {'frameon': True, 'fancybox': True, 'shadow': None}
#sns.set(style="dark")#, context="talk")
#sns.set_style('ticks')
fig = plt.figure(figsize=(12, 8))
ax1 = fig.add_subplot(111)
ax1.set_xlim(-8.2, 5.7)
ax1.set_ylim(-2.5, 1.5)
ax1.yaxis.set_major_formatter(FormatStrFormatter('%%.1f'))
# ax1.set_xlim(-10, 10)
# ax1.set_ylim(-3.3, 3.2)
#ax1.set_xlim(xmin=-2.5,xmax=2.0)
plt.tick_params(axis='x', labelsize=32)
plt.tick_params(axis='y', labelsize=32)
plt.xlabel(r'PC1', fontsize= 35)
plt.ylabel(r'PC2', fontsize= 35)

#print(A1[0][1], B1[0][1])
AB = np.vstack([pc1[0], pc2[0]])
z = gaussian_kde(AB)(AB)
df=pd.DataFrame({'x': pc1[0], 'y': pc2[0]})

# Sort the points by density, so that the densest points are plotted
last
idx = z.argsort()
for x1, y1 in zip(pc1[0], pc2[0]):
    x11, y11, z = x1[idx], y1[idx], z[idx]
    ax1.scatter(x11, y11, c=z, s=50, zorder=10, alpha=0.5, edgecolor
                =''')
#ax1.scatter(pc1[0], pc2[0], c= sns.xkcd_rgb["indigo"], alpha=0.5, s
            =130, marker='o', zorder=10.0, edgecolor='black', label='CLOUDY
            modelled halo PNe')
ax1.scatter(pc1[1], pc2[1], color= sns.xkcd_rgb["aqua"], s=130,
            marker='o', alpha=0.8, edgecolor='black', zorder=120.0, label='Obs
            . hPNe')
ax1.scatter(pc1[3], pc2[3], c=sns.xkcd_rgb['pale yellow'], alpha=0.8,
            s=90, marker='o', edgecolor='black', zorder=3.0, label='SDSS CVs')
ax1.scatter(pc1[5], pc2[5], c= "mediumaquamarine", alpha=0.8, s=90,
            edgecolor='black', marker='D', label='SDSS QSOs')
ax1.scatter(pc1[8], pc2[8], c= "goldenrod", alpha=0.8, s=120, marker
            ='^', edgecolor='black', label='SDSS SFGs')
ax1.scatter(pc1[2], pc2[2], c= "red", alpha=0.8, s=90, marker='s',
            edgecolor='black', zorder=3.0, label='Obs SySt')
#ax1.scatter(pc1[3], pc2[3], c= "red", alpha=0.8, s=120, marker='^',
            edgecolor='black', zorder=3.0, label='IPHAS SySt')
ax1.scatter(pc1[4], pc2[4], c= "gray", alpha=0.8, s=90, marker='D',
            edgecolor='black', zorder=133.0, label='Obs. HII regions in NGC
            55')

```

```

ax1.scatter(pc1[6], pc2[6], c= "lightsalmon", alpha=0.8, s=150,
            marker='*', edgecolor='black', label='Obs. YSOs')
#ax1.scatter(pc1[8], pc2[8], c= sns.xkcd_rgb["cerulean"], s=700,
            marker='*', edgecolor='black', zorder= 125, label='Sources
            selected in J-PLUS DR1')
#ax1.scatter(pc1[9], pc2[9], c= sns.xkcd_rgb["light green"], s=700,
            marker='*', edgecolor='black', zorder= 125, label='HASH sources in
            J/S-PLUS DR1')
ax1.scatter(pc1[7], pc2[7], c= sns.xkcd_rgb["mint green"], alpha=0.3,
            s=150, marker='*', edgecolor='black', zorder= 125, label='S-PLUS
            DR1 WDs')

#print(x[2])
#ax2.grid(which='minor')#, lw=0.3)
#ax1.legend(scatterpoints=1, ncol=2, fontsize=19.8, loc='lower center
            ', **lgd_kws)
ax1.grid()
#lgd = ax1.legend(loc='center right', bbox_to_anchor=(1.27, 0.5),
            fontsize=7.5, **lgd_kws)
#ax2.grid(which='minor', lw=0.5)
#sns.despine(bottom=True)
plt.tight_layout()
plt.tight_layout()
pltfile = 'Fig1-SPLUS-PC1-PC2-WD.pdf'
save_path = '../Dropbox/JPAS/Tesis/Fig'
file_save = os.path.join(save_path, pltfile)
plt.savefig(file_save)
plt.clf()

#####
#PC1 vs PC3 #####
#####

lgd_kws = {'frameon': True, 'fancybox': True, 'shadow': None}
#sns.set(style="dark")#, context="talk")
#sns.set_style('ticks')
fig = plt.figure(figsize=(12, 8))
ax2 = fig.add_subplot(111)
ax2.yaxis.set_major_formatter(FormatStrFormatter('%%.1f'))
ax2.set_xlim(-8.2, 5.7)
ax2.set_ylim(-1.1, 1.0)
plt.tick_params(axis='x', labels=32)
plt.tick_params(axis='y', labels=32)
plt.xlabel(r'PC1', fontsize= 35)
plt.ylabel(r'PC3', fontsize= 35)
#print(A1[0][1], B1[0][1])
AB = np.vstack([pc1[0], pc3[0]])
z = gaussian_kde(AB)(AB)
df=pd.DataFrame({'x': pc1[0], 'y': pc3[0]})

# Sort the points by density, so that the densest points are plotted
last
idx = z.argsort()

```

```

for x1, y1 in zip(pc1[0], pc3[0]):
    x11, y11, z = x1[idx], y1[idx], z[idx]
    ax2.scatter(x11, y11, c=z, s=50, zorder=10, alpha=0.5, edgecolor
                =''')
#ax2.scatter(pc1[0], pc3[0], c = sns.xkcd_rgb["indigo"], alpha=0.5, s
            =130, marker='o', edgecolor='black', zorder = 10.0, label='CLOUDY
            modelled halo PNe')
ax2.scatter(pc1[1], pc3[1], color= sns.xkcd_rgb["aqua"], s=130,
            marker='o', edgecolor='black', alpha=0.8, zorder=120.0, label='Obs
            . halo PNe')
ax2.scatter(pc1[3], pc3[3], c = sns.xkcd_rgb['pale yellow'], alpha
            =0.8, s=90, marker='o', edgecolor='black',zorder=3.0, label='SDSS
            CVs')
ax2.scatter(pc1[5], pc3[5], c = "mediumaquamarine", alpha=0.8, s=60,
            edgecolor='black', marker='D', label='SDSS QSOs')
ax2.scatter(pc1[8], pc3[8], c = "goldenrod", alpha=0.8, s=120, marker
            ='^', edgecolor='black', label='SDSS SFGs')
ax2.scatter(pc1[2], pc3[2], c = "red", alpha=0.8, s=90, marker='s',
            edgecolor='black', zorder=3.0, label='Obs SySt')
#ax2.scatter(pc1[3], pc3[3], c = "red", alpha=0.8, s=120, marker='^',
            edgecolor='black', zorder=3.0, label='IPHAS SySt')
ax2.scatter(pc1[4], pc3[4], c = "gray", alpha=0.8, s=90, marker='D',
            edgecolor='black', zorder=133.0, label='Obs. HII regions in NGC
            55')
ax2.scatter(pc1[6], pc3[6], c = "lightsalmon", alpha=0.8, s=150,
            marker='*', edgecolor='black', zorder = 11, label='Obs. YSOs')
#ax2.scatter(pc1[8], pc3[8], c = sns.xkcd_rgb["cerulean"], s=700,
            marker='*', edgecolor='black', zorder= 125, label='Obs. select in
            J-PLUS DR1')
#ax2.scatter(pc1[9], pc3[9], c = sns.xkcd_rgb["light green"], s=700,
            marker='*', edgecolor='black', zorder= 125, label='HASH sources in
            J-PLUS DR1')
ax2.scatter(pc1[7], pc3[7], c= sns.xkcd_rgb["mint green"], alpha=0.3,
            s=150, marker='*', edgecolor='black', zorder= 125, label='DR1 S-
            PLUS WDs')
ax2.minorticks_on()

ax2.legend(scatterpoints=1, ncol=2, fontsize=17.8, loc='upper center',
            **lgd_kws)
ax2.grid()
#ax2.grid(which='minor', lw=0.5)
#sns.despine(bottom=True)
plt.tight_layout()
#pltfile = 'Fig2-JPLUS-PC1-PC3-veri.pdf'
pltfile = 'Fig2-JPLUS-PC1-PC3-WD.pdf'
file_save = os.path.join(save_path, pltfile)
plt.savefig(file_save)
plt.clf()

#####
#PC2 vs PC3 #####
#####

```

```

lgd_kws = {'frameon': True, 'fancybox': True, 'shadow': None}
#sns.set(style="dark")#, context="talk")
#sns.set_style('ticks')
fig = plt.figure(figsize=(12, 8))
ax22 = fig.add_subplot(111)
ax22.yaxis.set_major_formatter(FormatStrFormatter('%%.2f'))
ax22.set_xlim(-9, 10)
ax22.set_ylim(-1.2, 1.5)
plt.tick_params(axis='x', labelsiz=32)
plt.tick_params(axis='y', labelsiz=32)
plt.xlabel(r'PC2', fontsize= 35)
plt.ylabel(r'PC3', fontsize= 35)
#print(A1[0][1], B1[0][1])
AB = np.vstack([pc1[0], pc3[0]])
z = gaussian_kde(AB)(AB)
df=pd.DataFrame({'x': pc1[0], 'y': pc3[0]})

# Sort the points by density, so that the densest points are plotted
last
idx = z.argsort()

for x1, y1 in zip(pc2[0], pc3[0]):
    x11, y11, z = x1[idx], y1[idx], z[idx]
    ax22.scatter(x11, y11, c=z, s=50, zorder=10, alpha=0.5, edgecolor
                = '')
#ax2.scatter(pc1[0], pc3[0], c = sns.xkcd_rgb["indigo"], alpha=0.5, s
            =130, marker='o', edgecolor='black', zorder = 10.0, label='CLOUDY
            modelled halo PNe')
ax22.scatter(pc2[1], pc3[1], color= sns.xkcd_rgb["aqua"], s=130,
            marker='o', edgecolor='black', alpha=0.8, zorder=120.0, label='Obs
            . halo PNe')
ax22.scatter(pc2[4], pc3[4], c = sns.xkcd_rgb['pale yellow'], alpha
            =0.8, s=90, marker='o', edgecolor='black', zorder=3.0, label='SDSS
            CVs')
ax22.scatter(pc2[6], pc3[6], c = "mediumaquamarine", alpha=0.8, s=60,
            edgecolor='black', marker='D', label='SDSS QSOs')
ax22.scatter(pc2[10], pc3[10], c = "goldenrod", alpha=0.8, s=120,
            marker='^', edgecolor='black', label='SDSS SFGs')
ax22.scatter(pc2[2], pc3[2], c = "red", alpha=0.8, s=90, marker='s',
            edgecolor='black', zorder=3.0, label='Obs SySt')
ax22.scatter(pc2[3], pc3[3], c = "red", alpha=0.8, s=120, marker='^',
            edgecolor='black', zorder=3.0, label='IPHAS SySt')
ax22.scatter(pc2[5], pc3[5], c = "gray", alpha=0.8, s=90, marker='D',
            edgecolor='black', label='Obs. HII regions in NGC 55')
ax22.scatter(pc2[7], pc3[7], c = "lightsalmon", alpha=0.8, s=150,
            marker='*', edgecolor='black', label='Obs. YSOs')
ax22.scatter(pc2[8], pc3[8], c = sns.xkcd_rgb["cerulean"], alpha=1.0,
            s=700, marker='*', edgecolor='black', zorder= 113, label='Obs.
            select in J-PLUS DR1')
ax22.scatter(pc2[9], pc3[9], c = sns.xkcd_rgb["light green"], alpha
            =1.0, s=650, marker='*', edgecolor='black', zorder= 113, label='
            HASH sources in J-PLUS DR1')

```

```

ax22.minorticks_on()
ax22.grid()
#ax2.grid(which='minor', lw=0.5)
#sns.despine(bottom=True)
plt.tight_layout()
pltfile = 'Fig3-JPLUS-PC2-PC3-v0.pdf'
file_save = os.path.join(save_path, pltfile)
plt.savefig(file_save)
plt.clf()

#####
#Weights #####
#####

filter_name = ['u', 'J0378', 'J0395', 'J0410', 'J0430', 'g', 'J0515',
              'r', 'J0660', 'i', 'J0861', 'z']
color = ["#CC00FF", "#9900FF", "#6600FF", "#0000FF", "#009999",
        "#006600", "#DD8000", "#FF0000", "#CC0066", "#990033", "#660033",
        "#330034"]
#color = ["#CC0066", "#CC0066", "#CC0066", "#CC0066", "#CC0066", "#
        CC0066", "#CC0066", "#CC0066", "#CC0066", "#CC0066", "#CC0066", "#
        CC0066"]
marker = ["s", "o", "o", "o", "o", "s", "o", "s", "o", "s", "o", "s"]

filter_ = []
for a in range(1, 13):
    filter_.append(a)

plotfile = "jplus-wight1.pdf"
fig = plt.figure(figsize=(14, 9))
ax = fig.add_subplot(1,1,1)
ax.yaxis.set_major_formatter(FormatStrFormatter('%%.2f'))
#ax.set_xlim(-10.0, 8.0)
#ax.set_ylim(-0.30, -0.28)
plt.tick_params(axis='x', labelsize = 32)
plt.tick_params(axis='y', labelsize = 32)
ax.set_xlabel(r'Filters', size = 45)
ax.set_ylabel(r'w$_1$$_', size = 45)
#ax.axhline(y=0, c='k')
for wl, mag, colors, marker_ in zip(filter_, w1, color, marker):
    ax.scatter(wl, mag, color = colors, marker=marker_, s=400, alpha
              =0.8, zorder=3)
plt.xticks(filter_, filter_name, rotation=45)
#plt.xticks(filter_)
file_save = os.path.join(save_path, plotfile)
plt.margins(0.06)
plt.subplots_adjust(bottom=0.17)
plt.tight_layout()
file_save = os.path.join(save_path, plotfile)
plt.savefig(file_save)
plt.clf()

```

```
#####

plotfile = "jplus-wight2.pdf"
fig = plt.figure(figsize=(14, 9))
ax = fig.add_subplot(1,1,1)
ax.yaxis.set_major_formatter(FormatStrFormatter('\%.2f'))
plt.tick_params(axis='x', labelszize = 32)
plt.tick_params(axis='y', labelszize = 32)
ax.set_xlabel(r'Filters', size = 45)
ax.set_ylabel(r'w$_2$ ', size = 45)
ax.axhline(y=0, color='k')
for wl, mag, colors, marker_ in zip(filter_, w2, color, marker):
    ax.scatter(wl, mag, color = colors, marker=marker_, s=400, alpha
              =0.8, zorder=3)
plt.xticks(filter_, filter_name, rotation=45)
file_save = os.path.join(save_path, plotfile)
plt.margins(0.06)
plt.subplots_adjust(bottom=0.17)
plt.tight_layout()
file_save = os.path.join(save_path, plotfile)
plt.savefig(file_save)
plt.clf()
#####

plotfile = "jplus-wight3.pdf"
fig = plt.figure(figsize=(14, 9))
ax = fig.add_subplot(1,1,1)
ax.yaxis.set_major_formatter(FormatStrFormatter('\%.2f'))
ax.set_ylim(-0.7, 0.6)
plt.tick_params(axis='x', labelszize = 32)
plt.tick_params(axis='y', labelszize = 32)
ax.set_xlabel(r'Filters', size = 45)
ax.set_ylabel(r'w$_3$ ', size = 45)
ax.axhline(y=0, c='k')
for wl, mag, colors, marker_ in zip(filter_, w3, color, marker):
    ax.scatter(wl, mag, color = colors, marker=marker_, s=400, alpha
              =0.8, zorder=3)
plt.xticks(filter_, filter_name, rotation=45)
file_save = os.path.join(save_path, plotfile)
plt.margins(0.06)
plt.subplots_adjust(bottom=0.17)
plt.tight_layout()
file_save = os.path.join(save_path, plotfile)
plt.savefig(file_save)
plt.clf()

```

Appendix B

Chemical abundances used to build the PN models

Table B.1 shows the chemical abundances used to computed the models of PNe using CLOUDY. We used the abundances of the PNe: K648, BB-1, DdDm-1, NGC 2242 and 006-41.9. The code input is the abundances of the elements, relative to hydrogen. An example might be $n(O)/n(H) = 4 \times 10^{-4}$. Abundances entered in the table bellow as “-20” are simply values chosen to be small enough to be of no consequence (for more information see Ferland et al., 2013).

| | | Planetary nebulae | | | | |
|---------|------------|-------------------|--------|--------|----------|-------------|
| Element | | K648 | BB-1 | DdDm-1 | NGC 2242 | PN 006-41.9 |
| | | $\log n(x)/n(H)$ | | | | |
| He | Helium | -1.04 | -0.95 | -1.02 | -1.01 | -1.04 |
| Li | Lithium | -20.00 | -20.00 | -20.00 | -20.00 | -20.00 |
| Be | Beryllium | -20.00 | -20.00 | -20.00 | -20.00 | -20.00 |
| B | Boron | -20.00 | -20.00 | -20.00 | -20.00 | -20.00 |
| C | Carbon | -3.50 | -3.15 | -4.80 | -4.15 | -4.00 |
| N | Nitrogen | -5.28 | -3.75 | -4.41 | -4.72 | -3.75 |
| O | Oxygen | -4.39 | -3.94 | -3.88 | -3.81 | -3.94 |
| F | Fluorine | -20.00 | -20.00 | -20.00 | -20.00 | -20.00 |
| Ne | Neon | -5.43 | -4.77 | -4.80 | -4.58 | -4.77 |
| Na | Sodium | -20.00 | -20.00 | -20.00 | -20.00 | -20.00 |
| Mg | Magnesium | -20.00 | -20.00 | -20.00 | -20.00 | -20.00 |
| Al | Aluminum | -20.00 | -20.00 | -20.00 | -20.00 | -20.00 |
| Si | Silicon | -5.00 | -5.00 | -5.00 | -5.00 | -5.00 |
| P | Phosphorus | -20.00 | -20.00 | -20.00 | -20.00 | -20.00 |
| S | Sulfur | -5.89 | -6.50 | -5.40 | -6.00 | -5.00 |
| Cl | Chlorine | -20.00 | -20.00 | -20.00 | -20.00 | -20.00 |
| Ar | Argon | -8.28 | -7.50 | -6.23 | -6.44 | -6.50 |

TABLE B.1: Abundances used to computed the grid of modelled spectra of halo PNe.

Appendix C

J-PLUS AstroQueries

Query implemented to select PN candidates in J-PLUS catalog:

```
SELECT * FROM jplus.MagABDualObj WHERE (MAG_APER_6_0[jplus::J0515] -
MAG_APER_6_0[jplus::J0660]) >= 2.7*(MAG_APER_6_0[jplus::J0515] -
MAG_APER_6_0[jplus::J0861]) + 2.15 AND (MAG_APER_6_0[jplus::J0515] -
MAG_APER_6_0[jplus::J0660]) >= 0.22 AND (MAG_APER_6_0[jplus::zSDSS] -
MAG_APER_6_0[jplus::J0660]) >= 0.35*(MAG_APER_6_0[jplus::zSDSS] -
MAG_APER_6_0[jplus::gSDSS]) + 0.82 AND (MAG_APER_6_0[jplus::zSDSS] -
MAG_APER_6_0[jplus::J0660]) >= -0.8*(MAG_APER_6_0[jplus::zSDSS] -
MAG_APER_6_0[jplus::gSDSS]) + 1.8 AND (MAG_APER_6_0[jplus::rSDSS] -
MAG_APER_6_0[jplus::J0660]) >= 0.43*(MAG_APER_6_0[jplus::rSDSS] -
MAG_APER_6_0[jplus::iSDSS]) + 0.65 AND (MAG_APER_6_0[jplus::rSDSS] -
MAG_APER_6_0[jplus::J0660]) <= -6.8*(MAG_APER_6_0[jplus::rSDSS] -
MAG_APER_6_0[jplus::iSDSS]) - 1.3 AND (MAG_APER_6_0[jplus::J0410] -
MAG_APER_6_0[jplus::J0660]) >= 8.0*(MAG_APER_6_0[jplus::gSDSS] -
MAG_APER_6_0[jplus::iSDSS]) + 4.5 AND (MAG_APER_6_0[jplus::J0410] -
MAG_APER_6_0[jplus::J0660]) >= 0.8*(MAG_APER_6_0[jplus::gSDSS] -
MAG_APER_6_0[jplus::iSDSS]) + 0.55 AND (MAG_APER_6_0[jplus::gSDSS] -
MAG_APER_6_0[jplus::J0515]) <= 0.12*(MAG_APER_6_0[jplus::J0660] -
MAG_APER_6_0[jplus::rSDSS]) - 0.01 AND (MAG_APER_6_0[jplus::gSDSS] -
MAG_APER_6_0[jplus::J0515]) <= -1.1*(MAG_APER_6_0[jplus::J0660] -
MAG_APER_6_0[jplus::rSDSS]) - 1.07 AND MAG_APER_6_0[jplus::rSDSS] < 20.0
AND MAG_ERR_APER_6_0[jplus::rSDSS] <= 0.2 AND
MAG_ERR_APER_6_0[jplus::gSDSS] <= 0.2 AND
MAG_ERR_APER_6_0[jplus::iSDSS] <= 0.2 AND
MAG_ERR_APER_6_0[jplus::zSDSS] <= 0.2 AND
MAG_ERR_APER_6_0[jplus::uJAVA] <= 0.2 AND
MAG_ERR_APER_6_0[jplus::J0378] <= 0.2 AND
MAG_ERR_APER_6_0[jplus::J0395] <= 0.2 AND
MAG_ERR_APER_6_0[jplus::J0410] <= 0.2 AND
```

```

MAG_ERR_APER_6_0[jplus::J0430] <= 0.2 AND
MAG_ERR_APER_6_0[jplus::J0515] <= 0.2 AND
MAG_ERR_APER_6_0[jplus::J0660] <= 0.2 AND
MAG_ERR_APER_6_0[jplus::J0861] <= 0.2 AND
FLAGS[jplus::rSDSS] <= 3.0 AND FLAGS[jplus::gSDSS] <= 3.0
AND FLAGS[jplus::iSDSS] <= 3.0 AND FLAGS[jplus::zSDSS] <= 3.0
AND FLAGS[jplus::uJAVA] <= 3.0 AND FLAGS[jplus::J0378] <= 3.0
AND FLAGS[jplus::J0395] <= 3.0 AND FLAGS[jplus::J0410] <= 3.0
AND FLAGS[jplus::J0430] <= 3.0 AND FLAGS[jplus::J0515] <= 3.0
AND FLAGS[jplus::J0660] <= 3.0 AND FLAGS[jplus::J0861] <= 3.0

```

Query for SySt candidates in J-PLUS catalog:

```

SELECT * FROM jplus.MagABDualObj WHERE MAG_ERR_APER_6_0[jplus::J0515] -
MAG_ERR_APER_6_0[jplus::J0660] <= 5.5*(MAG_ERR_APER_6_0[jplus::J0515] -
MAG_ERR_APER_6_0[jplus::J0861]) - 6.45 AND MAG_ERR_APER_6_0[jplus::J0515] -
MAG_ERR_APER_6_0[jplus::J0660] >= 0.98*(MAG_ERR_APER_6_0[jplus::J0515] -
MAG_ERR_APER_6_0[jplus::J0861]) - 0.16 AND MAG_ERR_APER_6_0[jplus::zSDSS] -
MAG_ERR_APER_6_0[jplus::J0660] <= -1.96*(MAG_ERR_APER_6_0[jplus::zSDSS] -
MAG_ERR_APER_6_0[jplus::gSDSS]) - 3.15 AND MAG_ERR_APER_6_0[jplus::zSDSS] -
MAG_ERR_APER_6_0[jplus::J0660] >= 0.2*(MAG_ERR_APER_6_0[jplus::zSDSS] -
MAG_ERR_APER_6_0[jplus::gSDSS]) + 0.44 AND MAG_ERR_APER_6_0[jplus::rSDSS] -
MAG_ERR_APER_6_0[jplus::J0660] >= -400*(MAG_ERR_APER_6_0[jplus::rSDSS] -
MAG_ERR_APER_6_0[jplus::iSDSS]) + 30.4 AND MAG_ERR_APER_6_0[jplus::rSDSS] -
MAG_ERR_APER_6_0[jplus::J0660] >= 0.39*(MAG_ERR_APER_6_0[jplus::rSDSS] -
MAG_ERR_APER_6_0[jplus::iSDSS]) + 0.73 AND (MAG_ERR_APER_6_0[jplus::J0410] -
MAG_ERR_APER_6_0[jplus::J0660]) >= -5.2*(MAG_ERR_APER_6_0[jplus::gSDSS] -
MAG_ERR_APER_6_0[jplus::iSDSS]) + 10.60 AND MAG_ERR_APER_6_0[jplus::J0410] -
MAG_ERR_APER_6_0[jplus::J0660] >= 1.9*(MAG_ERR_APER_6_0[jplus::gSDSS] -
MAG_ERR_APER_6_0[jplus::iSDSS]) - 1.43 AND MAG_ERR_APER_6_0[jplus::gSDSS] -
MAG_ERR_APER_6_0[jplus::J0515] >= -0.19*(MAG_ERR_APER_6_0[jplus::J0660] -
MAG_ERR_APER_6_0[jplus::rSDSS]) - 0.09 AND MAG_ERR_APER_6_0[jplus::gSDSS] -
MAG_ERR_APER_6_0[jplus::J0515] <= -2.9*(MAG_ERR_APER_6_0[jplus::J0660] -
MAG_ERR_APER_6_0[jplus::rSDSS]) - 2.2 AND MAG_ERR_APER_6_0[jplus::rSDSS] < 20.0
AND MAG_ERR_ISO_GAUSS[jplus::rSDSS] <= 0.2 AND
MAG_ERR_ISO_GAUSS[jplus::gSDSS] <= 0.2 AND
MAG_ERR_ISO_GAUSS[jplus::iSDSS] <= 0.2 AND
MAG_ERR_ISO_GAUSS[jplus::zSDSS] <= 0.2 AND
MAG_ERR_ISO_GAUSS[jplus::uJAVA] <= 0.2 AND
MAG_ERR_ISO_GAUSS[jplus::J0378] <= 0.2 AND
MAG_ERR_ISO_GAUSS[jplus::J0395] <= 0.2 AND

```

```
MAG_ERR_ISO_GAUSS[jplus::J0410] <= 0.2 AND  
MAG_ERR_ISO_GAUSS[jplus::J0430] <= 0.2 AND  
MAG_ERR_ISO_GAUSS[jplus::J0515] <= 0.2 AND  
MAG_ERR_ISO_GAUSS[jplus::J0660] <= 0.2 AND  
MAG_ERR_ISO_GAUSS[jplus::J0861] <= 0.2 AND  
FLAGS[jplus::rSDSS] <= 3.0 AND FLAGS[jplus::gSDSS] <= 3.0  
AND FLAGS[jplus::iSDSS] <= 3.0 AND FLAGS[jplus::zSDSS] <= 3.0  
AND FLAGS[jplus::uJAVA] <= 3.0 AND FLAGS[jplus::J0378] <= 3.0  
AND FLAGS[jplus::J0395] <= 3.0 AND FLAGS[jplus::J0410] <= 3.0  
AND FLAGS[jplus::J0430] <= 3.0 AND FLAGS[jplus::J0515] <= 3.0  
AND FLAGS[jplus::J0660] <= 3.0 AND FLAGS[jplus::J0861] <= 3.0
```

Appendix D

Refereed papers

This list presents the papers that contain my work and published during the PhD project.

1. *J-PLUS: tools to identify compact planetary nebulae in the Javalambre and southern photometric local universe surveys.*
L. A. Gutiérrez-Soto, D. R. Gonçalves, S. Akras, A. Cortesi, C. López-Sanjuan, M. A. Guerrero et al. 2020, *A&A*, 633, A123
2. *Bow shocks, bow waves, and dust waves. IV. Shell shape statistics.*
W. J. Henney, J. A. Tarango-Yong, **L. A. Gutiérrez-Soto** & S. J. Arthur.
Submitted to *MNRAS*.
3. *The Southern Photometric Local Universe Survey (S-PLUS): improved SEDs, morphologies, and redshifts with 12 optical filters.*
C. Mendes de Oliveira, T. Ribeiro, W. Schoenell, A. Kanaan, R. A. Overzier, ... **L. A. Gutiérrez-Soto**, et al. 2019, *MNRAS*, 489, 241.
4. *J-PLUS: The Javalambre Photometric Local Universe Survey.*
A. J. Cenarro, M. Moles, D. Cristóbal-Hornillos, A. Marín-Franch, A. Ederoclite, ... **L. A. Gutiérrez-Soto** et al. 2019, *A&A*, 622, A176.

J-PLUS: Tools to identify compact planetary nebulae in the Javalambre and southern photometric local universe surveys

L. A. Gutiérrez-Soto¹, D. R. Gonçalves¹, S. Akras¹, A. Cortesi², C. López-Sanjuan³, M. A. Guerrero⁴, S. Daflon⁵, M. Borges Fernandes⁵, C. Mendes de Oliveira², A. Ederoclite², L. Sodré Jr², C. B. Pereira⁵, A. Kanaan⁶, A. Werle^{2,6}, H. Vázquez Ramió⁷, J. S. Alcaniz⁵, R. E. Angulo⁷, A. J. Cenarro³, D. Cristóbal-Hornillos⁷, R. A. Dupke^{5,8,9}, C. Hernández-Monteagudo³, A. Marín-Franch⁷, M. Moles⁷, J. Varela³, T. Ribeiro^{10,11}, W. Schoenell¹², A. Alvarez-Candal⁵, L. Galbany^{13,14}, F. M. Jiménez-Esteban^{15,16}, R. Logroño-García⁷ and D. Sobral¹⁷

¹ Observatório do Valongo, Universidade Federal do Rio de Janeiro, Ladeira Pedro Antonio 43, 20080-090 Rio de Janeiro, Brazil
e-mail: lgutierrez@astro.ufrj.br

² Instituto de Astronomia, Geofísica e Ciências Atmosféricas, Universidade de São Paulo, 05508-090 São Paulo, Brazil

³ Centro de Estudios de Física del Cosmos de Aragón (CEFCA), Unidad Asociada al CSIC, Plaza San Juan 1, E-44001 Teruel, Spain

⁴ Instituto de Astrofísica de Andalucía, IAA-CSIC, Granada, Spain

⁵ Observatório Nacional, Rua Gal. José Cristino 77, 20921-400, Rio de Janeiro, RJ, Brazil

⁶ Departamento de Física, Universidade Federal de Santa Catarina, Florianópolis, SC, 88040-900, Brazil

⁷ Centro de Estudios de Física del Cosmos de Aragón, Plaza San Juan 1, 44001 Teruel, Spain

⁸ University of Michigan, Dept. Astronomy, 1085 S. University Ann Arbor, MI 48109, USA.

⁹ University of Alabama, Dept. of Phys. & Astronomy, Gallalee Hall, Tuscaloosa, AL 35401, USA

¹⁰ NOAO, P.O. Box 26732, Tucson, AZ 85726

¹¹ Departamento de Física, Universidade Federal de Sergipe, Av. Marechal Rondon, S/N, 49000-000 São Cristóvão, SE, Brazil

¹² Departamento de Astronomia, Instituto de Física, Universidade Federal do Rio Grande do Sul (UFRGS), Av. Bento Gonçalves 9500, Porto Alegre, RS, Brazil

¹³ PITT PACC, Department of Physics and Astronomy, University of Pittsburgh, Pittsburgh, PA 15260, USA.

¹⁴ Departamento de Física Teórica y del Cosmos, Universidad de Granada, E-18071 Granada, Spain

¹⁵ Departamento de Astrofísica, Centro de Astrobiología (CSIC-INTA), ESAC Campus, Camino Bajo del Castillo s/n, E-28692 Villanueva de la Cañada, Madrid, Spain

¹⁶ Spanish Virtual Observatory, Spain

¹⁷ Department of Physics, Lancaster University, Lancaster, LA1 4YB, UK

Received ?, 2019; accepted ?, 2019

ABSTRACT

Context. From the approximately $\sim 3,500$ planetary nebulae (PNe) discovered in our Galaxy, only 14 are known to be members of the Galactic halo. Nevertheless, a systematic search for halo PNe has never been performed.

Aims. In this study, we present new photometric diagnostic tools to identify compact PNe in the Galactic halo by making use of the novel 12-filter system projects, J-PLUS (Javalambre Photometric Local Universe Survey) and S-PLUS (Southern-Photometric Local Universe Survey).

Methods. We reconstructed the IPHAS (Isaac Newton Telescope (INT) Photometric H α Survey of the Northern Galactic Plane) diagnostic diagram and propose four new ones using i) the J-PLUS and S-PLUS synthetic photometry for a grid of photo-ionisation models of halo PNe, ii) several observed halo PNe, as well as iii) a number of other emission-line objects that resemble PNe. All colour-colour diagnostic diagrams are validated using two known halo PNe observed by J-PLUS during the scientific verification phase and the first data release (DR1) of S-PLUS and the DR1 of J-PLUS.

Results. By applying our criteria to the DR1s ($\sim 1,190$ deg²), we identified one PN candidate. However, optical follow-up spectroscopy proved it to be a H II region belonging to the UGC 5272 galaxy. Here, we also discuss the PN and two H II galaxies recovered by these selection criteria. Finally, the cross-matching with the most updated PNe catalogue (HASH) helped us to highlight the potential of these surveys, since we recover all the known PNe in the observed area.

Conclusions. The tools here proposed to identify PNe and separate them from their emission-line contaminants proved to be very efficient thanks to the combination of many colours, even when applied –like in the present work– to an automatic photometric search that is limited to compact PNe.

Key words. surveys – planetary nebulae: general – ISM: lines and bands – techniques: photometric

1. Introduction

Planetary nebulae (PNe) represent the final stage of the evolution of low-to-intermediate mass stars ($0.8-8.0M_{\odot}$), when the ejected asymptotic giant branch (AGB) and post-AGB material is ionised

by the UV radiation field of the hot and luminous descendant. Due to the high temperature of the central star, a typical PN spectrum shows a great variety of emission lines: not only the recombination lines of the Balmer series and He, but also collisionally excited lines from several elements like O, N, S, Ne, and Ar (e.g.

Figure 1 of Kwitner & Henry 2001). Given the wide range of temperatures of the central stars ($50\text{--}250\times 10^3\text{K}$), some PNe are lower-excitation nebulae, and their spectral characteristics can be very similar to those of H II regions (Osterbrock & Ferland 2006).

The AGB and post-AGB ejecta enrich the interstellar medium (ISM) with heavy elements that were produced during the evolution of the progenitor star. Thus, PNe provide important information about the production and evolution of chemical elements in the local Universe, and even more locally in the Milky Way (for reviews, see Magrini, Stanghellini, & Gonçalves 2012 and Gonçalves 2019).

In the recent past, several surveys have contributed to the discovery of new PNe. The AAO/UKST $H\alpha$ Survey (Parker et al. 2005), later called Macquarie/AAO/Strasbourg $H\alpha$ Planetary Nebula Catalogue (MASH catalogue, Parker et al. 2006), Southern $H\alpha$ Sky Survey Atlas (SHASSA; Gaustad et al. 2001), Wisconsin $H\alpha$ Mapper (WHAM; Haffner et al. 2003), and the Isaac Newton Telescope (INT) Photometric $H\alpha$ Survey of the Northern Galactic Plane (IPHAS; Drew et al. 2005), in which a number of PN candidates have been found in an automated manner (Viironen et al. 2009b,a; Sabin et al. 2010). Small, private surveys have also contributed to the discovery of new Galactic PNe (e.g. Boumis et al. 2003, 2006). The most recent compilation of PNe is published in the Hong Kong/AAO/Strasbourg/ $H\alpha$ PN database (HASH; Parker et al. 2016). To date, HASH contains 2401 true, 447 likely, and 692 possible Galactic PNe. More genuine PNe candidates have been recently reported in the UKIRT Wide-Field Imaging Survey (UWISH2) of the Northern Galactic Plane (Gledhill et al. 2018) and in the CORNISH catalogue (Irbator et al. 2018; Fragkou et al. 2018).

So far, only 14 PNe are confirmed members of the Galactic halo (Otsuka et al. 2015). These are low-metallicity objects, since they come from the oldest population of the Galaxy, with $\log(\text{O}/\text{H}) + 12 < 8.1$ (Peimbert 1978). Their height above the Galactic plane and their kinematics are additional criteria to locate them in the halo. Thus, halo PNe (hPNe) show large vertical distances from the Galactic plane, ~ 7.2 kpc (Otsuka et al. 2015). The understanding of the chemical evolution of the Galaxy can be improved by studying the old and metal-poor PNe located in the halo of our Galaxy, since these stars were born in the earlier phases of Galactic evolution (Otsuka et al. 2015).

The Javalambre Photometric Local Universe Survey (J-PLUS¹, Cenarro et al. 2019) and the Southern-Photometric Local Universe Survey (S-PLUS², Mendes de Oliveira et al. 2019) provide observations of the Galactic halo covering both northern and southern celestial hemispheres in a systematic way with twin telescopes using the same set of multi-band filters. In addition to the $H\alpha$ filter, which is already vastly applied to systematically searching for $H\alpha$ emitters such as PNe and symbiotic stars (SySt), the telescopes offer 11 more filters. In this work, we present and discuss new colour-colour diagnostic diagrams based on the available filters from J-PLUS and S-PLUS projects to identify halo planetary nebulae. Our main goal is to validate these tools, in addition to applying them to very first J-PLUS and S-PLUS data covering about $1,190\text{ deg}^2$ of the sky. We show that the J-PLUS and S-PLUS filter configuration provide a characterisation of the whole optical spectra of the sources and their potential to such an end with the completion of the surveys, thus opening new horizons for the search of PNe and SySt and other emission line systems.

¹ <https://www.j-plus.es>

² <http://www.splus.iag.usp.br>

Our paper is organised as follows: in Section 2, we summarise the observations related to J-PLUS and S-PLUS projects, as well as important information of the first data release for each survey. In Section 3, the synthetic photometry of the different emission-line sources are explored. Section 4 describes our selection method and the new diagnostic diagrams. Section 5 presents the validation of the colour-colour diagrams, using known hPNe observed by J-PLUS, and in terms of sources we recovered within the DR1 area, the PN candidate selected with our methodology. In Section 6 the results obtained after cross-match the J-PLUS and S-PLUS data with the HASH catalogue are discussed. In Section 7, we provide a general discussion and conclusions.

2. Observations

J-PLUS is a multi-filter imaging survey, which is being carried out from the Observatorio Astrofísico de Javalambre (OAJ, Cenarro et al. 2014), using the 83 cm Javalambre Auxiliary Survey Telescope (JAST/T80) and the T80Cam camera. This survey, which maps the northern sky, has a southern counterpart, the S-PLUS. The latter uses a twin telescope, the T80-South, located at the Cerro Tololo Interamerican Observatory (CTIO), in Chile. Both telescopes are equipped with cameras that provide a $\sim 2.0\text{ deg}^2$ field of view (FoV) of the sky, and each covers an area of around $8,500\text{ deg}^2$ in total. Their filter systems are made up of 12 filters spanning the optical range from $3,000$ to $10,000\text{Å}$, approximately. Although the prime goal of the J-PLUS survey is to perform the photometric calibration for the Javalambre Physics of the Accelerating Universe Astrophysical Survey (J-PAS; Benítez et al. 2015), it also provides a rich set of photometric data allowing the investigation of many classes of objects in the Galactic halo and in the local universe. For example, given their multi-filter configuration, they can be used to search for emission-line sources as done by previous narrow-band surveys.

J-PLUS and S-PLUS filter sets are formed of seven narrow-band filters; $J0378$, $J0395$, $J0410$, $J0430$, $J0515$, $J0660$ and $J0861$. They also include five broad-band Sloan Digital Sky Survey (SDSS) like filters (u , g , r , i and z , Fukugita et al. 1996), which are designed to detect the continuum of the sources. Table 3 and Table 2 of J-PLUS and S-PLUS Papers 0 (Cenarro et al. 2019; Mendes de Oliveira et al. 2019) specify the characteristics of the filters of the surveys, and the features targeted by the narrow-band ones. The data used here come from J-PLUS scientific verification data, the first J-PLUS data release, and the first S-PLUS data release.

The J-PLUS survey is growing at $\sim 1,000\text{ deg}^2/\text{year}$. Given the present rate of completion of the S-PLUS tiles, we anticipate that $4,500\text{ deg}^2$ may be covered by the end of 2020, and the full survey should be completed by the middle of 2023.

2.1. J-PLUS scientific verification data

These scientific verification data (SVD) comprise a group of well-known objects to test and challenge the scientific capabilities of J-PLUS (Cenarro et al. 2019). The J-PLUS SVD published observations of the galaxy clusters A2589 and A2593, M101, M49, the Arp313 triplet of galaxies, and a few nearby galaxies, including NGC 4470 and the Coma cluster. The Galactic PNe H 4-1 (Miller 1969) and PNG 135.9+55.9 (Tovmassian et al. 2001) were also included within these data.

2.2. First J-PLUS data release

The J-PLUS first data release (DR1³) is composed of 511 fields observed with the 12 narrow- and broad-band filters, and it covered 1,022 deg² of the sky. DR1 is based on images collected by the JAST/T80 telescope from November 2015 to January 2018. Around nine million objects are included in this first data release. The limiting magnitudes (5σ , 3'' aperture) in each filter are presented in Table 4 of Cenarro et al. (2019). The median point spread function (PSF) in the DR1 r-band images is 1.1''. The detection of the sources was done in the r-band using SExtractor (Bertin & Arnouts 1996), and the photometry in the 12 J-PLUS bands at the position of the detected sources was made using the aperture defined in the r-band image. Different types of apertures were used to perform the photometry: i) circular aperture photometry (SExtractor's MAG_APER) with apertures of different sizes (3'' and 6''), ii) isophotal photometry (SExtractor's MAG_ISO), iii) Kron photometry (SExtractor's MAG_AUTO), iv) Petrosian photometry (SExtractor's MAG_PETRO), v) photometry after degrading the images of all the bands to the worst PSF, vi) photometry after convolving all the images with a Gaussian kernel of $\sigma=1.5''$, and vii) photometry applying a PSF correction as that applied in (Molino et al. 2014). In the present work, we use the 6'' aperture. This choice follows the automatic method used by IPHAS photometry to find compact PNe, with a small angular diameter (typically $\leq 5''$, Viironen et al. 2009a). The 6''-aperture chosen also follows Akras, Guzman-Ramirez, & Gonçalves (2019c), who found that PNe with angular sizes larger than 6'' exhibit very low ($r - H\alpha$) colour index.

2.3. First S-PLUS data release

The S-PLUS DR1⁴ includes 80 fields of the Stripe-82 area, a rectangular area with coordinates $4^h < RA < 20^h$ and $-1.26^\circ < Dec < 1.26^\circ$. These fields were observed during the scientific validation process of the survey. DR1 contains about one million sources, and the limiting magnitude of each filter is presented in Table 8 of the S-PLUS presentation paper (Mendes de Oliveira et al. 2019). Sources were detected using SExtractor. Photometry was performed by adopting three types of aperture: i) a circular aperture of 3'' in diameter (SExtractor's APER), ii) Kron photometry (SExtractor's AUTO), and iii) petrosian photometry (SExtractor's PETRO). Similarly to the case of J-PLUS, we use the circular aperture of 3''. This aperture is the best within the three possibilities, since – in addition to the arguments given in Section 2.2 – it ensures that large objects with high surface brightness, like emission-line galaxies or H II regions, are not recovered (with this automated method).

The tools we use to identify PNe in the two surveys are synthetic photometry and colour-colour diagrams, which we describe in detail in the following sections.

3. Synthetic photometry

In order to recover the synthetic photometry of PNe and their contaminants, we follow the procedure developed by Aparicio Villegas et al. (2010), who characterised the ALHAMBRA photometric system. The magnitudes of any photometric system are defined by a set of AB magnitudes (Oke & Gunn 1983):

$$AB_\nu = -2.5 \log f_\nu - 48.6, \quad (1)$$

³ https://www.j-plus.es/datareleases/data_release_dr1

⁴ <https://datalab.noao.edu/splus/>

where the constant is obtained from the equation

$$48.6 = -2.5 \log F_0 \quad (2)$$

$F_0 = 3.63 \times 10^{-20} \text{ erg s}^{-1} \text{ cm}^{-2} \text{ Hz}^{-1}$ being the flux of Vega at $\lambda = 5,500 \text{ \AA}$. The term f_ν is the flux per unit of frequency [$\text{erg s}^{-1} \text{ cm}^{-2} \text{ Hz}^{-1}$].

The synthetic photometry is obtained from the convolution of the observed or modelled spectra with the transmission function or pass-band of a specific photometric system. The transmission function accounts for the transmission filter, the reflectivity of the telescope mirror, the transmission of the camera optics and the quantum efficiency of the detector used (Bessell 2005). By considering these characteristics of the photometric system, Eq. 1 turns to

$$AB_\lambda = -2.5 \log \frac{1}{c} \frac{\int f_\lambda S_\lambda d\lambda}{\int S_\lambda d\lambda/\lambda} - 48.60, \quad (3)$$

where c is the light speed, S_ν is the transmission function, and the units of f_λ are [$\text{erg s}^{-1} \text{ cm}^{-2} \text{ \AA}^{-1}$]. Therefore, Eq. 3 makes it possible to estimate the synthetic photometry (AB magnitude) in a specific photometric system.

The synthetic photometry or photo-spectra of several emission-line sources – PNe, SySt, cataclysmic variables (CVs), quasi-stellar objects (QSO), extragalactic H II regions, young stellar objects (YSOs), B[e] stars, and star-forming galaxies (SFGs) – were obtained through the convolution of the theoretical transmission curves of the J-PLUS and S-PLUS systems with the available optical spectra, as in Eq. 3.

The same procedure was also applied to a grid of photoionisation models for hPNe to obtain their synthetic magnitudes. For the hPN modelling, we adopted the photoionisation code, CLOUDY (Ferland et al. 2013). The initial parameters used to compute the models reflect the typical properties of the PN population located in the Galactic halo. They represent different sets of nebular abundances, with electron densities of $1,000 \text{ cm}^{-3}$, $3,000 \text{ cm}^{-3}$ and $6,000 \text{ cm}^{-3}$, of a spherically symmetric nebula with a radius of $2.7''$, at distance of 10 kpc. Central star (black body) effective temperatures from 50,000 K to 250,000 K, in steps of 10×10^3 K, and luminosities of 500, 1,000, 5,000 and 10,000 L_\odot were considered. We reddened the modelled spectra applying the reddening curve by Fitzpatrick (1999), and using two different colour excesses, $E(B - V) = 0.1$ and 0.2 , following the J-PLUS and S-PLUS average extinction of $E(B - V) = 0.1$ (Cenarro et al. 2019; Mendes de Oliveira et al. 2019).

Figure 1 comprises all synthetic photo-spectra recovered as explained above. Panels (a) and (b) display the photo-spectra of the Galactic hPN DdDm 1 (Kwitter & Henry 1998), and of an extragalactic PN located in NGC 205 (Gonçalves et al. 2014), as examples. Both objects show strong $H\alpha$ emission, with a continuum a little more intense in the blue than in the red part of the spectrum. Panels (c) and (d) show two CLOUDY modelled hPNe. Both have the same chemical abundance (equivalent to that of the hPN DdDm 1), and the same luminosity of $10^4 L_\odot$. The effective temperature and density of the model in panel (c) are of 60×10^3 K and $1,000 \text{ cm}^{-3}$ and for the model in panel (d) of 200×10^3 K and $6,000 \text{ cm}^{-3}$, respectively. So, the first model (panel c) corresponds to a low-excitation PN. The ionising star is not hot enough to produce such an [O III] emission able to stand out significantly in the g broad-band magnitude. The second model (panel d) represents a high-excitation PN. In this case, the magnitude of the g broad-band filter is impacted by the strong [O III] and [He II] emission lines. Note that the g-band also includes the $H\beta$ line, therefore

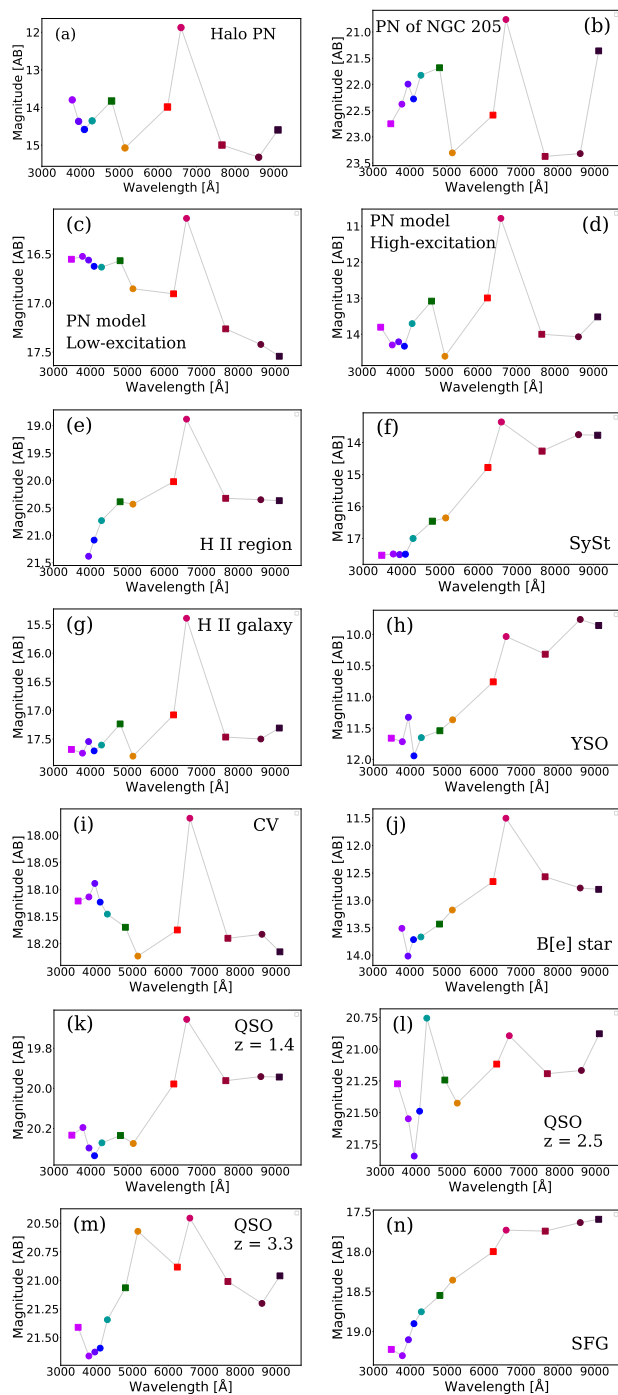


Fig. 1. J-PLUS and S-PLUS synthetic photo-spectra of several emission-line objects. The DdDm 1 PN (a). A PN in the dwarf galaxy NGC 205 (b). Two `CLOUDY` modelled PNe with $T_{\text{eff}}=60\times 10^3$ K and 200×10^3 K, and H density of 1000 cm^{-3} and 3000 cm^{-3} , which concern the abundances of the hPN DdDm 1 and $L=10,000 L_{\odot}$, (c, d). A H II region in the nearby galaxy NGC 55 (e). The SySt LMC 1 (f). The H II galaxy Mrk 1318 (g) from SDSS. The YSO RU Lup (h). A CV (i) from SDSS. A B[e] star (j). QSOs with redshift of 1.4 (k), $z = 2.5$ (l), and $z = 3.3$ (m), where the strong emission in the $J0660$ filter, is caused by the Mg II $\lambda 2798$, C III] $\lambda 1909$ and C IV $\lambda 1550$ emission lines, respectively. And, a star-forming galaxy (n). For this object, the $H\alpha$ line is responsible for the $J0660$ magnitude. Squares represent the SDSS-like broad-band filters. From left to right they are u , g , r , i , and z . Circles are the narrow-band filters, $J0378$, $J0395$, $J0410$, $J0515$, $J0660$, and $J0861$, from left to right.

it is not possible to disentangle the $H\beta$ and $[O\text{ III}]$ emission lines in the J-PLUS and S-PLUS photo-spectra and to quantify the level of excitation more precisely. The hPNe (modelled or observed) differ from Galactic-disc PNe in size, velocity, distance, and extinction (Howard et al. 1997; Otsuka et al. 2015). All the properties – high distances implying small angular sizes, poor in metals and low extinction – of hPNe, with the exception of the large velocities, make them occupy a specific locus in the colour-colour diagrams, significantly different to that of the disc PNe.

In addition to PNe, we also computed the photo-spectra of a number of other emission-line sources that mimic PNe. Panel (e) of Figure 1 shows the photo-spectrum of an extragalactic H II region located in the dwarf galaxy NGC 55 (Magrini et al. 2017), in which the $H\alpha$ emission is also perceptible. The low-excitation PN (on panel c) and the H II region show very similar photo-spectra, which will make them hard to distinguish within the J-PLUS and S-PLUS catalogues. Merrett et al. (2006) have shown that for low-luminosity objects, it is hard to distinguish PNe and H II regions, using the ratio between $[O\text{ III}]$ and $H\alpha+[N\text{ II}]$ emission lines. We encounter the same problem here, even using a wider range of wavelengths. We further investigate this issue, including morphological criteria, in Section 5. With the exception of the morphology, the same difficulty occurs for H II galaxies, as is shown in panel g, for a SDSS H II galaxy. At this point, it should be noted that the synthetic photometric magnitudes are below the limiting magnitudes for all the filters bluer than $4,500\text{ \AA}$, in the case of the extragalactic PN (panel b), and for u and $J0378$ filters in the case of the extragalactic H II region (panel e).

Panel (f) of Figure 1 presents the photo-spectrum of the SySt LMC1 (Munari & Zwitter 2002), displaying a clear $H\alpha$ emission with an increasing continuum to the longer wavelengths. The resolution of the J-PLUS and S-PLUS photometry allows to perceive undoubtedly the reddened nature of the SySt. As PNe, symbiotic stars are also constituted by an evolved star, in most cases a white dwarf (WD). They are interacting binary systems with a cold giant companion (red giant or Mira star) and an evolved hot star. The wind of the giant is ionized by the UV radiation from the evolved companion, thus resulting in a spectrum composed by both absorption features from the stellar photo-sphere of the giant (e.g. TiO and VO), and emission line features from the excited ions (Munari & Zwitter 2002; Corradi, Mikolajewska, & Mahoney 2003; Rodríguez-Flores et al. 2014; Iłkiewicz & Mikolajewska 2017; Akras et al. 2019; Angeloni et al. 2019). The photo-spectrum of a cataclysmic variable (CV) selected from the SDSS catalogue is also presented in Figure 1 (panel i). Cataclysmic variables are interacting binary systems, in which a white dwarf accretes gas from a main-sequence star, via Roche lobe outflow, forming an accretion disc. The Balmer lines are produced in the optically thin outer regions of the disc (Williams 1980). It is simple to notice that based on their photo-spectra, PNe of high and low excitation could be mistaken for CVs. Panel (h) brings the convolution results for a YSO, from Alcalá et al. (2014). An accretion disc, from where the $H\alpha$ emission emerges, is also present in this type of (pre-main-sequence) stars. The YSO's photometry shows a continuum that is stronger in the red part of the spectrum. Panel (j) displays a B[e] star (Lamers et al. 1998). B[e] stars have a surrounding nebula produced by large-scale mass loss involving one or more eruptions (Marston & McCollum 2006). Its photo-spectrum resembles that of both SySt and YSOs.

The J-PLUS and S-PLUS synthetic spectra of several SDSS QSOs, in specific redshift (z) ranges, were also included in our selection of emission-line objects. The QSOs in the redshift ranges

$1.3 < z < 1.4$, $2.4 < z < 2.6$, and $3.2 < z < 3.4$ possess features that resemble those of PNe, in other words, they could be misinterpreted as $H\alpha$ line emission at $z = 0$. At these redshift ranges, respectively, the $C\text{ IV } 1550 \text{ \AA}$, $C\text{ III] } 1909 \text{ \AA}$ and $Mg\text{ II } 2798 \text{ \AA}$ emission lines of QSOs fall into the $J0660$ ($H\alpha$) filter. In panel (k) of Figure 1, we have a QSO at $z = 1.4$, in which the excess of emission in the $J0660$ filter comes from the contribution of the $Mg\text{ II}$ emission line. Two more QSOs are presented in Figure 1: at $z = 2.5$ (panel l) and $z = 3.3$ (panel m). At these redshifts, the $C\text{ III]}$ and $C\text{ IV}$ emission lines are also detected in the $J0660$ band. The magnitudes of the $J0430$ band for the QSO at $z = 2.5$, and of the $J0515$ band for the QSOs at $z = 3.3$, indicate strong emissions, which are provided by the $L\alpha$ emission in both cases. Panel (n) of Figure 1 shows a star-forming galaxy from the SDSS. Its photo-spectrum exhibits a moderate $H\alpha$ emission and a continuum increasing for longer wavelengths. This is because these objects are embedded in hot gas and dust. Despite the fact that QSOs have strong emission lines that can be misidentified as $H\alpha$, their photo spectra are only moderately similar to those of PNe. It is worth mentioning that J-PLUS and S-PLUS can characterise not only the strong emission lines, but also the continua of these objects, thus allowing us to correctly differentiate QSO from PNe, which was a problematic task in projects dedicated to the search of PNe, which were using a fewer filters. Finally, we note that SFGs and YSOs have photo-spectra that are very different from those presented in Panel a and Panel b, and so they do not cause much impact on our research work.

4. Synthetic colour-colour diagrams: selection criteria

The photo-spectra of the emission-line sources just discussed in Figures 1 – for PNe, SySt, CVs, B[e], QSOs, extragalactic $H\text{ II}$ regions, YSOs, and SFGs – are now used to build diagnostic colour-colour diagrams. Our goal is to pinpoint the most relevant ones to discriminate PNe from the above systems.

4.1. IPHAS equivalent colour-colour diagram

Drew et al. (2005) designed the IPHAS survey (see Section 1) showing that the $(r' - H\alpha)$ vs $(r' - i)$ diagram is an optimal tool to select strong $H\alpha$ emission-line sources (Witham et al. 2008). IPHAS PNe candidates were selected using the above colour-colour diagram as well as the common $(J - H)$ vs $(H - K_s)$ 2MASS diagram. Their true nature was confirmed later on, spectroscopically (Corradi et al. 2008; Viironen et al. 2009b; Rodríguez-Flores et al. 2014; Sabin et al. 2014).

Given that the J-PLUS and S-PLUS filter systems include the three IPHAS filters, we reconstructed the IPHAS equivalent diagram in Figure 2. The $(r - J0660)$ colour clearly indicates an increasing excess of the $H\alpha$ emission line, while the $(r - i)$ one increases with the reddening, as previously stated in Corradi et al. (2008). Modelled PNe are found to display $(r - J0660) > 0.6$ due to their strong $H\alpha$ emission lines as well as $(r - i) < 0$. It should be noted that Figure 1 of Viironen et al. (2009b) shows that Galactic disc PNe have $(r - i) < 1$, so they are redder than the hPNe. The empirical (black) lines delimit the selection criteria for being PNe (PNe zone) and are meant to include most of the modelled hPNe and exclude the majority of the contaminants. The definition of the selection criteria or zones has been made visually. This holds for the IPHAS equivalent as well as the new colour-colour diagrams of the present study. The PNe zone is contaminated by extragalactic $H\text{ II}$ regions, especially for moderately lower

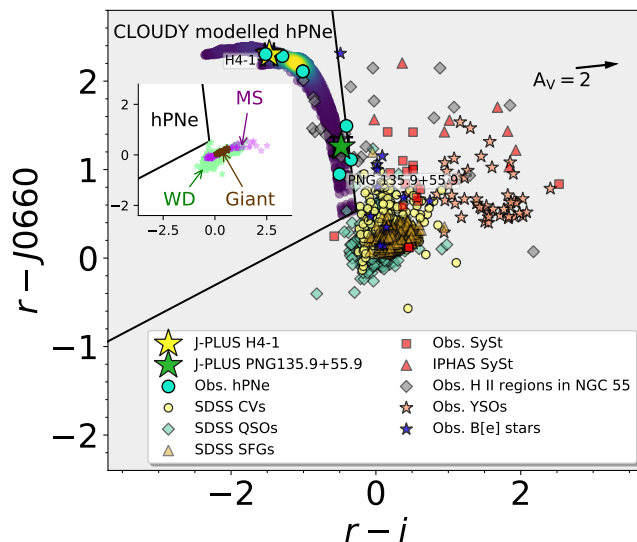


Fig. 2. J-PLUS and S-PLUS $(r - J0660)$ vs $(r - i)$ colour-colour diagram, equivalent to IPHAS $(r' - H\alpha)$ vs. $(r' - i')$. The big yellow and green stars with error-bars are the J-PLUS observations for H 4-1 and PNG 135.9+55.9, respectively. Included in the diagrams, there are families of *CLOUDY* modelled hPNe spanning a range of properties (density map region). Cyan circles represent hPN PNG 135.9+55.9 spectrum from SDSS, DdDM-1 (Kwitter & Henry 1998), NGC 2022, BB-1, H4-1 (Kwitter et al. 2003), and MWC 574 (Pereira & Miranda 2007). Grey diamonds represent $H\text{ II}$ regions in NGC 55 (Magrini, Gonçalves, & Vajgel 2017). Red boxes display Munari & Zwitter (2002); Munari & Jurdana-Šepić (2002) SySt, this group also includes external SySt from NGC 205 (Gonçalves et al. 2015), IC 10 (Gonçalves et al. 2008) and NGC 185 (Gonçalves et al. 2012), and red triangles correspond to IPHAS symbiotic stars (Rodríguez-Flores et al. 2014). Yellow circles correspond to cataclysmic variables (CVs) from SDSS. Orange triangles refer to SDSS star-forming galaxies (SDSS SFGs). SDSS QSOs at different redshift ranges are shown as light blue diamonds, and YSOs from Lupus and Sigma Orionis (Rigliaco et al. 2012; Alcalá et al. 2014) are represented by salmon stars. Blue stars refer to B[e] stars from Lamers et al. (1998). In the inset plot, the synthetic main sequence and giant stars loci from the library of stellar spectral energy distributions (SEDs, Pickles 1998) are represented by the purple and brown symbols, and the loci of white dwarf stars observed by S-PLUS (DR1, Mendes de Oliveira et al. 2019) are represented by the light green symbols. The limiting region applied in the candidate selection is shown by black lines for hPNe. The arrow indicates the reddening vector with $A_V \simeq 2$ mag. It was estimated by comparing the locus of unreddened models of PNe with the reddened ones.

$(r - J0660)$ colour indices or, equivalently, low-excitation nebulae. Therefore, our lists of PN candidates are not characterised by high purity. The distribution of main sequence (MS) and giant stars (purple and brown symbols in the inset figures) in the $(r - J0660)$ vs $(r - i)$ diagnostic diagram is such that both groups of stars occupy regions with lower $(r - J0660)$ index (< 1.2) and higher $(r - i)$ index (> 0) than the PNe zone (Drew et al. 2005; Corradi et al. 2008). White dwarf (WD) stars (light green symbols in inset figures) also present low $(r - J0660)$ index (> 0), however exhibit $(r - i)$ colour > -1 . Thus, there is no mixing between PNe and the bulk of MS, giant and WD stars. The observed PNe are well located in the PNe zone with high $(r - J0660) > 1$ (see also Viironen et al. 2009b,a).

4.2. New J-PLUS and S-PLUS colour-colour diagrams

Studying the photo-spectra of the PNe and their contaminants (Section 3), four new colour-colour diagrams were defined ($J0515 - J0660$) vs ($J0515 - J0861$), ($g - J0515$) vs ($J0660 - r$), ($z - J0660$) vs ($z - g$), and ($J0410 - J0660$) vs. ($g - i$) to search for PN candidates in the J-PLUS and S-PLUS catalogues.

In the first diagnostic diagram, high- and low-excitation PNe occupy distinct regions within the PNe zone. For instance, H 4-1, a moderate high-ionisation PN, exhibits ($g - J0515$) ≈ -2 , with T_{eff} around 132×10^3 K (Henry et al. (1996)), and MWC 574, a very low-excitation PN with ($g - J0515$) ≈ 0.0 , exhibits an [O III] emission even weaker than H β (Sanduleak & Stephenson 1972; Pereira & Miranda 2007). The ($J0515 - J0861$) colour index is associated with the continuum of the sources. Neither of these two filters contains strong emission lines. The ($J0515 - J0660$) colour provides an estimation of the H α excess.

Regarding the second diagnostic diagram, the ($g - J0515$) colour index yields the excess of the [O III] lines. Therefore, the higher the ($g - J0515$) colour, the higher the excitation of the nebula. This can be seen from the photo-spectra of two CLOUDY models with different stellar temperatures (panels *c* and *d* in Figure 1). We remind the reader, however, that the *g* broad-band filter is also affected by the H β and other emission lines down to about 4,000Å. The ($J0660 - r$) colour is to illustrate the H α emission as it has been explained in the previous section.

The ($z - J0660$) colour index also gives us an estimation of the H α excess, by taking into account the continuum at the very red part of the spectrum, while the ($z - g$) colour is directly related to the shape of the continuum from the blue to the red part of the spectrum. The QSOs and SFGs are concentrated in a very small area ($-2 < (z - J0660) < 1$ and $-2 < (z - g) < 1$), well separated from PNe.

Finally, ($g - i$) is another colour index associated with the shape of the continuum, and the ($J0410 - J0660$) colour reflects the H α excess, though using different parts of the spectrum in contrast with the previous diagrams. From panel *d* in Figure 3, we find that QSOs and SFGs show an increase in the ($J0410 - J0660$) colour as a function of the ($g - i$) colour, while PNe appear to have a more restricted range of ($g - i$) values between -2 and 0, and ($J0410 - J0660$) values from 0 to 4. Hence, the ($J0410 - J0660$) vs ($g - i$) colour-colour diagram can distinguish PNe from galaxies. The SySt and YSOs are found to lie in the right part of the plot ($(g - i) > 2$), which is indicative of their stronger emission in the near-IR. This last diagnostic diagram turns out to be very useful to assure low contamination by B[e] stars, differing from the first three diagrams.

Figure 3 and the colour-colour diagrams also show the loci of main sequence, giant and white dwarf stars, which clearly do not affect the PN selection criteria. Leaving aside the H II regions, all the colour-colour diagrams turned out to be very useful for identifying good PN and SySt candidates (a detailed analysis for SySt is to be presented in a forthcoming paper). The combination of several narrow- and broad-band filters to construct colour-colour diagrams allows characterising the whole optical spectrum of every source type. If a source simultaneously satisfies all the criteria of being a PN, the possibility of false positive identification, though not negligible, is small.

5. Validation of the colour-colour diagrams

Aiming to validate the tools to search for PNe in J-PLUS and S-PLUS, we followed two different methods. The first is to use the J-PLUS SVD (Section 2.1) and the second is by applying

Table 1. Synthetic and observed magnitudes of H 4-1 and PNG 135.9+55.9, for the 12 J-PLUS filters.

| Filter | H 4-1 | | PNG 135.9+55.9 | |
|--------------|-------|------------------|----------------|------------------|
| | Synt. | Obs. | Synt. | Obs. |
| <i>u</i> | 15.74 | 16.14 \pm 0.13 | 17.37 | 17.22 \pm 0.10 |
| <i>J0378</i> | 15.54 | 15.77 \pm 0.02 | 17.36 | 17.31 |
| <i>J0395</i> | 17.01 | 16.97 \pm 0.06 | 17.35 | 17.28 \pm 0.12 |
| <i>J0410</i> | 17.14 | 17.11 \pm 0.03 | 17.43 | 17.43 \pm 0.10 |
| <i>J0430</i> | 16.61 | 16.68 \pm 0.07 | 17.48 | 17.48 \pm 0.13 |
| <i>g</i> | 15.59 | 15.61 \pm 0.04 | 17.62 | 17.74 \pm 0.07 |
| <i>J0515</i> | 17.63 | 17.62 \pm 0.04 | 17.86 | 17.80 \pm 0.07 |
| <i>r</i> | 15.75 | 15.77 \pm 0.04 | 17.97 | 17.92 \pm 0.07 |
| <i>J0660</i> | 13.45 | 13.47 \pm 0.04 | 17.02 | 16.66 \pm 0.08 |
| <i>i</i> | 17.28 | 17.24 \pm 0.05 | 18.47 | 18.40 \pm 0.07 |
| <i>J0861</i> | 17.44 | 17.60 \pm 0.03 | 18.69 | 18.55 \pm 0.07 |
| <i>z</i> | 17.23 | 17.30 \pm 0.09 | 18.72 | 18.61 \pm 0.10 |

the previously presented selection criteria (Section 4) to the DR1 (very limited in area) of each of these surveys.

5.1. SVD validation

Two hPNe, H 4-1 and PNG 135.9+55.9, were observed during the scientific verification phase of the J-PLUS, as described in Section 2.1. The instrumental magnitudes were calculated for each object using IRAF⁵. In order to find the calibrated magnitudes, we used the zero point provided by the unit of processing and data analysis (UPAD) inside the J-PLUS collaboration. The resulting photo-spectra are shown in Figure 15 of the J-PLUS presentation paper (Cenarro et al. 2019). In Table 1, we compare the synthetic and observed magnitudes of these hPNe. For H 4-1, the two magnitudes are very compatible, with a difference smaller than 0.07, except for the *u* and *J0378* filters, whose differences are 0.4 and 0.23, respectively. As for PNG 135.9+55.9, the synthetic and observed magnitudes are found to be in very good agreement, with, on average, a difference smaller than 0.1 mag. The only discrepant magnitude is the one of the *J0660* filter, for which the difference reaches 0.35 mag.

The positions of H 4-1 and PNG 135.9+55.9 in the colour-colour diagrams –based on their J-PLUS observations– are shown in Figures 2 and 3 as yellow and green stars, respectively. H 4-1 satisfies all five criteria of being a PN (see Figures 2 and 3), while PNG 135.9+55.9 passes four of them, violating the ($g - J0515$) colour criterion given in panel (*b*) of Figure 3. We note, however, that this PN is located close to the border of the PN zone. This border was defined in a conservative way, to avoid more contamination of H II regions and SySt, since low-excitation PNe and H II regions are extremely hard to differentiate.

5.2. DR1 validation

In order to apply the colour-colour diagrams to the J-PLUS and S-PLUS data releases, there are a few cleaning instructions (FLAGS) that need to be considered, since they avoid artefacts. For J-PLUS, we used two FLAGS. One responsible for excluding the objects that have neighbours, bright and close enough to significantly affect the photometry, or that have bad pixels (more than 10% of the integrated area affected). The other FLAG allows us to exclude objects originally blended with another one. In the case of S-PLUS, only one FLAG was applied, which avoids

⁵ Image Reduction and Analysis Facility; <http://iraf.noao.edu/>

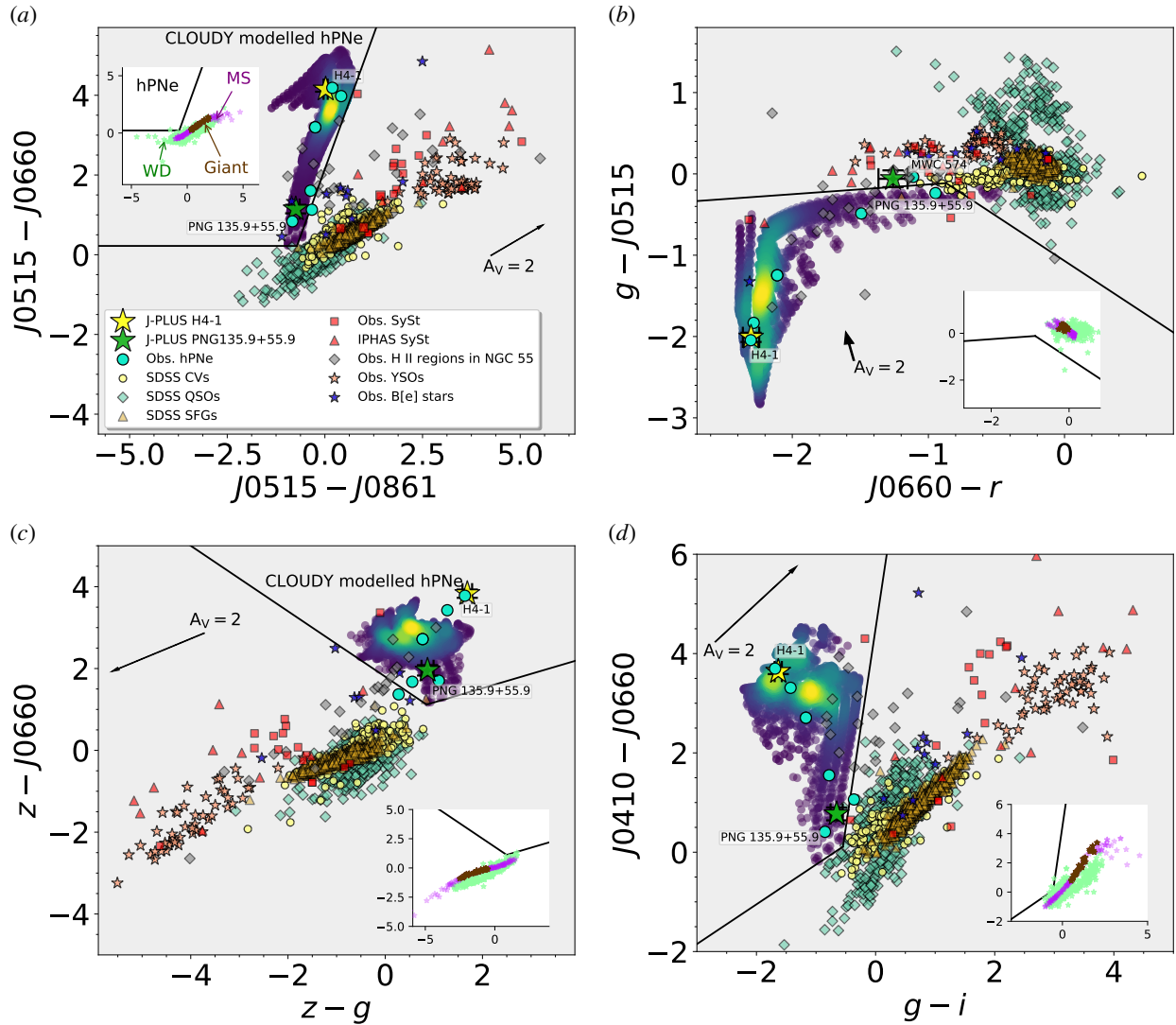


Fig. 3. J-PLUS and S-PLUS (a) ($J0515 - J0660$) vs ($J0515 - J0861$), (b) ($g - J0515$) vs ($J0660 - r$), (c) ($z - J0660$) vs ($z - g$), and (d) ($J0410 - J0660$) vs ($g - i$) colour-colour diagrams. The error bars are smaller than the symbols. The arrows indicate the reddening vectors with $A_V \approx 2$ mag. The symbols are the same as in Figure 2.

the objects for which the aperture photometry is likely biased by neighbour sources or by more than 10% of bad pixels. Note that not considering the sources flagged with these known issues affects the selection, because of the quality of the photometry.

To encounter the best way of applying all five selection criteria described in Section 4, we follow a few validating steps, using the J-PLUS data set. To ensure the recovery of the largest amount of potential candidates due to lack of detection in some filters, we explore how the limiting magnitude errors for different sets of filters affect the results: (i) by limiting the error associated with the magnitudes corresponding to IPHAS-like magnitudes (i , r and $J0660$), and admitting any error for the other 9 photometries, (ii) by limiting the magnitude errors of the $J0660$ and broad-band filters, and finally, (iii) by limiting the magnitude errors of all narrow- and broad-band filters. Whenever it applies, the limiting magnitude error is ± 0.2 . All the procedure was performed with the 6'' aperture.

Since option (i) is the least restrictive of all, it returned a higher number of sources, nine in total. With this option, we

are allowing sources that are faint in any other band (high uncertain photometry) or even not detected at all, except in i , r , and $J0660$ bands. Among the selected sources, which are known objects and classified either by the Set of Identifications, Measurements and Bibliography for Astronomical Data (SIMBAD) or the NASA/IPAC Extragalactic Database (NED), there are four H II regions, two H II galaxies, one WR star, and one PN. An additional source (NED/SDSS 'extended or galaxy') that also matches all criteria, but for which a detailed search in the literature does not show any further information (not even redshift or recession velocity), was identified as a PN candidate.

To test whether further limitations would minimise the number of contaminants, we use step (ii) of the validation process. This option accounts for the fact that the continuum of PNe is usually faint, with the consequence of uncertain photometry (large errors) in the narrow-band filters. Therefore, this time we limited the errors in the $H\alpha$ and broad-band magnitudes. Four sources are returned in this case, they are the two known H II galaxies, the

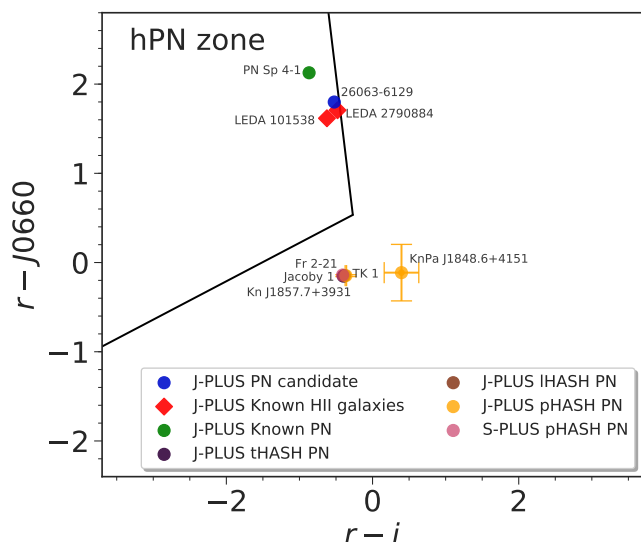


Fig. 4. J-PLUS ($r - J0660$) vs ($r - i$) colour-colour diagram with the objects selected from J-PLUS DR1. The blue circle represents the PN candidate with ID 26063-6129, the green circle is the known PN Sp 4-1, the red diamonds are the H II galaxies LEDA 2790884 and LEDA 101538. The matches of the J-PLUS and S-PLUS data with the HASH catalogue are also presented in the diagrams. In agreement with the classification of HASH PN database. The purple circle is the true PN (tHASH PN) Jacoby 1, the brown circle is the likely PN (lHASH PN) TK 1 and the orange circles represent the possible PNe (pHASH PN) Kn J1857.7+3931, and KnPa J1848.6+4151. These objects were observed by J-PLUS. The pHASH PN Fr 2-21 is indicated by the magenta circle. This source was found in S-PLUS DR1. See text for further details. The error bars are smaller than the symbols.

known PN, and the PN candidate described in step (i). We note that this time no H II regions were selected.

As a final test, we try the most restrictive way of applying the selection criteria, as in step (iii), for which all 12 magnitude errors are limited. The result is shown in Figures 4 and 5. By applying the selection criteria in this way, we identify the same four sources as in (ii). Thus, this last step emphasises the robustness of the results obtained in step (ii), and proves that the imposed error limitation does not compromise the analysis.

No PN candidate is identified in S-PLUS DR1. We find that one true, one likely, and three possible PNe from the HASH catalogue were observed by either J-PLUS or S-PLUS. All these objects are presented in the selection diagrams (Figure 4 and Figure 5), and discussed in the rest of this section as well as in Section 6.

5.3. Photometry and spectroscopy of the PN candidate

The location of the PN candidate, with ID in J-PLUS DR1 26063-6129, (J2000 RA: J09 50 20.92, DEC: 31 29 11.02) is represented by the blue circle in Figures 4 and 5. The source displays a clear $H\alpha$ excess (see Figure 6). Also, from the (b), (c), and (d) diagrams of Figure 5, it is possible to argue that this candidate has moderate [O III] and/or $H\beta$ emission. In fact, the ($g - J0515$), ($z - g$) and ($z - i$) colours have approximate values of -0.5, 0.5, and -0.6, respectively, indicating low to moderate contribution of the [O III] and/or $H\beta$ lines to the g -band magnitude.

Figure 6 displays the PN candidate photo-spectrum, whose shape is very similar to that of typical PNe in the J-PLUS and S-PLUS configurations (see, for instance, panels (a) and (b) of

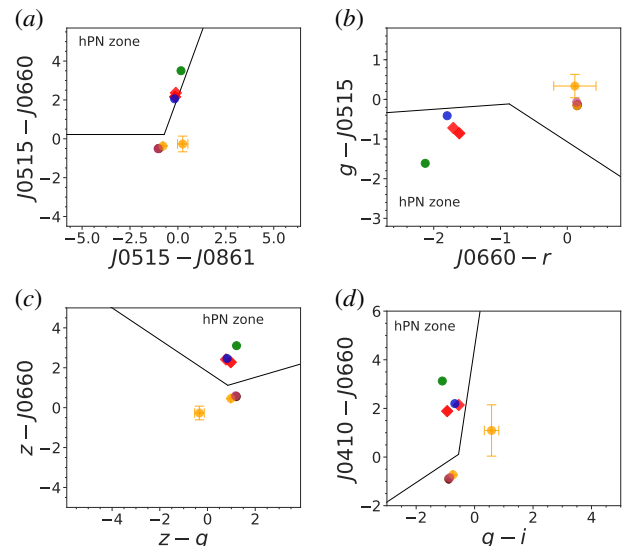


Fig. 5. J-PLUS and S-PLUS (a) ($J0515 - J0660$) vs ($J0515 - J0861$), (b) ($g - J0515$) vs ($J0660 - r$), (c) ($z - J0660$) vs ($z - g$), and (d) ($J0410 - J0660$) vs ($g - i$) colour-colour diagrams. The symbols are the same as in Figure 4.

Figure 1), with strong emission lines and relatively flat continuum. From its J-PLUS $H\alpha$ image, we derived an angular radius of ~ 1.5 arcsec. This figure also presents a composite g , r , and i image centred on the candidate. It clearly shows another object, a diffuse emission, which we identified as the UGC 5272 galaxy, at 7 Mpc (Garrido et al. 2004; (Karachentsev et al. 2014)). If the candidate was at the distance of UGC 5272, it would have a size of 40-50 pc, and it would be a H II region. It could also be a Milky Way halo source, at 30 to 40 kpc, for instance, displaying a 0.2 to 0.3 pc size.

The PN candidate was observed with the 2.54-m INT at Roque de los Muchachos observatory in La Palma (Spain), on November 15 2018, using the Intermediate Dispersion Spectrograph (IDS). The spectrum of the candidate, together with the J-PLUS photometry, is presented in Figure 7. The fluxes of the emission lines detected in our spectrum are presented in Table 2. Based on the $H\alpha$, $H\beta$, and $H\gamma$ lines, its extinction is 0.35. From the observed central wavelength of the detected lines, we also derived the heliocentric velocity of the source, 515 km s^{-1} . This value agrees with the heliocentric velocity of the galaxy ($513 \pm 2 \text{ km s}^{-1}$ Garrido et al. 2004), and it confirms that our J-PLUS PN candidate belongs to UGC 5272. The [S II] $\lambda\lambda 6716/6731$ diagnostic ratio of 1.75 suggests a very tenuous H II region.

5.4. Recovering DR1 known $H\alpha$ emitters

One PN and two H II galaxies were recovered applying our selection methodology to the J-PLUS catalogue.

PN Sp 4-1 (J2000 RA: 19 00 26.5, DEC: 38 21 07.99), also called PN G068.7+14.8, is a previously confirmed compact Galactic PN (Acker et al. 1992; Moreno-Ibáñez et al. 2016). In the diagrams of Figures 4 and 5, Sp 4-1 is represented by the green circle. The colours ($J0515 - J0660$) and ($g - J0515$) are estimated to be 3.4 and -1.6, respectively. The former colour clearly indicates a strong $H\alpha$ emitter, while the latter implies a significant contribution from the [O III] and $H\beta$ lines to the g -band. The upper panel of Figure 8 displays its photo-spectrum and corresponding image.

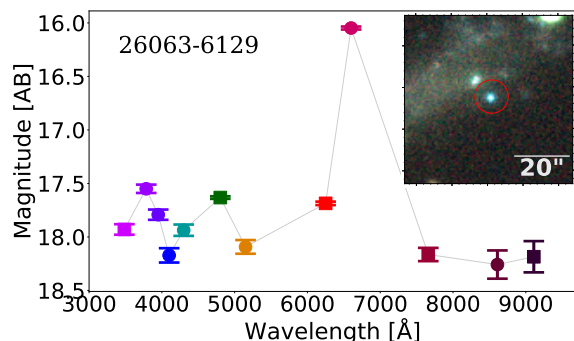


Fig. 6. Photo spectrum and a combination of the g , r , and i broad-band images of the J-PLUS PN candidate.

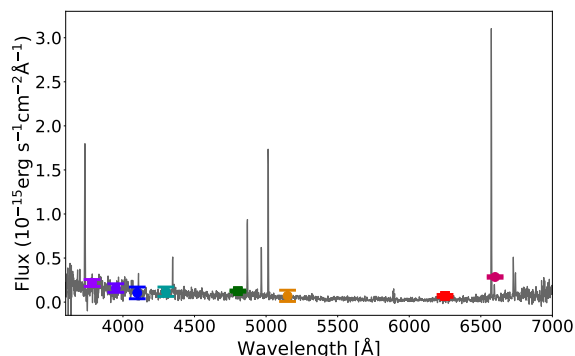


Fig. 7. INT IDS spectrum (not corrected by extinction) of the J-PLUS PN source. The coloured points represent the J-PLUS photometry in flux units.

Table 2. Emission line fluxes of J-PLUS PN candidate. The five columns show, respectively, the line identification, the rest frame and observed central wavelengths, the observed fluxes, and the extinction corrected intensities.

| Line | $\lambda_{\text{rest}}(\text{Å})$ | $\lambda_{\text{Obs}}(\text{Å})$ | F^a | I^a |
|----------------------------|-----------------------------------|----------------------------------|-------|-------|
| [O II] ^b | 3727.0 | 3734.3 | 290.6 | 357.8 |
| H δ | 4101.7 | 4108.4 | 24.8 | 28.7 |
| H γ | 4340.5 | 4347.3 | 41.7 | 46.2 |
| H β | 4861.4 | 4869.1 | 100.0 | 100.0 |
| [O III] | 4958.9 | 4966.8 | 67.9 | 66.6 |
| [O III] | 5006.8 | 5014.8 | 199.4 | 193.7 |
| [He I] | 5875.6 | 5888.9 | 29.6 | 24.9 |
| H α | 6562.8 | 6573.5 | 373.7 | 288.5 |
| [N II] | 6583.4 | 6594.4 | 22.3 | 17.2 |
| [S II] | 6716.4 | 6727.3 | 53.2 | 40.3 |
| [S II] | 6730.8 | 6742.0 | 30.4 | 23.1 |
| F(H β) ^c | – | – | 3.246 | – |

Notes. ^(a) In units of $H\beta = 100$. ^(b) Blended line. ^(c) In units of $10^{-15} \text{ erg cm}^{-2} \text{ s}^{-1}$.

There is no doubt that these data correspond to those of a typical PN photo-spectrum, of a roundish and compact object with full width at half maximum (FWHM) ~ 1.3 arcsec.

LEDA 2790884 (J2000 RA: 8 25 55.50, DEC: 35 32 32.01) is a H II galaxy (blue compact galaxy) at $z \sim 0.0024$ (Moiseev et al. 2010). The loci where the system is represented in the diagrams of Figures 4 and 5 (one of the red diamonds) corresponds to that of a low-excitation PN, in agreement with the expectations from

the H II regions. The photo-spectrum and image of this source are shown in the middle panel of Figure 8.

LEDA 101538 (J2000 RA: 16 16 23.51, DEC: 47 02 02.64), the red diamond in Figure 5, is a H II galaxy (blue compact dwarf galaxy) at $z \sim 0.002$, with a very blue colour, which indicates that it is likely a starburst (Ann et al. 2015). The photo-spectrum of this galaxy is presented in the lower panel of Figure 8. The spectra of the H II galaxies are very similar to those of giant extragalactic H II regions (Sargent & Searle 1970). For this reason, *LEDA 101538* lies in the PN zone, even though it is not a PN.

6. DR1 vs. the complete PNe catalogue - HASH

We cross-matched the J-PLUS and S-PLUS data with the HASH catalogue (Parker et al. 2016). We remind the reader that this catalogue contains all known PNe, which are classified as *true*, *likely* and *possible* PNe. We found four matches with J-PLUS, and one with S-PLUS. The J-PLUS ones appear in the colour-colour diagrams as purple (1 true PN), brown (1 likely PN), and orange (2 possible PNe) circles, while the S-PLUS match is the dark magenta (1 possible PN) circle in Figures 4 and 5. It is simple to see from these diagnostic diagrams that, following our selection criteria, none of these sources are classified as PNe, all being located outside the PN zone. Four of these HASH sources are located in the zone of very blue WDs. Why does this happen? Below, we describe each source, thus highlighting that their sizes preclude their automatic recovery by our criteria.

6.1. J-PLUS

Jacoby 1 (J2000 RA: 15 21 46.56, DEC: 52 22 04.05) is classified as a true (tHASH) PN, previously reported by Jacoby & van de Steene (1995). The low ($r - J0660$) and ($J0515 - J0660$) colour indices are indicative of very weak, or totally absent, H α line-emission. The first panel of Figure 9 displays the photo-spectrum, which turns out to be typical for white dwarfs (e.g. Figure 14 of Cenarro et al. 2019) and its combined image (right inset image of the figure). Following Tweedy & Kwitter (1996), *Jacoby 1* is a highly evolved PN of ~ 11 arcmin in size. Such large sizes can not be recovered/found by automatic photometric criteria, this is only possible by visual inspection of the fields (e.g. Sabin et al. 2014). We managed to detect the H α emission from the PN by applying a Gaussian smoothing filter of 10 pixels to the combined RGB – $J0660$, r , and i – as shown in the left inset in Figure 9.

TK 1 (J2000 RA: 08 27 05.52, DEC: 31 30 08.10) is a likely (lHASH) PN, of up to 15 arcmin (Tweedy & Kwitter 1996). Its position in our colour-colour diagrams is very close to *Jacoby 1* suggesting similar spectral characteristics (see photo-spectrum in the second panel of Figure 9). So, we suggest that the recovered emission is that of a WD star, in agreement with Rebassa-Mansergas et al. (2015). The above technique that recovered the nebular emission of *Jacoby 1* was used, though it could not confirm the nebula that is possibly surrounding this white dwarf.

Kn J1857.7+3931 (J2000 RA: 18 57 42.24, 39 31 00.13) is a possible (pHASH) PN. It shares the same position in the diagnostic diagrams, as well as an akin photo-spectrum, with *Jacoby 1* and *TK 1* (see Figure 9). Nevertheless, when we looked for the extended nebula, this was not detected. We argue that *Kn J1857.7+3931* is also a WD star, possibly associated with a nebular emission too faint to be detected by J-PLUS.

KnPa J1848.6+4151 (J2000 RA: 18 48 38.36, DEC: 41 51 02.52), another pHASH PN, is located far from the other HASH objects in our colour-colour diagrams (orange circle with large

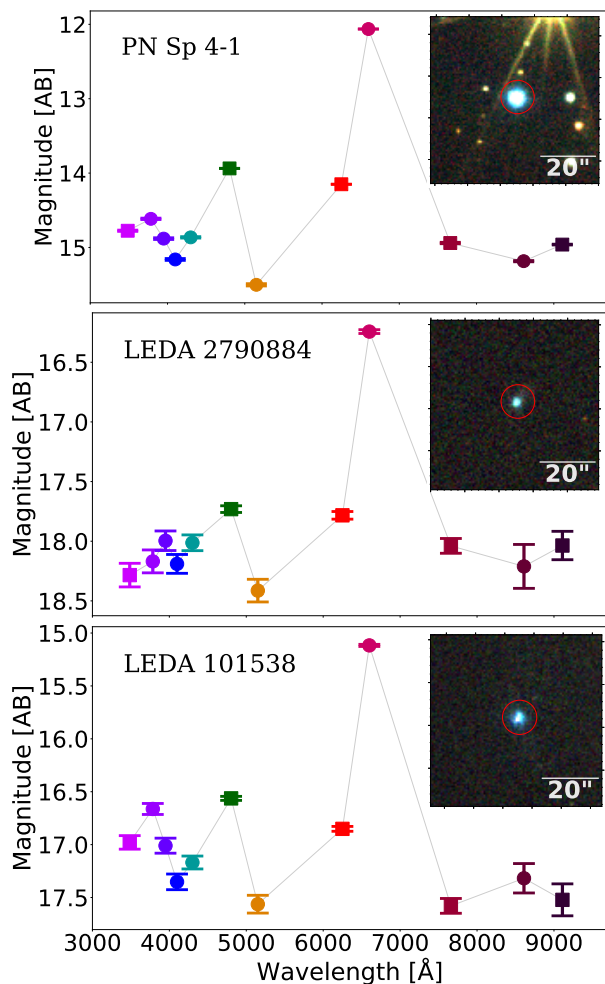


Fig. 8. J-PLUS photo-spectra and corresponding images of disc Galactic PN Sp 4-1 (*upper panel*), H II galaxy LEDA 2790884 (*middle panel*) and H II galaxy LEDA 101538 (*lower panel*). These objects were recovered by applying the colour-colour diagrams. The images resulted from the combination of the J-PLUS broad-band filters: *g*, *r*, and *i*.

error bar), and again with no $H\alpha$ excess. *KnPa J1848.6+4151* lies in the regime of SDSS SFG and QSOs (fourth panel of Figure 9). It is a very faint object with $r \sim 19.5$ and its estimated angular size is of $\sim 10.3''$. *KnPa J1848.6+4151* is very likely a galaxy (e.g. Figure 16 of Cenarro et al. 2019; Alam et al. 2015; Greiss et al. 2012), and less likely to be a genuine PN.

6.2. S-PLUS

Fr 2-21 (J2000 RA: 21 26 21.17, DEC: 00 58 34.22) is also called PHL 4, and previously identified as a hot subdwarf (Kilkenny 1984), in addition to being a pHASH PN. It is located very close to the other HASH objects in the diagnostic diagrams. Its properties (Figure 10) suggest another WD. No extended nebula was found combining J0660, *r* and *i* images.

7. Discussion and Conclusions

The results described above highlight the potential of the data provided by J-PLUS and S-PLUS to explore the population of planetary nebulae in the Galactic halo. The developed photometric

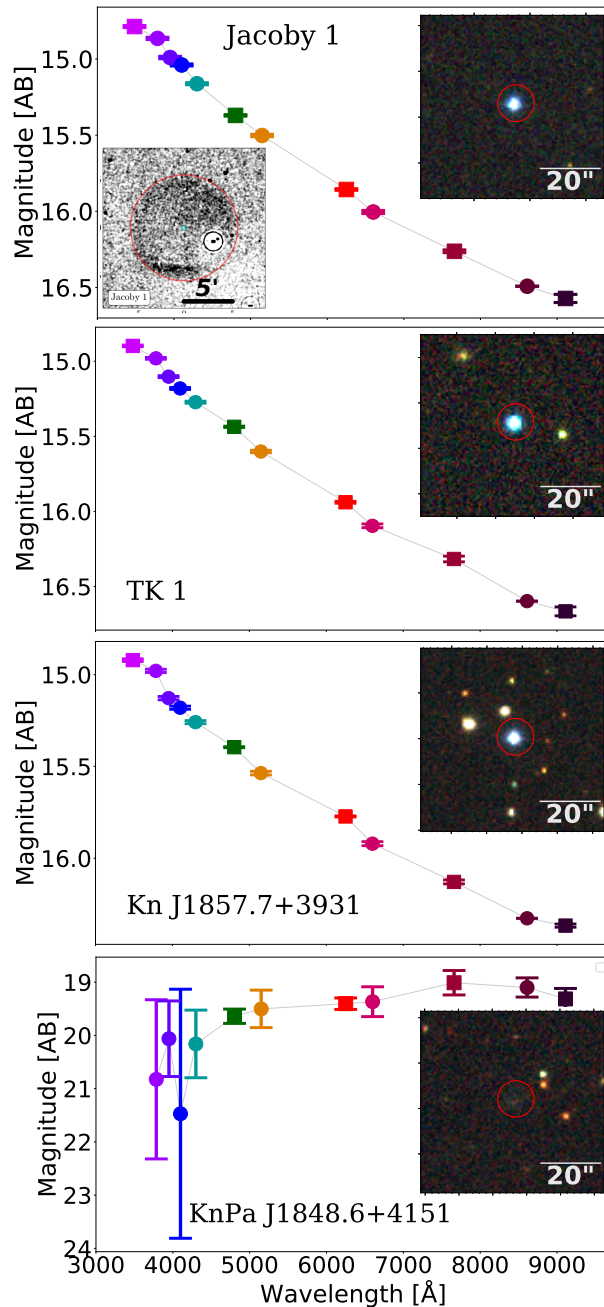


Fig. 9. (*First panel*) J-PLUS photo-spectra, corresponding composite images (*upper-right inset image*), as in Figure 8 and composite – J0660, *r*, and *i* – image (*lower-left inset image*) of tHASH PN Jacoby 1. The extended PN is clearly visible, as indicated by the red circle. The $H\alpha$ emission is detected by applying a Gaussian smoothing filter of 10 pixels. Photo-spectra and corresponding images of IHASH PN TK 1 (*second panel*), pHASH PNe Kn J1857.7+3931 (*third panel*), and KnPa J1848.6+4151 (*fourth panel*) of the HASH PN catalogue.

tools used to identify strong emission-line sources were applied to the very limited area surveyed up to now – in both J-PLUS and S-PLUS – returning promising results.

Our selection criteria were very successful in avoiding all the strong emission-line emitters present in the fields, apart from the compact H II regions (H II galaxies), which means that J-PLUS and S-PLUS can really do a good job in terms of searching

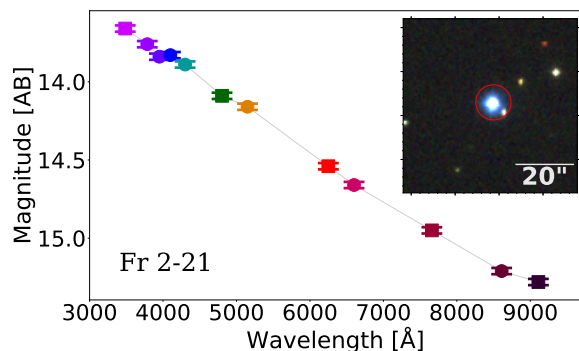


Fig. 10. S-PLUS photo-spectrum of Fr 2-21 and corresponding image. This object is classified as possible PN in the HASH catalogue.

for PNe, at the same time minimising the list of spectroscopic follow-up candidates. As anticipated in Section 3, the ability of photometrically distinguish PNe and H II regions is strongly hampered by the similarities between low-excitation PNe and H II regions. Therefore, our only way of avoiding lots of H II regions among the candidates is by limiting the automatic search to compact PN. For this reason, we adopt apertures up to 6 arcsec. Unfortunately, the first PN candidate identified in these surveys turned out to be a H II region located in the UGC 5271 galaxy, which resembles a compact PN.

The larger planetary nebulae with lower density and corresponding lower surface brightness are more difficult to discover. These objects are essentially undetectable by survey methods. The cross-match between the HASH and J-PLUS/S-PLUS catalogues made this point very clear. The magnitudes of the resultant PNe matches correspond only to the photometry of the central WDs, as can be seen from their photo-spectra with no H α emission.

As in the case of IPHAS, a parallel study needs to be done in order to find extended PNe (Sabin et al. 2014). It is necessary to bin the images in order to increase the surface brightness of the extended nebula and make their recovery feasible by visually inspecting one by one the images of the surveys.

In conclusion, we considered the photometric systems of two twin imaging surveys (J-PLUS and S-PLUS), by using the synthetic photometry of different types of strong emission-line sources, to select the best combination of filters and construct diagnostic colour-colour diagrams to isolate hPNe. We reproduced the equivalent IPHAS and proposed four new diagnostic colour-colour diagrams to separate hPNe from SySt, CVs, B[e] stars, QSOs, extragalactic H II regions, star-forming galaxies, and young stellar objects. We find that there is a high probability that a candidate found by our criteria will end up being a genuine PN if it is located well within the PN zones in the IPHAS equivalent and the other four colour-colour diagrams we proposed. It is also true that J-PLUS and S-PLUS are not completely successful at discriminating low-excitation PNe from compact H II regions (H II galaxies). We have validated our colour-colour diagrams through the photometry of the known hPNe H 4-1 and PNG 135.9+55.9 observed by J-PLUS during the SVD phase, and by applying them to the J-PLUS DR1 and S-PLUS DR1, which make up an observed area of the sky of $\sim 1,190$ deg 2 .

Having proven that our selection criteria are very effective in selecting PN candidates, even considering the contamination by H II regions/galaxies, we intend to continuously apply these photometric tools to the forthcoming J-PLUS and S-PLUS data releases, to provide a more complete list of hPN candidates for spectroscopic follow-up.

Acknowledgements. The authors acknowledge anonymous referee for very insightful comments and for helping us to significantly improve our paper. We thank J. A. Caballero and R. Lopes de Oliveira for their useful comments and suggestions. LAGS acknowledges the support of CAPES -the Brazilian Federal Agency for Support and Evaluation of Graduate Education within the Ministry of Education of Brazil. DRG thanks the partial support of CNPq (grant 304184/2016-0) and S.A. acknowledges CAPES for a fellowship from the National Postdoctoral Program (PNPD). L.G. was funded by the European Union’s Horizon 2020 research and innovation programme under the Marie Skłodowska-Curie grant agreement No. 839090. R.L.O. was partially supported by the Brazilian agency CNPq (PQ 302037/2015-2). This work is based on observations made with the JAST/T80 telescope at the Observatorio Astrofísico de Javalambre (OAJ), in Teruel, owned, managed and operated by the Centro de Estudios de Física del Cosmos de Aragón. Funding for the J-PLUS Project has been provided by the Governments of Spain and Aragón through the Fondo de Inversiones de Teruel, the Spanish Ministry of Economy and Competitiveness (MINECO: under grants AYA2015-66211-C2-1-P, AYA2015-66211-C2-2, AYA2012-30789 and ICTS-2009-14), and European FEDER funding (FCDD10-4E-867, FCDD13-4E-2685). The Brazilian agencies FAPESP and the National Observatory of Brazil have also contributed to this project. We acknowledge the OAJ Data Processing and Archiving Unit (UPAD) for reducing and calibrating the OAJ data used in this work. This study used data collected at the T80-South, a new 0.826 meter telescope carried out by S-PLUS project. The T80-South robotic telescope (Mendes de Oliveira et al. 2019) was founded as a partnership between the São Paulo Research Foundation (FAPESP), the Observatório Nacional (ON), the Federal University of Sergipe (UFS) and the Federal University of Santa Catarina (UFSC), with important financial and practical contributions from other collaborating institutes in Brazil, Chile (Universidad de La Serena) and Spain (CEFCa). We want to thank to the S-PLUS team for the reducing and calibrating of the data. This research has made use of the HASH PN database at hashpn.space. Funding for the Sloan Digital Sky Survey IV has been provided by the Alfred P. Sloan Foundation, the U.S. Department of Energy Office of Science, and the Participating Institutions. SDSS-IV acknowledges support and resources from the Center for High-Performance Computing at the University of Utah. The SDSS web site is www.sdss.org. SDSS-IV is managed by the Astrophysical Research Consortium for the Participating Institutions of the SDSS Collaboration including the Brazilian Participation Group, the Carnegie Institution for Science, Carnegie Mellon University, the Chilean Participation Group, the French Participation Group, Harvard-Smithsonian Center for Astrophysics, Instituto de Astrofísica de Canarias, The Johns Hopkins University, Kavli Institute for the Physics and Mathematics of the Universe (IPMU) / University of Tokyo, the Korean Participation Group, Lawrence Berkeley National Laboratory, Leibniz Institut für Astrophysik Potsdam (AIP), Max-Planck-Institut für Astronomie (MPIA Heidelberg), Max-Planck-Institut für Astrophysik (MPA Garching), Max-Planck-Institut für Extraterrestrische Physik (MPE), National Astronomical Observatories of China, New Mexico State University, New York University, University of Notre Dame, Observatório Nacional / MCTI, The Ohio State University, Pennsylvania State University, Shanghai Astronomical Observatory, United Kingdom Participation Group, Universidad Nacional Autónoma de México, University of Arizona, University of Colorado Boulder, University of Oxford, University of Portsmouth, University of Utah, University of Virginia, University of Washington, University of Wisconsin, Vanderbilt University, and Yale University.

References

- Acker, A., Marcout, J., Ochsenbein, F., et al. 1992, The Strasbourg-ESO Catalogue of Galactic Planetary Nebulae. Parts I, II.
- Akras, S., Guzman-Ramirez, L., & Gonçalves, D. R. 2019c, Monthly Notices of the Royal Astronomical Society, 488, 3238
- Akras, S., Guzman-Ramirez, L., Leal-Ferreira, M. L., & Ramos-Larios, G. 2019, ApJS, 240, 21
- Alam, S., Albareti, F. D., Allende Prieto, C., et al. 2015, ApJS, 219, 12
- Alcalá, J. M., Natta, A., Manara, C. F., et al. 2014, VizieR Online Data Catalog, 356
- Angeloni, R., Gonçalves, D. R., Akras, S., et al. 2019, AJ, 157, 156
- Ann, H. B., Seo, M., & Ha, D. K. 2015, ApJS, 217, 27
- Aparicio Villegas, T., Alfaro, E. J., Cabrera-Caño, J., et al. 2010, AJ, 139, 1242
- Benítez, N., Dupke, R., Moles, M., et al. 2015, in Highlights of Spanish Astrophysics VIII, ed. A. J. Cenarro, F. Figueras, C. Hernández-Monteagudo, J. Trujillo Bueno, & L. Valdivielso, 148–153
- Bertin, E. & Arnouts, S. 1996, Astronomy and Astrophysics Supplement Series, 117, 393
- Bessell, M. S. 2005, ARA&A, 43, 293
- Boumis, P., Akras, S., Xilouris, E. M., et al. 2006, MNRAS, 367, 1551
- Boumis, P., Paleologou, E. V., Mavromatakis, F., & Papamastorakis, J. 2003, MNRAS, 339, 735

- Cenarro, A. J., Moles, M., Cristóbal-Hornillos, D., et al. 2019, *A&A*, 622, A176
- Cenarro, A. J., Moles, M., Marín-Franch, A., et al. 2014, in *Proc. SPIE*, Vol. 9149, *Observatory Operations: Strategies, Processes, and Systems V*, 91491I
- Corradi, R. L. M., Mikolajewska, J., & Mahoney, T. J., eds. 2003, *Astronomical Society of the Pacific Conference Series*, Vol. 303, *Symbiotic Stars Probing Stellar Evolution*
- Corradi, R. L. M., Rodríguez-Flores, E. R., Mampaso, A., et al. 2008, *A&A*, 480, 409
- Drew, J. E., Greimel, R., Irwin, M. J., et al. 2005, *MNRAS*, 362, 753
- Ferland, G. J., Porter, R. L., van Hoof, P. A. M., et al. 2013, *rmxaa*, 49, 137
- Fitzpatrick, E. L. 1999, *PASP*, 111, 63
- Fragkou, V., Parker, Q. A., Bojičić, I. S., & Aksaker, N. 2018, *MNRAS*, 480, 2916
- Fukugita, M., Ichikawa, T., Gunn, J. E., et al. 1996, *AJ*, 111, 1748
- Garrido, O., Marcelin, M., & Amram, P. 2004, *MNRAS*, 349, 225
- Gaustad, J. E., McCullough, P. R., Rosing, W., & Van Buren, D. 2001, *PASP*, 113, 1326
- Gledhill, T. M., Froebrich, D., Campbell-White, J., & Jones, A. M. 2018, *MNRAS*, 479, 3759
- Gonçalves, D. R., Magrini, L., de la Rosa, I. G., & Akras, S. 2015, *MNRAS*, 447, 993
- Gonçalves, D. R., Magrini, L., Munari, U., Corradi, R. L. M., & Costa, R. D. D. 2008, *MNRAS*, 391, L84
- Gonçalves, D. R., Magrini, L., Teodorescu, A. M., & Carneiro, C. M. 2014, *MNRAS*, 444, 1705
- Gonçalves, D. R., Teodorescu, A. M., Alves-Brito, A., Méndez, R. H., & Magrini, L. 2012, *MNRAS*, 425, 2557
- Gonçalves, D. R. 2019, in *IAU Symposium*, Vol. 344, *Dwarf Galaxies: From the Deep Universe to the Present*, ed. K. B. W. McQuinn & S. Stierwalt, 161–177
- Greiss, S., Steeghs, D., Gänsicke, B. T., et al. 2012, *AJ*, 144, 24
- Haffner, L. M., Reynolds, R. J., Tuftes, S. L., et al. 2003, *ApJS*, 149, 405
- Henry, R. B. C., Kwitter, K. B., & Howard, J. W. 1996, *ApJ*, 458, 215
- Howard, J. W., Henry, R. B. C., & McCartney, S. 1997, *MNRAS*, 284, 465
- Ikiewicz, K. & Mikolajewska, J. 2017, *A&A*, 606, A110
- Irabor, T., Hoare, M. G., Oudmaijer, R. D., et al. 2018, *VizieR Online Data Catalog*, 748
- Jacoby, G. H. & van de Steene, G. 1995, *AJ*, 110, 1285
- Karachentsev, I. D., Kaisina, E. I., & Makarov, D. I. 2014, *AJ*, 147, 13
- Kilkenny, D. 1984, *MNRAS*, 211, 969
- Kwitter, K. B. & Henry, R. B. C. 1998, *ApJ*, 493, 247
- Kwitter, K. B. & Henry, R. B. C. 2001, *ApJ*, 562, 804
- Kwitter, K. B., Henry, R. B. C., & Milingo, J. B. 2003, *PASP*, 115, 80
- Lamers, H. J. G. L. M., Zickgraf, F.-J., de Winter, D., Houziaux, L., & Zorec, J. 1998, *A&A*, 340, 117
- Magrini, L., Gonçalves, D. R., & Vajgel, B. 2017, *MNRAS*, 464, 739
- Magrini, L., Stanghellini, L., & Gonçalves, D. R. 2012, in *IAU Symposium*, Vol. 283, *IAU Symposium*, 251–258
- Marston, A. P. & McCollum, B. 2006, in *Astronomical Society of the Pacific Conference Series*, Vol. 355, *Stars with the B[e] Phenomenon*, ed. M. Kraus & A. S. Miroshnichenko, 189
- Mendes de Oliveira, C., Ribeiro, T., Schoenell, W., et al. 2019, *MNRAS*, 489, 241
- Merrett, H. R., Merrifield, M. R., Douglas, N. G., et al. 2006, *MNRAS*, 369, 120
- Miller, J. S. 1969, *ApJ*, 157, 1215
- Moiseev, A. V., Pustilnik, S. A., & Kniazev, A. Y. 2010, *MNRAS*, 405, 2453
- Molino, A., Benítez, N., Moles, M., et al. 2014, *MNRAS*, 441, 2891
- Moreno-Ibáñez, M., Villaver, E., Shaw, R. A., & Stanghellini, L. 2016, *A&A*, 593, A29
- Munari, U. & Jurdana-Šepić, R. 2002, *A&A*, 386, 237
- Munari, U. & Zwitter, T. 2002, *A&A*, 383, 188
- Oke, J. B. & Gunn, J. E. 1983, *ApJ*, 266, 713
- Osterbrock, D. E. & Ferland, G. J. 2006, *Astrophysics Of Gas Nebulae and Active Galactic Nuclei (Sausalito: University Science Books)*
- Otsuka, M., Hyung, S., & Tajitsu, A. 2015, *ApJS*, 217, 22
- Parker, Q. A., Acker, A., Frew, D. J., et al. 2006, *MNRAS*, 373, 79
- Parker, Q. A., Bojičić, I. S., & Frew, D. J. 2016, in *Journal of Physics Conference Series*, Vol. 728, *Journal of Physics Conference Series*, 032008
- Parker, Q. A., Phillipps, S., Pierce, M. J., et al. 2005, *MNRAS*, 362, 689
- Peimbert, M. 1978, in *IAU Symposium*, Vol. 76, *Planetary Nebulae*, ed. Y. Terzian, 215–223
- Pereira, C.-B. & Miranda, L.-F. 2007, *A&A*, 467, 1249
- Pickles, A. J. 1998, *PASP*, 110, 863
- Rebassa-Mansergas, A., Liu, X.-W., Cojocaru, R., et al. 2015, *MNRAS*, 450, 743
- Rigliaco, E., Natta, A., Testi, L., et al. 2012, *A&A*, 548, A56
- Rodríguez-Flores, E. R., Corradi, R. L. M., Mampaso, A., et al. 2014, *A&A*, 567, A49
- Sabin, L., Parker, Q. A., Corradi, R. L. M., et al. 2014, *MNRAS*, 443, 3388
- Sabin, L., Zijlstra, A. A., Wareing, C., et al. 2010, *pasa*, 27, 166
- Sanduleak, N. & Stephenson, C. B. 1972, *ApJ*, 178, 183
- Sargent, W. L. W. & Searle, L. 1970, *ApJ*, 162, L155
- Tovmassian, G. H., Stasińska, G., Chavushyan, V. H., et al. 2001, *A&A*, 370, 456
- Tweedy, R. W. & Kwitter, K. B. 1996, *ApJS*, 107, 255
- Viironen, K., Greimel, R., Corradi, R. L. M., et al. 2009a, *A&A*, 504, 291
- Viironen, K., Mampaso, A., Corradi, R. L. M., et al. 2009b, *A&A*, 502, 113
- Williams, R. E. 1980, *ApJ*, 235, 939
- Witham, A. R., Knigge, C., Drew, J. E., et al. 2008, *MNRAS*, 384, 1277

Appendix E

Talks and posters in scientific meetings

1. *Tools to identify planetary nebulae and symbiotic stars.*
L. A. Gutiérrez-Soto, Denise R. Gonçalves, Stavros Akras and the J-PLUS & S-PLUS collaborations. 10th S-PLUS Meeting. 2019, São Paulo, Brazil. **Contributed talk.**
2. *Photometric tools to select planetary nebulae and symbiotic stars in J-PLUS and S-PLUS surveys.*
L. A. Gutiérrez-Soto, Denise R. Gonçalves, Stavros Akras and J-PLUS & S-PLUS collaborations. II Workshop: chemical abundances in gaseous nebulae. 2019, São José dos Campos, São Paulo, Brazil. **Contributed poster.**
3. *Detecting Galactic halo planetary nebulae and symbiotic stars in multi-band photometric surveys.*
L. A. Gutiérrez-Soto, D. R. Gonçalves & S. Akras. XXXth General Assembly of the International Astronomical Union (IAU). Division G: Stars and Stellar Physics, 2018, Vienna, Austria. **Contributed talk.**
4. *Galactic halo planetary nebulae and symbiotic stars in multi-band photometric surveys.*
L. A. Gutiérrez-Soto, D. R. Gonçalves & S. Akras. Workshop "Science with SOAR and Gemini telescopes: preparing for the GMT". 2018, São José dos Campos, São Paulo, Brazil. **Contributed talk.**
5. *S-PLUS, J-PLUS and J-PAS in the search for planetary nebulae.*
L. A. Gutiérrez-Soto, D. R. Gonçalves, S. Akras, A. Cortesi, S. Daflon, et al. XLI Reunião Anual da Sociedade Astronômica Brasileira 2017, 2018, São Paulo, Brazil. Boletim da Sociedade Astronômica Brasileira, 30, no. 1, 158-159. **Contributed poster.**
6. *Identifying Galactic halo PN candidates in the imaging surveys: J-PLUS/S-PLUS and J-PAS.*

L. Gutiérrez-Soto, D. R. Gonçalves, S. Akras, A. Cortesi, A. Ederoclite, et al., Latin American Regional IAU Meeting (LARIM) Cartagena 2016, 2017, Cartagena de Indias, Colombia. *Rev. Mex. Astron. Astrofís. (Serie de Conferencias)*, Vol. 49, pp. 162-162. **Contributed poster.**

S-PLUS, J-PLUS and J-PAS in the search for planetary nebulae

L. A. Gutiérrez-Soto¹, D. R. Gonçalves¹, S. Akras², A. Cortesi³, S. Daflon², A. Ederoclite⁴, M. Borges Fernandes², C. Mendes de Oliveira³, C. B. Pereira², K. Viironen⁴ & S-PLUS, J-PLUS and J-PAS collaborations

¹ Observatório do Valongo, Universidade Federal do Rio de Janeiro, Rio de Janeiro, Brazil

² Observatório Nacional - Ministério da Ciência, Tecnologia, Inovações e Comunicações, Brazil

³ IAG - Universidade de São Paulo, Brazil

⁴ Centro de Estudios de Física del Cosmos de Aragón, Pza. San Juan 1, E-44001, Teruel, Spain

Abstract. From the approximately 3,000 planetary nebulae (PNe) discovered in our Galaxy, only 14 are found to be members of the halo. Moreover, a systematic search for halo PNe was never done. We have developed tools to identify PNe in the Javalambre-Physics of the Accelerating Universe Astrophysical Survey (J-PAS) and related surveys, S-PLUS and J-PLUS, taking advantage of their great combination of narrow- and broad-band filters. The spectra of several classes of emission-line objects, which were convolved to the three photometric systems, were applied to the principal component analysis in order to find the most adequate combinations of colour to discriminate halo PNe from other objects. Here we propose colour-colour diagrams, based on these spectra. The diagrams separate halo PN candidates from other sources that resemble PNe (symbiotic stars; star-forming galaxies; cataclysmic variables; QSOs and extragalactic H II regions). We include, in our preliminary results, the photometry of a couple of halo PNe actually observed by the J-PLUS survey. Altogether, we show it is possible to discriminate halo PNe from other sources using different techniques which enclose important spectral nebular features.

Resumo. Das aproximadamente 3000 nebulosas planetárias (NPs) descobertas em nosso Galáxia, apenas 14 são membros do halo. Além disso, uma busca sistemática de NPs do halo nunca foi feita. Desenvolvemos ferramentas para detectar essas fontes no Javalambre-Physics of the Accelerating Universe Astrophysical Survey (J-PAS) e nos surveys, S-PLUS e J-PLUS, aproveitando sua ótima combinação de filtros estreitos e largos. Os espectros de vários tipos de objetos com linhas de emissão, que foram convolvidos para os três sistemas fotométricos, foram utilizados com a análise de componentes principais para encontrar as combinações de cor mais adequadas para discriminar NPs do halo de outros objetos. Aqui propomos novos diagramas cor-cor, que separam as NPs de outras fontes com linhas (estrelas simbióticas, galáxias formadoras de estrelas, variáveis cataclísmicas, QSOs e regiões H II extragalácticas). Incluímos em nossos resultados, a fotometria de um par de NPs observadas por J-PLUS. Ao todo, mostramos que é possível discriminar NPs de outras fontes usando diferentes técnicas que envolvem importantes características espectrais.

Keywords. Galaxy: halo – planetary nebulae – ISM: lines and bands

1. Motivation

Planetary nebulae (PNe) are a kind of emission line nebula that represent a short phase of the stellar evolution of low- and intermediate-mass stars ($0.8M_{\odot}$ - $8.0M_{\odot}$). During the unstable AGB phase, stars eject their outer layers into the interstellar medium resulting in an enrichment in heavy elements. Approximately, 3,000 PNe have been identified in our Galaxy (Parker et al. 2012). Of these, only fourteen objects are located in the Galactic halo (Otsuka et al. 2015). Halo PNe are interesting objects because they provide important information about the evolution of old and low-mass stars of in the halo, and allow the early chemical conditions of the Galaxy to be studied.

A number of new Galactic PNe were identified in the equatorial plane (Viironen et al. 2009) by using the $(r' - H\alpha)$ vs $(r' - i')$ colour-colour diagram in the Isaac Newton Telescope (INT) Photometric $H\alpha$ Survey of the Northern Galactic Plane (IPHAS; Drew et al. 2005). The multi-filter J-PAS, J-PLUS¹ and S-PLUS² surveys are more suitable surveys for searching PNe in the direction of Galactic halo. The combination of narrow- and broad-band filters in these surveys (in total, 56, 12 and 12, respectively) allow us to identify objects with prominent emission lines. We use the principal component analysis (PCA) to search for the most adequate combination of colours that distinguish halo PNe from their contaminants. Several colour-colour

diagrams have been generated and explored in order to separate halo PNe from other emission line objects.

2. Results

The synthetic magnitudes of various classes of objects were calculated for the filters in the three surveys, using available observed spectra, and a set of photo-ionization models for halo PNe. The spectra of PNe: DdDm-1, NGC 242 and MWC 574 were taken from Kwitter & Henry (1998), Kwitter et al. (2003) and Pereira & Miranda (2007), respectively, while the spectra of PNe H 4-1 and PNG 135.9+55.9 were obtained from the SDSS. The spectra of the rest of the objects: cataclysmic variables (CVs), star-forming galaxies and quasistellar objects (QSOs) with different redshift ranges are also from SDSS. Galactic disk symbiotic stars (SySts) were taken from Munari & Zwitter (2002) and IPHAS (Rodríguez-Flores et al. 2014), while the extragalactic SySts in IC10, NGC 185 and in NGC 205 were gathered from Gonçalves et al. (2015). Finally, H II regions in NGC 55 (Magrini et al. 2017) are also included in this analysis.

Fig. 1 displays the S-PLUS colour-colour diagram (J0515 – J0660) vs (J0515 – J0861). Halo PNe with strong $H\alpha$ emission are placed at the upper left. The J-PLUS colour-colour diagram (J0660 – gSDSS) vs (J0660 – rSDSS) is presented in Fig. 2. Note that the known PNe: H 4-1 and PNG135.9+55.9 (blue and green circles with errorbars, respectively) observed in the J-PLUS survey, during the phase of the data science verification, are located

¹ The Javalambre-Photometric Local Universe Survey

² The Southern Photometric Local Universe Survey

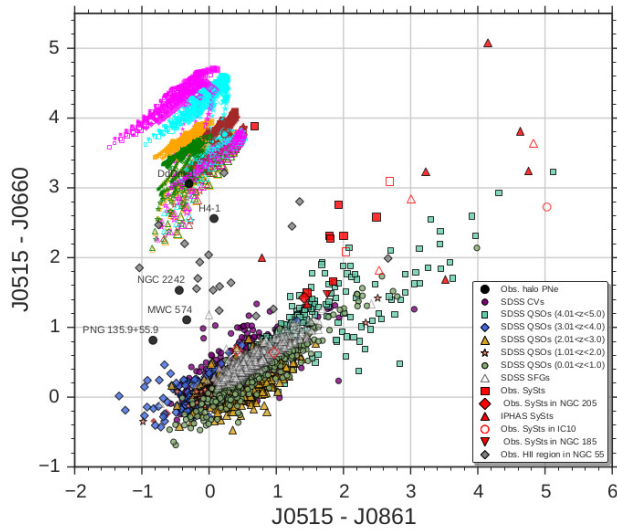


FIGURE 1. The S-PLUS colour-colour diagram (J0515-J0660) vs (J0660-J0861). Families of cloudy modelled halo PNe (the pink, cyan, orange, green and brown symbols) spanning a range of halo PN properties are included. These models represent different sets of nebular abundances, with densities of 6000 cm^{-3} (filled symbols) and 3000 cm^{-3} (empty symbols), for a spherically symmetric nebula of $2.7''$ in radius, at a distance of 10 kpc. Central star black-body effective temperatures and luminosities are from 50×10^3 to $250 \times 10^3 \text{ K}$, in steps $10 \times 10^3 \text{ K}$; and 0.5, 1.0, 5.0 and $10 \times 10^3 L_{\odot}$. The rest of the symbols are as follows: halo PNe (black circles); QSOs with redshift in the range from 0.01 to 1.0 (light green circles); 1.01 to 2.0 (light orange stars); 2.01 to 3.0 (light orange triangles); 3.01 to 4.0 (light blue diamonds); and 4.01 to 5.0 (green boxes), CVs (violet circles); star-forming galaxies (black, open triangles); symbiotic stars (red boxes); extragalactic symbiotic stars (red diamonds); symbiotic stars from IPHAS (red triangles); extragalactic H II region (gray diamonds).

very close to the regime where halo PNe are expected. The J-PAS colour-colour diagram (J4200 – J5001) vs. (J4200 – J8400) is shown in Fig. 3. The J4200 – J5001 colour is prominent for modelled and some observed halo PNe, due to the strong [O III] emission. The halo PNe MWC 574 and PNG135.9+55.9 are found at the bottom side of the diagram in the regime of QSOs. This may be associated with the very low O abundance in these PNe (e. g. Sandin et al. 2010), which results in a J4200 – J5001 colour index close to zero. A combination of colours from narrow- and broad-band filters seems to be efficient in the identification of PNe.

Acknowledgements. LAGS, DRG and SA acknowledge the support of CAPES and CNPq.

References

- Drew, J. E., Greimel, R., Irwin, M. J., et al. 2005, *MNRAS*, 362, 753
 Gonçalves, D. R., Magrini, L., de la Rosa, I. G., & Akras, S. 2015, *MNRAS*, 447, 993
 Kwitter, K. B., & Henry, R. B. C. 1998, *ApJ*, 493, 247
 Kwitter, K. B., Henry, R. B. C., & Milingo, J. B. 2003, *PASP*, 115, 80
 Magrini, L., Gonçalves, D. R., & Vajgel, B. 2017, *MNRAS*, 464, 739
 Munari, U., & Zwitter, T. 2002, *A&A*, 383, 188
 Otsuka, M., Hyung, S., & Tajitsu, A. 2015, *ApJS*, 217, 22
 Parker, Q. A., Cohen, M., Stupar, M., et al. 2012, *MNRAS*, 427, 3016
 Pereira, C.-B., & Miranda, L.-F. 2007, *A&A*, 467, 1249
 Rodríguez-Flores, E. R., Corradi, R. L. M., Mampaso, A., et al. 2014, *A&A*, 567, A49
 Sandin, C., Jacob, R., Schönberner, D., Steffen, M., & Roth, M. M. 2010, *A&A*, 512, A18

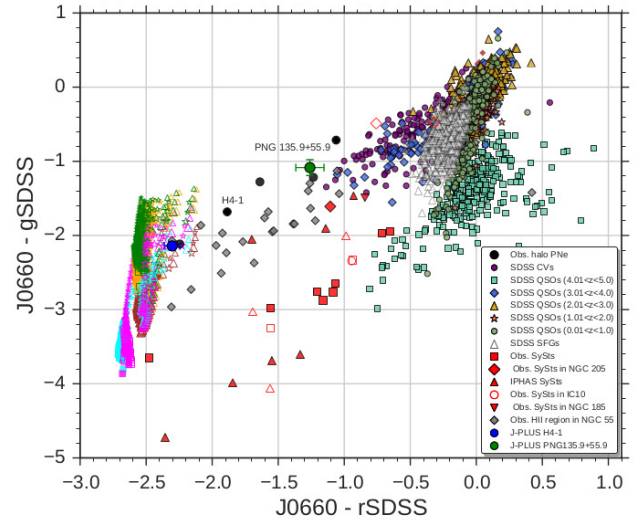


FIGURE 2. The J-PLUS colour-colour diagram (J0660 – gSDSS) vs (J0660 – rSDSS). The blue and green symbols with errorbars are the J-PLUS observations for H 4-1 and PNG 135.9+55.9 respectively. The rest of the symbols are the same as in Fig. 1.

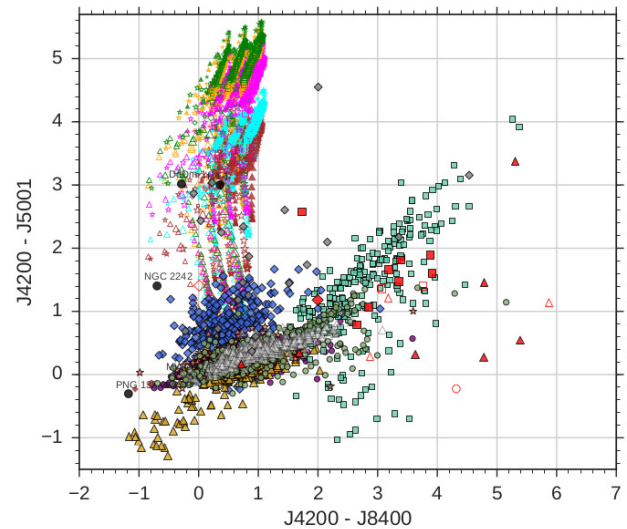


FIGURE 3. The J-PAS colour-colour diagram (J4200 – J5001) vs (J4200 – J8400). The symbols are the same as in Fig. 1.

Viironen, K., Mampaso, A., Corradi, R. L. M., et al. 2009, *A&A*, 502, 113

ESTIMATION OF THE STELLAR EFFECTIVE
TEMPERATURE AND STELLAR WIND
DETECTION IN A HERBIG AE/BE TYPE
STAR FROM SPECTRA ACQUIRED IN
BOGOTÁ - COLOMBIA

I. L. Guasca Garnica¹, O. L. Ramírez Suárez²,
B. Oostra Vannoppen³, G. Chaparro Molano²,
and O. A. Restrepo Gaitán²

We present the results of spectroscopic observations in the range of 4280-6800 Å of AB Aur, a Herbig Ae/Be type star. These observations were carried out at the Observatory of the Universidad de los Andes in Bogotá - Colombia in 2015. We select the 4280-6000 Å spectral window for fitting our data to a black-body model of the star. In this range, the effects due to circumstellar disk emission are negligible and the neighborhood of the prominent accretion H α emission line is neglected. In this window the dominant lines due atomic processes are the Balmer series lines H β and H γ . We remove data around 3σ for each of these lines in order to ignore quantum effects. We model the stellar continuum by doing a Monte Carlo bootstrap-sampled fitting of three parameters: (i) a bolometric correction factor due to atmospheric absorption and/or defect electronics, (ii) measured (relative) continuum flux, and (iii) stellar temperature T_{eff} . We obtain a value for the stellar temperature of 9400K-9700K, in agreement with the temperature reported by Tannirkulam et al. 2008. We also successfully fitted the H lines using a two-component gaussian fit, which shows the effects of stellar wind on top of the gas accretion onto the star. Our measurements strongly suggest that even in the harsh observational conditions present in Colombia, it is possible to obtain quality astronomical data for teaching astrophysics at an undergraduate level.

¹ Semillero de Astronomía, Universidad Pedagógica Nacional, Bogotá, Colombia.

² Grupo de Simulación, Análisis y Modelado (SiAMo), Universidad ECCI, Bogotá, Colombia (oramirez@ecci.edu.co).

³ Observatorio Astronómico, Universidad de los Andes, Bogotá, Colombia.

IDENTIFYING GALACTIC HALO PN
CANDIDATES IN THE IMAGING SURVEYS:
J-PLUS/S-PLUS AND J-PAS

L. Gutiérrez-Soto¹, D. R. Gonçalves¹, S. Akras²,
A. Cortesi³, A. Ederoclite⁴, T. Aparício-Villegas^{2,5},
M. Borges-Fernandes², S. Daflon², C. B. Pereira²,
C. Mendes de Oliveira³, K. Viironen⁴, and the
J-PAS Collaboration

Halo planetary nebulae (HPNe) are able to reveal important information about stellar and chemical evolution in galaxies. Their characteristic low continuum and strong emission lines make them good objects to be searched by multi-filter imaging surveys. Given that only 14 HPNe are known in the Galaxy, we are exploring colour-colour diagrams to search for these sources in Javalambre/Southern Photometric Local Universe Survey (J-PLUS/S-PLUS) and the Javalambre-Physics of the Accelerating Universe Astrophysical Survey (J-PAS). They are narrow- and broad-band imaging cosmological surveys, with 12 and 54 filters, respectively.

The J-PAS survey will be able to observe 8500 deg² of Northern sky, it will detect sources up to magnitude $m_{\text{AB}} \sim 23$. In the case of the J-PLUS survey the limit magnitudes is around $m_{\text{AB}} \sim 21.5$. The S-PLUS survey will observe more than 6000 deg² and it will map the Southern sky.

Other optical emission lines sources, such as Galactic and extragalactic symbiotic stars (SySts), cataclysmic variables (CVs), QSOs at different redshifts, star-forming galaxies (SFGs), extragalactic H II regions and supernova remnants (SNR) can mimic PNe. Therefore, we explore different colour-colour diagrams in order to highlight those that can better identify HPN candidates, separating them from these other objects.

¹ Observatório do Valongo, Universidade Federal do Rio de Janeiro, Ladeira Pedro Antonio 43, 20080-090 Rio de Janeiro, Brazil (lgutierrez@astro.ufrj.br).

² Observatório Nacional, MCTI, Brazil.

³ IAG, Universidade de São Paulo, Brazil.

⁴ Centro de Estudios de Física del Cosmos de Aragón, Spain.

⁵ Instituto de Astrofísica de Andalucía, Spain.